

1.0

1.1

1.25

4.5
5.0
5.6
6.3
7.1
8.0
9.0
10.0

1.4

2.8

3.2

3.6

4.0

2.5

2.2

2.0

1.8

1.6

AD-A189 139

REPORT DOCUMENTATION PAGE

Form Approved
OMB No. 0704-0188

1a. REPORT SECURITY CLASSIFICATION UNCLASSIFIED		1b. RESTRICTIVE MARKINGS	
2a. SECURITY CLASSIFICATION AUTHORITY		3. DISTRIBUTION STATEMENT Approved for public release and sale in distribution is unlimited.	
2b. DECLASSIFICATION/DOWNGRADING SCHEDULE		4. PERFORMING ORGANIZATION REPORT NUMBER(S) Gas Delivery System and Beamline Studies for the Test Beam Facility of the Collider Detector at Fermilab	
6a. NAME OF PERFORMING ORGANIZATION Texas A&M University		6b. OFFICE SYMBOL (if applicable)	
6c. ADDRESS (City, State, and ZIP Code) College Station, TX 77843		5. MONITORING ORGANIZATION REPORT NUMBER(S) Final approval on 4 Dec 87	
8a. NAME OF FUNDING/SPONSORING ORGANIZATION		7a. NAME OF MONITORING ORGANIZATION HQDA, MILPERCEN, ATTN: DAPC-OPA-E	
8b. OFFICE SYMBOL (if applicable)		7b. ADDRESS (City, State, and ZIP Code) 200 Stovall St, Alexandria, VA 22332	
8c. ADDRESS (City, State, and ZIP Code)		9. PROCUREMENT INSTRUMENT IDENTIFICATION NUMBER	
10. SOURCE OF FUNDING NUMBERS		10. SOURCE OF FUNDING NUMBERS	
		PROGRAM ELEMENT NO.	PROJECT NO.
		TASK NO.	WORK UNIT ACCESSION NO.
11. TITLE (Include Security Classification) GAS DELIVERY SYSTEM AND BEAMLINE STUDIES FOR THE TEST BEAM FACILITY OF THE COLLIDER DETECTOR AT FERMILAB (Unclassified)			
12. PERSONAL AUTHOR(S) FRANKE, Henry Gerhart III			
13a. TYPE OF REPORT Final	13b. TIME COVERED FROM 870701 TO 871106	14. DATE OF REPORT (Year, Month, Day) 8712	15. PAGE COUNT 243
16. SUPPLEMENTARY NOTATION Approved for public release; distribution is unlimited.			
17. COSATI CODES		18. SUBJECT TERMS (Continue on reverse if necessary and identify by block number)	
FIELD	GROUP	SUB-GROUP	
		Fixed-Target Charged Particle Beamline; Test Beam Facility; High Energy Physics; Thesis submitted in partial fulfillment of requirements for a Master of Science degree in Physics.	
19. ABSTRACT (Continue on reverse if necessary and identify by block number)			
A fixed-target test beam facility has been designed and constructed at the Meson Test (MT) site to support studies of components of the Collider Detector at Fermi National Accelerator Laboratory (CDF). <i>It</i> assisted in the design and construction of the test beam facility gas delivery system, and I conducted the initial studies to document the ability of the MT beamline to meet the needs of CDF. Analysis of the preliminary performance data on MT beamline components and beam tunes at required particle energies is presented. Preliminary studies show that the MT beamline has the necessary flexibility to satisfy most CDF requirements now. <i>Key words</i>			
20. DISTRIBUTION/AVAILABILITY OF ABSTRACT <input checked="" type="checkbox"/> UNCLASSIFIED/UNLIMITED <input type="checkbox"/> SAME AS RPT. <input type="checkbox"/> DTIC USERS		21. ABSTRACT SECURITY CLASSIFICATION UNCLASSIFIED	
22a. NAME OF RESPONSIBLE INDIVIDUAL CPT Henry G. Franke III		22b. TELEPHONE (Include Area Code) (817) 547-5767	22c. OFFICE SYMBOL E

DTIC ELECTE
S
DEC 17 1987
E

Gas Delivery System and Beamline Studies for the Test Beam Facility of
the Collider Detector at Fermilab

HQDA, MILPERCEN (DAPC-OPA-E)
200 Stovall Street
Alexandria, VA 22332

Final Approval on 4 Dec 87

Approved for public release; distribution is unlimited.

A thesis submitted to Texas A&M University, College Station, TX 77843,
in partial fulfillment of the requirements for the degree of Master of
Science (Physics).

87 12 10 023

GAS DELIVERY SYSTEM AND BEAMLINE STUDIES FOR THE
TEST BEAM FACILITY OF THE COLLIDER DETECTOR AT FERMILAB

A Thesis

by

HENRY GERHART FRANKE III

Submitted to the Graduate College of
Texas A&M University
in partial fulfillment of the requirement for the degree of
MASTER OF SCIENCE

December 1987

Major Subject: Physics

Accession For	
NTIS GRA&I	<input checked="" type="checkbox"/>
DTIC TAB	<input type="checkbox"/>
Unannounced	<input type="checkbox"/>
Justification	
By _____	
Distribution/	
Availability Codes	
Dist	Avail and/or Special
A-1	

GAS DELIVERY SYSTEM AND BEAMLINER STUDIES FOR THE
TEST BEAM FACILITY OF THE COLLIDER DETECTOR AT FERMILAB

A Thesis

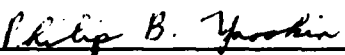
by

HENRY GERHART FRANKE III

Approved as to style and content by:



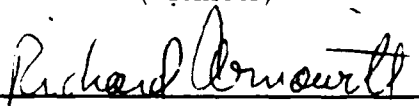
Thomas Meyer
(Chairman of Committee)



Philip B. Yasskin
(Member)



Robert C. Webb, Sr.
(Member)



Richard L. Arnowitt
(Head of Department)

December 1987

ABSTRACT

Gas Delivery System and Beamline Studies for the
Test Beam Facility of the Collider Detector at Fermilab. (December 1987)

Henry Gerhart Franke III, B.S., Texas A&M University

Chairman of Advisory Committee: Dr. Thomas Meyer

A fixed-target test beam facility has been designed and constructed at the Meson Test (MT) site to support studies of components of the Collider Detector at Fermi National Accelerator Laboratory (CDF). I assisted in the design and construction of the test beam facility gas delivery system, and I conducted the initial studies to document the ability of the MT beamline to meet the needs of CDF. Analysis of the preliminary performance data on MT beamline components and beam tunes at required particle energies is presented. Preliminary studies show that the MT beamline has the necessary flexibility to satisfy most CDF requirements now.

ACKNOWLEDGMENTS

I wish to express my deep appreciation to Roger Tokarek and Dr. John Cooper, both of Fermi National Accelerator Laboratory, who gave a great deal of themselves and of their time in supporting my efforts to understand charged-particle beam transport and the workings of the Meson Test beamline. Their patience and good will made this project an enjoyable one. I also wish to acknowledge Fermi National Accelerator Laboratory for its support in carrying out my research and the United States Army for providing me the opportunity to pursue this degree under the fully-funded advanced civil schooling program. This work has been supported in part by the U.S. Department of Energy under Contract No. DE-AS05-81ER40039.

TABLE OF CONTENTS

	ABSTRACT	iii
	ACKNOWLEDGMENTS	iv
	TABLE OF CONTENTS	v
	LIST OF TABLES	viii
	LIST OF FIGURES	ix
 CHAPTER		
I	INTRODUCTION	1
II	OVERVIEW OF THE COLLIDER DETECTOR AT FERMILAB	5
	A. The Collider Detector at Fermilab	5
	B. Small Angle Counters	7
	C. The Magnet	7
	D. Tracking	9
	E. Calorimetry	10
	F. Muon Detectors	15
	G. What the Particles Produced See	15
	H. Data Acquisition System	16
	I. Trigger	17
	J. Initial Runs at CDF	18
III	CDF GAS CALORIMETRY AND THE FORWARD/BACKWARD HADRON CALORIMETERS	20
	A. Introduction	20
	B. Gas Calorimetry in CDF	21
	C. Monitoring of Gas Gain	24
	D. The Forward/Backward Hadron Calorimeters	25
	E. Testing Calorimeter Performance	30
	F. Tests on Chamber Aging	34

TABLE OF CONTENTS (Continued)

CHAPTER		Page
IV	CDF TEST BEAM FACILITY AT THE MESON TEST SITE	36
	A. CDF Test Beam Requirements	36
	B. Status of the CDF Test Beam Facility	39
	C. The MT Test Beam	41
V	GAS DELIVERY SYSTEM FOR THE CDF TEST BEAM FACILITY	43
	A. Design Guidelines	43
	B. Final Design	47
VI	OVERVIEW OF THE MESON TEST BEAMLINER	49
	A. Introduction	49
	B. The Beamline	51
	1. Current Configuration	51
	2. Naming Convention for Beamline Devices	54
	3. Critical Devices	59
	4. The Spill Cycle	59
	5. Effects of the MW Beamline	61
	C. Modes of Operation	61
	D. Energy Acceptance	67
	E. Beam Optics	71
	1. Dipole Magnets	74
	2. Quadrupole Magnets	77
	3. First-Order Matrix Formalism for Beam Transport	84
	F. Computer Analysis and Design Considerations	91
	G. Particle Production	98

TABLE OF CONTENTS (Continued)

CHAPTER	Page
VII	STUDY OF MESON TEST BEAMLINE COMPONENTS . . . 110
	A. Introduction 110
	B. Targets 110
	C. Collimators 123
	D. Magnets 132
	E. Beam Stops and Beam Dumps 133
	F. Beam Analyzing Devices 142
	G. Secondary Emission Monitors 143
	H. Proportional Wire Chambers 145
	I. Single Wire Drift Chambers 148
	J. Scintillation Counters 155
	K. Triggers 159
	L. Tagging Systems 162
VIII	BEAM TRANSPORT AND UPDATED COMPUTER ANALYSIS FOR THE MESON TEST BEAMLINE 163
	A. Beam Tuning 163
	B. Experimental Yields 171
	C. Contamination Studies 175
	D. Updated Computer Analysis 177
IX	SUMMARY 191
	REFERENCES 196
	APPENDIX A. THE CDF COLLABORATION 200
	APPENDIX B. TEST BEAM GAS SUPPLY SYSTEM 201
	APPENDIX C. MESON WEST BEAMLINE 218
	APPENDIX D. BEAM TRANSPORT HISTOGRAMS 224
	VITA 230

LIST OF TABLES

Table	Page
I. Summary of CDF calorimeter properties	11
II. Detector elements requiring gas mixtures to be studied during the first test beam run	44
III. MT beamsheet	52
IV. Physical characteristics of magnets and collimators in the MT beamline	95
V. Percent particle content of the secondary beam leaving Be targets with 400 GeV incident protons	106
VI. Bend angles of dipole magnets in the MT beamline	108
VII. Atomic and nuclear properties of selected materials	111
VIII. Production targets, converters, and absorbers in the MT beamline	115
IX. Effective radiation lengths of material in the MT beamline, other than targets	124
X. Scintillation counters in the MT beamline	158
XI. Nominal and experimental current settings for 245, 160, and 80 GeV secondary beam transport	168
XII. Calculated magnetic fields and current settings for 227, 151, and 75 GeV secondary hadron beam transport	179
XIII. Calculated initial phase space acceptance at the MT2TGT-series targets for secondary beam transport	188
XIV. Calculated 227, 151, and 75 GeV secondary hadron beam dimensions at the CDF wedge fixture	188
XV. A preliminary experimental tune for 227 GeV secondary hadron transport	189
XVI. Equipment list for the CDF test beam facility gas supply system	211
XVII. Meson West (MW) beamsheet	215

LIST OF FIGURES

Figure	Page
1. Isometric view of the CDF detector	6
2. Elevation side view of one-half of the CDF detector	8
3. Non-overlapping projective tower geometry in the CDF endplug calorimeters	13
4. Grids of hadron calorimeter towers in one quadrant of the CDF detector	14
5. Gas gain vs. voltage curve illustrating gas amplification in a proportional chamber	22
6. Beam's eye view of the CDF forward/backward hadron calorimeter .	27
7. Cross section of a forward/backward hadron calorimeter proportional chamber	29
8. Positions scanned during performance tests on the forward/ backward hadron calorimeter in Oct 1985	32
9. Floor plan of the CDF test beam facility at the Meson Test site . .	40
10. The beamsheet coordinate system	51
11. MT beamline components plotted in horizontal position x vs. longitudinal position	55
12. Beamline component symbols	56
13. The spill cycle	60
14. Secondary production of high energy electrons in the MT beamline .	64
15. The MT2TGT1 converter target	65
16. Energy acceptance of a magnet string	70
17. The central trajectory coordinate system	73
18. Charged particle path in the bending plane of a dipole magnet . . .	76
19. Dipole magnet cross section showing \mathbf{B} and \mathbf{F} components and the central trajectory coordinates	78
20. Quadrupole magnet cross sections with the central trajectory coordinates	78

LIST OF FIGURES (Continued)

Figure	Page
21. Components of \mathbf{B} and \mathbf{F} for a horizontally-focusing quadrupole magnet	79
22. Focusing and defocusing by a horizontally-focusing quadrupole magnet	81
23. Unsymmetric focusing by a quadrupole doublet	83
24. Point-to-point focusing with a quadrupole doublet	83
25. Point-to-parallel focusing with a quadrupole doublet	83
26. The dimensions of a two-dimensional phase space ellipse in terms of ellipse matrix elements	90
27. The effects of a drift space on a two-dimensional phase space ellipse	90
28. The primary 800 GeV proton beam profile at the MT secondary production targets	97
29. The production of neutral pions as a function of secondary momentum at three fixed angles	104
30. Beryllium target pion production efficiency f vs. L/λ ,	112
31. Beam's eye schematic view of a ferris wheel target	113
32. Efficiency of lead as a converter in pair production vs. radiation length L_R	116
33. MT2TGT1 target relative efficiency in producing secondary 245 GeV hadron beams as a function of lead thickness	118
34. MT2TGT2 target relative efficiency in producing secondary 245 GeV hadron beams as a function of lead thickness	119
35. MT2TGT3 target relative efficiency in producing secondary 245 GeV hadron beams as a function of lead thickness	120
36. MT3TGT1 target relative efficiency in producing tertiary 160 GeV hadron beams as a function of lead thickness	121
37. Radiation lengths L_R accumulated down the MT beamline, excluding moveable targets	126

LIST OF FIGURES (Continued)

Figure	Page
38. MT3CH1 collimator effectiveness in reducing the intensity of the 245 GeV secondary hadron beam	128
39. MT3CV collimator effectiveness in reducing the intensity of the 245 GeV secondary hadron beam	129
40. MT3CH2 collimator effectiveness in reducing the intensity of the 245 GeV secondary hadron beam	130
41. Schematic diagrams of collimators	131
42. Reducing momentum acceptance using collimators	131
43. Data sheet for the 6-3-120 beamline dipole magnet	134
44. Magnetic excitation curve for the 6-3-120 beamline dipole magnet	135
45. Data sheet for the 5-1.5-120 EPB dipole magnet	136
46. Magnetic excitation curve for the 5-1.5-120 and 3.5-1.5-120 EPB dipole magnets	137
47. Data sheet for the 4-4-30 vernier magnet	138
48. Magnetic excitation curve for the 5-4-30 trim vernier magnet	139
49. Data sheet for the 3Q120 EPB quadrupole magnet	140
50. Magnetic excitation curve for the 3Q120 EPB quadrupole magnet	141
51. Cross section of a secondary emission monitor	144
52. Cross section of a beam proportional wire chamber	147
53. Efficiency vs. applied high voltage for a typical beam proportional wire chamber	149
54. Cross section of the edge of a cell of a single wire drift chamber	151
55. Efficiency vs. applied high voltage for MT6SWDC	153
56. Electron drift velocity vs. the drift field for a typical single wire drift chamber	154
57. Typical plastic scintillation counter	157

LIST OF FIGURES (Continued)

Figure	Page
58. Efficiency vs. applied high voltage for MT6SC1	160
59. Beam trigger logic	161
60. Beam profiles at MT3PWC, MT4PWC, and MT6PWC1 for the experimental 245 GeV secondary hadron transport tune	169
61. Normalized experimental yields vs. beam energy for secondary hadron transport	173
62. Normalized experimental yields vs. beam energy for tertiary hadron and electron transport	174
63. Percent muon contamination vs. beam energy for secondary hadron transport	176
64. Computed yields by particle type at MT3PWC for secondary hadron transport at 227, 151, and 75 GeV	181
65. Computed yields by particle type at MT6PWC1 for secondary hadron transport at 227, 151, and 75 GeV	182
66. Computed transfer matrix element R_{12} vs. longitudinal distance z along the MT beamline	184
67. Computed transfer matrix element R_{34} vs. longitudinal distance z along the MT beamline	185
68. Computed transfer matrix element $ R_{16} = \Delta p/p $ vs. longitudinal distance z along the MT beamline	186
69. Beam profiles at MT3PWC, MT4PWC, and MT6PWC1 for the experimental tune for 227 GeV secondary hadron transport	190
70. CDF test beam facility gas supply control area	198
71. Schematic flow diagram for the gas supply system to the Central Muon Detector chambers	199
72. Schematic flow diagram for the gas supply system to the endplug EM calorimeter chambers	200
73. Schematic flow diagram for the gas supply system to the endplug hadron calorimeter chambers	201

LIST OF FIGURES (Continued)

Figure	Page
74. Schematic flow diagram for the gas supply system to the forward EM calorimeter chambers	202
75. Schematic flow diagram for the gas supply system to the forward hadron calorimeter chambers	203
76. Schematic flow diagram for the gas supply system to the Central EM Strip chambers	204
77. Schematic flow diagram for the stage 1 controls of the gas pressure buffer system for the forward EM calorimeter chambers	205
78. Schematic flow diagram for the stage 2 controls of the gas pressure buffer system for the forward EM calorimeter chambers	206
79. Schematic flow diagram for the distribution manifold for the forward EM calorimeter chambers	207
80. Schematic flow diagram for the stage 1 controls of the gas pressure buffer system for the forward hadron calorimeter chambers	208
81. Schematic flow diagram for the stage 2 controls of the gas pressure buffer system for the forward hadron calorimeter chambers	209
82. Schematic flow diagram for the distribution manifold for the forward hadron calorimeter chambers	210
83. Meson West (MW) beamline components plotted in x vs. z up to the MW6 enclosure	219
84. Particle distribution vs. horizontal coordinate x at the CDF target area	221
85. Particle distribution vs. vertical coordinate y at the CDF target area	222
86. Particle density in the x - y plane at the CDF target area	223
87. Particle momentum vs. x at the CDF target area	224
88. Particle distribution vs. momentum at the CDF target area	225

CHAPTER I

INTRODUCTION

The *Collider Detector at Fermilab (CDF)* gives physicists the ability for the first time to explore the realm of high energy proton-antiproton colliding beam physics beyond center-of-mass energies of 1 TeV. The CDF is a unique spectrometer designed specifically to study the interactions of particles at these energies. It is the product of many years of work by a large collaborative effort of physicists and technicians from accelerator laboratories and universities in this country and overseas.

In order to make use of the data from CDF taken during collision runs of the accelerator at Fermilab, the detector itself must be fully understood first. The process of analyzing the detector and its components is a massive undertaking, requiring dedicated resources and personnel. The majority of testing is carried out by removing detector components from the collision hall and then studying their response in fixed-target test beam facilities.

The most recent test beam facility developed for CDF is located at the Meson Test (MT) site; it must include the necessary computing and data acquisition electronics, gas supply system, and component support fixtures in order to recreate the environment of the collision hall as closely as possible. The fixed-target beamline itself must provide particle beams which can support the needs of CDF to properly study detector components.

My responsibilities in making the CDF test beam facility at Meson Test a reality fell into two areas: (1) to assist in the design and construction of the test beam

Style and format conform to *Reviews of Modern Physics*.

facility gas delivery system, and (2) to conduct preliminary studies to understand and document the operation of the MT beamline and its components.

The MT test beam facility will be used by CDF during the next several years to continue the study of the detector. The gas delivery system must have enough inherent flexibility to allow it to support a variety of components undergoing different tests. Besides providing assistance in the general design of the gas delivery system, I reproduced the CDF gas quality monitoring system for use in the test beam facility, and I built the gas supply components mounted at the forward fixture, which supports Texas A&M University's forward hadron calorimeter.

The MT beamline was designed through computer analysis using standard beamline analysis programs. Because the MT beamline was only recently installed, the results of these programs constituted the only data on beamline performance, with no experimental studies to determine actual performance. I carried out preliminary beamline studies to determine the necessary tunes to produce particle beams of required energies and to document the ability of the beamline to meet CDF requirements. The following tasks were established, with the understanding that available time and equipment would limit detailed study:

(1) Establish the CDF Experimental Areas test beam computer account necessary to carry out beamline control and analysis. This account would be used in the future by CDF personnel during actual fixed-target runs.

(2) Determine the optimum tunes and production rates for the secondary 245, 160, and 80 GeV hadron beams transported to the CDF target area.

(3) Develop tunes and determine production rates for a spectrum of energies for secondary hadron transport (10 to 245 GeV) and for tertiary hadron and electron transport (10 to 200 GeV) to the CDF target area.

- (4) Determine beamline collimator effectiveness.
- (5) Map out pertinent transfer matrix elements which characterize the transport characteristics of the MT beamline.
- (6) Determine beam profiles at the target for the primary tunes.
- (7) Plateau the various particle detectors in the beamline, as necessary.
- (8) Determine the hadron, electron, and muon composition of the beam for certain tunes.
- (9) Document the operational capabilities of the threshold Čerenkov counter and the synchrotron radiation detector as electron tagging devices in the beamline. (This task could not be carried out since these devices and necessary test equipment were not available.)
- (10) Produce a resource document on the MT beamline to be used by CDF personnel and containing the results of objectives (1) through (9) listed above. Chapters VI, VII, and VIII, as well as Appendices C and D, would serve as this reference.

To provide background information on the Collider Detector at Fermilab and to present the results of my work on the CDF test beam facility at the Meson Test site, this thesis has been organized into nine chapters. Following this Introduction, Chapter II provides an overview of the Collider Detector by summarizing pertinent documentation on CDF. Chapter III presents principles of the gas calorimetry in CDF and summarizes the results of studies conducted by Texas A&M University researchers on the forward/backward hadron calorimeters, which were constructed for CDF by the university's High Energy Physics Group. Background information on the CDF test beam facility at the Meson Test site is included in Chapter IV. Chapter V discusses the details of the CDF test beam gas delivery system and its

final design configuration (the first research objective). Chapters VI, VII, and VIII include the results of my preliminary beamline studies and analysis of beamline components, with Chapter VI presenting an overview of the MT beamline and its design, Chapter VII describing the beamline components, and Chapter VIII providing the results of beam tuning, beam intensity studies, and updated computer analysis (the second research objective). Chapter IX concludes the thesis with a summary of research results.

CHAPTER II

OVERVIEW OF THE COLLIDER DETECTOR AT FERMILAB

A. The Collider Detector at Fermilab

The Collider Detector at Fermilab (CDF) is located at the Fermi National Accelerator Laboratory in Batavia, IL. CDF is a large multipurpose spectrometer installed in the B0 straight section of the Tevatron main accelerating superconducting ring and is designed to study proton-antiproton (pp) colliding-beam physics at 2 TeV center-of-mass energy.¹ It is in this energy domain that particles with masses in the range of 150 to 500 GeV/c² and jets with momentum transfers of 100 to 400 GeV can be uniquely investigated.² The current CDF collaboration is listed in Appendix A.

An isometric view of the detector is shown in Figure 1. The CDF detector is made up of three major assemblies: the central detector, which can be moved intact from the collision hall, and the symmetric forward and backward detectors. The detector covers nearly the entire solid angle about the interaction region, with complete 360° coverage in the azimuthal angle ϕ and coverage from 2° to 178° in the polar angle θ . The central assembly covers the angular region $10^\circ < \theta < 170^\circ$, while the forward and backward assemblies cover the ranges $2^\circ < \theta < 10^\circ$ and $170^\circ < \theta < 178^\circ$, respectively.

In high transverse momentum (p_t) reactions, the natural coordinates for describing particle kinematics in hadron colliders are the pseudorapidity η

$\ln \tan \theta/2$, the azimuthal angle ϕ , and the transverse momentum p_t .³ The density of particles in typical inelastic collisions is basically uniform in η - ϕ phase space.⁴

CDF detector components fall under the headings of small angle counters, the

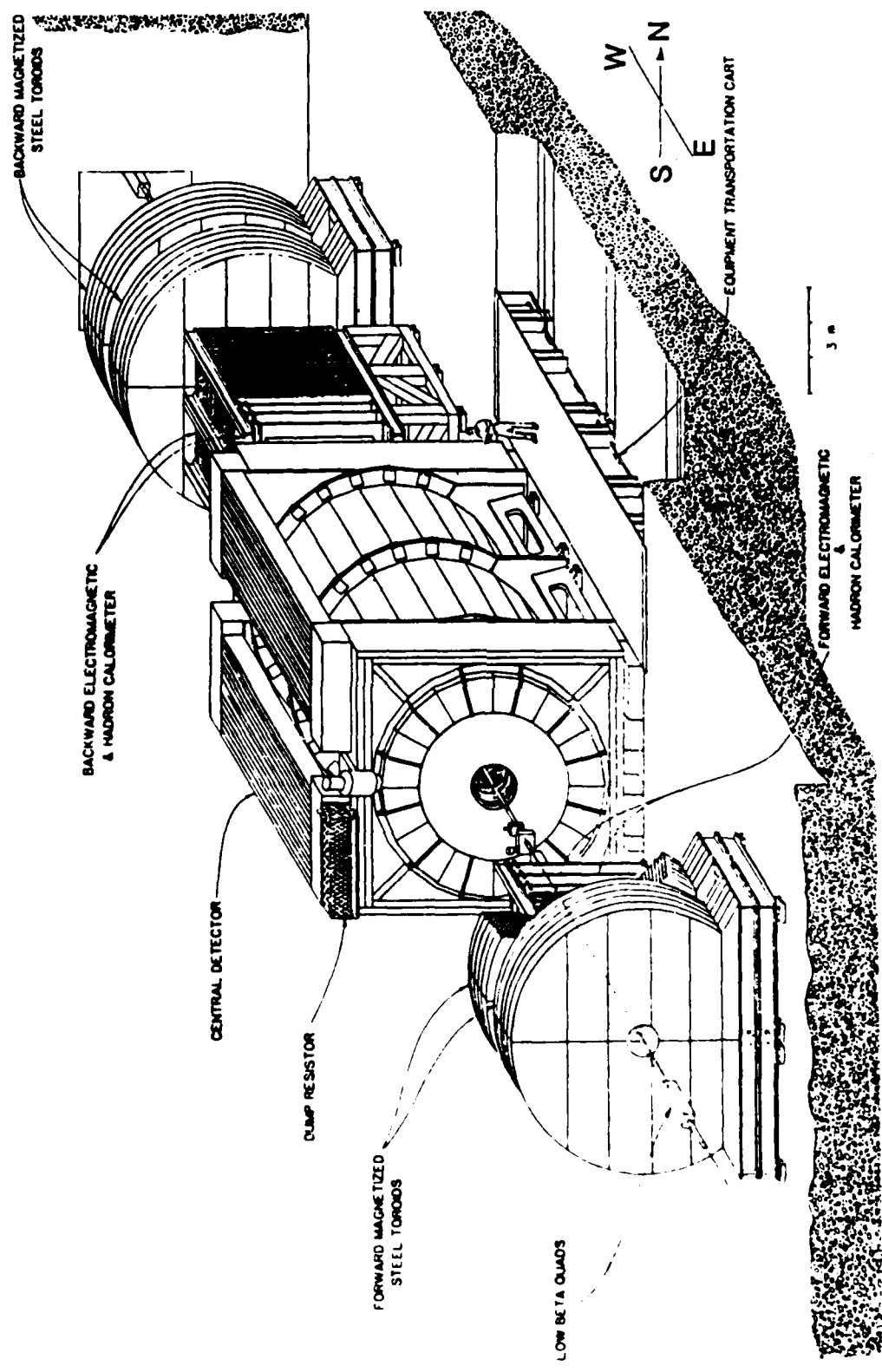


FIG. 1. Isometric view of the CDF detector (from Eaton²).

magnet, tracking, calorimetry, and muon detectors.⁵ An elevation side view of one-half of the detector is shown in Figure 2, with major components labeled. The CDF detector is symmetric about the interaction point; for convenience in identifying components, each "half" of the detector is broken up into four regions: central, endwall, endplug, and forward.

B. Small Angle Counters

Small angle counters include scintillator beam-beam trigger counters and forward silicon microstrip detectors. The *Beam-Beam Counters* are a scintillator hodoscope surrounding the beampipe directly in front of the *Forward Electromagnetic Calorimeters*. They are used in the lowest level triggering, provide precise timing signals, and can measure the z position of the interaction vertex. The *Forward Silicon Detectors* are inside the beampipe at positions from 6 to 55 m from the detector center; they detect very small angle diffractive and elastic scattering and determine accelerator luminosity.

C. The Magnet

The CDF detector is built around a superconducting solenoid magnet which is 3 m in diameter and 5 m long and which produces a uniform magnetic field of 1.5 T coaxial with the beam direction. The iron in the endplug and endwall calorimetry along with the magnet's return yoke (which also provides the structural support for the central assembly) form the return path for the central solenoid magnetic field. Only a small part of the flux is returned through the central calorimetry iron. Together with the enclosed drift chambers the magnet is used to determine the trajectories, the sign of the electric charge, and momenta of charged particles

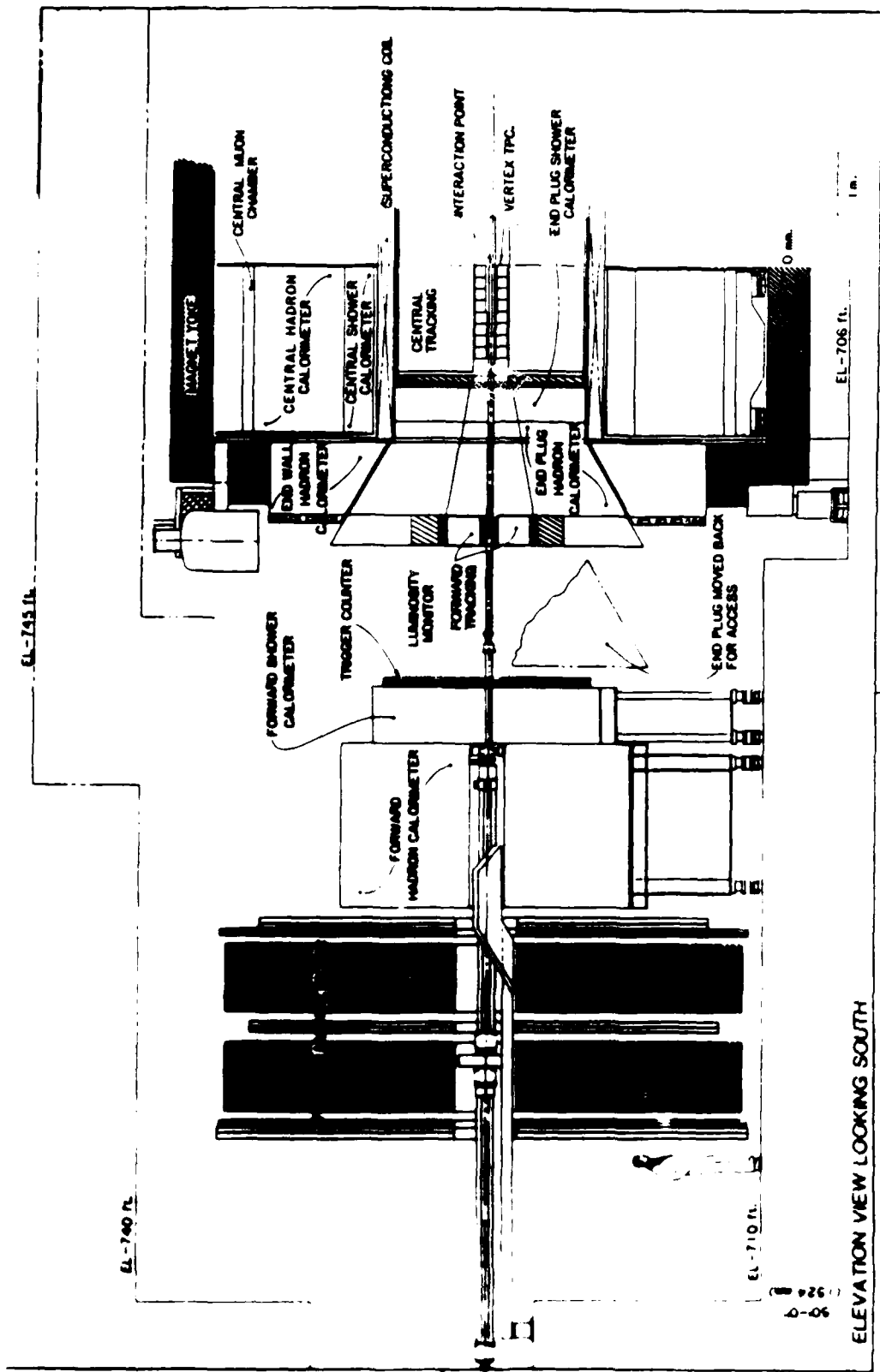


FIG 2. Elevation side view of one-half of the CDF detector (from Eaton²).

produced with polar angles $10^\circ < \theta < 170^\circ$. Momentum resolution at 50 GeV/c is $\Delta p_t/p_t = 0.002 p_t$ (in GeV/c) for polar angles greater than 40° but deteriorates to no less than $0.15 p_t$ with smaller polar angles.

D. Tracking

The CDF's tracking and calorimetry cover roughly ± 4 units in pseudorapidity η and 2π in azimuthal angle ϕ . The four systems which make up tracking are the Vertex Time Projection Chamber, the Central Tracking Chamber, the Central Drift Tubes, and the Forward Tracking Chamber. These tracking systems allow for the visual reconstruction of charged particle tracks over the full coverage of the CDF calorimetry.

The Vertex Time Projection Chamber (VTPC) is the innermost tracking system and surrounds the beampipe. It provides good r - z tracking ability and is sensitive to particles with polar angles greater than 3° . The principal roles of the VTPC are to record the occurrence of multiple events and to provide three-dimensional information about general event topology for use in pattern recognition by the calorimetry and the Central Tracking Chamber.

The Central Tracking Chamber (CTC) is a large axial wire drift chamber surrounding the VTPC. Innermost layers cover the region $\theta = 14^\circ$; outermost layers cover $\theta = 40^\circ$.

At the outer edge of the CTC are the Central Drift Tubes (CDT), an array of axial drift tubes which use charge division to simultaneously measure r , ϕ , and z . The CDT information is used as a "seed" in track reconstruction in the central region.

The Forward Tracking Chamber (FTC) completes the tracking coverage by

covering the region $2^\circ < \theta < 10^\circ$. It is a radial wire drift chamber which resides in the annulus between the beampipe and the endplug calorimeters and determines the azimuthal coordinate ϕ of particles passing through the holes in the magnet's endplugs.

E. Calorimetry

The calorimetry is characterized by projective tower structure, good granularity, and good energy resolution.⁵ The intent was to insure particle detection and identification and energy measurement. The calorimeters are all of the sampling type and are either electromagnetic (EM) shower counters or hadron calorimeters. Calorimetry consists of seven systems: central EM calorimeters (CEM), central hadron calorimeters (CHA), endwall hadron calorimeters (EHA), endplug EM calorimeters (PEM), endplug hadron calorimeters (PHA), forward/backward EM calorimeters (FEM), and forward/backward hadron calorimeters (FHA). Calorimeter properties are summarized in Table I.

The angular coverage of the calorimeters is 2π in the azimuthal angle ϕ and from -4.2 to +4.2 units in pseudorapidity η , except that the forward hadron calorimeter has incomplete η -coverage in the intervals of $-4.2 < \eta < -3.6$ and $3.6 < \eta < 4.2$. As mentioned earlier, expressed in θ this coverage is $2^\circ < \theta < 178^\circ$.

Calorimeters are arranged with a "front" part made up of EM shower counters followed by a "back" part of hadron calorimeters. The EM and hadron calorimeters use lead and steel, respectively, for radiators. The sampling medium is scintillator in the central region (central and endwall calorimeters), where polar angles θ are greater than 30° . Wavelength shifters and phototubes are used for readout. Scintillation plastic was chosen for its good energy resolution. For smaller polar

TABLE I. Summary of CDF calorimeter properties (from Abe et al.⁴).

	Central		Endwall		Endplug		Forward	
	EM	Hadron	Hadron	EM	Hadron	EM	Hadron	
η -coverage	0-1.1	0-0.9	0.7-1.3	1.1-2.4	1.3-2.4	2.2-4.2	2.3-4.2	
Tower size, $\Delta\eta \times \Delta\phi$	-0.1x0.26	-0.1x0.26	-0.1x0.26	0.09x0.09	0.09x0.09	0.1x0.09	0.1x0.09	
Longitudinal samples in tower	1*	1	1	3	1	2	1	
Active medium	polystyrene scintillator	acrylic scintillator	acrylic scintillator	Proportional tube chambers with cathode pad readout				
Scintillator thickness or proportional tube size	0.5 cm	1.0 cm	1.0 cm	0.7x0.7cm ²	1.4x0.8cm ²	1.0x0.7cm ²	1.5x1.0cm ²	
Number of Layers	31	32	15	34	20	30	27	
Absorber	Pb	Fe	Fe	Pb	Fe	94% Pb, 6% Sb	Fe	
Absorber thickness	0.32cm	2.5cm	5.1cm	0.27cm	5.1cm	0.48cm	5.1cm	
Typical phototube or wire high voltage	-1100V	-1500V	-1100V	+1700V	+2120V	+1900V	+2200V	
Typical phototube or wire gain	1.2x10 ⁵	6x10 ⁵	10 ⁶	2x10 ³	2x10 ⁴	5x10 ³	10 ⁴	
Typical tower signal	-4 pC/GeV	-4 pC/GeV	-4 pC/GeV	+1.25 pC/GeV	+1.3 pC/GeV	+2 pC/GeV	+0.7 pC/GeV	
Energy resolution σ/E at 50 GeV	2%	11%	14%	3%	20%	4.5%	2.5%	
Typical position resolution at 50 GeV	0.2x0.2cm ²	10x5cm ²	10x5cm ²	0.2x0.2cm ²	2x2cm ²	0.2x0.2cm ²	3x3cm ²	
Characteristic total width of azimuthal boundary region	3.5cm	4.1cm	3.8cm, 8.9cm alternating	0.9cm	0.6cm	0.7cm, 3.2cm**	1.3cm, 3.2cm**	

*An imbedded proportional tube chamber at shower maximum gives some additional information. The quoted position resolution is measured with this chamber.

**The first number is for the vertical boundary, the second for the horizontal.

angles θ forward of 30° (endplug and forward calorimeters), gas proportional chambers with strip readout of resistive cathode pads and anode wire bunches are used, chosen because of economy, resistance to radiation damage, and flexibility of geometry.⁴

All calorimeters are divided into cells so that they have a projective tower geometry covering each element of solid angle. The CDF calorimetry is segmented into about 5000 of these towers or solid angle elements. When viewed from the nominal beam-beam interaction point, each tower of each calorimeter subtends a solid angle of roughly constant η and ϕ . Figure 3 illustrates this tower geometry in the endplug calorimeters. This tower segmentation corresponds to rectangles in η - ϕ phase space and makes use of the prediction of roughly constant particle and jet density in all towers of the calorimetry. Tower geometry allows for an unambiguous spatial localization of the energy deposition within the calorimeters.² Figure 4 shows the grid of hadron calorimeter towers in one quadrant of the detector, together with system boundaries (often termed "cracks"). The grid of EM calorimeter towers is essentially the same.

The grids in η - ϕ space are chosen small enough to insure good granularity. Partons (quarks and gluons) are characterized by the production of hadron jets. The granularity, or tower dimensions in the phase space, is chosen to resolve these jets without attempting the extreme task of being able to measure reliably every particle within the jet. A typical high p_t jet will form a circular pattern in η - ϕ space with a diameter of roughly 1 unit in η ;⁶ the calorimeter towers are approximately 0.1 units in η over the entire range from -4.2 to 4.2 and between 5° and 15° in ϕ . The ϕ divisions are 5° in the central region where $\theta > 30^\circ$ (central and endwall calorimeters) and 15° in the forward region (endplug and forward calorimeters).

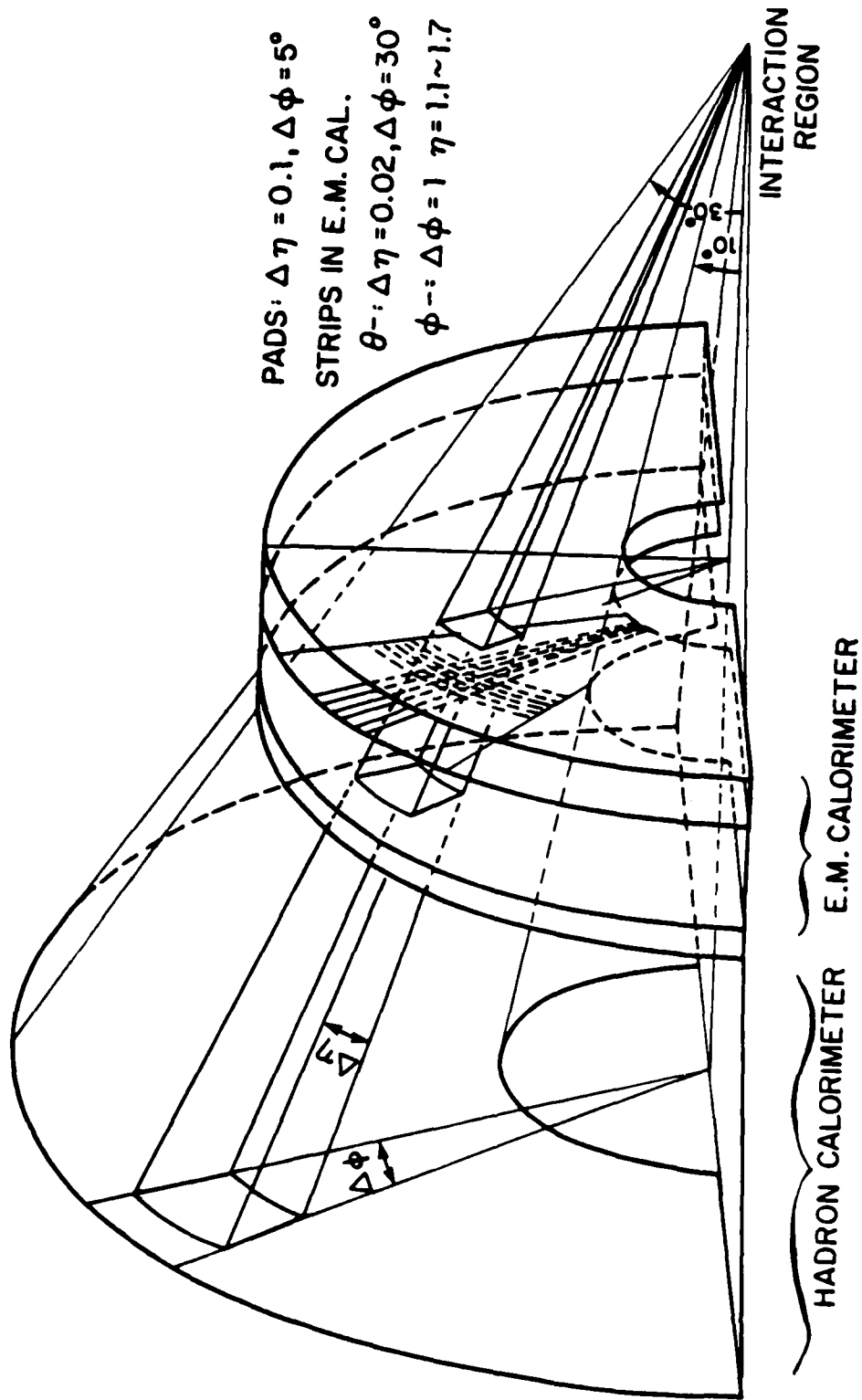


FIG. 3. Non-overlapping projective tower geometry in the CDF endplug calorimeters (from Asano et al.¹).

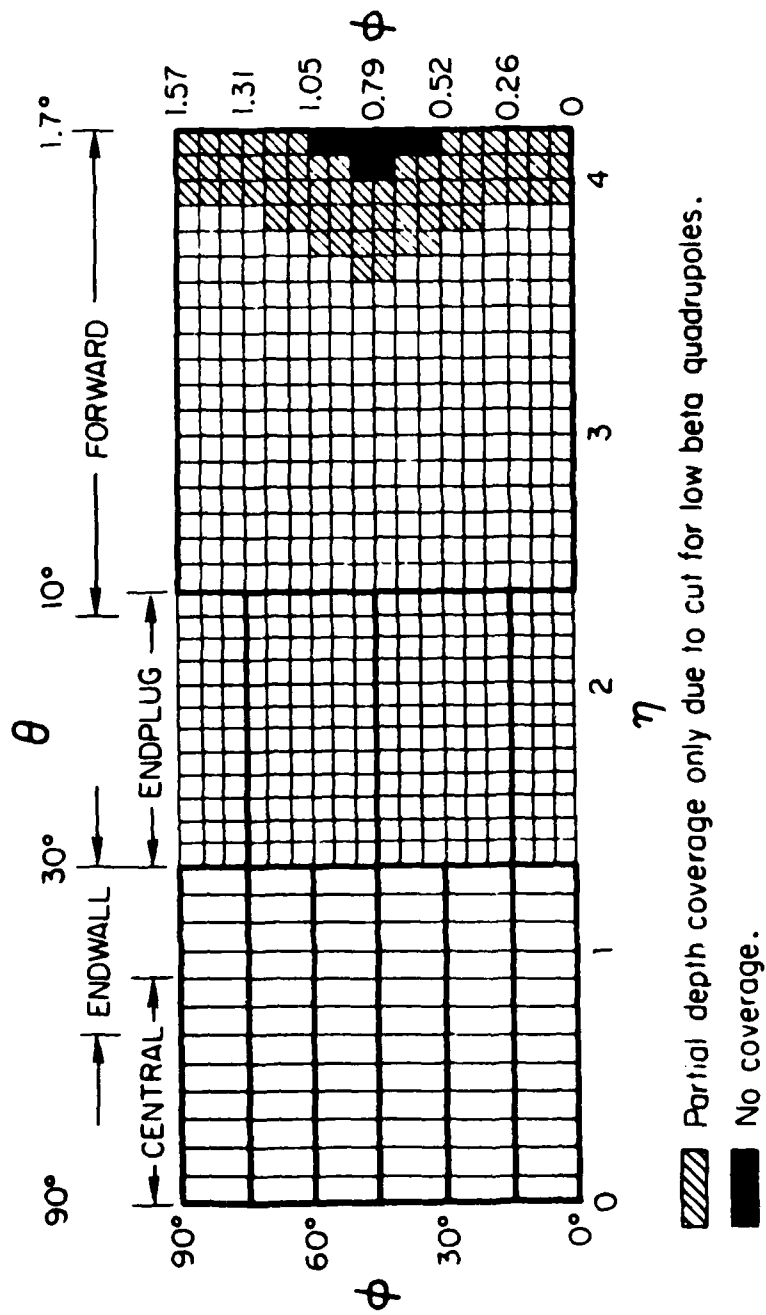


FIG. 4. Grids of hadron calorimeter towers in one quadrant of the CDF detector (from Abe et al.⁴).

Calorimeters are especially suited to higher-energy collider machines since the energy resolution $\Delta E/E$ of most calorimeters varies with energy as $1/\sqrt{E}$. As energies increase, resolution improves.

F. Muon Detectors

Muon detectors include the Central Muon Detector and the Forward Muon Detector. The Central Muon Detector lies outside the central hadron calorimeter and provides muon detection over the range $55^\circ < \theta < 125^\circ$. The Forward/Backward Muon Detectors each consist of two large magnetized steel toroids 7.6 m in diameter and 1 m thick. These toroids rest directly behind the forward hadron calorimeter and are instrumented with drift chambers. Each toroid has four coils which generate a 1.8 T field in the steel for momentum analysis of muons. These detectors cover the ranges of $2^\circ < \theta < 17^\circ$ and $163^\circ < \theta < 178^\circ$, respectively. Currently there are gaps in muon coverage for $2^\circ < \theta < 55^\circ$ and $125^\circ < \theta < 163^\circ$. Additional muon detectors to cover these ranges will be part of a future upgrade of CDF.

G. What the Particles Produced See

After leaving the vacuum chamber, particles produced by $p\bar{p}$ collisions in the angular region covered by the central assembly pass in sequence through: (1) a drift chamber tracking system which measures charged particle momenta in the 1.5 T magnetic field of the solenoid magnet, (2) less than 1 radiation length of material either from the solenoid coil and cryostat or the end plate of the drift chambers, (3) about 20 radiation lengths of highly segmented EM shower counters, (4) about 5 absorption lengths of highly segmented hadron calorimeters, and (5) tracking chambers for muon identification. Over a restricted angular region of the central

assembly, the magnet return yoke will provide additional material in the path of particles, improving muon identification.

Particles produced in the forward or backward direction at angles between 2° and 10° to the beamline pass through holes in the endplugs of the magnet and enter either the forward or backward assembly. The directions of charged particles are measured by drift chambers in the front part of the assembly. Following this, the particles then enter a segmented EM shower counter and then a hadron calorimeter. Finally, on the end of the assembly are two sets of magnetized iron toroids and drift chambers which provide momentum analysis for muons produced in the angular ranges $2^\circ < \theta < 17^\circ$ (forward) and $163^\circ < \theta < 178^\circ$ (backward).

H. Data Acquisition System

There are about 75,000 electronics channels of detector information situated in about 150 electronics crates mounted on the detector on or near the respective components. A clock which is synchronized to the accelerator radio frequency system delivers timing signals to the electronics. The front-end electronics are different depending on whether the information is from a calorimeter or from a tracking chamber.

The information processed by the front-end electronics is passed to a FASTBUS-based system in the CDF counting room.¹ This system performs additional processing on the information, generates triggers, and formats the information for transfer to VAX minicomputers and eventually the storage medium.

The redundant analog-based bus information transfer (RABBIT) system is used for readout of the calorimeters.² The RABBIT system is designed for use in a high-rate environment. Charge sensitive amplifiers and sample-and-hold capacitors

in individual RABBIT modules store data taken before and after an event. The differences between these two are the voltages which are multiplexed over the analog bus of each RABBIT crate and are digitized by a 16-bit Analog to Digital Converter (ADC) slotted in the crate. The integration times currently used for calorimeter signals are relatively long, about $0.6 \mu\text{sec}$ for the scintillator phototube signals and about $1.6 \mu\text{sec}$ for the proportional chamber pad signals (some of which have large source capacitances of up to 100 nF).⁴ Amplifier gain shifts of up to 15% are observed for the channels connected to the largest source capacitances. An on-card calibration system is used to measure the overall electronics gain, so that such effects can be corrected for during data processing. The rms electronics noise on an individual channel is equivalent to about 0.3 GeV of energy deposition in a calorimeter tower, compared to the full scale set at about 400 GeV .

The readout of the tracking chambers is significantly different. The analog signals from these chambers are passed to conventional pulse amplifier-shaper-discriminator modules. Shaped pulses are then transmitted to Time to Digital Converters (TDCs) in FASTBUS crates in the CDF counting room.

I. Trigger

The CDF trigger is a three-level decision making process, designed to reduce the basic interaction rate of $70,000 \text{ Hz}$ expected at a luminosity of $10^{30} \text{ cm}^{-2} \text{ sec}^{-1}$ to a few Hz written to tape.²

The level 1 decision is made between beam crossings (less than $3.5 \mu\text{sec}$) to accept or reject the event for digitization. The goal of level 1 is to reduce the trigger rate to less than about 5000 events/sec in order to limit the deadtime due to level 2. This trigger is derived from fast analog signals provided by the calorimeter

front-end electronics and which represent the energy deposition in the calorimeters. Other ingredients can be introduced to the level 1 decision requirements.

The level 2 decision typically requires about $10 \mu\text{sec}$ and sometimes longer for interesting events. During this time the detector is dead and the data in the front-end electronics is held on sample-and-hold capacitors or in shift registers awaiting the final decision. Level 2 looks for pattern of energy deposition, high p_t tracks associated with muon hits, missing p_t , and other similar inputs.

The level 3 trigger is a microprocessor-based system that has access to all the digitized data from the event and can do at least partial event reconstruction. A network of approximately 100 microprocessors running in parallel is planned; each microprocessor will work on a different event and will have about one second for each event if the rate of events passing level 2 is about 100 events/sec. If the microprocessor accepts the event, the event data is uploaded to the VAX for output on a storage medium.

J. Initial Runs at CDF

The first beam-beam run for the CDF detector was the systems test/engineering run conducted in Oct 1985. The available detector components were the Beam-Beam Counters, the Vertex Time Projection Chambers, the Central Muon Detector, and the central and endwall calorimeters. The data acquisition system necessary to support the calibration and readout of these components was operational, as was the level 1 trigger. Collisions with a center-of-mass energy of 1.6 TeV were observed, with luminosities in the range of 10^{23} to $10^{24} \text{ cm}^{-2} \text{ sec}^{-1}$.

The first physics run with the CDF detector took place from Jan to May 1987. The detector was tested and commissioned during the period from 1 Jan to 1 Mar,

and the major data-taking part of the run was conducted between 1 Mar and 10 May. The detector was virtually complete in all its systems, and 30 nb^{-1} of data was collected on tape, with a data logging rate of about 1 Hz , as expected. Peak luminosity of beam was about $1.5 \cdot 10^{29} \text{ cm}^{-2} \text{ sec}^{-1}$.

CHAPTER III
CDF GAS CALORIMETRY
AND THE FORWARD BACKWARD HADRON CALORIMETERS

A. Introduction

Texas A&M University's participation in the CDF collaboration has included the design, construction, and testing of the forward backward hadron calorimeters (FHA) as part of the forward backward spectrometer assemblies.⁷ The FHA is representative of the gas calorimetry in CDF which will be studied in the new CDF test beam facility beginning in Fall 1987.

Conceptually, a calorimeter is a block of matter which intercepts the primary high-energy particle and is of sufficient length to cause it to interact and deposit all its energy inside the detector volume in a subsequent cascade or "shower" of increasingly lower energy particles. Eventually most of the incident energy is dissipated and appears in the form of heat. Some (usually a very small) fraction of the deposited energy goes into the production of a more useful signal (e.g., scintillation light, Cerenkov light, or ionization charge) which is proportional to the initial energy. In principle, the uncertainty in the energy measurement is governed by statistical fluctuations in the shower development, and the fractional resolution $\Delta E/E$ improves with increasing energy E as $1/\sqrt{E}$.

Calorimetric detectors offer many attractive capabilities in high-energy physics experiments in addition to their energy response:⁸ (1) they are sensitive to neutral as well as charged particles, (2) the size of the detector scales logarithmically with particle energy E for a given relative momentum resolution $\Delta p/p$ (whereas, for example, magnetic spectrometer size scales with \sqrt{p}), (3) with segmented detectors,

information on the shower development allows precise measurement of position and angle of the incident particle, (4) the differences in response to electrons, muons, and hadrons can be used in particle identification, (5) their fast-time response allows operation at high particle rates, and (6) the pattern of energy deposition can be used for real time event selection.

The best available technology for observing multi-jet structure in events is sampling calorimetry.¹ In order to separate electrons from hadrons, two types of calorimeters are installed in CDF. EM shower counters using relatively high Z materials are placed in front of hadron calorimeters employing much longer interaction lengths. As discussed earlier, non-overlapping projective tower geometry is used in all CDF calorimeters.

B. Gas Calorimetry in CDF

Gas calorimetry in CDF is based on multi wire proportional chambers, which operate in the proportional gas amplification region of the gas gain-voltage curve (see Figure 5). Gas amplification occurs when a minimum ionizing particle loses energy through collisions with molecules of the gas in the chamber (about 30 eV per collision), producing electron positive ion pairs along its path. High voltage differences between anode wires and cathode pads in the chamber create electrostatic fields which cause these ion pairs to separate. The free electrons produce an avalanche as each primary electron travels in regions of increasingly high electrostatic fields towards the anode wires, gaining energy and interacting with the fill gas molecules. In the proportional operating region, the output current signals from a calorimeter are directly proportional to the energy of the initial minimum ionizing particle, assuming all its energy is deposited in the calorimeter.

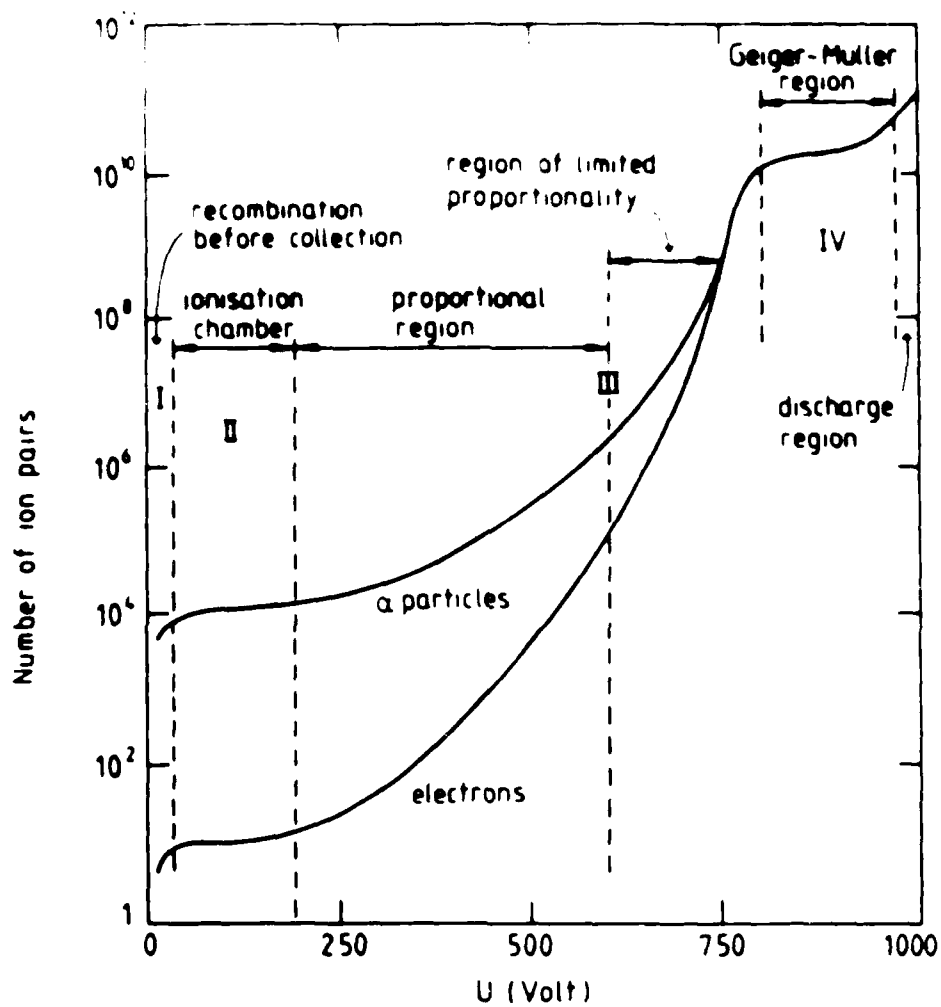


FIG. 5. Gas gain vs. voltage curve illustrating gas amplification in a proportional chamber (from Sauli⁹).

CDF gas calorimetry utilizes a 50% argon (Ar)/50% ethane (C_2H_6) gas mixture with small additions of isopropyl alcohol (C_3H_7OH). Argon is the basic ionization gas used for gas amplification; noble gases experience amplification at much lower fields than more complex molecules. However, excited noble gas atoms produced during the avalanche process return to the ground state only through the radiative process, and the minimum energy of emitted photons (11.6 eV for argon) is well above the ionization potential for any metal making up the cathode (7.7 eV for copper, for example). Photoelectrons thus can be extracted from the cathode, which then can initiate a new avalanche very soon after the primary one. Argon ions migrate to the cathode and are neutralized by extracting an electron; the balance of the remaining energy is either radiated as a photon or is used up in secondary emission (extraction of another electron from the metal surface), also resulting in a spurious avalanche. Even at moderate gains of 10^3 to 10^4 , these processes induce a permanent discharge regime.⁹

Polyatomic molecules, particularly ones with more than four atoms, can absorb photons in a wide energy range due to their large numbers of non-radiative excited states (rotational and vibrational). Most hydrocarbons and alcohols cover the ranges which include the energy of photons emitted by argon, including ethane. Ethane is thus used as a quenching gas to suppress photoelectrons and electrons from secondary emission, allowing gains in excess of 10^6 .

Following the ionization process molecular recombination produces liquid or solid polymers which will deposit on cathode and anode, eventually modifying the operation of the counter. This is referred to as aging of the counter.¹⁰ Ethane is a polymerizing quencher, but non-polymerizing quenchers (such as alcohols, aldehydes, and acetates) which strongly suppress the aging process have such

low vapor pressures compared with hydrocarbons so as to make them inefficient quenchers by themselves. For example, isopropyl alcohol has a vapor pressure of 30 Torr at 20°C. Fortunately, addition of even small amounts of a non-polymerizing quencher with an ionization potential below those of the other constituents of the gas mixture will result in the production of non-polymerized species at the cathode due to ion exchange mechanisms. Isopropyl alcohol, with an ionization potential of 10.1 eV, is the predominant quencher used in CDF gas calorimetry.

Use of a single inorganic quenching gas such as carbon dioxide (CO_2) would also avoid the aging process, but Ar/ CO_2 mixtures tend to display instability of operation at the high gains necessary in the gas calorimetry at CDF.¹¹ However, these gas mixtures are used in the tracking chambers at CDF.

Continuous gas flow is maintained through calorimeter chambers for two reasons. First, the quenching gas molecules are quickly "used up" at high particle rates because the excited molecules require a relatively long time to return to the ground state, so that they must be flushed out and replaced. Second, chambers tend to have large surface areas where gas leaks are common as a result of the construction techniques used.

C. Monitoring of Gas Gain

Gas gain is extremely sensitive to even small fluctuations in high voltage, pressure, temperature, and gas mixture composition. A 10% change in gas gain is observed for a high voltage change of 10 V (when $V \sim 2000\text{V}$), a pressure change of 1% (pressure in Torr), a temperature change of 1% (temperature in K), or a 1% change in gas mixture composition.

Several steps are taken to control and monitor gas gain changes. The chambers

of a given sector are all operated at the same high voltage. Changes in gas gain due to variations in pressure, temperature, or gas composition are tracked by calibrated monitor tubes (commonly called "Bensinger tubes" at CDF). Monitor tubes are placed on the detector at the gas input and output of all gas calorimeters. Gain changes of 25% over a 24-hour period have been recorded when a pressure front moves through Fermilab, but different monitor tubes show the same gain change to within 2%. Through test beam data it is hoped to establish the connection between gain changes in the calorimeters and in the monitor tubes so that monitor tube gain changes can be used for accurate corrections. Eventually it is expected that the precision with which calorimeter gain changes can be tracked with monitor tubes will be about about 2%: currently it is estimated to be about 10%.⁴ In addition to the monitor tubes mounted on the detector and correlated to specific components, a separate gas quality system samples the argon/ethane gas mixture flowing to the gas calorimetry during event runs. This system uses a calibrated monitor tube to determine gas composition while holding pressure and temperature fixed. This monitor tube is read out along with all the monitor tubes in the collision hall by the data acquisition system about every 15 min.

D. The Forward/Backward Hadron Calorimeters¹²

As the center-of-mass energy is raised in colliding-beam experiments, the fraction of the total physics acceptance in the central region of pseudorapidity η decreases as the total total pseudorapidity range for the interaction products increases.¹² Thus, as the energy is increased, the sophistication and segmentation of detectors must increase in the range forward of the central pseudorapidity region. The forward-backward spectrometer assemblies are required to extend the necessary

coverage and are designed to provide EM and hadronic shower calorimetry and muon identification and momentum analysis in the angular region of $2^\circ < \theta < 10^\circ$ with respect to either beam direction.

The forward/backward hadron calorimeter (FHA) has been designed to detect and measure the energies of hadrons in the pseudorapidity range of $2.2 \leq |\eta_i| \leq 4.2$ with full azimuthal angle ϕ coverage with respect to the beam axis (see Figure 4).

Each of the forward/backward hadron calorimeters has been segmented into four independent sections, or octants, which provide the necessary full azimuthal coverage when stacked around the beampipe. Each octant consists of 27 ($7' \times 7' \times 2''$) steel plates, which have been welded into two groups of 14 plates each to facilitate assembly, and 27 ($6.5' \times 6.5' \times 1''$) proportional chambers, which are located between neighboring plates. The total calorimeter system contains nearly 400 tons of steel and 216 chambers.

The cathode surface of each proportional chamber has been segmented into 20 bins in pseudorapidity ($\Delta\eta=0.1$) and 18 bins in azimuthal angle ($\Delta\phi = 5^\circ$). Thus the cathode pads at fixed η and ϕ on each of the 27 chambers in an octant form the necessary projective tower whose apex is the interaction point a distance of 280" from the calorimeter face, assuring approximately uniform occupancy rates for each detector element in typical high energy interactions. The signals from each chamber pad at fixed η and ϕ in an octant are summed together to give the total energy signal for a given projective tower. Figure 6 shows the assembly of one of the calorimeters from a beam's eye view. The cathode pad array in the last chamber in each octant of the calorimeter is shown to illustrate the segmentation.

Figure 7 shows the details of the chamber construction. The chambers are constructed using an aluminum extrusion of T-cross section and an epoxy fiberglass

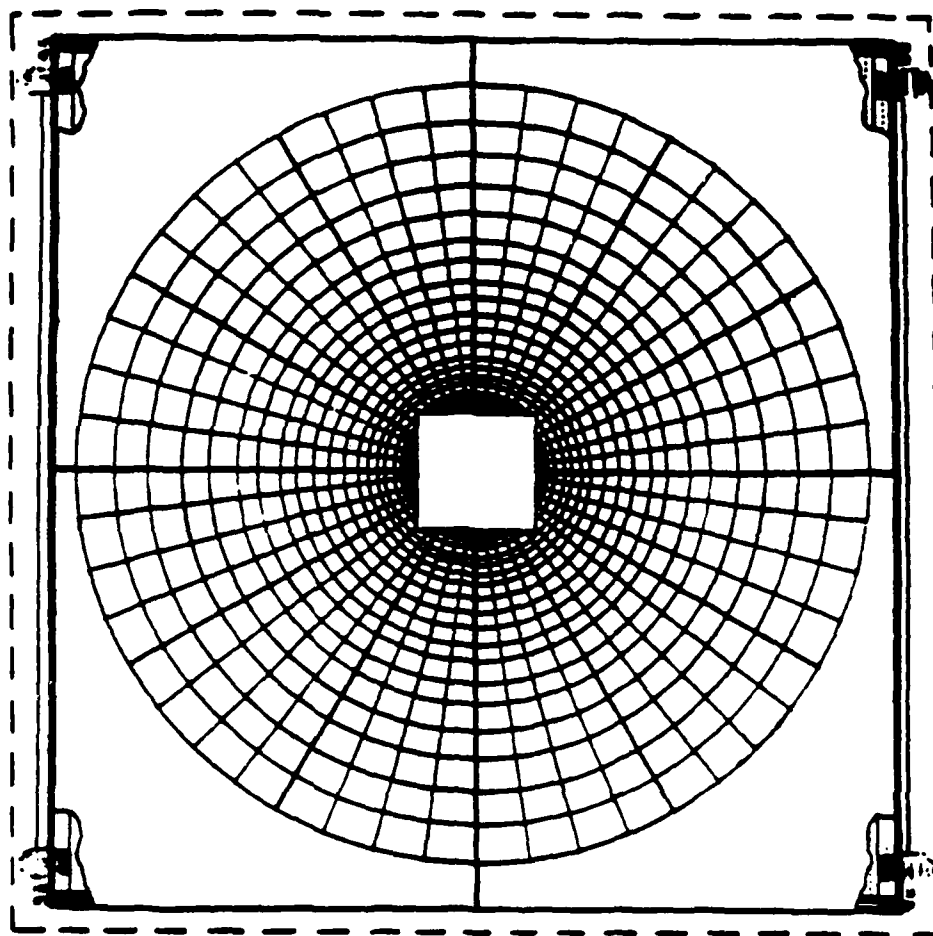


FIG. 6. Beam's eye view of a forward/backward hadron calorimeter (from Cihangir et al.¹²). Grids shown are for the last chamber in the calorimeter.

circuit board to form the basic cell structure. The T-shaped extrusions are glued to an aluminum base plate, resulting in an open channel structure. Each channel in this structure has dimensions of $0.4'' \times 0.6'' \times 77''$. At the ends of each structure is inserted an injection-molded plastic plug used to locate and fix the sense wires in each cell. A $0.002''$ diameter nickel-flashed and gold-plated tungsten wire is then stretched with 250 g of tension between each of these terminating blocks and soldered in place, centering the wires in each cell. The cells are then closed at the top by gluing the cathode circuit board over the open face using a specially formulated conducting epoxy. The circuit board is positioned with the conducting copper pads placed on the outside of the cells; another custom-blended conducting epoxy glue is applied to the fiberglass side of the cathode circuit board in order to sense the induced signals on the cathode pads. The typical surface resistivity achieved using this epoxy is in the range of 10 to 20 $M\Omega$ /cathode pad.

The signals on each of the 360 cathode pads of a chamber are bussed to the edge of the chamber using flat ribbon cables, which are soldered directly to the cathode circuit board and are terminated at the chamber's edge in a ribbon connector header. The chamber gas volume is then closed off by installing a final aluminum cover spaced above the cathode circuit board by $0.25''$ to allow for a reserve gas supply and space for the passage of ribbon cables and headers. The completed chamber is completely sealed with only the signal and high voltage connections penetrating the gas volume. This construction results in a very small pad capacitance to ground, with typical values for an individual pad on the order of 10 pF.

In addition to the charge information available from each cathode pad in the calorimeter, signals may also be read out from the chambers' sense wires. For this purpose each chamber is segmented into six sections of about 20 wires each. These

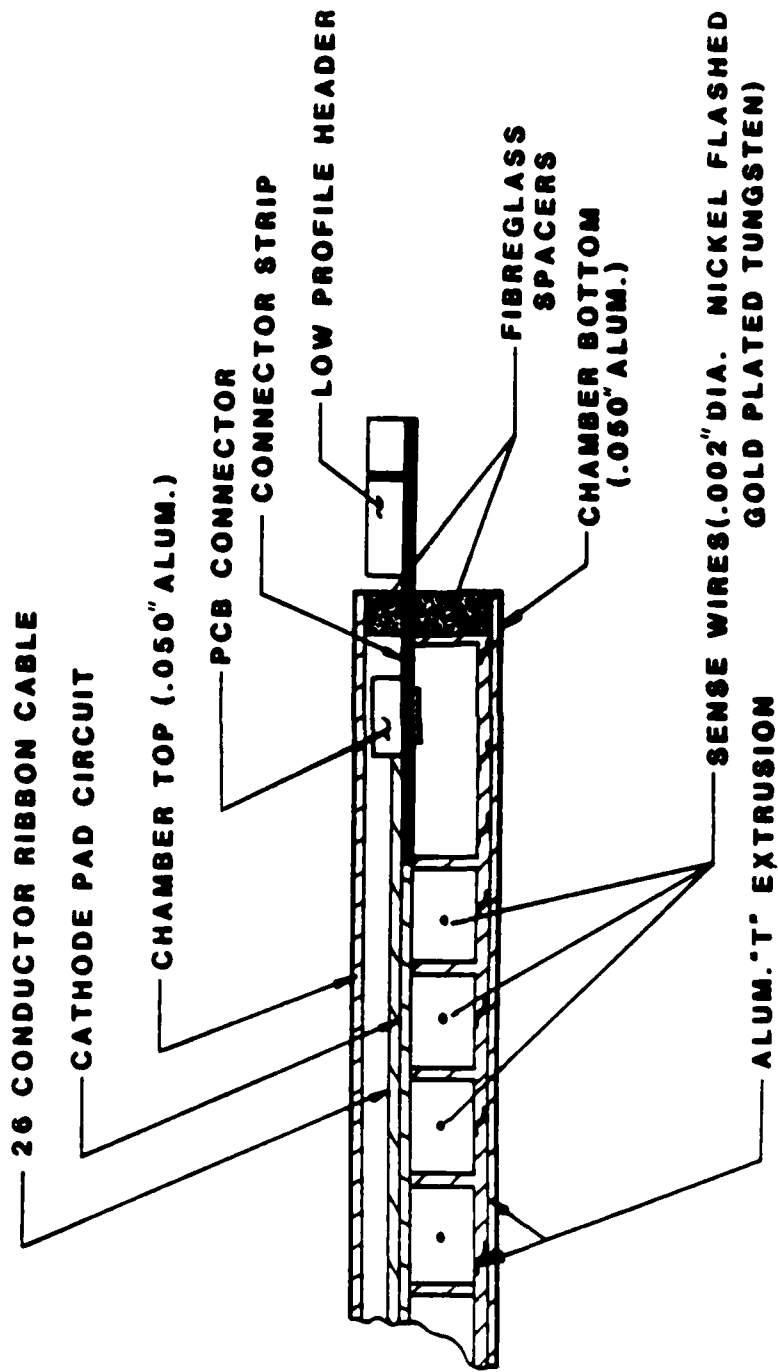


FIG. 7. Cross section of a forward/backward hadron calorimeter proportional chamber (from Cihangir et al.¹²).

signals can be used to independently monitor the performance of the calorimeters as well as to provide information on the longitudinal development of showers in the calorimeter. With gas mixtures of 50% argon/50% ethane, the chamber's high voltage operating range is between 1.9 and 2.4 kV.

E. Testing Calorimeter Performance^{12,13}

Cosmic ray tests were conducted during construction to determine chamber performance using minimum ionizing cosmic ray muons.

(1) Uniformity tests of the RC time constant of the cathode pads (including the conducting epoxy, cathode pad, and amplifier circuit) demonstrated that, while time constants of 10 to 30 μsec were observed for different chambers, the time constant over the surface of each chamber was uniform to better than 10%.

(2) Gain versus high voltage for each chamber was measured. As expected, the pulse height response to variations in high voltage is characteristically exponential in nature.

(3) Cosmic ray data was used to define the conversion from pulse height in pC to number of equivalent particles (*nep*) to assist in the comparison of results for FHA chambers to those of other calorimeters. The convention is that one equivalent particle (*ep*) is the charge deposited by one minimum ionizing particle which traverses the entire calorimeter.

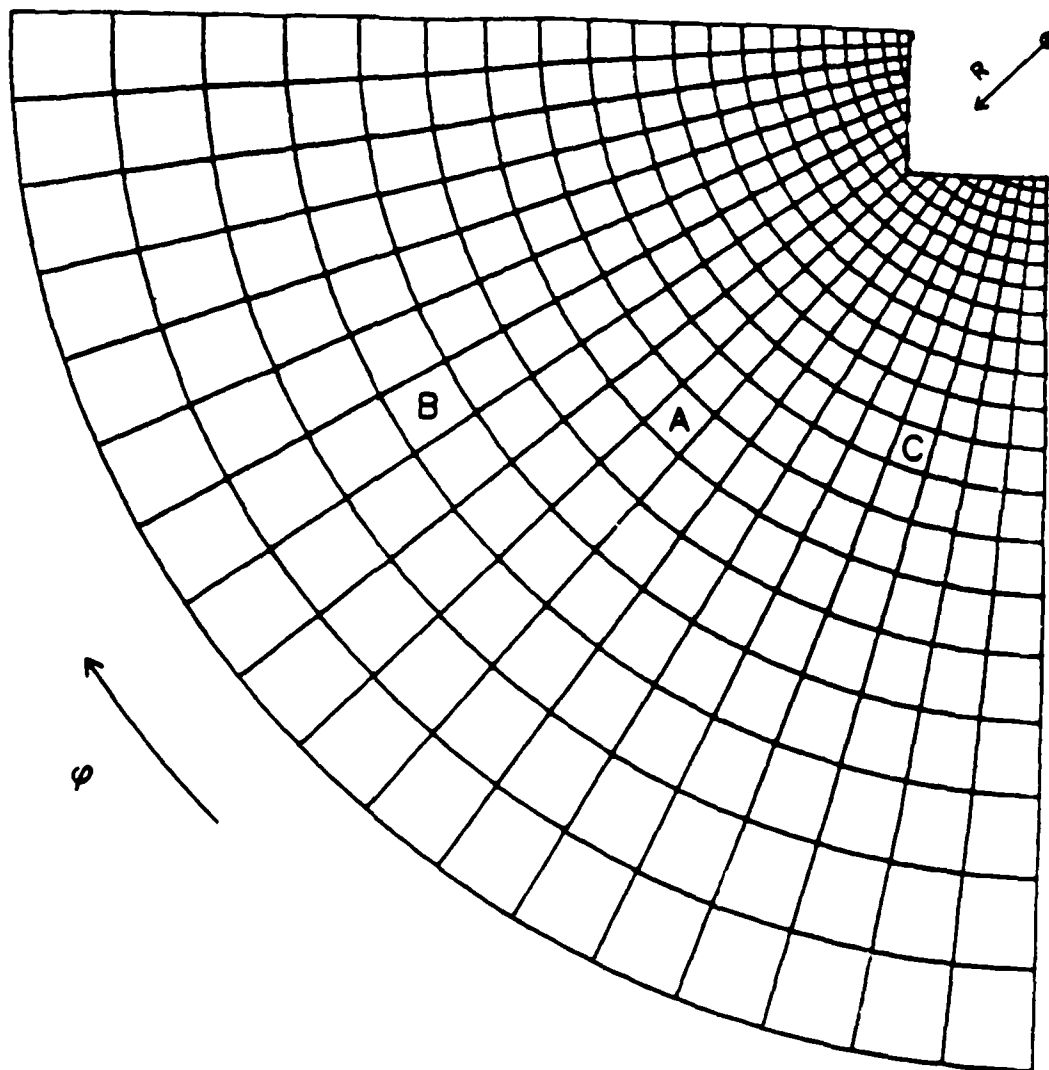
The performance of one octant of the FHA was studied using the fixed-target test beam at the Meson Bottom (MB) site in May 1985. The MB test beam provided a momentum-analyzed beam of hadrons, electrons, and muons in the range of 20 to 200 GeV/c, with a characteristic momentum bite of about 4%. Space limitations at the site allowed for only a limited position scan of the calorimeter (the three areas

of the calorimeter studied are labelled as A, B, and C in Figure 8). The information determined in this test beam run is indicative of the data sought for all calorimetry components studied.

During the test run, data was recorded at different positions of the calorimeter using hadrons, electrons, and muons over a range of beam momenta and as a function of chamber high voltage. Beam momentum and impact position were determined using beam proportional wire chambers (PWC's). On-line histogramming packages and off-line analysis programs were used to study data recorded on magnetic tape. Tests were done to determine linearity, uniformity, and resolution of calorimeter energy response, position resolution, longitudinal and transverse shower development in the calorimeter, response to electrons and muons, and effect on response with the FEM simulated in front of the FHA calorimeter.

(1) The nominal operating high voltage for the chambers was first determined by investigating the behavior of energy resolution over a range of high voltage settings. Hadrons of 100 GeV/c momentum incident on the calorimeter were used to study the rms deviation of the signal response distribution as a function of chamber high voltage. Best resolution was found to occur at 2.2 kV.

(2) For an ideal calorimeter, the peak of the total energy distribution readout should be proportional to the incident particle's energy. Plots of average pulse height in *nep* as a function of the beam energy for the three locations A, B, and C of the calorimeter showed linear response up to 200 GeV with no evidence of saturation in the calorimeter output response at the high-energy end of these measurements. Based on energy loss per *ep* in the calorimeter, the observed energy response was calculated to be 40% of the total hadron energy. No statistically significant differences in calorimeter response was noted between positions A, B,



position	R_{entrance} (cm)	R_{exit} (cm)	ϕ
A	74.90	98.35	42.5°
B	101.35	133.05	57.5°
C	61.29	80.44	17.5°

FIG. 8. Positions scanned during performance tests on the forward/backward hadron calorimeter in Oct 1985 (from Cihangir et al.¹²).

and C, demonstrating uniformity of energy response.

(3) A study of the resolution of the calorimeter as a function of the hadron shower energy supported the predicted energy dependence of $\Delta E/E$. At the operating voltage of 2.2 kV, plotting the calorimeter's energy resolution $\Delta E/E = \alpha\sqrt{E}$ yielded 1.41 GeV^{1/2} for α .

(4) The position resolution inherent in the calorimeter was measured by comparing the location of the shower center of gravity with the impact position of the beam particle as given by the beam PWC's. The rms deviation in the distribution of differences between these two values taken for different locations A, B, and C as a function of incident hadron energy showed a tendency of the spatial resolution to worsen as pad size increased (i.e., as distance from the beam axis increased) and that statistical fluctuations reduced resolution at lower beam energies. Resolution was better than 3 mm for energies greater than 120 GeV, but was only about 5 mm at 40 GeV.

(5) Spatial development of hadron showers in the calorimeter was investigated using input from adjacent cathode pad towers and the anode wire planes. Longitudinal development of single showers was studied by measuring energy deposited in all layers following the plane of shower origin for three different beam energies (40, 100, and 200 GeV). It was found that the shower maximum occurred at about one interaction length into the calorimeter and that the longitudinal energy distribution could be described by a simple exponential function of the form $e^{-a\lambda}$, where a depends on the beam energy and λ is the number of interaction lengths into the calorimeter. It was also learned that the fraction of energy which leaked out of the downstream end of the calorimeter was 2%, 3%, and 4%, respectively, for the beam energies studied.

(6) The transverse shower shape was studied by measuring the fraction of the shower energy appearing in cathode pads about the center of gravity of a given shower. Transverse shower shape could also be described by a simple exponential function of the form $e^{-\delta/c}$, where δ is the transverse distance from the shower center of gravity to the center of the cathode pad of interest.

(7) Tests were run on the calorimeter response to electrons and muons. As expected, electrons tended to initiate showers much sooner in the calorimeter than did hadrons, and these showers were totally contained in the front quarter of the calorimeter. At the nominal operating voltage, chamber gains were such that muon signals could not be reliably separated from pedestal variations in the ADC system.

(8) Lastly, a run was made with the calorimeter taking hadron shower data with lead bricks stacked in front of the calorimeter to simulate the FEM. Because a passive absorber was used to simulate the FEM, only qualitative observations could be made. Roughly 50% of the hadrons incident on the combined system had not interacted before reaching the first hadron calorimeter chamber. In this case, energy response of the FHA was essentially the same as before. For the other 50%, the energy distribution was shifted to an average lower energy with a larger rms error. In the complete CDF detector, hadrons which begin to shower in the EM system will have this energy measured.

F. Tests on Chamber Aging¹⁴

Alcohols mixed with ionization gases in wire chambers normally extend the life of the chambers by preventing the aging of wires and by controlling the onset of glow mode discharge. Although ethyl alcohol is used most often, it cannot be used in the FHA because it dissolves the resistive glue used in chamber construction. Isopropyl

alcohol is safe for use. Small prototypes of a chamber were used to determine the efficiency of isopropyl alcohol in preventing aging. It was found that the RC time constant of pulses generated by Fe^{55} sources, as well as pulse height and full width at half maximum (FWHM), did not differ before and after aging tests.

The gain change at a fixed high voltage was measured as a function of the amount of alcohol in the gas mixture flowing through the chambers. The amount of alcohol is controlled by varying the temperature of the alcohol bubbler, refrigerator through which the gas mixture passes. It was learned that gain changed with increasing amounts of alcohol in the argon-ethane mixture, where temperature was varied in 5° increments from -10° to 10° C.

CHAPTER IV

CDF TEST BEAM FACILITY AT THE MESON TEST SITE

A. CDF Test Beam Requirements

To study and calibrate the various elements of the CDF detector, separate fixed-target test beam facilities must be used, since CDF itself is located in the main ring of the superconducting Tevatron and necessary particle beams with variable energies cannot be made available there.

Earlier test beam studies have been carried out at the Neutrino West (NW) site and at the Meson Bottom (MB) site from Dec 1983 to Jul 1984 and from Nov 1984 to Aug 1985. These test beam facilities have since been dismantled. A more permanent fixed-target test beam facility is being constructed at the Meson Test (MT) site and will initially support both CDF and experiment T755 (Yale University's high-resolution streamer chamber).

CDF has a continuing need for a well-understood beam of known energy for calibration and further study of the calorimetry over the entire life of the detector. For this reason CDF requested a dedicated test beam facility be made available.¹⁵ Specifically, CDF required a test beam facility which would allow for:

(1) Calibration of electromagnetic (EM) calorimeters to an accuracy of 1% and hadronic calorimeters to an accuracy of about 3%.

(2) A high energy beam of up to 300 GeV to study saturation and shower leakage in the gas calorimetry.

(3) A low energy beam of 1 to 10 GeV to understand in detail the nonlinearity in scintillator calorimetry, the muon trigger rate in the central muon detector, and the anomolous energy deposition due to slow thermal neutrons (on the order of 1

MeV) resulting in signals in the 10 GeV range in all gas calorimetry.

CDF also made specific requests for beam parameters necessary to meet the objectives listed above.¹⁶ The original parameters requested include:

- (1) A beam of 1 to 300 GeV energy range for both hadrons and electrons.
- (2) Particle identification, *either* by
 - (a) Having a "pure" hadron beam with less than 1:2000 electron contamination and a pure "electron" beam with less than 1:2000 hadron contamination (with muon contamination acceptable in both), *or* by
 - (b) Having a beam with particle-by-particle tagging to the above levels.
3. A muon beam, with hadron and electron contamination acceptable.
4. A momentum tagging system so that the momentum of each particle can be measured with an accuracy better than 0.3%.
5. Less than 20,000 particles per spill cycle but more than 20 particles per spill cycle over the entire energy range.

In order to meet the needs of CDF and other applicable experiments, the Meson Test beamline was recently designed and installed, with the first beam to target recorded on 6 Jul 1987.

To provide long-term support tailored to CDF requirements in the coming years, a CDF test beam facility has been constructed in the Meson Lab building, where the MT beam emerges from the Meson test beam tunnel complex.

The critical guideline in designing and constructing all operational parts of the CDF test beam facility is to duplicate those in the actual CDF at B0 as closely as possible. This insures that all test beam data will be reproducible in the CDF collision hall. Besides budgetary constraints, the major difficulty in fully implementing this guideline is the fundamental difference between CDF, built

around a colliding beam nexus, and the test beam facility, which is based on a fixed-target beamline.

Following the first physics run of the CDF, which was completed in May 1987, CDF set specific goals for the first fixed-target test beam run planned for Oct 1987 through Jan 1988.¹⁶ The aim is to have a much more thorough understanding of the calorimetry before the next colliding-beam physics run beginning in Mar 1988. Due to delays in production of hardware and software necessary for the test beam facility, it is doubtful that all of these goals will be met before the first test beam run ends, but they are still used as guidelines in preparing the test beam facility for operation. These goals are:

- (1) Detailed studies of detector response to very low and very high energy particles.
- (2) Calibration of the remaining FHA chambers which were not available for calibration during past test beam runs.
- (3) Recalibration of subsets of other calorimeter systems.
- (4) Studies of the interfaces between separate calorimeter systems in the detector (so-called "crack" studies).
- (5) Studies of a prototype silicon vertex detector, a high resolution drift chamber to be placed on the vacuum beam pipe as part of CDF in the collision hall in a future upgrade.
- (6) Testing of a very forward calorimeter, which will be located 100 m on either side of the interaction point in the collision hall, allowing for the detection of very small angle diffractive and elastic scattering.
- (7) Testing of a 90° crack chamber, which may be installed in a future CDF upgrade.

B. Status of the CDF Test Beam Facility

A floor plan of the CDF test beam facility is shown in Figure 9. The facility includes a counting house, a gas delivery and monitoring system, three fixtures to support detector elements, a beam stop, and a fence to control access.

The counting house is an air-conditioned, sprinkler-protected building constructed inside the Meson Lab. One room houses a VAX 11-750 computer and the majority of the data acquisition electronics. The second room is occupied by the shift crew and has computer terminals, computer output printers, a beam control console, and television screens to help monitor detector component status.

The gas delivery system occupies space outside the counting house, with the major control and monitoring stations placed outside the fence for access during beam runs. The gas delivery system is described in detail in Chapter V. The controlled-access fence satisfies Fermilab safety requirements, insuring that personnel cannot gain entry to the fixture area while the beam is running. The beam stop at the downstream end of the facility has a moveable aperture which allows beam to reach the T755 experimental area when needed.

The three fixtures are designed to hold certain fractions of the CDF detector components, as well as the necessary front-end electronics and parts of the gas delivery system. Each fixture can roll laterally on tracks through angles of about 30° on each side of the beam axis and can be raised and lowered hydraulically to provide as much coverage as possible of the detector elements by the beam. Fixtures may be rotated completely out of the beamline. The upstream fixture is the wedge fixture; for the first run it will hold parts of the Central Muon Detector (CMU) and the Central Electromagnetic Strip Detector (CES). The middle fixture is the plug fixture, which will support parts of the plug EM calorimeter (PEM) and the plug

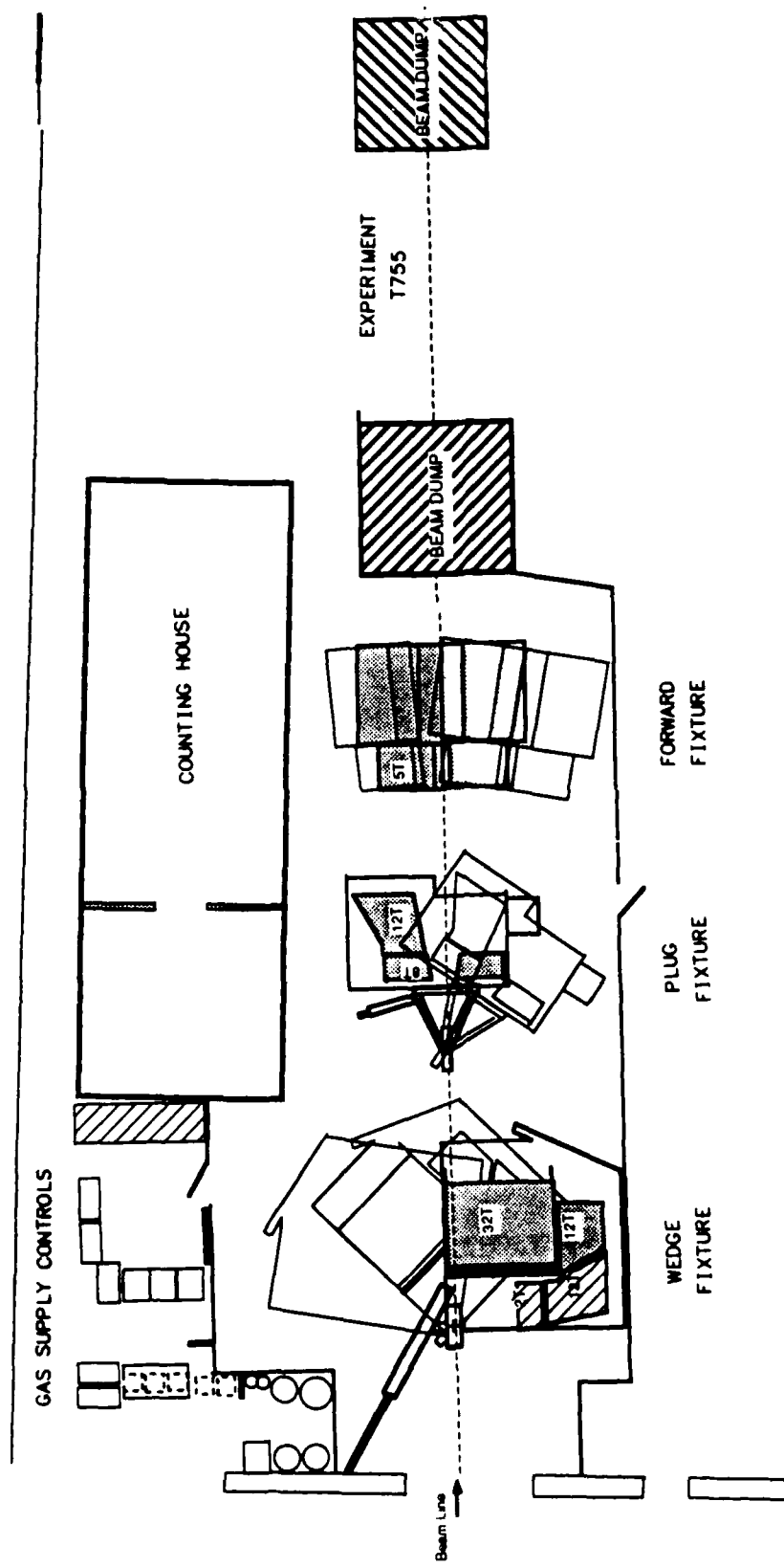


FIG. 9. Floor plan of the CDF test beam facility at the Meson Test site.

hadron calorimeter (PHA). One octant each of the forward EM calorimeter (FEM) and the forward hadron calorimeter (FHA) are mounted on the forward fixture, located farthest downstream.

Future improvements are planned for the CDF test beam facility. A unistrut-supported Herculite enclosure will be erected around the fixture area to provide environmental control and protection for the fixtures. This structure will include air conditioning and heating systems and will prevent dirt and rainwater leaking through the Meson Lab roof from reaching the fixtures. This structure will enclose approximately 30,000 ft^3 and will allow for temperature inside to be maintained at $70^\circ \pm 10^\circ F$. The wedge fixture will be replaced or modified and the plug fixture will be modified by 1989 so that they will be capable of supporting additional detector elements. This will allow for configurations which more closely resemble those in the CDF, so that more detailed studies of detector response to particles passing through the interfaces between detector elements can be carried out.

C. The MT Test Beam

The MT test beam is split off as a secondary beam from the Meson West (MW) beam, which consists of 800 GeV primary protons extracted directly from the Tevatron through a beamline system called the Switchyard. The MT beam is called a secondary beam because it is produced by colliding the MW beam's 800 GeV protons with one of three lead (Pb) targets and then bending the product particles (mostly pions) through a series of dipole magnets. The MT beamline was originally designed to produce 245, 160, and 80 GeV hadrons, depending on which Pb target is used.

A tertiary beam of lower energy particles (at least 10 to 220 GeV), either

of hadrons or electrons, is produced by colliding the secondary beam of 245 GeV hadrons with Pb targets further downstream in the beamline.

Due to the parasitic nature of the MT beam, the intensity of the MW beam directly affects particle production rates in the MT beam. To meet all of the beam parameters required by CDF, the MW beam intensity must reach certain levels. However, during the Fall 1987 fixed-target run, MW beam users require intensities well below these levels, making it impossible to satisfy all CDF MT beam requirements. In future runs, however, MW beam intensities are expected to be high enough to fulfill all requirements. It is also significant that experiment T755 demands beam parameters quite different from those of CDF, so that their beamline analysis and tunes will in most cases be of minimal value to CDF.

A more detailed discussion of beamline components and modes of operation is presented in Chapters VI and VII.

CHAPTER V

GAS DELIVERY SYSTEM FOR THE CDF TEST BEAM FACILITY

A. Design Guidelines

During the first run of the CDF test beam facility, six detector elements will be studied which require the supply of gas mixtures. These elements are listed in Table II, together with the gas mixtures normally used in CDF at B0 and the gas flow rates expected in the test beam facility.

A major goal of the first test beam run is to study the energy response of selected detector elements when different gas mixtures are used. To maximize beam time, different gas mixtures have to be run simultaneously to different elements.

To insure necessary flexibility of the gas delivery system, the following design guidelines were established:

(1) Each detector element would have an independent gas supply. This would require separate control and monitoring systems from the gas source to each element.

(2) Up to three gas mixtures might be delivered simultaneously: 50% argon/50% ethane, 95% argon/5% carbon dioxide, and 88.5% argon/10% carbon dioxide/1.5% methane. Because the argon/ethane mixture is used predominantly, a gas supply trailer would be used to save space in the test beam facility that would be lost to gas bottles. Under high flow rates, time would also be lost to frequent changing of gas bottles. A CDF gas supply trailer holds 263.5 gal of the argon/ethane mixture under 300 psia, which equates to 5380 SCFH (standard cubic feet per hour) of this mixture. Under normal operating conditions at the test beam facility, this would supply enough argon/ethane to last a month. Another major benefit of a gas supply trailer is the stability of gas quality it would provide. During the first CDF

TABLE II. Detector elements requiring gas mixtures to be studied during the first test beam run. Gas mixtures shown are those currently used in CDF.

Detector Element	Gas Mixture	Flow Rate [SCFH]	Flush Rate [SCFH]	Stored Volume ft^3	Alcohol	Alcohol Temp [C]
CMU	50% Ar/50% Ethane	0.5	1.0	24	Isopropyl	0
PEM	50% Ar/50% Ethane	0.5	3.0	52	Isopropyl	-5
PHA	50% Ar/50% Ethane	1.0	3.0	16	Ethanol	0
FEM	50% Ar/50% Ethane	1.5	3.0	21	Isopropyl	10
FHA	50% Ar/50% Ethane	2.5	5.0	108	Isopropyl	10
CES	80% Ar/20% CO ₂	0.4	-	0.9	-	-
CMU Inert Jacket	N ₂	0.5	-	-	-	-

CMU = Central Muon Detector

PEM = Endplug Electromagnetic Calorimeter

PHA = Endplug Hadron Calorimeter

FEM = Forward Electromagnetic Calorimeter

FHA = Forward Hadron Calorimeter

CES = Central Electromagnetic Strip Detector

physics run, trailer gas quality was never poorer than 51%/49%, while gas bottle quality was often as poor as 55%/45%, and once was 60%/40%. A trailer stand with underground feed lines to the Meson Lab would have to be built. Argon/carbon dioxide mixtures would be supplied from bottles inside the facility but outside the controlled-access fence.

(3) Nitrogen would be used to purge detector elements when gas mixtures are changed. Purge flow rates are different for each detector element, but generally are two to five times the normal gas flow rate, depending on the detector element. An inert jacket of nitrogen would be maintained around the wedges, flowing at a rate of about 0.2 SCFH, for two reasons: (a) all gas calorimeters lose efficiency when air, and particularly oxygen, leak into their chambers; the CMU wedges tend to leak more than other detectors and are more sensitive to oxygen impurities, and (b) nitrogen reduces the potential spark hazard created by exposed high voltage cables at the wedges. An inert volume of nitrogen for the wedge fixture is feasible because all detector elements are confined inside a metal jacket. Finally, nitrogen would be used to dilute the argon/ethane gas mixture leaving the fixtures to levels below ethane's lower explosive limit before the gas is vented to the atmosphere. To save space, a 165 l dewar would be located in the facility outside the fence. This dewar will provide 4060 SCFH of nitrogen. A nitrogen bottle would be needed to maintain necessary pressure in the dewar, and a heat exchanger would be included at the dewar output to prevent freezing.

(4) Separate alcohol bubblers refrigerators would be part of the gas supply line to each detector element (except to the CES); controls would allow routing of gas mixtures around the refrigerators when alcohol is not required. Detector elements use isopropyl or ethyl alcohol as an additional quenching gas in the

argon/ethane mixture (see Table II for alcohol type and nominal temperature setting of refrigerators). Alcohol is not required when argon/carbon dioxide mixtures are run.

(5) A special gas pressure buffer system is used in the CDF collision hall to maintain the FHA and FEM chambers at exactly atmospheric pressure, even while gas is flowing.¹⁷ These chambers, with their large surface area to volume ratios, will rupture at only 0.1" of Hg above or below atmospheric pressure. The buffer system protects the chambers from such damage. A single buffer system supports each adjacent octant of the FEM and FHA in the collision hall. A comparable gas pressure buffer system would be designed and constructed for the forward fixture, but with the capability to act independently for each calorimeter system.

(6) The gas delivery system would accommodate the ability of all three fixtures to move about on their tracks. Where necessary, flexible hose must replace the more durable metal piping normally used.

(7) Gas quality would be monitored every 15 minutes directly by the data acquisition system, as is done in CDF at B0. The gas quality monitoring system used in CDF would be reproduced with appropriate modifications.

(8) All safety requirements would be met. The most significant safety hazard is ethane, which is explosive.^{18,19} Ethane must be properly vented to the atmosphere, where dilution eliminates the hazard. All feed lines must not contact electronics or cables. Ethane detectors with the necessary electronics and alarms would be installed at key locations.

(9) The most efficient means of determining leaks in the gas supply system is to monitor the oxygen levels in the gas mixtures leaving the fixtures. This information is also useful for experimenters, since gas calorimetry chamber efficiency is reduced

by even small amounts of impurities (particularly oxygen) in the gas flow mixture. An automated oxygen monitoring system would be included as part of the gas supply system.

B. Final Design

Schematic diagrams of the final design of the gas supply system for the CDF test beam facility are shown in Appendix B. This appendix includes: (1) the floor plan for the gas supply system controls located outside the controlled-access fence, (2) schematic diagrams of the apparatus transporting gas mixtures to and from each of the detector elements, (3) schematic diagrams of the gas pressure buffer system for the FHA and FEM chambers, and (4) an equipment list identifying all components of the gas supply system.

Gas flow rates are expected to be 6 SCFH in the normal operating mode and up to 15 SCFH in the flush mode for the first test beam run. When the wedge and plug fixtures are upgraded to hold more chambers, rates will increase to 12 SCFH in the normal operating mode and to 30 SCFH in the flush mode.

Gas piping is 0.5" stainless steel welded pipe except where flexible hose is required to accommodate the movement of the fixtures. Here Cajon smooth-bore teflon flex hose is used. This tubing is preferred because its walls do not degas, which would add impurities to the gas mixture reaching the chambers.

The CDF argon/ethane gas supply trailer is parked on a hardstand 50' south of the Meson Lab and against the adjoining west-side berm. Trailer changes will require flow shutdown for one hour, using valves located at the hardstand. All contaminated lines are purged with nitrogen during reconnection. Gas bottle changes for argon/carbon dioxide gas mixtures inside the Meson Lab require no

special precautions.

The alarm system for gas leaks will consist of four ethane detectors, with one located under each fixture and the fourth in the gas control racks. Should the control module send an alarm, power to all fixtures (including chamber DC high voltage and 60 and 400 Hz power) will be shunt tripped automatically. The alarm level will normally be set at 20% of the lower explosive limit for ethane.

Each detector element using the argon/ethane mixture has its own start-up procedures, but all follow the following guidelines:²⁰

(1) All chambers are leak tested elsewhere before installation in the test beam facility.

(2) Flow is first started using nitrogen at flush flow rates (usually two to five times the normal flow rate); this flow is maintained for at least five volume changes.

(3) If possible, a system leak check is carried out by comparing input nitrogen flow rate to output flow, or by overpressuring the detector element's chambers and observing the decay time of the overpressure in the absence of flow.

(4) The ethane alarm system is checked before argon/ethane flow is begun.

(5) Argon/ethane flow is started at flush flow rates and an immediate check is performed with a hand-held ethane leak detector.

(6) After at least five volume changes, the argon/ethane flow rates are reduced to normal operating levels, and a final pass is made with ethane leak detectors. At this time high voltage tests are performed.

(7) Shutdowns for extended periods of several weeks or months require a complete purge using nitrogen.

CHAPTER VI

OVERVIEW OF THE MESON TEST BEAMLINE

A. Introduction

The beamline installed at the Meson Test (MT) site is one of the newest fixed-target beamlines at Fermilab. It is somewhat unique in that it is parasitic directly off of another beamline, the Meson West (MW) beamline, also recently designed and installed. Roger Tokarek, a beamline physicist at Fermilab, designed both beamlines and is responsible for providing assistance to experimenters using the MT and MW beams.

Design of the MT beamline began at the end of 1985. The primary design consideration was to produce the maximum possible energy particles at the target area. First beam to target was recorded on 6 Jul 1987. Roger Tokarek and I determined preliminary tunes (i.e., magnet current settings) to maximize yields and optimize beam profiles at the target for the three primary design energies of the beamline during the period from Jul to Aug 1987. The first two users of the MT beam are CDF and experiment T755 (Yale University's high resolution streamer chamber); each requires very different types of beam, so that each must carry out its own beamline and tune studies.

A beamline is always in a state of flux, as components are added, removed, or replaced. Tunes are continuously improved upon throughout the life of the beamline. The quality of the beam itself changes frequently as the transport systems delivering the primary proton beam to production targets are continually altered and retuned. Because the MT beam is parasitic to the MW beam, MW experimenters also affect MT beam quality as they retune components upstream of the MT beamline. Thus

my beamline studies represent a snapshot of the MT beamline as it existed in Jul to Oct 1987. While these studies may truly be labeled preliminary, they provide valuable information on the beamline. They are particularly significant to the CDF test beam facility's first run in Fall 1987 since further studies may be limited before the run ends in Jan 1988.

Two major errors in the beamline were discovered in mid-Sep and early Oct of this year, after the majority of my beamline studies were completed. First, it was learned that the second pair of focusing quadrupole magnets had polarities opposite those that were assumed. All computer analysis and subsequent tuning based on nominal magnet current settings from this analysis were carried out based on the assumed polarities. The second and more significant error involved the energy of the primary proton beam used to produce the MT beam. The MT beamline was designed based on 900 GeV energy primary protons being delivered to the production targets at the beginning of the MT beamline, allowing for optimum production and transport of 245, 160, or 80 GeV secondary particles (thus the reason these are called the "primary tune" energies), depending on which production target is used. In reality, 800 GeV protons arrive at these targets, resulting instead in optimum production of 227, 151, or 75 GeV secondary particles. Again, however, all computer analysis, tuning, and other studies were conducted based on 245, 160, and 80 GeV secondary production.

The effect these errors have on the results of the preliminary beamline studies will be discussed where appropriate, but the usefulness of the data from these studies is not significantly reduced. At the end of this chapter, updated computer analysis based on the correct primary proton beam energy of 800 GeV and the subsequent secondary particle energies will be presented.

B. The Beamline

1. Current Configuration

The MT beamline is described in terms of the spatial coordinates x , y , and z , as defined in Figure 10 below. The coordinate z generally points along the direction the beam travels (that is, it points downstream). Looking downstream, positive x points in the horizontal direction to the left and positive y points up in the vertical direction. The origin and the exact direction of z is determined arbitrarily by surveying personnel.

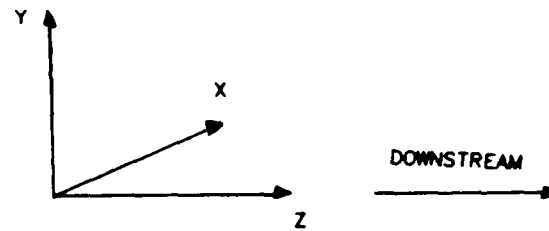


FIG. 10. The beamsheet coordinate system.

The exact location of beamline components is determined by survey personnel. The position of MT beamline components and their associated device names are listed on the MT beamsheet in Table III. The location given is that of the geometric center of each component. The horizontal displacement of MT beamline components is plotted in x versus z in Figure 11. While there is substantial displacement in x

TABLE III. MT beamsheet.

M-TEST 87/10/04.

Z CENT. (FT)	X CENT. (IN)	Y CENT. (IN)	ELEMENT CODE	POWER SUPPLY
118.8	1.59	.41	• MT .03% AL TARGET, NOT MOVEABLE	MT2TGT0
129.3	1.74	.42	21' ED/S DIPOLE, ROLLED 1.5 DEG.	MW2WD1-3
145.2	2.05	.43	• MT 227 GEV TARGET, MOVEABLE	MT2TGT1
151.2	2.17	.44	6-3-120, ROLLED 16.85 DEG.	MW2WD2-1
157.3	2.31	.45	• MT 151 GEV TARGET, MOVEABLE	MT2TGT2
163.5	2.45	.45	6-3-120, ROLLED 16.85 DEG.	MW2WD2-2
169.6	2.61	.45	• MT 75 GEV TARGET, MOVEABLE	MT2TGT3
175.7	2.77	.45	6-3-120, ROLLED 16.85 DEG.	MW2WD2-3
256.5	5.64	.15	EPB DIPOLE, ROLLED 6.16 DEG.	MT2WU-1
267.4	6.08	.12	EPB DIPOLE, ROLLED 6.16 DEG.	MT2WU-2
278.4	6.58	.10	EPB DIPOLE, ROLLED 6.16 DEG.	MT2WU-3
289.4	7.15	.09	EPB DIPOLE, ROLLED 6.16 DEG.	MT2WU-4
300.4	7.78	.08	EPB DIPOLE, ROLLED 6.16 DEG.	MT2WU-5
546.4	23.18	.02	3Q120	MT3Q1
555.4	23.74	.02	HORIZONTAL COLL, VAC	MT3CH1
561.9	24.15	.01	VERTICAL COLL, VAC	MT3CV
570.9	24.71	.01	3Q120	MT3Q2
578.6	25.19	.01	VERTICAL TRIM, 5-4-30	MT3V
744.8	35.60	-.03	HORIZ VACUUM COLLIMATOR	MT3CH2
747.9	35.80	-.03	BEAM PWC, 2 MM	MT3PWC
748.3	35.82	-.03	SCINTILLATION COUNTER	MT3SC
748.9	35.86	-.03	TARGET, FERRIS WHEEL	MT3TGT1
754.7	36.22	-.03	EPB DIPOLE - HORIZONTAL SWEEPER	MT3SW
765.2	36.88	-.03	BEAM STOP	MT3BS
799.5	39.03	-.04	CONVERTER, FERRIS WHEEL	MT3CON1
805.0	39.38	-.04	EPB DIPOLE, ROLLED 25.9 DEG.	MT3WU
816.4	40.13	-.03	EPB DIPOLE, ROLLED 25.9 DEG.	MT3WU
996.8	52.48	.44	BEAM PWC, 2 MM	MT4PWC
997.6	52.54	.45	ELECTRON KILLER, FERRIS WHEEL	MT4CON
1003.4	52.94	.46	3Q120	MT4Q1
1025.3	54.44	.52	3Q120	MT4Q2
1084.7	58.51	.67	CERENKOV COUNTER	MT4CC
1137.2	62.11	.81	SCINTILLATION COUNTER	MT4SC
1138.3	62.18	.82	SINGLE WIRE DRIFT CHAMBER	MT4SWDC

TABLE III, Continued

Z CENT. (FT)	X CENT. (IN)	Y CENT. (IN)	ELEMENT CODE	POWER SUPPLY
1208.6	67.00	1.00	SINGLE WIRE DRIFT CHAMBER	MT5SWDC1
1215.5	67.46	1.02	EPB DIPOLE	MT5E-1
1227.0	68.18	1.05	EPB DIPOLE	MT5E-2
1238.5	68.84	1.08	EPB DIPOLE	MT5E-3
1250.0	69.44	1.11	EPB DIPOLE	MT5E-4
1261.5	69.97	1.14	EPB DIPOLE, 5" GAP	MT5E-5
1273.9	70.48	1.17	SYNCHROTRON RADIATION DETECTOR	MT5SRD
1282.4	70.82	1.19	SINGLE WIRE DRIFT CHAMBER	MT5SWDC2
1365.8	74.20	1.41	SINGLE WIRE DRIFT CHAMBER	MT6SWDC
1366.3	74.22	1.41	SCINTILLATION COUNTER	MT6SC1
1366.3	74.22	1.41	SCINTILLATION COUNTER	MT6SC2
1366.5	74.23	1.41	SCINTILLATION COUNTER	MT6SC3
1367.0	74.25	1.42	SCINTILLATION COUNTER	MT6SCV
1368.8	74.32	1.42	BEAM PWC, 2 MM CDF APPARATUS	MT6PWC1
1442.8	77.32	1.61	BEAM PWC, 2 MM H, 1 MM V	MT6PWC2
1449.0	77.57	1.63	INTERMEDIATE BEAM STOP/DUMP	MT6BS1
1454.6	77.75	1.64	SCINTILLATION COUNTER	MT6SCMU
1469.6	78.40	1.68	T755 STREAMER CHAMBER	
1482.5	78.92	1.72	MT FINAL BEAM DUMP	

down the beamline, the MT beamsheet shows that vertical displacement is quite small, only ranging from $-0.04''$ to $1.72''$. The fact that horizontal movement of the beam is much greater than vertical movement affects relative beam spread in both planes, as will be explained in Section E. Commonly used symbols for beamline devices are shown in Figure 12, and device names are explained more fully below. It is not accidental that magnets are represented by familiar optical devices such as prisms and lenses, as will be seen in the section on beam optics presented below.

The MT beamline is a positively-charged particle beam transport system, due to the direction of the magnetic fields of the bending magnets, which bend these particles to the next transport device. Negatively charged particles, bent in the opposite direction, are swept out of the beamline.

The MT beam is termed a "secondary beam" since it is produced by colliding a primary beam of particles onto a secondary production target, creating secondary particles of various energies. Based on the downstream magnet field strengths and the aperture sizes of transport devices, a small range of energies may be selected for transport to the final target area. Tertiary production targets may also be introduced in the MT beamline downstream of the secondary production targets, so that tertiary beams may be produced and transported to the final target area.

2. Naming Convention for Beamline Devices

Beamline components are monitored and controlled remotely through the experimental areas central PDP-11 computer, using the Experimental Areas Beamline Control System (EPICS).²¹ CAMAC (Computer Automated Measurement and Control) system electronics serve as the physical connection between the central computer and the beamline devices. Although CAMAC is an internationally ac-

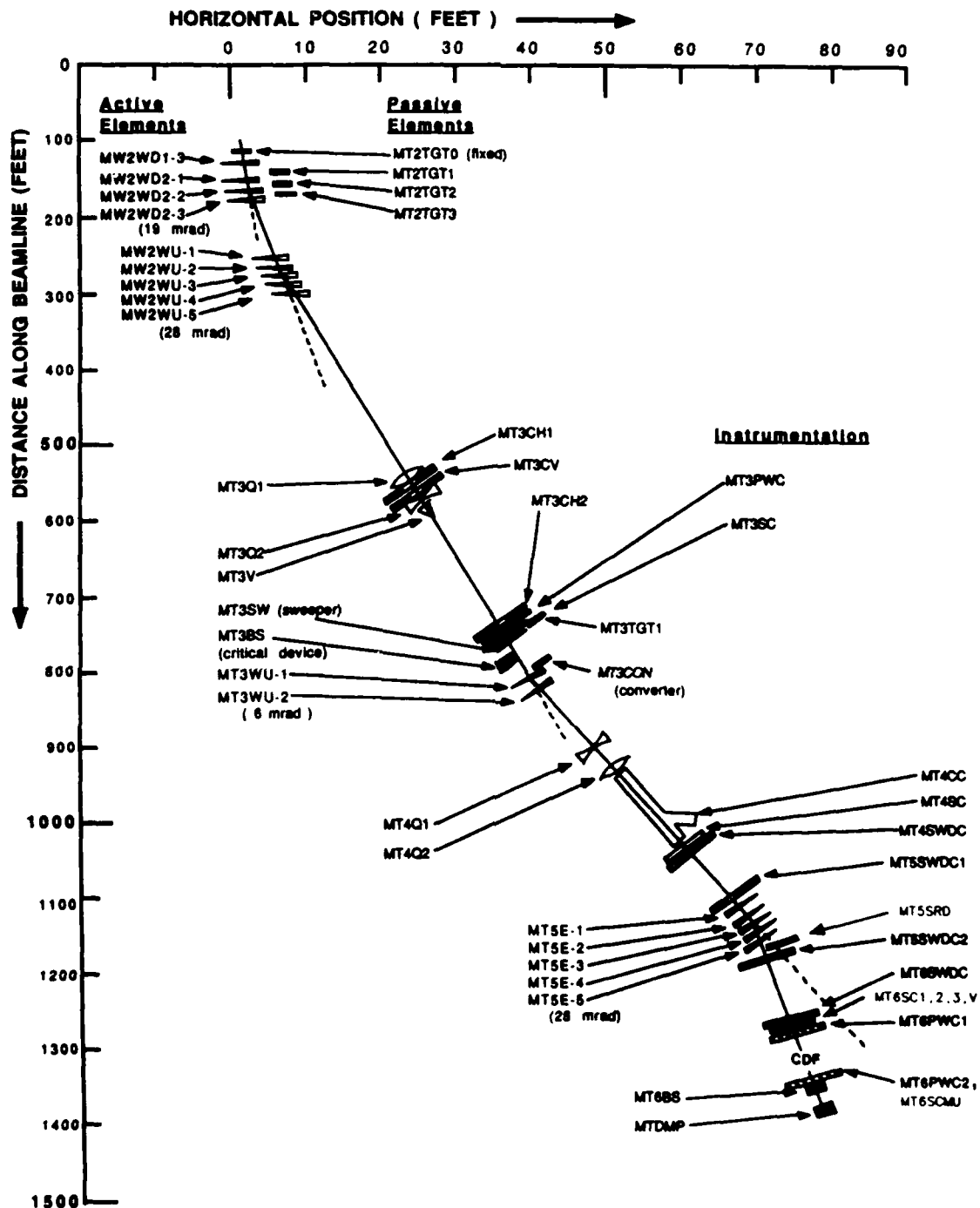


FIG. 11. MT beamline components plotted in horizontal position x vs. longitudinal position.

Active Elements

	DIPOLE MAGNET
	TRIM DIPOLE MAGNET
	HORIZONTAL FOCUSING QUADRUPOLE
	HORIZONTAL DEFOCUSING QUADRUPOLE

Passive Elements

	FERRIS WHEEL TARGET OR CONVERTER
	COLLIMATOR
	BEAM STOP

Instrumentation

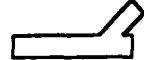
	SCINTILLATION COUNTER
	BEAM PROPORTIONAL WIRE CHAMBER
	THRESHOLD CERENKOV COUNTER
	SINGLE WIRE DRIFT CHAMBER

FIG. 12. Beamline component symbols.

cepted set of standards for electronics-computer instrumentation, Fermilab uses its own nonstandard serial communications link over CAMAC electronics.²²

Beamline components are given device names retained in the central EPICS computer's memory so that beamline operators may access and control these devices remotely.²³ The device name has the format A B C DDDDDD and gives at least four types of information:

- (1) A - Area in which the device is located.
- (2) B - *Beamline* in which the device is located.
- (3) C - *Enclosure* in which the device is located.
- (4) - DDDDDD - *Type and function* of the device (from one to six characters in this field).

Pertinent device types and functions are designated by the following codes:

Q = Quadrupole magnet

W = Dipole bending magnet which bends to the west (looking downstream)*

E = Dipole bending magnet which bends to the east (looking downstream)*

U = Dipole bending magnet which bends the beam up*

D = Dipole bending magnet which bends the beam down*

V = Trim magnet which bends in the vertical plane

CH = Collimator with horizontal collimating jaws

CV = Collimator with vertical collimating jaws

TGT = Target

PWC = Proportional wire chamber

PWCS = Proportional wire chamber scanner

SEM = Secondary emission monitor

SC = Scintillation counter

CC = Čerenkov counter

SRD = Synchrotron radiation detector

BS = Beam stop

BD = Beam dump

* (Designations depend on the charge of particles being transported.)

A typical name would be MT2WU-1, where

M = Meson area

T = Test beamline

3 = Enclosure 3

W = Dipole magnet which bends to the west

U = Dipole magnet which bends up

1 = First magnet in the magnet string MT2WU.

This illustrates the fact that magnets, particularly bending dipole magnets in high energy beamlines, often are employed in strings, or series of magnets. Normally each magnet in a string has the same current setting, so that strings are treated as if they were one longer magnet. Besides providing greater bending angles, strings allow the use of linear instead of curved magnets in the beamline. Curved magnets are required if the bend angle would cause the loss of significant numbers of particles as they scrape the wall of a linear magnet in their arced path. The magnetic fields of curved magnets are not uniform and are much more difficult to work with.

For purposes of radiation safety, beamlines are run in underground tunnels. Each beamline is divided into sections identified by the enclosure which allows access to that given part of the beamline. These sections are separated by walls, also for safety reasons.

3. Critical Devices

Critical devices are those beamline components which most readily allow the shutdown of a beam in case of an emergency, such as an unauthorized access by personnel. In the case of the MT beamline, the MT2WU magnet string and the MT3BS and MT6BS1 beam stops are the critical devices. These devices can only be controlled by Experimental Areas Operations personnel and not by beam users. If controlled-access gates or doors are opened improperly, these devices are automatically deactivated by the central computer.

4. The Spill Cycle

Beam is sent to the experimental areas on a cyclic basis, termed the "spill cycle." Protons are accelerated in a series of bunches until they attain energies of 1 TeV, when they are extracted from the Tevatron ring into the Switchyard, where the primary proton beam is split and distributed to the experimental areas.

The spill cycle is a 57.2 sec long, and is divided into six precise segments called T-times (see Figure 13). The actual "spill" of beam to the experimental areas normally begins at the start of T5 and is complete by the beginning of T6 (a time span of 20 sec). While beam intensity should remain constant throughout the spill, experience has shown that this is often not true.

Most beamline magnets are ramped to necessary current settings to coincide with the arrival of the spill; once spill is complete, currents are reduced to zero. This is done to conserve energy and to reduce the chance of overheating the magnets.

5. Effects of the MW Beamline

Because the MT beam is split off from the MW beam using production targets,

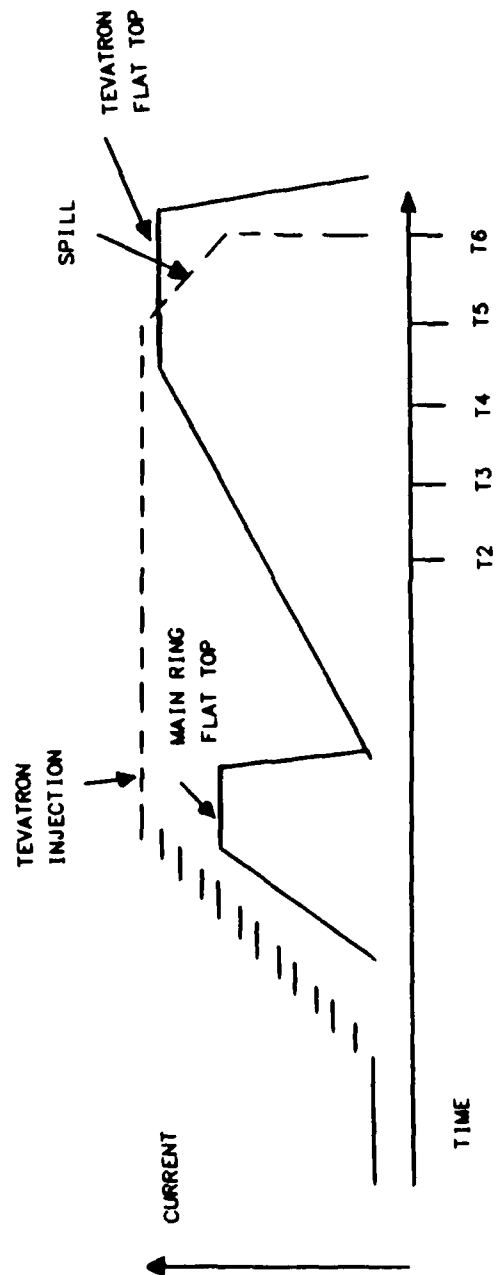


FIG. 13. The spill cycle.

the quality of the MW beam directly affects the quality of the MT beam. The possibility of MT beam quality degradation can be readily determined by monitoring the MW beam profile and particle yields at the MW6 enclosure. For this reason MT beam users are interested in the configuration of the MW beamline at least up to the end of this enclosure. In fact, the MT beamline cannot be activated unless the MW beamline is being operated at least up to the MW7DUMP beam dump, because of the MT beamline's parasitic nature.²⁴ A beamsheet for the MW beamline is presented at Appendix C, as well as a schematic diagram (not to scale) showing both the MW and MT beamlines, up to the end of the MW6 enclosure.

The maximum intensity planned for the primary proton beam delivered to the MW beamline and the MT beamline's secondary production targets is 1×10^{12} particles per spill (this is also the maximum rate allowed by radiation safety²⁴). For the Fall 1987 fixed-target run, however, MW beam users require rates lower than this maximum value (usually not more than 5×10^{11} particles per spill), reducing the production rates for the MT beam during this period.

C. Modes of Operation

In order to study the response of electromagnetic and hadron calorimeters and muon detectors, it is necessary to produce hadrons (pions, protons, and kaons), electrons, and muons. (Note that because the MT beam is a positively-charged particle transport beamline, positrons and not electrons are actually transported to the target area. Nonetheless, the convention is to refer to the transport of electrons, ignoring the actual sign of the particle delivered.) Often test beam users prefer a preponderance of either hadrons or electrons in the beam. To this end, several possible modes of operation of the beamline have been developed using various

targets and converters. The current modes of operation are discussed below.

(1) *Production of a secondary hadron beam.* This is the normal mode of operation of the MT beamline. It is often called the secondary pion mode since pions are the predominant hadron produced and transported. Unlike negatively-charged particle transport systems, where very few antiprotons are produced, positively-charged particle transport beamlines produce a large proportion of protons,²⁵ so that the "pion" beam is in reality a substantially mixed hadron beam.

The only target introduced in the beamline is one of the secondary production targets, MT2TGT1, MT2TGT2, or MT2TGT3, each of which are successively placed upstream of one of the three magnets in the MW2WD2 string, in the order given. Depending on which target is used, the mean energy of the beam is automatically selected based on the bending strength of the remaining magnets in the string downstream of that target. By original design, then, use of MT2TGT1, MT2TGT2, or MT2TGT3 would produce a mean energy of 245, 160, or 80 GeV, respectively, leaving the last aperture of the string. For this reason, these targets were often called the "245 GeV target," the "160 GeV target," and the "80 GeV target," as listed. This terminology will be retained throughout the remainder of this thesis for the sake of clarity. In reality, it has been learned that with an 800 GeV primary proton beam reaching these targets instead of the originally expected 900 GeV beam, use of these targets actually produce mean energies of 227, 251, or 75 GeV, respectively, leaving the final aperture of the string.

Each target is structured like a ferris wheel so that various thicknesses of lead (Pb), or no target at all, may be introduced into the beamline, allowing for some control of the production rates of secondary particles.

Another ferris wheel target, MT4CON, may be used to introduce thin Pb

targets into the beamline further downstream. Although additional interactions will occur with this target in place, it is not meant to be used as a tertiary production target. Instead, its major function is to reduce the number of electrons in the beam. As a high Z material, Pb causes electrons to lose energy more quickly than do hadrons traveling through the target; energy is lost through electromagnetic interactions with the atoms of the material. Most electrons lose enough energy that they can no longer be transported through the next beamline component aperture. Thus Pb serves here as an electron absorber, and the MT4CON target is commonly dubbed an "electron killer." MT4CON may be used to reduce the number of electrons in the hadron beam reaching the target area.

(2) *Secondary production of high energy electrons.* This is an untested mode of operation, designed to produce high energy electrons of the order of 245 GeV. Computer analysis done earlier suggests the possibility of production rates of up to 1000 electrons for a primary proton beam intensity of $5 \cdot 10^{11}$ particles spill. A 6-mil thick aluminum (Al) target, labeled MT2TGT0, is permanently in the beamline between the second and third magnets in the MW2WD1 cryogenic magnet string (see Figure 14). A small number of secondary particles are produced, including neutral pions (π^0) and other neutral particles. Neutral pions are extremely short-lived particles, traveling a mean distance of 0.05 mm at 245 GeV before they decay into two high energy photons ($\gamma\gamma$). The neutral particles are not bent by the final MW2WD2-3 magnet, while all charged particles of the primary proton beam, as well as secondary charged particles, are bent. While secondary products from MT2TGT0, including the photons resulting from the decay of neutral pions, are actually spread over a full range of production angles, the peak of the distribution is centered about the central trajectory of the original incoming beam. The centers

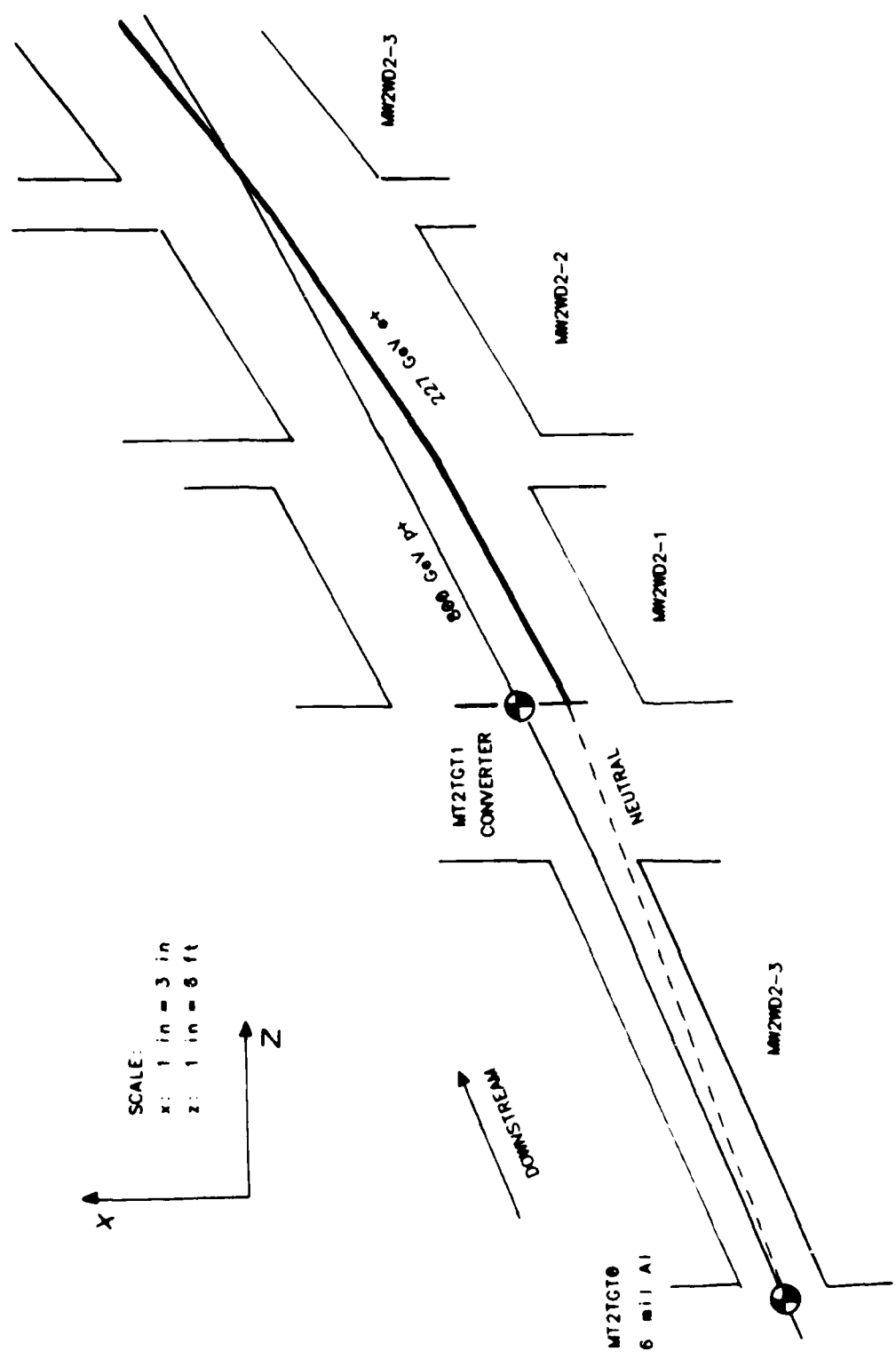


FIG. 14. Secondary production of high energy electrons in the MT beamline.

of the neutral and charged beams reaching MT2TGT1 are separated by 0.7". One setting of the ferris wheel target places a specially designed converter in the beamline, as shown in Figure 15.

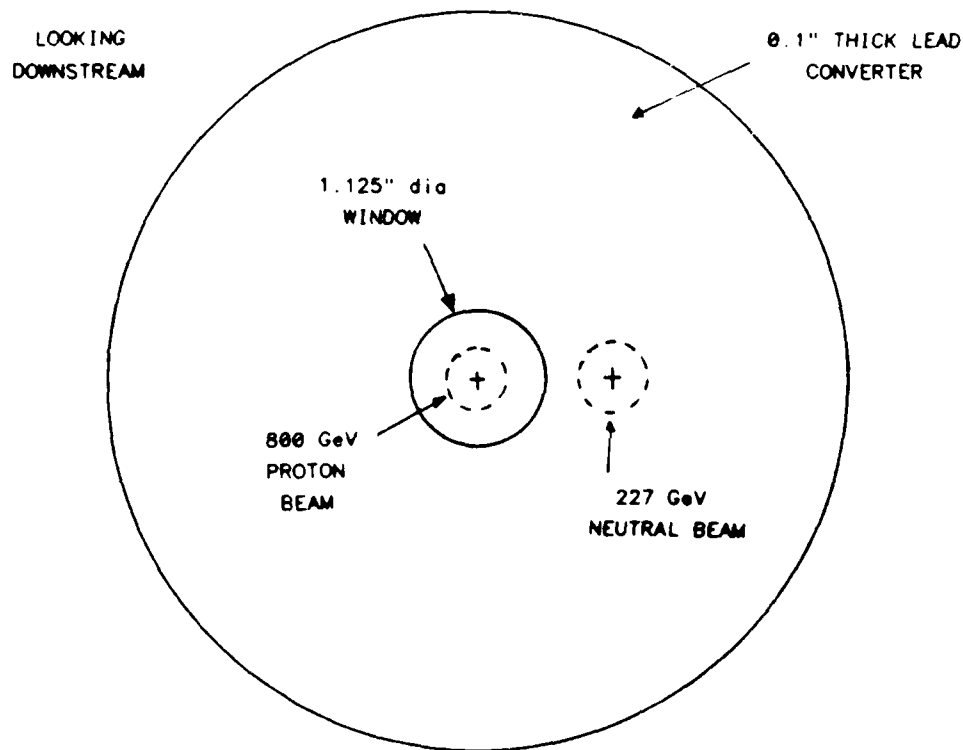


FIG. 15. The MT2TGT1 converter target.

The converter has a 1.125" hole in its center, allowing unobstructed passage of the primary proton beam. The high energy photons, however, will strike 0.1" of Pb, where some are converted to electron-positron pairs ($e^- e^+$) due to electromagnetic interactions with the material's nuclei (high Z nuclei improve production rates for

this interaction). As charged particles, positrons of the order of 245 GeV energy are then transported down the remainder of the beamline to the target area. Very low production rates are expected, since MT2TGT0 is very thin, leading to small numbers of π^+ 's, and both this target and the converter must produce particles of the right type, energy, and production angle. Electron beam transport to the target area is made more difficult since the beam is produced off-center of the central trajectory of the beamline.

(3) *Tertiary production of lower energy hadrons.* This makes use of the second common mode of operation of the MT beamline. MT3TGT1 is introduced into the beamline as a production target to create a tertiary beam of particles. While the secondary beam reaching this target can be produced with the 245, 160, or 80 GeV target, normally the 245 GeV target is used so as to produce the highest possible energy daughter particles reaching MT3TGT1. Again, both neutral and charged particles are produced over a wide range of energies and production angles. The magnet current settings of the bending magnets downstream of the target determine which energies are transported to the final target area. If only MT3TGT1 is placed in the beamline, we again get a hadron beam at the final target area. This tertiary beam, however, will see peak production rates at energies below that of the original secondary beam, although useful rates may be transported over the full range of 10 to 245 GeV (including noninteracting hadrons at the upper energy limit. If production of hadrons of energies in the ranges between 245, 160, and 80 GeV (and especially energies below 80 GeV) were not possible using the secondary mode, then this tertiary mode might be relied upon to produce intermediate and low end energy hadrons. This might entail the use of secondary beam energies of 160 and 80 GeV, as well as that of 245 GeV. MT4CON could also be introduced in the beamline to

purify the tertiary hadron beam.

(4) *Tertiary production of lower energy electrons.* The primary design of the tertiary mode, however, is to create electron beams. Downstream of MT3TGT1 is a dipole bending magnet, MT3SW, which is turned on to full strength in order to sweep all charged particles out of the beamline. Only neutral particles, including high energy photons from neutral pion decay, reach the next beamline device. Here a converter, MT3CON1, is also placed into the beamline. Again, photons are converted to electron-positron pairs. Depending on the magnet settings of magnets further downstream, certain energy positrons are selected for transport to the target area. As in the secondary electron mode, only very low production rates are expected. As with hadrons, in order to produce an electron beam of energies between 245, 160, and 80 GeV, as well as below 80 GeV, it may be necessary to use secondary incident beams at MT3TGT1 of energies lower than 245 GeV.

These are the four basic modes of operation now available to the MT beamline. They may be modified by moving targets and converters in the beamline, or replacing targets themselves with targets of different thickness and material. Desirable modifications will be discussed later.

D. Energy Acceptance

The three tunes to transport 245, 160, and 80 GeV particles created at the MT2TGT targets were termed the "primary tunes" (in the case of the originally expected 900 GeV incident proton beam) since they should allow for the maximum beam intensities possible compared to all other energies which may be transported to the final target area. (Because the primary proton beam energy is in reality 800 GeV, the actual primary tunes should occur at 227, 151, and 75 GeV).

The energy acceptance of a magnet is determined by its magnetic field strength and its apertures. Thus a central energy E is transported down the centerline of a bending dipole, with a possible energy spread of ΔE about this central energy also being bent through the magnet without loss or interaction at the magnet's walls. The beamline's energy acceptance is then determined by the succession of magnets making up the beamline, each set for optimum transport of the given central energy and each with its own effective aperture.

Whenever a target is used, a spray of daughter particles is created with a large spectrum of energies over a large range of production angles with respect to the incident beam. These are not uniform distributions. Production energies depend on the type of interaction, and smaller production angles are naturally favored as a consequence of conservation of linear momentum as observed in the lab frame.

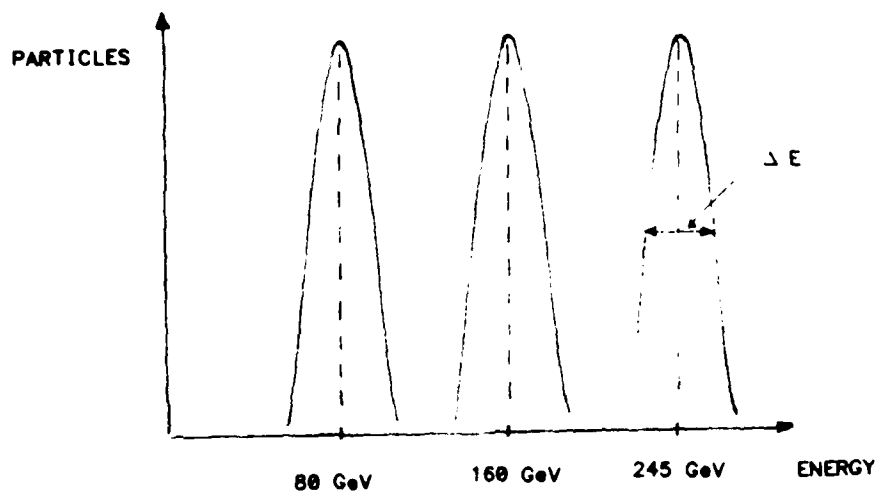
Thus calling MT2TGT1 the "245 GeV target," for example, is misleading. In reality, it is the fact that the secondary beam must then pass through the bending radius of all three magnets of the MW2WD2 magnet string which determines that the central energy of the emerging beam will be 245 GeV. (Figure 14 illustrates this.) Particles produced at MT2TGT2 must only pass through the last two magnets. Because each magnet is run at the same current, each produces the same magnetic field and has the same bending radius. Thus a central energy of 160 GeV, or two-thirds the magnitude of 245 GeV, emerges from the magnet string. Similarly, particles off MT2TGT3 emerge from the string with a central energy of 80 GeV, or one-third of 245 GeV. Thus the magnets downstream of a target actually decide the production energy to be transported.

In the case of the MT beamline, the MW2WD2 magnets which determine the initial central energies transported out of the MW beamline cannot be controlled

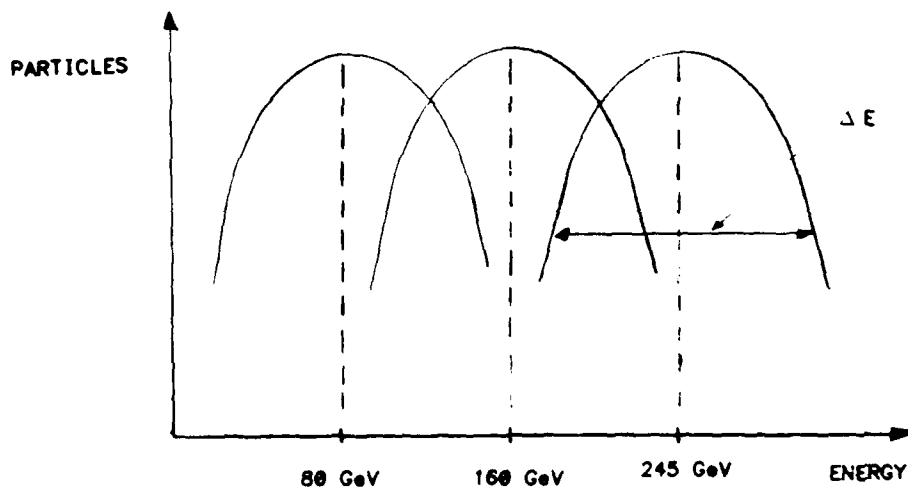
by MT beam users. These magnets are set by MW beam users to properly transport the primary proton beam further downstream in their beamline. When the primary proton beam energy turned out to be 800 GeV and not 900 GeV, the magnet currents had to be reduced to transport the correct energy through the MW2WD2 bend. These new current settings also reduced the central energies of the secondary beam transported to the MT beamline, resulting in the actual primary tunes occurring at 227, 151, and 75 GeV. Because MW beam users will often adjust the currents of the MW2WD2 magnets to optimize their beam, these central energies are not fixed, but will also fluctuate. Normally, however, MW2WD2 current settings are changed only slightly, so that there will be negligible effect on the MT beam.

A major concern in designing the MT beamline was the range of possible energies which could be provided at the final target area. Because the MW2WD2 magnetic fields were already determined, it was possible that only a limited number of energies would be available, with a small range centered about each primary energy of 245, 160, and 80 GeV [see Figure 16(a)]. This would occur if the spread of energies leaving the MW2WD2 string about each central energy were narrow due to a small energy acceptance of the string. If, on the other hand, the energy spread about the central energy emerging from the string were quite broad, then magnets farther downstream could be set at any number of tunes to select a wide range of energies for further transport to the final target area. As seen in Figure 16(b), sufficiently broad energy acceptance would allow for the transport of a continuous range of energies, although beam intensity would be reduced the farther removed the desired energy is from the central energy.

My beamline studies have shown that the energy spread leaving the MW2WD2



(a)



(b)

FIG. 16. Energy acceptance of a magnet string.

string is indeed quite broad, so that the MT beamline is capable of transporting a continuous spectrum of energies over a wide range by scaling the fields of magnets downstream of the MW2WD2 string about the values given in the three primary tunes.

Because the preliminary beamline studies were carried out based on the assumption that the primary tunes were at 245, 160, and 80 GeV, the tunes used to determine yields for all energies were not the optimum tunes to actually maximize beam intensity. Nonetheless, the tunes themselves do in fact transport the desired energies. Since the assumed primary energies of 245, 160, and 80 GeV lie relatively close to the actual primary energies of 227, 151, and 75 GeV, respectively, on the broad energy production curves, rates of production should be comparable to those determined in the future when corrected tunes are developed. Thus the data taken in these preliminary studies can be expected to be comparable with that of future studies.

For most of the studies done on beamline components, the optimized 245, 160, and 80 GeV primary tunes were used. When time was limited, only the 245 GeV tune, as the original baseline tune, was used.

E. Beam Optics

The word "optics" is most commonly found in relation to light and involves the study of lenses, prisms, and other devices which affect the travel of light. Charged particle beam optics is the science of using magnetic fields to bend and direct the paths of a group of moving charged particles. A beam of particles can be influenced in a manner analogous to the focusing of light by an optical lens or the dispersion into colors by a prism. Particle beams may be deflected, focused to a small spot,

or have their particles selected by momentum.

A collection of moving charged particles constitutes a beam when the particles are all moving in the same direction with nearly the same momentum and have a small separation transverse to the general direction of motion. Spatial extent must be small enough to pass through the aperture of magnets and other beamline devices.²⁶

The MT beamline is a relatively simple beamline, with only drift spaces, dipole magnets, quadrupole magnets, and collimators serving as optical devices. All magnets in this beamline provide static magnetic fields. All magnets have midplane symmetry with their fields oriented perpendicularly to the direction of motion of the beam.

A charged particle with charge q and velocity \mathbf{v} in a magnetic field \mathbf{B} experiences a force \mathbf{F} which is given by

$$\mathbf{F} = q\mathbf{v} \times \mathbf{B}. \quad (1)$$

The direction of the force is perpendicular to both the velocity vector and the magnetic field. The force is greatest when the velocity vector is perpendicular to the magnetic field. The force is related to the time rate of change of momentum by

$$\frac{d\mathbf{p}}{dt} = \mathbf{F}. \quad (2)$$

Equations (1) and (2) give an equation of motion with time the independent variable, but in charged particle optics, we are more interested in determining the path a charged particle follows than in its position as a function of time. The independent variable is then taken to be the longitudinal distance z along a particular one of the many trajectories passing down the beamline. We choose

a reference or central trajectory against which we compare all other possible trajectories and define our coordinate system such that the z axis coincides at all times with the central trajectory's forward motion: thus the central trajectory has no transverse motion with respect to this moving coordinate system (see Figure 17).

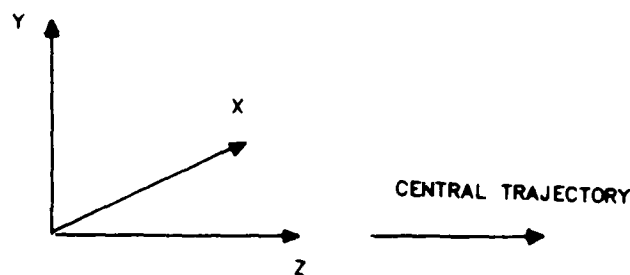


FIG. 17. The central trajectory coordinate system.

This coordinate system is not to be confused with the coordinate system defined in Figure 10 for our beamline maps and beamsheets. The coordinate system in Figure 10 is a fixed coordinate system where the direction of the z axis is arbitrarily chosen by the surveying team.

Optical devices in most secondary charged particle transport systems have a plane of symmetry. For convenience, the *midplane of symmetry* or *central plane* is taken to be the horizontal plane (the x - z plane of the coordinate system in Figure 17). A system with midplane symmetry has the following characteristics: (1) the

magnetic field at the central plane is always perpendicular to the central plane; (2) any north magnetic pole above the central plane is accompanied by a south pole at the mirror point below the central plane; and (3) magnetic field lines will exhibit reflection symmetry with respect to the central plane, but with the direction of the magnetic field below the plane opposite to that given by simple reflection. In actual beamlines, the central plane may be vertical or even rolled at an angle with respect to the horizontal plane. This can be corrected for in calculations using proper transformations of coordinates.

In a uniform magnetic field, a charged particle whose velocity vector is perpendicular to the field moves in a circular path. The radius ρ of the circle is related to the magnitude of the momentum p of the particle, its charge q , and the magnetic field strength B by

$$p = qB\rho. \quad (3)$$

The quantity $(B\rho)$ is termed the *magnetic rigidity* of a charged particle.²⁷ Assuming particles of charge ± 1 , equation (3) is most often expressed using conventional units as²⁶

$$p[\text{GeV}/c] = \frac{B[kG]\rho[m]}{33.356}. \quad (4)$$

The actual direction of the curved path depends on the direction of the magnetic field and the charge sign of the particle, as seen in equation (1).

1. Dipole Magnets

Equation (3) is the basis for describing the optical properties of the bending dipole magnets, which produce uniform magnetic fields (normally expressed in kG)

between their coils. Dipoles are so called because they have two poles of opposite polarity.

The principal functions of dipole magnets are to bend particle beams and to separate particles of different momenta (thus the practice of representing these magnets with the symbol for a prism). Dipole magnets also have some small focusing properties, but these are totally negligible in high energy beamlines. As seen in equation (3), different momenta are separated by different angles as particles travel through the dipole magnetic field, so that adjusting the dipole magnetic field allows one to determine which momenta are actually transmitted through the system. Too high or too low a momentum will result in the particle either striking the walls of the magnet (i.e., not escaping the aperture of the dipole) or, escaping this, having spread so far from the central trajectory that the particle misses the aperture of the next beamline device.

Following a bend through a dipole, the dispersion in momentum in a beam leads to a spatial dispersion in the bending plane of the magnet. Because the MT beamline's dipole magnets do a great deal more bending in the horizontal plane than in the vertical plane, we can expect the horizontal spread in the beam to significantly exceed the vertical spread. In the case of the MT2WU dipole string following the MW2WD2 string, for example, the overall effect of these two bending systems is to create successive horizontal spreads, while the vertical spread due to MW2WD2 bending down is mostly offset by MT2WU bending up.

For high energy beamlines, the arc length traveled by the beam is nearly the effective length of the bending dipole (see Figure 18), so that an alternate form of equation (3) is

$$p[\text{GeV}/c] = \frac{B[kG]L[m]\theta[mrad]}{0.033356}, \quad (5)$$

where L is the effective length of the magnet and θ is the angle the beam is bent through. Because these arc lengths are nearly straight lines through normal secondary beamline dipoles, these dipoles are straight magnets, which simplify the generation of uniform fields. If bend angles were substantial, then dipoles would themselves have to be constructed with a bend so that particles would not strike the walls during their travel through the magnet.

Figure 19 shows a schematic view of the cross section of a dipole magnet looking

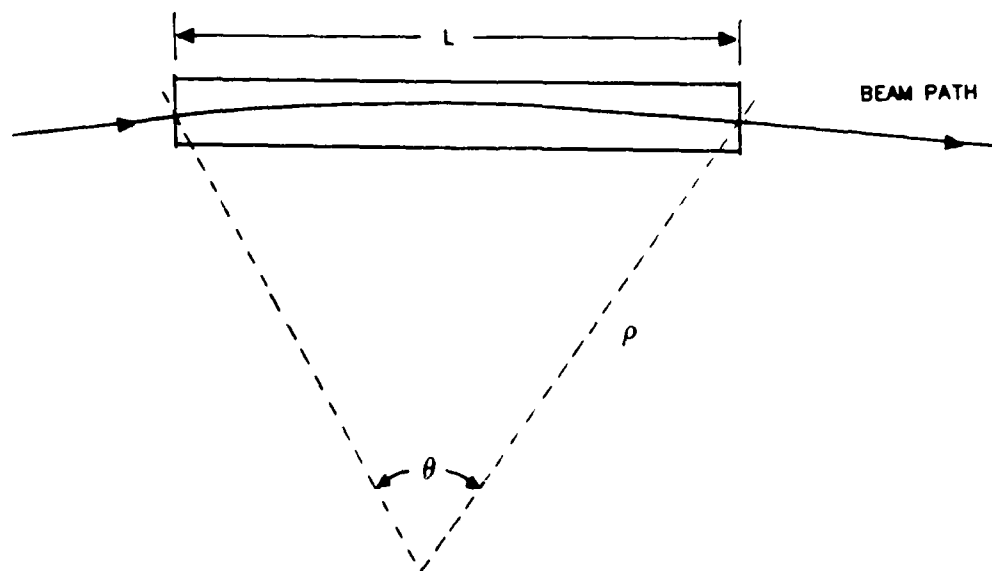


FIG. 18. Charged particle path in the bending plane of a dipole magnet.

downstream assuming transport of a positively-charged beam; the central trajectory is shown superimposed. Note that the bending plane is the central plane.

2. Quadrupole Magnets

Quadrupole magnets are used to focus a beam of particles. Quadrupoles have four poles of alternating polarity so as to produce a variety of field strengths and directions at different locations. The field strength of a quadrupole is directly proportional to the distance from the magnet's axis (the magnetic field strength gradient is normally measured in kG/m or kG/m).

Figure 20 shows the two orientations of magnetic poles for the quadrupoles used in the MT beamline; the central trajectory coordinate system is shown superimposed, centered on the magnet's axis and on the central plane. Figure 21 gives a more detailed view of the magnetic field and force components for the configuration shown in Figure 20(a). These figures show cross sections of the magnets looking downstream and assuming transport of a positively-charged beam.

Positively-charged particles entering the quadrupole field at different locations will be bent in different directions by different field strengths. Note that there is no net field along the axis of the magnet. Looking at Figure 20(a), we see that such particles entering the magnet along the y axis will be bent in toward the center of the magnet, while particles entering along the x axis will be bent away from the center. The farther away from the axis these particles enter, the greater the bend due to the increased field strength.

Thus the quadrupole magnet in Figure 20(a) is *focusing* in the vertical plane and *defocusing* in the horizontal plane. This illustrates the basic property of all quadrupoles constructed like those in Figure 20: these magnets always focus in

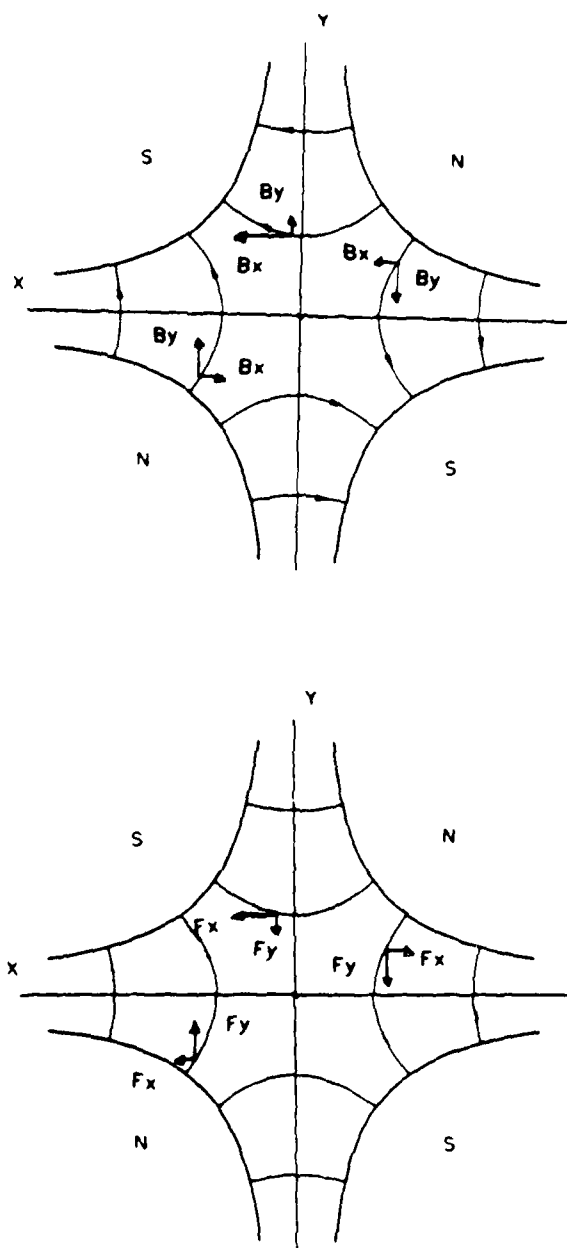


FIG. 21. Components of \mathbf{B} and \mathbf{F} for a horizontally-focusing quadrupole magnet.

one plane and defocus in the opposite plane. It is for this reason that the same quadrupole magnet is either represented by a convex (convergent) lens symbol or by a concave (divergent) lens symbol, depending on which plane is being viewed. Figure 22 charts the focusing, defocusing property of the quadrupole singlet of Figure 20(a).

Figure 22 also illustrates other similarities with light optics. In the focusing plane, we see that the bent trajectory will eventually intersect the central trajectory, bringing the ray to a focus in that plane. The quadrupole may be characterized by a focal length in this plane. Focal lengths of quadrupole singlets and of combinations of quadrupoles is generally momentum dependent. We can also speak of the magnification M of the image in that plane at some location past the quadrupole. A negative value for M indicates that the image has been inverted.

A singlet makes a real image only in one plane, while beam transport requires focusing in both planes. Because a single quadrupole defocuses in one plane, quadrupoles are always employed in combinations in beamlines to form lens systems. The two most common systems are doublets and triplets. Lens systems are used to correct for beam spot problems caused by dispersion of the beam, especially over long drift spaces following bending dipoles. While each quadrupole in a system will focus in one plane and defocus in the other, proper combinations of quadrupoles with opposite polarities can be designed to produce an overall focus in both planes.

There are four basic optical modes, or types of imaging, which lens systems may be used to achieve: point to point, point to parallel, parallel to point, and parallel to parallel (analogous to imaging in light optics). Optical modes may be different for the vertical and horizontal planes even when using the same lens system.

A doublet lens consists of two magnets (or magnet strings) with opposite polarity, both often of the same length. A doublet is not symmetric in its focus in

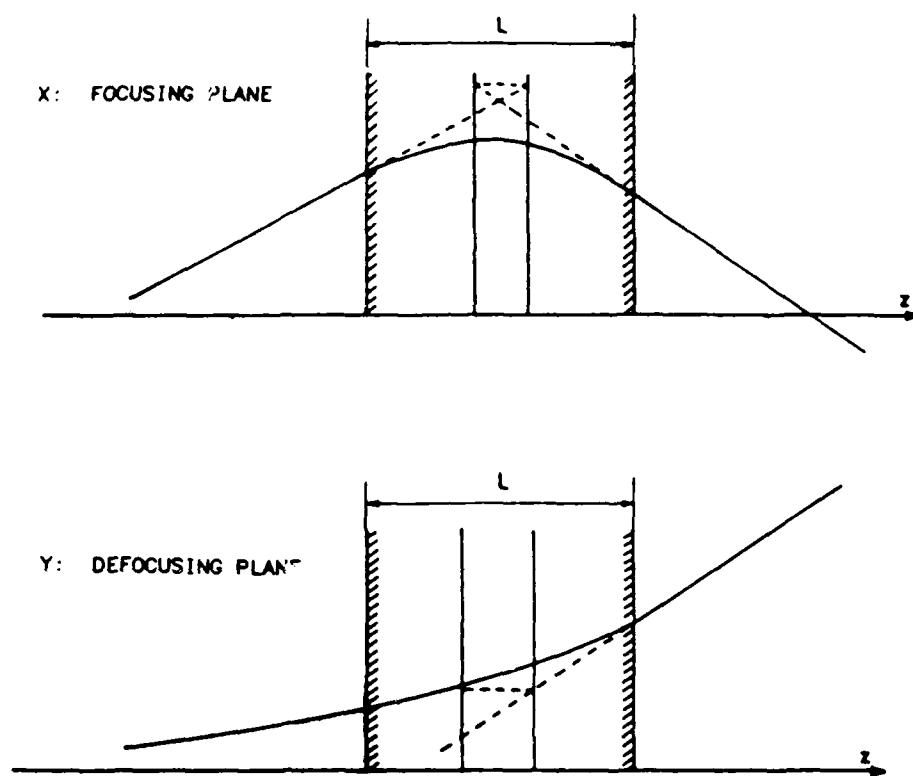
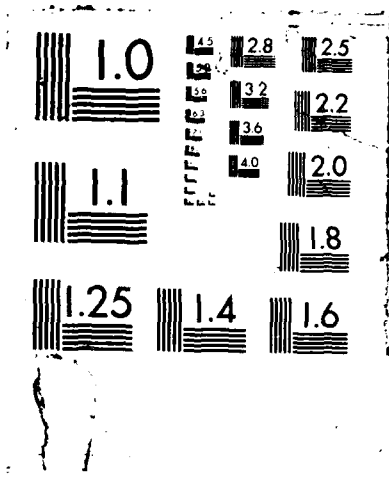


FIG. 22. Focusing and defocusing by a horizontally-focusing quadrupole magnet.



the vertical and horizontal planes, resulting in different magnifications in the two planes and causing a first-order image distortion. The ratio M_x/M_y may be as high as 20:1 for some doublets.²⁷ Thus the doublet will focus more in one plane than in the other, depending on the order of the polarity of the magnets in the lens system. This property is actually useful in the MT beamline, where horizontal spread of the beam is much more pronounced than the vertical spread and requires greater focusing by the quadrupole lens to tighten the beam profile in the horizontal plane.

Figure 23 illustrates the doublet's property of unsymmetric focusing. Figures 24 and 25 show examples of how doublets may be used to achieve point-to-point focusing and point-to-parallel focusing, respectively.

The most common triplet lens system is a symmetric triplet, consisting of two quadrupoles of identical polarities and lengths, separated by a quadrupole of opposite polarity and twice the length, all with the same field gradients. The most significant result of this configuration is a symmetric focus in both planes, so that $M_x/M_y=1$.

Doublets and triplets both have advantages and disadvantages.²⁸ Doublets are less expensive and take up less space because they require fewer magnets and less power. Their unsymmetric focus may be useful but makes calculations more difficult. Triplets are simple to deal with since they behave like a simple thin lens located at the center of the system. Their focal length changes more slowly as a function of momentum.

The MT beamline has been designed on the basis of point-to-point-to-point focusing in both the horizontal and vertical planes. The initial point is the image at the secondary targets in the MW2WD2 string. The first point focus is at MT3PWC, near the target MT3TGT1, used to create the tertiary beam. Focusing here also

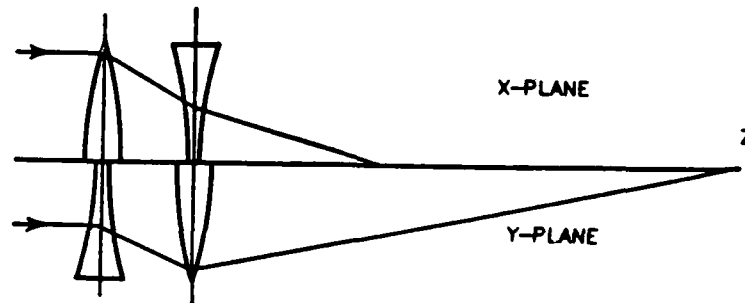


FIG. 23. Unsymmetric focusing by a quadrupole doublet.

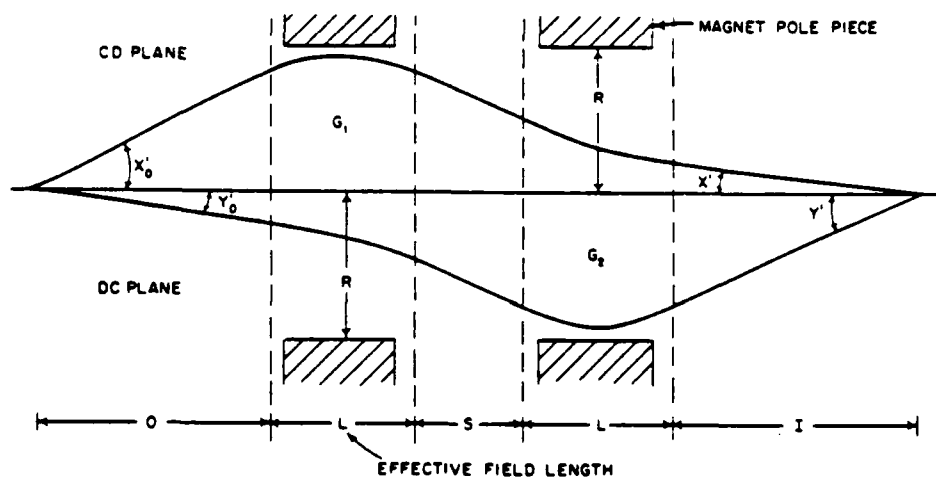


FIG. 24. Point-to-point focusing with a quadrupole doublet (from Sedman²⁸).

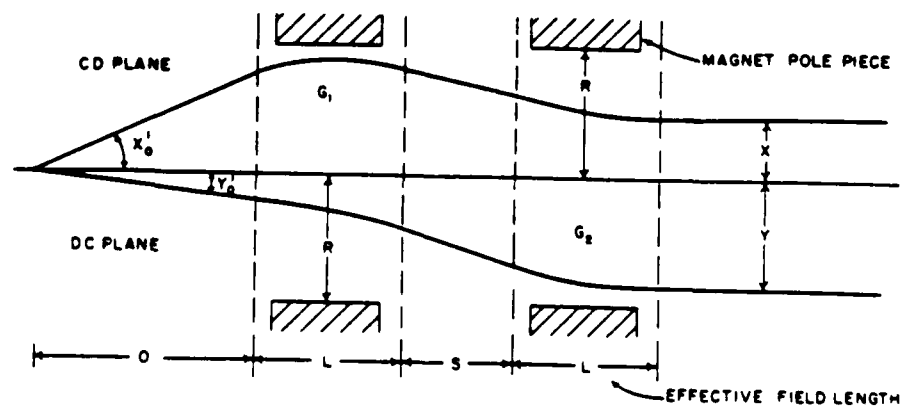


FIG. 25. Point-to-parallel focusing with a quadrupole doublet (from Sedman²⁸).

corrects for dispersion in the beam due to the upstream dipole strings and drift spaces so that beam is not lost due to aperture acceptance past MT3PWC. The final focus is at MT6PWC1, effectively focusing the beam spot on the fixtures in the CDF target area. This illustrates the primary use of point focusing: to place maximum beam intensity over a small area of a target.

Doublet lens systems are used in the MT beamline simply because there were a limited number of magnets available. Doublets are useful because of their unsymmetric focusing, which can be taken advantage of in the MT beamline to compensate for the large horizontal dispersion in the beam caused by the bending dipoles.

3. First-Order Matrix Formalism for Beam Transport

We normally consider a particle in a six-dimensional phase space with coordinates (x, y, z, p_x, p_y, p_z) , with time the independent variable. However, for charged particle transport, we represent an arbitrary particle's position and direction of travel by a column vector \mathbf{X} whose coordinates in six-dimensional phase space are $(x, x', y, y', \ell, \delta)$ with z the independent variable and all coordinates taken with respect to the reference or central trajectory. Thus

$$\mathbf{X} = \begin{pmatrix} x \\ x' \\ y \\ y' \\ \ell \\ \delta \end{pmatrix}, \quad (6)$$

where

x = the horizontal displacement of the arbitrary ray with respect to the central trajectory.

$x' = p_x/p_z$, the horizontal direction tangent the ray makes with the central trajectory; because in high energy beams this value is small, this coordinate is often replaced by θ , the angle the ray's projection makes in the horizontal plane with respect to the central trajectory.

y = the vertical displacement of the arbitrary ray with respect to the central trajectory.

$y' = p_y/p_z$, the vertical direction tangent the ray makes with the central trajectory; because in high energy beams this value is small, this coordinate is often replaced by ϕ , the angle the ray's projection makes in the vertical plane with respect to the central trajectory.

ℓ = the longitudinal separation of the particle relative to a particle traveling on the central trajectory with the central momentum (we are not concerned with this coordinate in the MT beam).

$\delta = \Delta p/p$, the fractional deviation of the momentum of the particle with respect to the central momentum.

The effect of the passage of a charged particle through a magnetic element or a drift space may be represented to first order by a square unitary matrix called the transfer matrix \mathbf{R} ($|\mathbf{R}| = 1$ as a consequence of Liouville's theorem²⁶). Thus the coordinates $\mathbf{X}(1)$ of the particle at the end of an element are given in terms of the coordinates $\mathbf{X}(0)$ at the beginning of the element by the linear transformation

$$\mathbf{X}(1) = \mathbf{R}\mathbf{X}(0). \quad (7)$$

The effect of n successive elements, each represented by its individual transfer matrix \mathbf{R}_i , is given by the total transfer matrix of the entire system,

$$\mathbf{R} = \mathbf{R}_n \dots \mathbf{R}_2 \mathbf{R}_1. \quad (8)$$

The full six-by-six transfer matrix for a static magnetic system with horizontal midplane symmetry is

$$\begin{pmatrix} x(z) \\ x'(z) \\ y(z) \\ y'(z) \\ \ell(z) \\ \delta(z) \end{pmatrix} = \begin{pmatrix} R_{11} & R_{12} & 0 & 0 & 0 & R_{16} \\ R_{21} & R_{22} & 0 & 0 & 0 & R_{26} \\ 0 & 0 & R_{33} & R_{34} & 0 & 0 \\ 0 & 0 & R_{43} & R_{44} & 0 & 0 \\ R_{51} & R_{52} & 0 & 0 & 1 & R_{56} \\ 0 & 0 & 0 & 0 & 0 & 1 \end{pmatrix} \begin{pmatrix} x_0 \\ x'_0 \\ y_0 \\ y'_0 \\ \ell_0 \\ \delta_0 \end{pmatrix}. \quad (9)$$

\mathbf{X}_0 is a constant vector representing the particle as it first entered the system at $z = 0$, so that the values of R_{ij} are dependent on z . The zero elements in the fifth column occur because x, x', y, y' , and δ are independent of the path length difference ℓ . The zero elements in the sixth row are a result of static magnetic fields, which make the scalar momentum a constant of the motion.

As long as central plane symmetry is retained, the four-by-four upper lefthand submatrix in equation (9) will decompose into two two-by-two submatrices. In fact, with central plane symmetry with all bending taking place in the horizontal plane, we can write

$$x(z) = x_0 R_{11}(z) + x'_0 R_{12}(z) + \delta_0 R_{16}(z) \quad (10)$$

and

$$y(z) = y_0 R_{33}(z) + y'_0 R_{34}(z). \quad (11)$$

If successive elements are rotated with respect to one another, so that their magnetic midplanes do not correspond, then in general there is mixing of the x and

y planes, and additional correlations exist. In general, then, the four-by-four upper lefthand submatrix is entirely filled in, as are the fifth row and sixth column.

The matrix elements R_{ij} have a certain physical meaning and thus are worth plotting versus the longitudinal extent of the beamline in order to study its transport characteristics.²⁹ We have: R_{11} and R_{33} relating spatial magnification in the horizontal and vertical planes, respectively; R_{12} and R_{34} relating the angular magnification, or focusing properties, of the beamline in the horizontal and vertical planes, respectively, and R_{16} relating the fractional momentum spread.

This is particularly straightforward in cases when there is central plane symmetry or a focus at the central trajectory, where many elements of the \mathbf{R} matrix are zero. For example, R_{11} gives the magnification M_x in the horizontal plane at a point of focus in that plane, since $R_{12} = 0$ in these cases.

In a similar but much more complicated fashion, second-order matrix formalism may be introduced.^{27,28} This is done by including the second-order term of the Taylor series expansion representing the deviation of an arbitrary trajectory from the central trajectory, so that

$$x_i(z) = \sum_{j=1}^6 R_{ij}(x_j)_0 + \sum_{j=1}^6 \sum_{k=1}^6 T_{ijk}(x_j)_0(x_k)_0, \quad (12)$$

with T_{ijk} the second-order matrix element.

In the previous discussion of static magnetic optical systems, we have only looked at the transmission characteristics of individual particle trajectories. But a beamline transmits many such trajectories with a variety of initial coordinates, so it is useful to have a method to treat many trajectories at one time. An extension of the matrix algebra discussed earlier allows us to represent the transmitted beam to first order with great accuracy as an ellipsoid in the six-dimensional phase space. The

extent of this ellipsoid is termed the *beam envelope*, and the ellipsoid contains the region of phase space containing the particle trajectories. There may be a uniform distribution, a Gaussian distribution, or some other density function describing the distribution of these trajectories in this region. This ellipsoid is often simply called the *beam ellipse*.

The equation of the ellipse is

$$\mathbf{X}'\sigma^{-1}\mathbf{X} = \mathbf{1}, \quad (13)$$

where \mathbf{X}' is the transpose of the coordinate vector \mathbf{X} and σ is a real, positive definite, symmetric matrix.

Given an initial ellipsoidal representation $\sigma(0)$ of the beam, the ellipse's transformation through the beamline is given by

$$\sigma(z) = \mathbf{R}\sigma(0)\mathbf{R}' , \quad (14)$$

so that the beam ellipse matrix remains an ellipse under first-order transformations (which is not generally true under higher-order transformations). By application of Liouville's theorem, the volume of the region enclosed by the ellipse remains unchanged under the transformation. Physical interpretations of various projections of the beam ellipsoid can be made.²⁷

In working with beam ellipses, we can determine the region of the initial phase space which can be transmitted by a given beamline; this region is called the initial phase space "acceptance" of the beamline and can be specified in the variables x, x', y, y' , and δ . The phase space volume which can be transmitted by a beamline is limited by the effective apertures of the components of the beamline, including the magnets and collimators.

Some of the basic concepts of the beam ellipse can be illustrated by considering a two-dimensional phase space in (x, x') . The ellipse matrix would have the form

$$\sigma = \begin{pmatrix} \sigma_{11} & \sigma_{12} \\ \sigma_{12} & \sigma_{22} \end{pmatrix}. \quad (15)$$

Physical interpretations of the matrix elements (see Figure 26) give the maximum extent of the ellipse in the x and x' directions as the square root of the diagonal elements:

$$x_{max} = \sqrt{\sigma_{11}}, \quad (16)$$

$$x'_{max} = \sqrt{\sigma_{22}}. \quad (17)$$

The area of the ellipse is given in terms of the determinant of the ellipse matrix, so that

$$A = \pi |\sigma|^{1/2}. \quad (18)$$

The correlation between x and x' , which specifies the orientation of the ellipse, is given by

$$r_{12} = \frac{\sigma_{12}}{\sqrt{\sigma_{11}\sigma_{22}}}. \quad (19)$$

Figure 27 shows an example of the transformation of the ellipse σ_0 by a two-dimensional \mathbf{R} matrix representing a drift space of distance L :

$$\mathbf{R}_{drift} = \begin{pmatrix} 1 & L \\ 0 & 1 \end{pmatrix}. \quad (20)$$

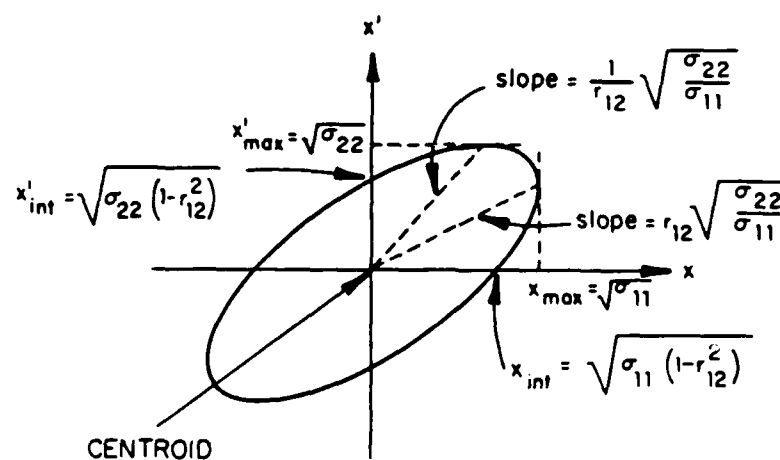


FIG. 26. The dimensions of a two-dimensional phase space ellipse in terms of ellipse matrix elements.

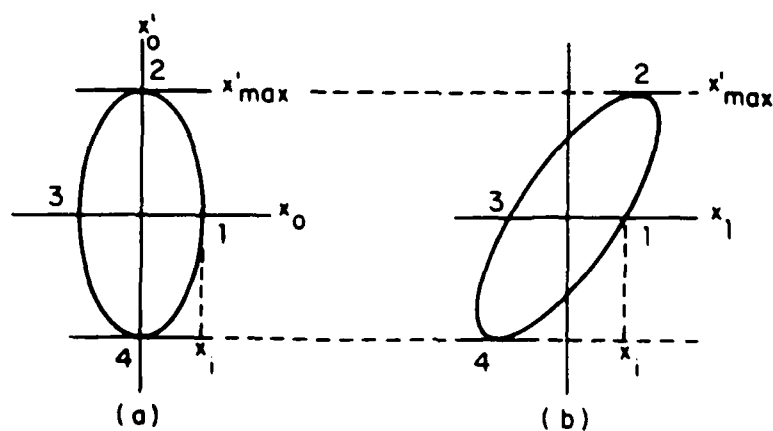


FIG. 27. The effects of a drift space on a two-dimensional phase space ellipse. The ellipse (a), after traversing a drift space, will become ellipse (b).

F. Computer Analysis and Design Considerations

Beamlines are designed and analyzed through an iterative application of any of several standard charged-particle transport computer simulation programs; at Fermilab, the TRANSPORT^{27,30,31} and TURTLE³² program packages are used.

TRANSPORT is a computer package used to design charged-particle beam transport systems by finding the first-order (or, if desired, the first- and second-order) matrix multiplication solution for a set of sequential magnetic elements with static fields. For the first-order solution, it does this by fitting the transfer matrix \mathbf{R} representing the transformation of an arbitrary ray with respect to a reference trajectory and/or fitting the phase space ellipse matrix σ representing a bundle of rays transformed by the system. The program has the provision to vary some of the physical parameters of the elements comprising the system and to impose constraints on the beamline design. These may include magnetic fields and their gradients, lengths and shapes of magnets, spacings between magnetic elements, and the initial beam accepted into the system.

In principle, TRANSPORT is capable of searching for and finding the first- or second-order solution to any physically realizable problem, but in reality the program can only carry out numerical calculations. If the programmer does not understand basic beamline transport theory, he may devise an unsolvable problem quite easily.

Once the beamline configuration is finalized, this program is particularly useful in determining the nominal magnet current settings necessary to transport a given initial phase space ellipse with a given central momentum. Because the program requires a reference trajectory with a central momentum, the program must be rerun when determining nominal tunes for various central momenta. For each tune,

the program will provide \mathbf{R} matrix and σ matrix elements at specified locations along the beamline.

The central trajectory concept is key to the TRANSPORT program. For the MT beamline, nominal tunes were calculated for transport of central momenta of 245, 160, and 80 GeV leaving the primary target at a 0° production angle. In reality, computations should have been based on central momenta of 227, 151, and 75 GeV leaving the targets at a 0° production angle. Because the MW2WD2 magnet string has currents fixed, these latter momenta actually represent the particles which leave the string's aperture traveling on the central trajectory; the former momenta may leave the aperture considerably off the reference trajectory. This requires a complete reapplication of the program to determine new nominal tunes.

TRANSPORT is not a ray tracing program, but instead transforms an initial six-dimensional phase space ellipse from the beginning to the end of a beamline. It does not account for the apertures of magnets, collimators, and other beamline devices. TURTLE is designed to be used after the application of TRANSPORT. TURTLE is a ray tracing program with no fitting capability which is applicable to beamlines with small phase space acceptance. Through a Monte Carlo process it "throws" rays representing particles over the possible range of momenta and production angles off of the production target, and then tracks each ray's progress separately down the beamline, calculating the fraction of rays (and thus the initial phase space acceptance) which are actually transported through the beamline. It does this by solving the differential equations of motion directly, accounting for apertures and for chromatic and geometric aberrations of all orders due to second-order effects caused by the beamline's magnetic devices.

The program has the provision to represent the beam at any point along

the beamline by histograms giving the distribution of rays over any of the phase space coordinates. An add-on package to TURTLE allows for calculations for a given particle type (normally protons, pions, and kaons) produced at the target, accounting for the decay of unstable particles as well, so that production rates per particle type may be determined.

A special version of TURTLE, called RAYGEL, has been developed at Fermilab to determine electron-positron production and transport based on the ($\pi^0 \rightarrow \gamma\gamma$, $\gamma \rightarrow e^-e^-$) cascade process. This program was used to determine production rates for the secondary electron beam mode of operation.

Note that in order to study the production and transport of tertiary beams in a beamline, these programs can only be applied if the beamline is, in effect, broken up into two successive beamlines, each of which must be analyzed separately. For this reason, computer analysis of tertiary modes is not carried out.

Since experimental analysis takes months to complete, data from computer analysis often is the only information available on possible beamline characteristics.

The MT beamline can be considered a relatively simple beamline, since it includes only three bending dipole strings, two quadrupole doublets, and a single trim magnet. Nonetheless, this beamline was a challenge to design. The fact that the MT beamline is split off from another beamline in an open hall (as opposed to using a target box), made it somewhat unique in design at Fermilab. Space in the open tunnels was extremely limited, and necessary magnets were in short supply. The beamline had to be designed to transport high energy particles through large bends, taxing the capability of available magnets, whose configuration was further constrained by the lack of tunnel space. The beam pipe connecting the tunnels and the target areas in the Meson Lab were already present, determining the necessary

bend angles.

Space was so limited that instead of following the preferred practice of using different dipole magnets to bend in the vertical and horizontal planes, magnets had to be rolled so as to bend in both planes simultaneously. This creates additional correlations in the x and y planes and makes computer analysis more difficult.

The optical mode of point-to-point-to-point focusing determined the location and types of quadrupole lens systems.

The key design requirement was to deliver the highest energy particles possible to the target area. Because CDF required separate particle by particle momentum tagging, momentum spread was not a critical factor. CDF experimenters are satisfied with a $1'' \times 1''$ beam spot size at the target, which can be easily defined using separate triggering systems with the requirement that the beam itself be tightly focused. With a need for only 20,000 particles per spill, maximization of beam intensity through the beamline is only significant when transporting low energy secondary and tertiary beams, where actual production rates are already low.

The physical characteristics of beamline devices, such as their apertures, lengths, and maximum field strengths were significant constraints on design of the MT beamline. Table IV lists these physical characteristics for the MT magnets and collimators.

The primary 800 GeV proton beam reaching the first MT production targets has the following parameters: $(\Delta x)_{FWHM} = 8 \text{ mm}$, $(\Delta y)_{FWHM} = 8 \text{ mm}$, and $\Delta p/p = 0.1\%$. Figure 28 shows the profile of this beam in the horizontal and vertical planes as recorded just upstream of the MT production targets. Note the Gaussian distribution of particle density in the beam envelope.

TABLE IV. Physical characteristics of magnets and collimators in the MT beamline.

Device Name	Aperture ^a		Length [in]	Maximum Field	Maximum Current [A]	Angle of Roll ^b [deg]
	Horiz [in]	Vert [in]				
MW2WD-1	6	3	120	13.5 kG	1100	-16.85
MW2WD-2	6	3	120	13.5 kG	1100	-16.85
MW2WD-3	6	3	120	13.5 kG	1100	-16.85
MT2WU-1	3.5	1.5	120	15.5 kG	1700	6.16
MT2WU-2	3.5	1.5	120	15.5 kG	1700	6.16
MT2WU-3	3.5	1.5	120	15.5 kG	1700	6.16
MT2WU-4	3.5	1.5	120	15.5 kG	1700	6.16
MT2WU-5	3.5	1.5	120	15.5 kG	1700	6.16
MT3Q1	3 (dia)		120	5 kG/in	100	0
MT3CH1	4	4		-	-	-
MT3CV	4	4		-	-	-
MT3Q2	3 (dia)		120	5 kG/in	100	0
MT3V	5	4	30	3.6 kG	180	0
MT3CH2	4	4		-	-	-
MT3SW	3.5	1.5	120	15.5 kG	1700	0
MT3WU-1	3.5	1.5	120	15.5 kG	1700	25.9
MT3WU-2	3.5	1.5	120	15.5 kG	1700	25.9
MT4Q1	3 (dia)		120	5 kG/in	100	0
MT4Q2	3 (dia)		120	5 kG/in	100	0

TABLE IV, Continued

Device Name	Aperture ^a		Length [in]	Maximum Field	Maximum Current [A]	Angle of Roll ^b [deg]
	Horiz [in]	Vert [in]				
MT5E-1	3.5	1.5	120	15.5 kG	1700	0
MT5E-2	3.5	1.5	120	15.5 kG	1700	0
MT5E-3	3.5	1.5	120	15.5 kG	1700	0
MT5E-4	3.5	1.5	120	15.5 kG	1700	0
MT5E-5	5	1.5	120	15.5 kG	1700	0
Vacuum Beam Pipe	6 (dia)		-	-	-	-

- a. Before magnets are rolled.
- b. Angle of roll is the angle which the magnet is rotated about its centerline axis with respect to the horizontal plane. Looking downstream, clockwise rotations are taken as positive.

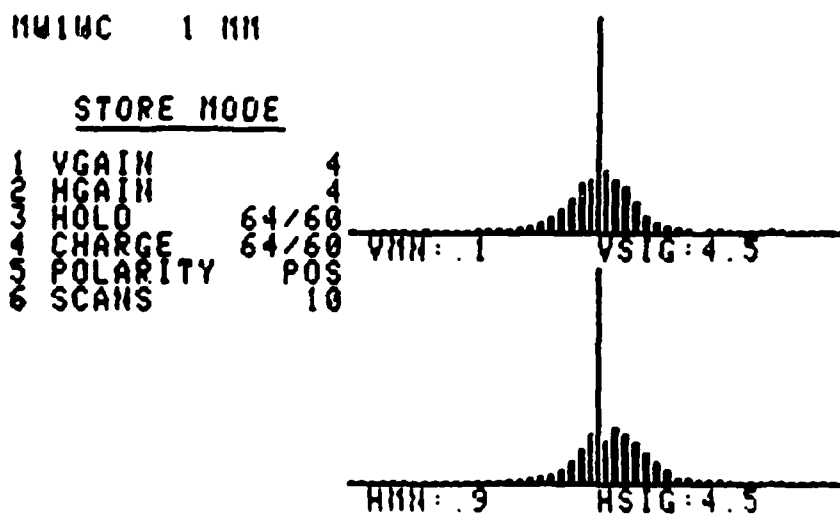


FIG. 28. The primary 800 GeV proton beam profile at the MT secondary production targets.

G. Particle Production

Determining the production rates of various types of secondary particles when a high energy beam interacts with the material of a target is very complex. Secondary particles are produced over a range of momenta and production angles. The production rate at a given angle and momentum is dependent on the momentum and the angle of incidence of the primary beam striking the target, as well as the type of particle making up the primary beam and the type of material making up the target.

Target thickness also affects production rates, since different particle types have characteristic absorption cross sections for different target materials. In addition, cascading increases with target thickness, so that a daughter particle can itself react with the target and produce other product particles.

An additional complication in determining yields downstream of the target is due to the decay of unstable particles produced by the targets. Decay products increase in number, while the parent particles decrease in number, with beamline length. Thus the secondary beam changes its make-up over time, which makes the calculation of production off of tertiary targets more difficult.

The greatest uncertainties come in, however, if the high energy beam has the opportunity to interact with material other than targets along the beamline. This occurs for a variety of reasons: the beam strays from the central trajectory and scrapes the beam pipe or the walls of a magnet or collimator; the beam profile is wide enough that the beam strikes a device aperture; a collimator is purposefully placed in the beamline to reduce intensity or select momentum; or the beam will interact with the material of detectors and air in the beamline where vacuum cannot be maintained. These interactions cannot all be eliminated, and have a tendency

to change with different tunes.

Several quantities are often referred to when dealing with particle interactions with media.

(1) *Nuclear interaction length.* The nuclear interaction length (λ_I) is the mean distance a particle travels through a medium before it undergoes some type of interaction with the nuclei of the atoms in the medium. Interactions can include absorption with resulting daughter particles or some other process where the incident particle does not lose its identity.

(2) *Absorption length.* The absorption length (λ_s) is the mean distance a particle travels before undergoing an interaction with the atoms of the medium such that the parent particle no longer exists. From the above definition, $\lambda_s < \lambda_I$.

(3) *Radiation length.* The radiation length (L_R) is defined as the distance over which a high energy electron (> 1 GeV for most materials) losses all but a fraction $1/e$ of its energy to bremsstrahlung, on average. This is a convenient way to measure the thickness of media through which electromagnetically interacting particles travel, since for most electromagnetic processes (bremsstrahlung, Coulomb scattering, showering, pair production, etc.) over a large energy interval, some or all of the dependence on the medium is contained in L_R .

(4) *Pair production.* Pair production occurs when a photon of sufficient energy converts into an electron-positron pair as the photon traverses a strong electromagnetic field, such as that surrounding a nucleus or electron.

Due to the difficulties in particle production calculations, the answer is to simply run studies to experimentally determine production rates for different incident energies and modes of operation for a given test beam, but these studies are often very time consuming. Thus experimenters normally rely on calculated

production rates until experimental data is available. These calculated values may also be used as a benchmark for beamline efficiency. Calculations are most often carried out using empirical formulas based on experimental data. Calculations are usually considered reliable only to within a factor of 2 in applications to beamlines.

Reliable experimental data on production rates only exists for particular types of primary beams at certain incident energies, targets of specific materials and thickness, and secondary particles, energies, and production angles. In some cases experimental data can be adapted for similar situations. For example, to a certain approximation, yields from incident proton interactions change with incident energies as \sqrt{s} , where s is the center-of-mass energy. To first order then (and well within acceptable limits), calculations can be made over a wide range of incident energies based on experimental data for some central incident energy.

Data on proton-proton beam collision interactions and proton beam interactions with fixed targets such as hydrogen (H), beryllium (Be), and lead (Pb) are most common. For fixed-target studies, though, only certain types of product particles are concentrated on. Data on other types of incident particle beams is less common. Collision data can be used for fixed-target calculations by converting from the center-of-mass frame to the lab frame. Materials with atomic number Z near a documented material will usually behave in a similar fashion as a target medium.

In many cases, however, greater relative accuracy is reached using an empirical particle production formula based on experimental data. Such an empirical formula has been adapted for use in the TURTLE program for secondary high energy beamlines. This particle production formula is for incident proton beams interacting with thick targets (up to one interaction length) and was developed by Malensek^{33,34} using experimental data taken by Atherton et al.,²⁵ who made precise measurements

of particle production from 400 GeV protons incident on Be targets.

Malensek has developed a simple analytical formula that accurately predicts the momentum and angular distribution of produced particles. The laboratory differential cross sections in units of produced secondary particle per (srad)(GeV/c)(incident proton) on a 500 mm Be target is given by

$$\frac{\partial^2 N}{\partial P \partial \Omega} = K p \frac{(1 - X)^A (1 + 5e^{-DX})}{(1 + p_t/M^2)^4}, \quad (21)$$

where

$$K = B/400$$

$$X = p/p_{inc}$$

p = laboratory momentum of the produced particle

p_{inc} = incident primary proton momentum

p_t = transverse momentum of the produced particle

and A , B , D , and M^2 are constants dependent on the type particle produced and are given in reference 33. The data fits the formula well up to $X = 0.75$, with errors of less than 10%.

This formula can be readily modified for other target lengths and materials. The target for the original formula is 500 mm of Be. To correct for different target lengths (still assuming a Be target) of thickness L (in cm), the empirical formula is multiplied by the factor $f(L)/f(500)$, where f is the target production efficiency given by

$$f(L) = \frac{e^{-L/\lambda_s} - e^{-L/\lambda_p}}{1 - \lambda_p/\lambda_s}, \quad (22)$$

where λ_s is the absorption lengths (in cm) for the produced secondary particles (which may be protons) and λ_p is the absorption length (in cm) for protons. This

formula is based on the simple model where the produced secondary either escapes the material or is absorbed with no daughter particles created. This is a reasonable model as long as the target is about one interaction length or less. This formula for target production efficiency f shows that f is material dependent, but plotting f versus L/λ_s for various target media for a given secondary demonstrates that the efficiency curve does not deviate much for these different materials. (For that matter, plotting the efficiency curve for different secondary particles for the same medium shows that a plot for one particular secondary provides reasonable values for all secondaries. Finally, acceptable values within a factor of 2 for f may be determined from an efficiency curve using λ_I in place of λ_s .) For secondary proton production, $\lambda_s = \lambda_p$ and equation 22 simplifies to

$$f(L) = \frac{l}{\lambda_p} e^{-L/\lambda_p}. \quad (23)$$

For accurate determination of λ_s for a given secondary energy, Carroll et al.³⁵ have developed an empirical formula fitting experimental data they have taken.

To correct for materials other than Be used for target media, Malensek provides plots of conversion factors versus X which are used to multiply the empirical formula for the final corrected result.

Application of the empirical formula gives the initial beam flux at the end of the target. To determine the beam flux at another point downstream of the target, the initial flux (differential cross section multiplied by the flux of the incident beam) is integrated over the accepted phase space region for the point of the beamline being considered.

TURTLE can provide the initial phase space region at any point in the beamline. However, add-on packages to TURTLE based on Malensek's empirical

formula give the program the capability to calculate the rate of secondary hadron production off of a target per interacting proton, and also give the fraction of these particles which will actually reach the final target area; decay is also taken into account. The result need only be corrected for target materials other than Be by applying conversion factors from Malensek.

It is possible to use TRANSPORT and TURTLE to calculate tertiary beam production rates, but the process is much more complicated. There are no provisions in these programs for an intermediate target in the beamline, so that the beamline must be split up and treated as two successive beamlines. The TURTLE add-on package is based on incident protons only, but in the case of a positive charge transport system like the MT beamline, a significant fraction of the beam is protons. To within a factor of 2, the production rates due to incident pions are comparable to those due to protons, as long as $X \leq 0.5$; however, as $X \rightarrow 1$ above this limit, production rates are significantly different.³⁶

Determining the production of electrons is made difficult by the comparative lack of experimental data. The primary source of electrons in this beamline is the cascade process discussed earlier. Neutral pions are one product of incident hadron interaction with targets; neutral pions decay into two high energy photons almost immediately, traveling on the order of 0.05 mm before they decay. The photons created will convert to an electron-positron pair if they interact with target material.

Malensek suggests that for incident proton interactions, π^0 production rates are comparable to those for π^- , so that his empirical formula may be used directly. Atherton calculates that π^0 production favors production angles near 0° (see Figure 29).

Neutral pions decay into two high energy photons 98.8% of the time. In π^0

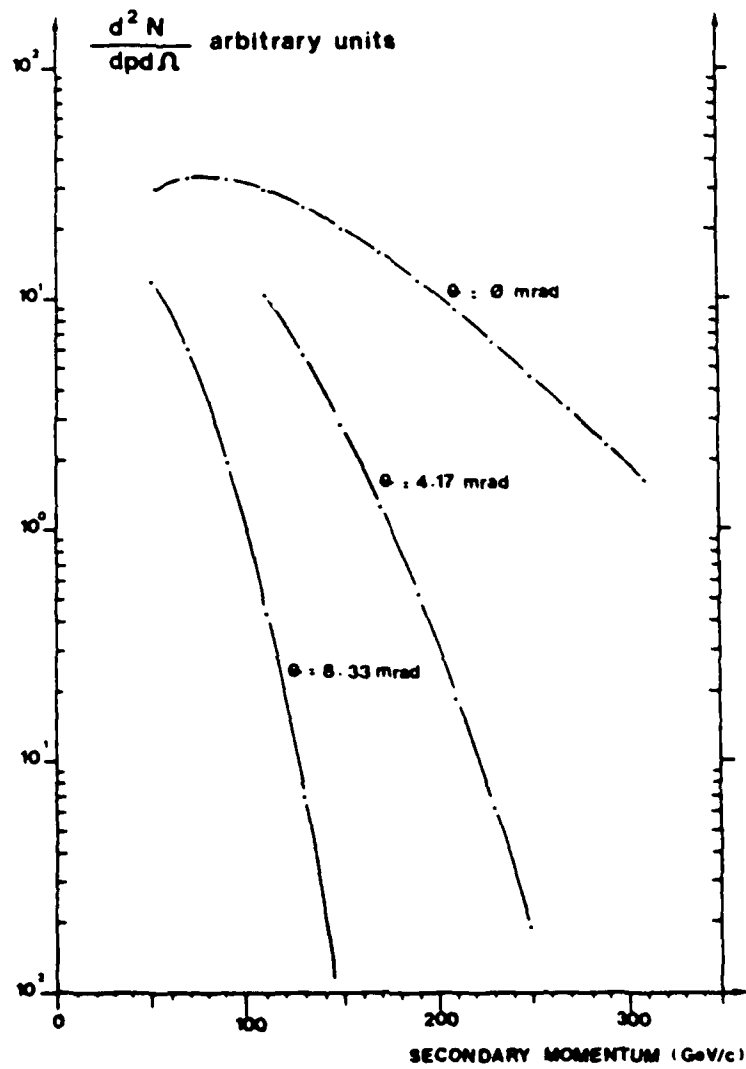


FIG. 29. The production of neutral pions as a function of secondary momentum at three fixed angles (from Atherton et al.²⁵).

decay, photon has a flat energy distribution extending from $E(1+\beta)/2$ to $E(1-\beta)/2$, where $\beta = v/c = p/E$, and E , v , and p are the π^0 's energy, velocity, and momentum, respectively, at the time of decay. When viewed from the π^0 's center-of-mass frame, the photons are distributed uniformly over all production angles. However, relativistic effects result in a cone-shaped envelope of photons as seen in the lab frame, with the apex at the decay point and the maximum possible production angle θ_{lab} given by $1/\gamma$, where $\gamma = (1 - \beta^2)^{-1/2} = p/m$. For a 245 GeV π^0 , for example, maximum θ_{lab} is 0.55 mrad.

For photons of infinite energy, the total pair production cross section σ is

$$\sigma = \frac{7}{9} \frac{A_w}{L_R N_A}, \quad (24)$$

with A_w the atomic weight of the material and N_A Avogadro's number. This is accurate to within a few percent for photons down to about 1 GeV energy for most materials.

Atherton has experimental data on electron-positron production rates for 400 GeV incident protons on Be targets for secondary energies up to 120 GeV (see Table V). It is pointed out that in these studies electrons produced at the target with energies of 200 GeV and above could not be transported to the end of the beamline.

When charged particles are accelerated, they produce synchrotron radiation and as a result lose energy. For a relativistic particle of charge q , velocity $\beta = v/c$, energy E , and traveling in a circular orbit of radius ρ , the energy loss per revolution is given by:³⁷

$$\Delta E_{loss}/rev [\text{MeV}] = \frac{4\pi}{3} \frac{q^2}{\rho} \beta^3 \gamma^4. \quad (25)$$

TABLE V. Percent particle content of the secondary beam leaving Be targets with 400 GeV incident protons
(from Atherton et al.²⁵).

P (GeV/c)	P _T (MeV/c)	Target length (mm)	e ⁻	π ⁻	K ⁻	\bar{p}	e ⁺	π ⁺	K ⁺	P
60	0	100	11.2 ± 0.3	79.3 ± 1.0	6.4 ± 0.2	3.1 ± 0.2	7.1 ± 0.2	69.7 ± 0.7	7.4 ± 0.1	15.8 ± 0.3
		300	22.0 ± 0.7	69.2 ± 1.0	6.2 ± 0.2	2.5 ± 0.1	14.4 ± 0.4	63.3 ± 0.7	6.93 ± 0.07	15.4 ± 0.3
		500	28.2 ± 0.8	64.2 ± 1.2	5.5 ± 0.2	2.1 ± 0.1	19.2 ± 0.6	58.9 ± 0.8	6.69 ± 0.09	15.2 ± 0.3
120	500	100	1.83 ± 0.05	84.9 ± 0.8	8.71 ± 0.11	4.63 ± 0.08	0.99 ± 0.07	67.8 ± 0.9	9.5 ± 0.2	21.7 ± 0.5
		300	3.57 ± 0.11	83.4 ± 0.8	8.84 ± 0.11	4.23 ± 0.07	1.91 ± 0.13	65.6 ± 0.9	9.0 ± 0.2	22.7 ± 0.5
		500	4.63 ± 0.14	82.5 ± 0.8	9.06 ± 0.12	3.83 ± 0.07	2.33 ± 0.16	64.6 ± 0.8	9.7 ± 0.2	23.4 ± 0.6
200	0	100	2.8 ± 0.7	89.5 ± 1.1	5.87 ± 0.07	1.86 ± 0.03	1.1 ± 0.2	57.6 ± 0.7	4.55 ± 0.05	36.7 ± 0.6
		300	8.0 ± 0.8	84.6 ± 1.1	5.79 ± 0.07	1.64 ± 0.02	2.8 ± 0.6	55.9 ± 0.9	4.69 ± 0.06	36.7 ± 0.5
		500	9.1 ± 0.9	83.5 ± 1.2	5.87 ± 0.07	1.49 ± 0.02	3.9 ± 0.8	54.5 ± 1.1	4.80 ± 0.06	36.7 ± 0.6
300	300	100	1.7 ± 0.3	89.4 ± 0.7	6.81 ± 0.08	2.16 ± 0.03	0.5 ± 0.1	49.1 ± 0.6	5.80 ± 0.07	44.6 ± 0.7
		300	4.3 ± 0.9	86.8 ± 1.0	6.90 ± 0.08	1.95 ± 0.03	1.3 ± 0.3	48.3 ± 0.6	5.82 ± 0.07	44.6 ± 0.7
		500	5.2 ± 1.0	86.2 ± 1.2	6.92 ± 0.08	1.76 ± 0.03	1.6 ± 0.3	47.9 ± 0.7	6.05 ± 0.07	44.5 ± 0.7
500	500	100	1.1 ± 0.2	89.2 ± 0.3	7.13 ± 0.09	2.58 ± 0.04	0.3 ± 0.1	43.6 ± 0.5	6.69 ± 0.08	49.5 ± 0.7
		300	2.6 ± 0.5	87.8 ± 0.8	7.23 ± 0.09	2.35 ± 0.04	0.7 ± 0.2	43.0 ± 0.5	6.78 ± 0.08	49.5 ± 0.7
		500	3.7 ± 0.7	86.7 ± 1.0	7.40 ± 0.09	2.13 ± 0.03	1.1 ± 0.2	42.8 ± 0.5	7.02 ± 0.08	49.0 ± 0.7
200	0	100	-	(a) 95.0 ± 0.6	4.30 ± 0.13	0.66 ± 0.03	-	(a) 21.0 ± 0.6	2.49 ± 0.10	76.5 ± 0.5
		300	-	95.0 ± 0.6	4.33 ± 0.13	0.60 ± 0.02	-	20.8 ± 0.6	2.55 ± 0.10	76.6 ± 0.5
		500	-	95.0 ± 0.6	4.44 ± 0.13	0.55 ± 0.02	-	21.8 ± 0.7	2.78 ± 0.11	75.4 ± 0.5
300	500	100	-	94.2 ± 0.6	5.05 ± 0.20	0.76 ± 0.03	-	16.4 ± 0.5	3.12 ± 0.09	80.4 ± 1.6
		300	-	94.1 ± 0.6	5.21 ± 0.21	0.69 ± 0.03	-	17.1 ± 0.5	3.28 ± 0.10	79.6 ± 1.0
		500	-	94.3 ± 0.6	5.15 ± 0.21	0.60 ± 0.02	-	17.5 ± 0.5	3.44 ± 0.10	79.0 ± 0.9
300	0	100	-	98.9 ± 0.4	1.04 ± 0.02	0.047 ± 0.002	-	-	(b)	-
		300	-	98.9 ± 0.4	1.10 ± 0.02	0.046 ± 0.002	-	-	-	-
		500	-	98.8 ± 0.4	1.13 ± 0.02	0.042 ± 0.002	-	-	-	-
500	500	100	-	98.8 ± 0.4	1.17 ± 0.04	0.046 ± 0.002	-	2.03 ± 0.04	0.617 ± 0.012	97.3 ± 0.5
		300	-	98.8 ± 0.4	1.20 ± 0.04	0.048 ± 0.002	-	2.09 ± 0.04	0.638 ± 0.019	97.3 ± 0.5
		500	-	98.8 ± 0.4	1.19 ± 0.04	0.041 ± 0.002	-	2.01 ± 0.04	0.641 ± 0.012	97.3 ± 0.5

Note: a) For p > 200 GeV/c the e⁺'s produced in the target are lost before the CEDARs owing to synchrotron radiation in the bending magnets.

b) 300 GeV/c, P_T = 0 positives were not measured.

For relativistic particles the amount of energy loss is strongly dependent on mass, so that the energy loss of an electron compared to that of a proton, both of the same initial energy and experiencing the same acceleration, goes as $(m_p/m_e)^4$. For electrons where $\beta \simeq 1$,

$$\Delta E_{loss}/rev \simeq \frac{0.0885(E[\text{GeV}])^4}{\rho[m]}. \quad (26)$$

The energy δE lost by an electron of energy E bent through a circular arc by a dipole magnet of length L and with a uniform magnetic field of strength B is given by³⁸

$$\delta E[\text{MeV}] = 0.013(E[\text{GeV}])^2(B[\text{kG}])^2L[m]. \quad (27)$$

Energy lost when traveling through quadrupole magnets is much more difficult to calculate since quadrupole fields bend charged particles through non-circular paths.

The beamline used by Atherton included several large bend angles, so that electrons initially in the range of 200 GeV were losing energy through synchrotron radiation at such a high rate that the resultant momenta fell outside the momentum acceptance of the beamline.

Although the MT beamline has fewer bends, the bend angles are comparable. If the energy acceptance through these bends is relatively small, it is possible that electrons in the range of 200 to 245 GeV produced in the secondary electron mode of operation may not reach the final target area. With fewer bends to travel through, tertiary electron beams should not be significantly affected by this process. The bend angles in the MT beamline are listed in Table VI. Table VI also shows the energy loss of an electron initially of 245 GeV energy as it passes through each dipole in the MT beamline; the total energy loss through the dipoles is about 8.4

TABLE VI. Bend angles for dipole magnets in the MT beamline.

Dipole Magnet Device Name	Bend Angle ^a [mrad]	Angle in Horiz Plane [mrad]	Angle in Vert Plane [mrad]	Electron δE ^b GeV
MW2WD2-1	5.035	4.819	1.459	0.37
MW2WD2-2	5.035	4.819	-1.459	0.37
MW2WD2-3	5.035	4.819	-1.459	0.37
MT2WU-1	5.622	5.590	0.603	0.72
MT2WU-2	5.622	5.590	0.603	0.72
MT2WU-3	5.622	5.590	0.603	0.72
MT2WU-4	5.622	5.590	0.603	0.72
MT2WU-5	5.622	5.590	0.603	0.72
MT3WU-1	3.260	2.933	1.424	0.18
MT3WU-2	3.260	2.933	1.424	0.18
MT5E-1	5.594	5.594	0	0.53
MT5E-2	5.594	5.594	0	0.53
MT5E-3	5.594	5.594	0	0.53
MT5E-4	5.594	5.594	0	0.53
MT5E-5	5.594	5.594	0	0.53

- a. Bend angle in the bending, or central, plane; positive angles are taken as counterclockwise when looking down on the plane.
- b. Energy lost to synchrotron radiation for an electron initially at 245 GeV when first entering the beamline.

GeV. If the electron does not travel along the central axis of a quadrupole, it will experience an energy loss while undergoing focusing. These losses may also be substantial. Note that the secondary electron beam is created off-center of the central trajectory in the MW2WD-2 string.

RAYGEL, a modification of TURTLE, will calculate electron production rates created by the normal cascade process, and allows for the placement of both an initial production target and a downstream converter used to induce pair production. It carries out a Monte Carlo analysis based on the formulas presented above. For the MT beamline, RAYGEL predicted production rates of 1000 electrons at the final target area with an initial proton beam intensity of 5×10^{11} particles/spill for the secondary electron mode. The effect of synchrotron radiation is not calculated in this program.

Muons are primarily a product of the decay of pions and kaons in the beam, as opposed to being created from targets by incident beams. Substantial muon halos surrounding the desired beam often are a nuisance to the beam user, occurring most often when the beam interacts with the material in the beamline.

CHAPTER VII

STUDY OF MESON TEST BEAMLINE COMPONENTS

A. Introduction

Using the concepts put forward earlier in Chapter VI, a more detailed discussion and analysis of the components of the MT beamline will be presented. In some cases little or no experimental data is currently available, because the device was only recently installed, ancillary items necessary to run tests were not available, or beam time was not available.

B. Targets

A target is any material placed in the beamline to cause the particles in the beam to undergo some desired interaction. While targets are given names to reflect their intended purpose in the beamline, the fact is that any intervening matter (including air) are characterized by interaction and radiation lengths and will affect the beam as if it were a target. No target can be designed to exclusively carry out only one function; competing processes are always taking place. A target can only be optimized by selecting material and target thickness so that the desired function governs over others. Table VII lists pertinent atomic and nuclear properties of selected materials.

Figure 30 shows a plot of Be target production efficiency f versus L/λ , for production of π^+ , where L is the target thickness and λ , is the absorption length for π^+ in Be. As discussed earlier, this plot can be used to determine necessary target thickness for a required efficiency for other materials besides Be, and will give adequate values for production of other hadron secondaries, as well. If absorption

TABLE VII. Atomic and nuclear properties of selected materials.

Material	Z	A_w	λ_I [cm] ^a	L_R [cm] ^a	Density g/cm ³ ^b	Refractive Index n ^c
He	2	4.00	(3.39×10^5)	(5.28×10^5)	(0.1785)	(35)
Be	4	9.01	40.7	35.3	1.848	
N ₂	7	14.01	(6.90×10^4)	(3.15×10^4)	(1.2506)	(300)
Al	13	26.98	39.4	8.89	2.70	-
Ti	22	47.89	28.3	3.55	-	-
Fe	26	55.85	16.8	1.76	7.87	-
Pb	82	207.19	17.1	0.56	11.35	-
Air			(7.07×10^4)	(3.04×10^4)	(1.205)	(293)
BGO (Bi ₄ Ge ₃ O ₁₂)			22.0	1.12	7.1	2.15
Polystyrene (CH) ^d			79.5	42.4	1.032	1.581
Lucite (C ₅ H ₈ O ₂)			70.8	34.4	1.18	1.49
Mylar (C ₅ H ₄ O ₂)			61.7	28.7	1.39	-
G-10 plate ^e			53.1	19.4	1.7	-

- a. Values in () are for gases at 20°C and 1 atm.
- b. Values in () are in units of g/l and are for gases at 20°C and 1 atm.
- c. Values in () are $(n-1) \times 10^6$ for gases.
- d. Typical scintillator material, e.g., PILOT B and NE102A have an atomic ratio H/C = 1.10.
- e. G-10 plate, typically 60% SiO₂ and 40% epoxy.

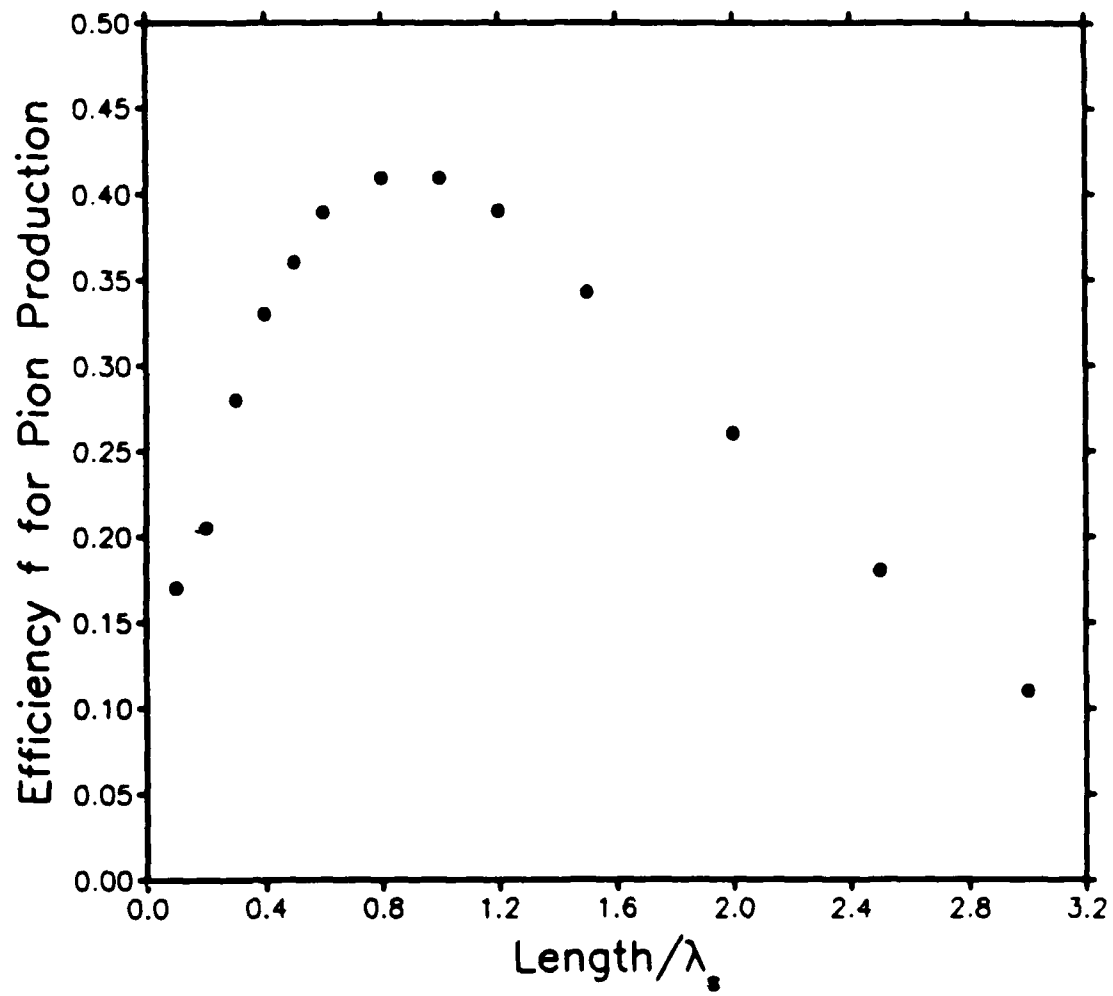


FIG. 30. Beryllium target pion production efficiency f vs. L/λ_s .

lengths are not available, interaction lengths λ_I may be substituted. From the plot the maximum efficiency occurs when $L/\lambda_s = 0.86$. Note that the efficiency curve is only useful when dealing with materials of about one interaction length or less, since daughter particle interactions producing additional particles are not considered.

Except for MT2TGT0, all targets, converters, and absorbers in the MT beamline are a standard design ferris-wheel style target which can rotate one of four windows into the beamline. In this beamline, the 6" diameter windows are either empty or hold Pb squares of various thicknesses which serve as the actual target. Pb targets come in standard thicknesses of 0.1" increments. Nonstandard thicknesses require machining off-site. Figure 31 shows a simple schematic beam's eye view of a ferris wheel target.

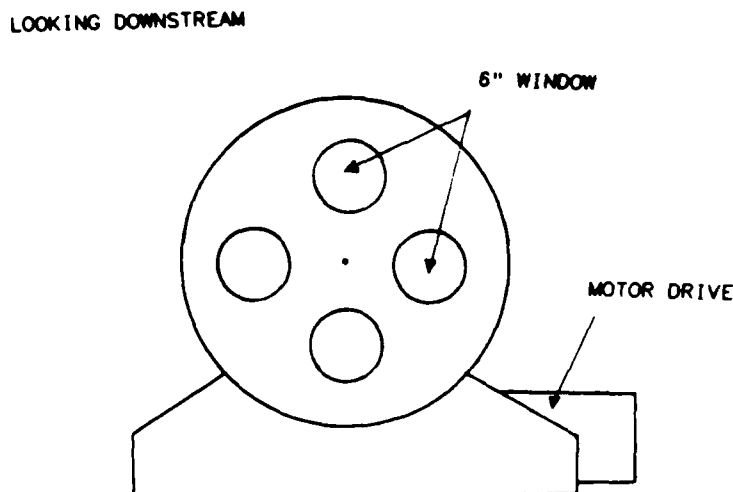


FIG. 31. Beam's eye schematic view of a ferris wheel target.

Table VIII lists pertinent data on the targets, converters, and absorbers in the MT beamline.

Each one is discussed in more detail below.

(1) *MT2TGT0*. This is the only fixed target in the MT beamline, and the only one not made of Pb. This target is fixed in place between the second and third bending dipole magnets of the MW2WD1 cryogenic string and is Al 6 mil thick. The function of this target is to produce a neutral beam (of which high energy photons from the decay of π^0 are of interest) for use in the secondary electron mode of operation of the beamline. The target was limited in thickness to insure that the heat generated during the interaction of the 800 GeV primary proton beam with the target would not quench the adjacent cryogenic magnets. The target produces about 0.5 W of heat per spill, compared to a maximum acceptable value of 5 W.

(2) *MT2TGT1*, *MT2TGT2*, *MT2TGT3*. Currently termed the 245, 160, and 80 GeV targets, respectively, each has Pb targets of thickness 0.1", 0.3", and 0.6", except *MT2TGT1*, whose 0.3" Pb target has been replaced by a 0.1" Pb target with a 1.125" hole centered in the target (see Figure 15). This particular target is used as a converter in photon pair production to produce a secondary electron beam, while allowing the primary proton beam to pass without interaction. The target is of minimum thickness so that the electrons, once produced in the target, are not in turn absorbed by the target. The efficiency of Pb as a converter has been determined experimentally at Fermilab and is plotted versus radiation length L_R in Figure 32. The optimum thickness is $0.7 L_R$, although a wide range of values centered about this value will provide comparable efficiencies. A prime candidate material to replace Pb as a converter is Be, which has 0.4 the interaction length of Pb, but 68 times the radiation length, so that significantly greater numbers of

TABLE VIII. Production targets, converters, and absorbers in the MT beamline.

Device Name	Use	Target Material	Thickness in	Fraction of λ_I	Fraction of L_R	Mode of Operation ^a
MT2TGT0	Prod	Al	0.0006	$3.87 \cdot 10^{-5}$	$1.72 \cdot 10^{-4}$	SE
MT2TGT1	Conv	Pb	0.1	0.15	0.45	SE
MT2TGT1	Prod	Pb	0.1	0.15	0.45	SH
		Pb	0.6	0.89	2.72	
MT2TGT2	Prod	Pb	0.1	0.15	0.45	SH
		Pb	0.3	0.45	1.36	
		Pb	0.6	0.89	2.72	
MT2TGT3	Prod	Pb	0.1	0.15	0.45	SH
		Pb	0.3	0.45	1.36	
		Pb	0.6	0.89	2.72	
MT3TGT1	Prod	Pb	0.1	0.15	0.45	TE, TH
		Pb	0.2	0.30	0.91	
		Pb	0.3	0.45	1.36	
MT3CON1	Conv	Pb	0.1	0.15	0.45	TE
		Pb	0.2	0.30	0.91	
		Pb	0.3	0.45	1.36	
MT4CON	e^+	Pb	0.1	0.15	0.45	Purify
	Abs	Pb	0.2	0.30	0.91	hadron
		Pb	0.3	0.45	1.36	beams

a. SE secondary electron, SH secondary hadron, TE tertiary electron, TH tertiary hadron.

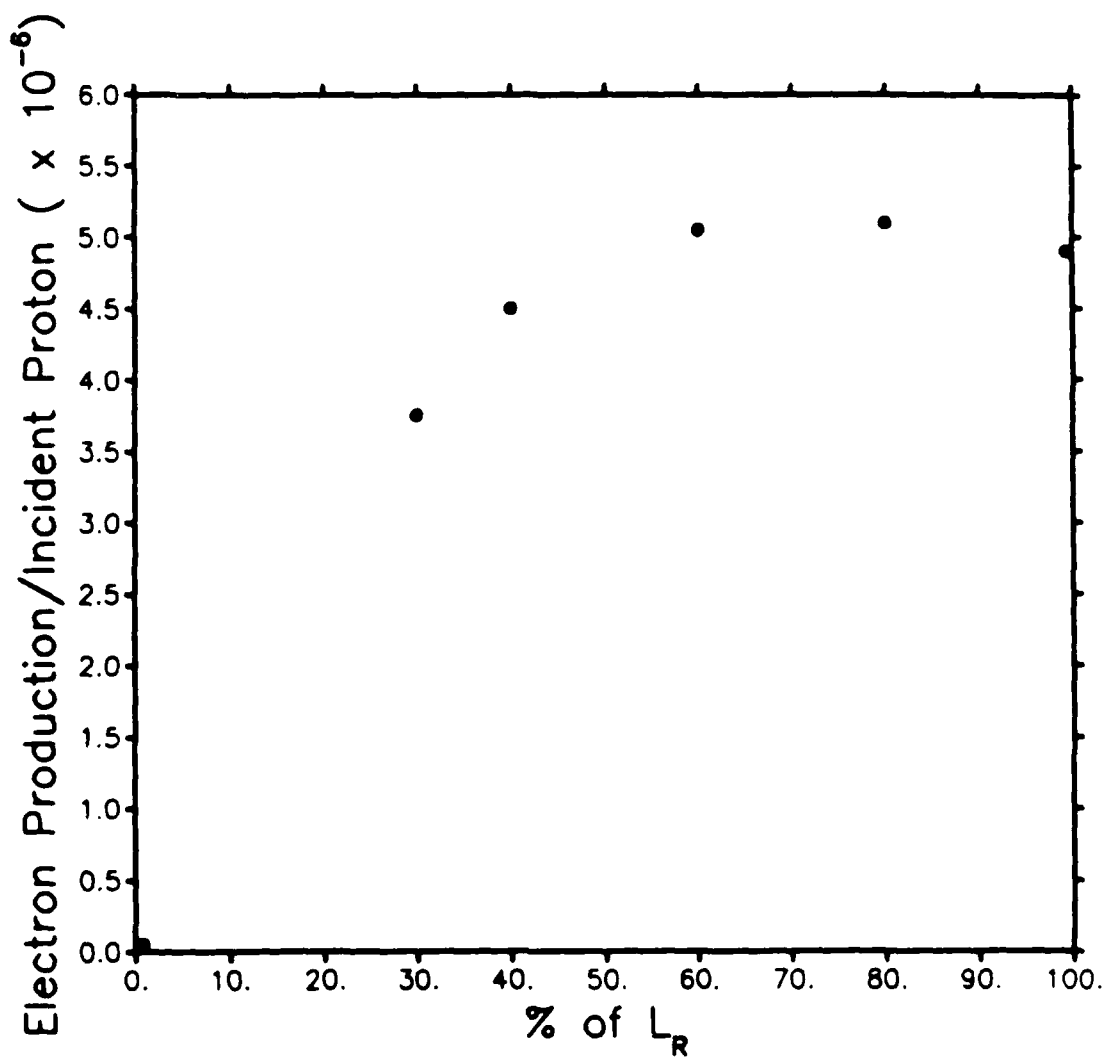


FIG. 32. Efficiency of lead as a converter in pair production vs. radiation length L_R .

electrons created in the material will escape with transportable energies.

All other mounted Pb targets are used to produce the secondary hadron beam. Their thickness was limited by the requirement that the targets have an efficiency f of 10% or less. This would insure the minimum degradation of the MW beam intensity and profile, and would keep muon contamination of the MW beam within acceptable limits. Because of this requirement, only one of the three ferris wheel targets may be activated at one time.

Relative target efficiency as a function of PB thickness in producing 245 GeV secondary hadron beams reaching the final target area for MT2TGT1, 2, and 3 are plotted in Figures 33, 34, and 35, respectively.

(3) *MT3TGT1*. MT3TGT1 is used as a production target to create a tertiary beam of particles and has 0.1", 0.2", and 0.3" thick Pb targets. This target has two possible uses: to create lower energy tertiary hadron beams or to initiate the sequence necessary to create lower energy tertiary electron beams.

In the tertiary hadron mode MT3TGT1 is used by itself. In this case the thickest target is usually employed to achieve maximum production rates. The tertiary hadron mode was expected to produce a hadron beam with useful rates at the low energy end of the scale. Studies to compare yields for incident secondary hadron energies other than 245 GeV have not been carried out. Figure 36 plots MT3TGT1 efficiency as a function of Pb thickness in producing 160 GeV tertiary hadron beams reaching the final target area.

In the tertiary electron mode, MT3TGT1 is employed with the MT3SW sweeper magnet and the MT3CON1 converter. In this situation, one of the two thinner Pb targets may be used to insure that, when neutral pions produced in the target immediately decay while still in the target, the resulting photons are not

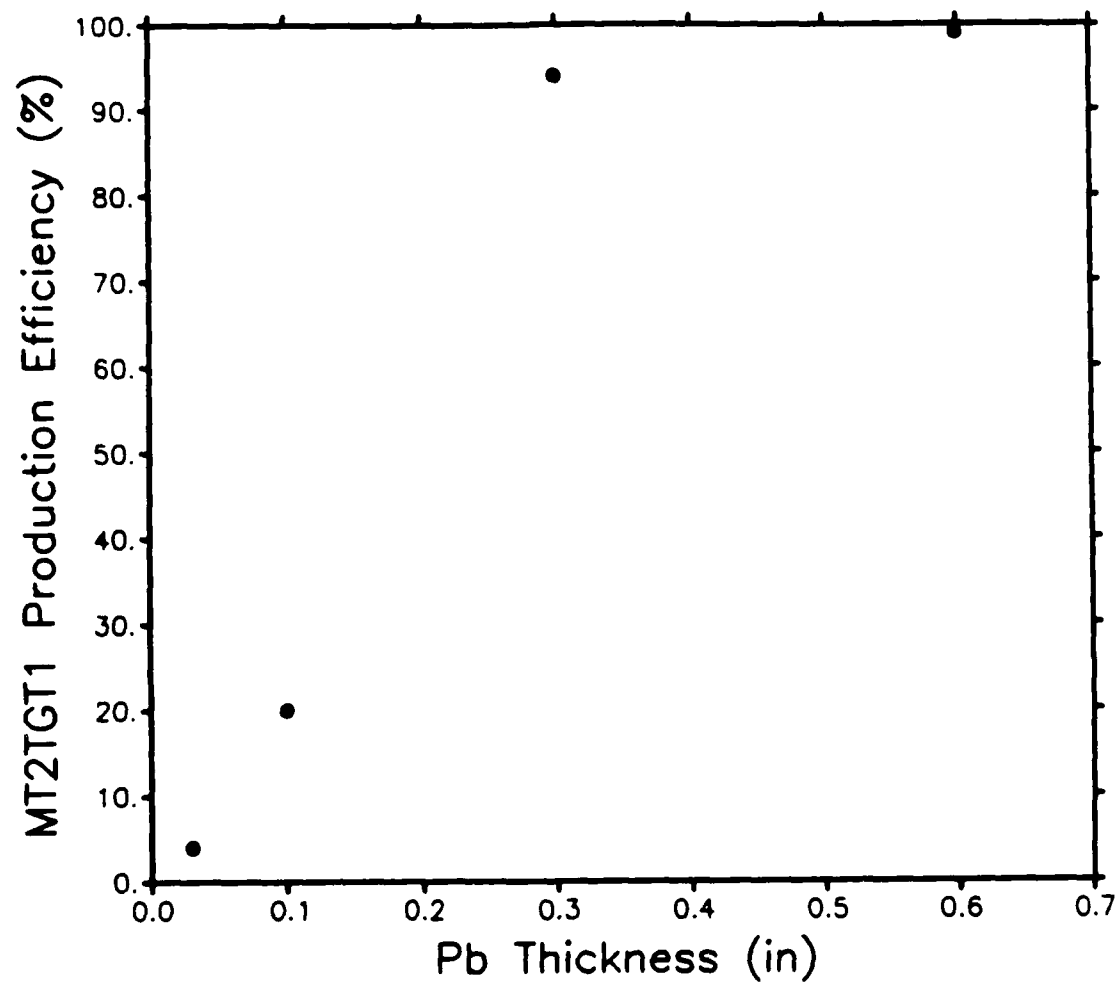


FIG. 33. MT2TGT1 target relative efficiency in producing secondary 245 GeV hadron beams as a function of lead thickness.

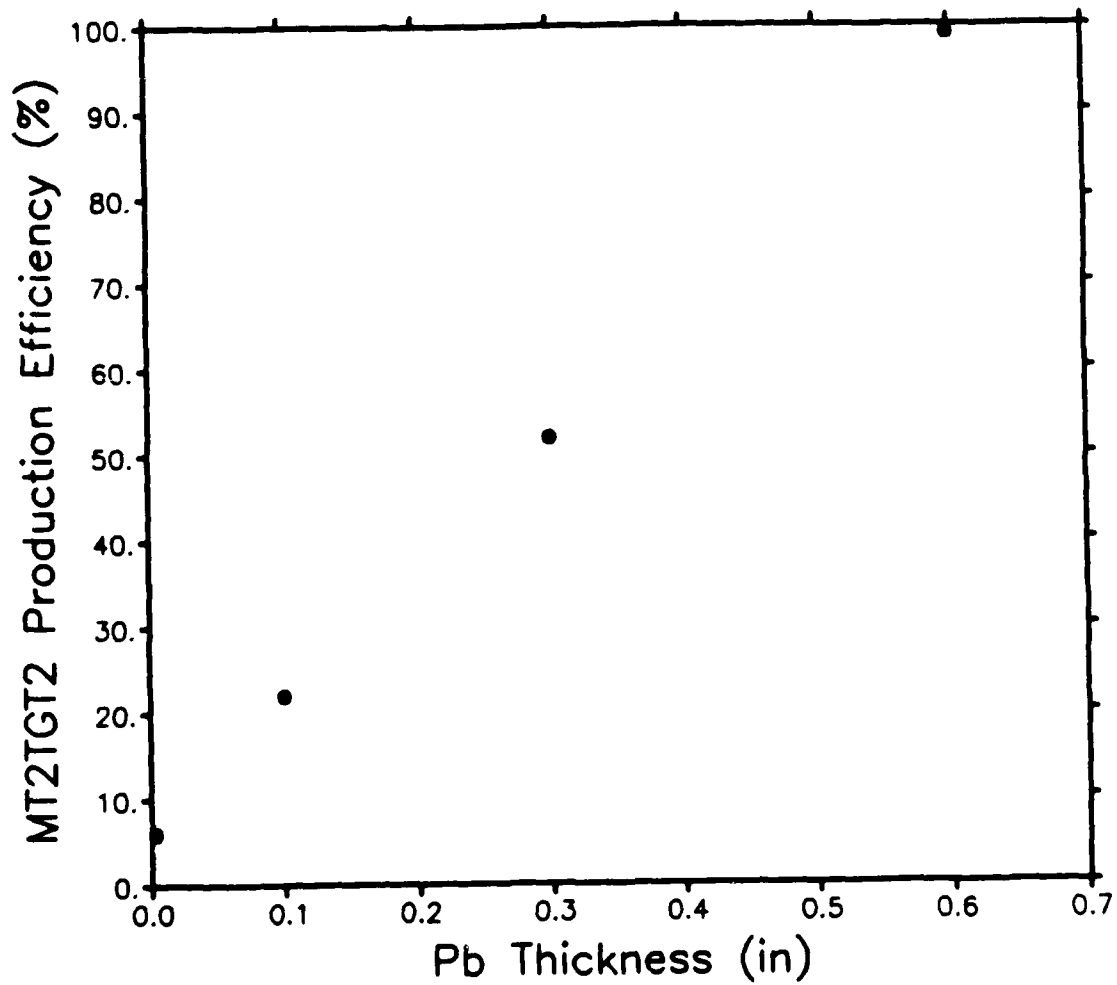


FIG. 34. MT2TGT2 target relative efficiency in producing secondary 245 GeV hadron beams as a function of lead thickness.

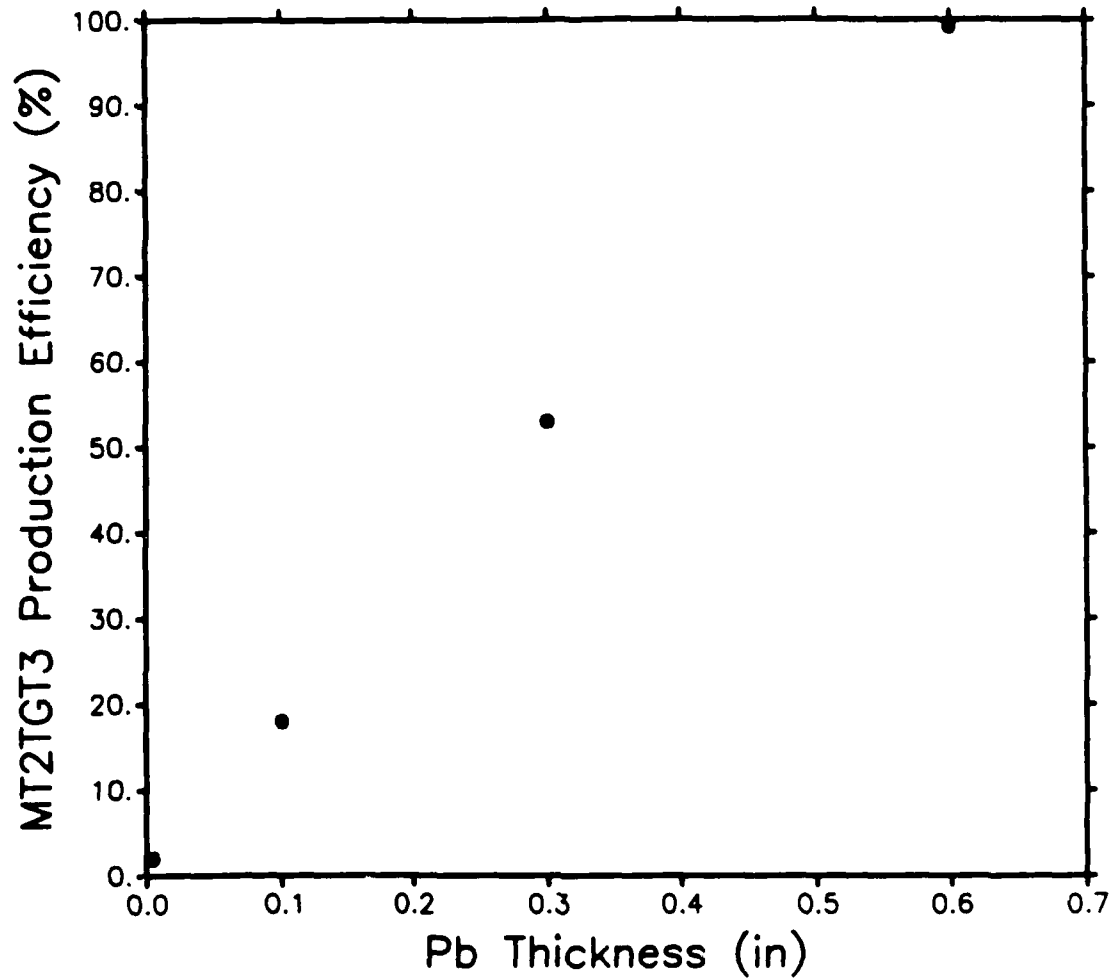


FIG. 35. MT2TGT3 target relative efficiency in producing secondary 245 GeV hadron beams as a function of lead thickness.

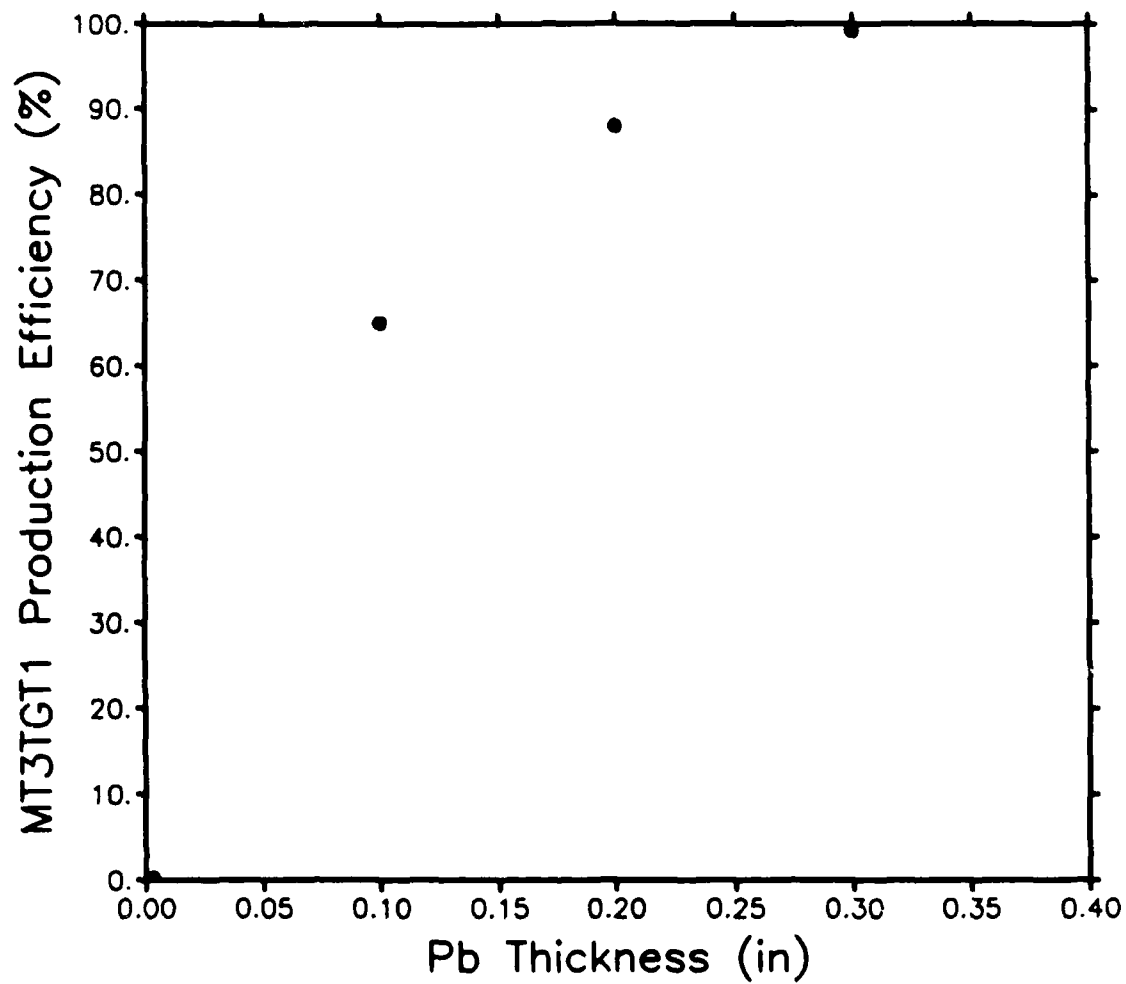


FIG. 36. MT3TGT1 target relative efficiency in producing tertiary 160 GeV hadron beams as a function of lead thickness.

converted to electron-positron pairs. It is imperative that photons are not converted before the beam reaches the MT3SW magnet, which is turned on at maximum field to sweep all charged particles out of the beam (this greatly increases the purity of the final beam to final target area). Which thickness target is optimum can only be determined experimentally.

(4) *MT3CON1*. This target is used as a converter only, producing the tertiary electron beam by initiating the conversion of high energy photons created in neutral pion decay to electron-positron pairs. From Figure 32 it is seen that the 0.3" Pb target is closest to the optimum thickness of 0.39" for Pb when used as a converter. Only very low yields are expected for the tertiary electron mode.

As argued earlier, Be might be the preferred material for the converter. The difference in radiation lengths between Pb and Be is significant enough to allow Be converters a substantial output of electrons over Pb. The difficulty with Be is that it is a major health hazard, requiring special handling.

(5) *MT4CON*. This target serves as an electron absorber, so that it is termed an "electron killer." Pb targets are available in thicknesses of 0.1", 0.2", and 0.3". The idea is to use the optimum thickness which absorbs the majority of the electrons in a beam (thus purifying a hadron beam) but which keeps the number of hadron interactions within the target to a minimum. This can only be determined when the electron tagging devices in the beamline are operational. Until these devices are ready for use, *MT4CON* could be used to roughly determine whether beams assumed to be mostly electrons are in fact so. For beams with a high fraction of electrons, yields should drop off dramatically when *MT4CON* is in place. However, this target was only recently installed, so that it was unavailable for such first-order contamination tests.

(6) *Inherent Electron Absorbers.* Besides the targets purposefully placed in the beamline to cause interactions, other matter is encountered by the beam, including the material of the vacuum beam pipe windows, the proportional wire chambers, the single wire drift chambers, the scintillation counters, the windows and mirrors of the threshold Čerenkov counter (as well as the fill gas of the counter), and the air itself where no vacuum is maintained. These materials are effectively production targets and electron absorbers whose small interaction lengths and radiation lengths successively add up as the beam travels downstream.

Their most significant effect is to reduce the intensity of electron beams before it reaches the final target area. While it is impossible to remove all of this material from the beamline, it may be feasible to at least reduce some of it. Table IX lists the effective radiation lengths L_R of material other than targets in the MT beamline. Figure 37 illustrates the successive addition of radiation lengths down the length of the beamline.

C. Collimators

Collimators are one of the two beamline devices which are directly used to control beam intensity, profile, and momentum bite (the other being magnets).

A collimator is generally a large block of steel or iron, often having adjustable apertures, which allow for the selection of beam profile or angular divergence. It can be used to absorb the beam halo and, if closed farther, can be used to control beam intensity.

The three collimators in the MT beamline each have two large steel jaws mounted in a steel casing; the jaws are opened and closed by means of a motor drive controlled by CAMAC electronics modules. The jaws of MT3CH1 and MT3CH2

TABLE IX. Effective radiation lengths of material in the MT beamline, other than targets.

Material and Length	Center in z (ft)	λ_I (%)	L_R (%)
MT2TGT0, 12 mil Al	118.8	.0039	.0172
Beam Pipe Window, 6 mil Ti	145.0	.0212	.169
Air, 24.8"	157.4	1.07	2.48
Beam Pipe Window, 6 mil Ti	169.8	.0212	.169
Beam Pipe Window, 6 mil Ti	747.9	.0212	.169
MT3PWC + $\frac{1}{8}$ " G-10	747.9	.798	1.71
MT3SC, $\frac{1}{4}$ "	748.3	.799	1.50
Air, 3'	748.5	.129	.300
Beam Pipe Window, 6 mil Ti	749.1	.0212	.169
Beam Pipe Window, 6 mil Ti	798.5	.0212	.169
Air, 2'	799.5	.0860	.200
Beam Pipe Window, 6 mil Ti	800.7	.0212	.169
Beam Pipe Window, 6 mil Ti	996.0	.0212	.169
MT4PWC + $\frac{1}{8}$ " G-10	996.8	.798	1.71
Air, 2.4'	997.2	.103	.240
Beam Pipe Window, 6 mil Ti	998.4	.0212	.169
Beam Pipe Window, 6 mil Ti	1031.7	.0212	.169
Air, 1'	1032.2	.0430	.100
CC Mylar Window, 10 mil	1032.7	.0412	.0885
CC He Fill Gas, 104'	1084.7	.932	.594

TABLE IX, Continued

Material and Length	Center in <i>z</i> (ft)	λ_I (%)	L_R (%)
CC Lucite Mirror, $\frac{1}{8}$ "	1103.7	.448	.923
CC Mylar Window 10 mil	1136.7	.0412	.0885
MT4SC, $\frac{1}{4}$ "	1137.2	.799	1.50
MT4SWDC	1138.3	.0670	.383
Air, 2.6'	1138.4	.112	.260
Beam Pipe Window, 6 mil Ti	1139.3	.0212	.169
Beam Pipe Window, 6 mil Ti	1207.9	.0212	.169
MT5SWDC1	1208.6	.0670	.383
Air, 1.5'	1208.6	.0645	.150
Beam Pipe Window, 6 mil Ti	1209.4	.0212	.169
Beam Pipe Window, 6 mil Ti	1281.7	.0212	.169
MT5SWDC2	1282.4	.0670	.383
Air, 1.5'	1282.4	.0645	.150
Beam Pipe Window, 6 mil Ti	1283.2	.0212	.169
Beam Pipe Window, 6 mil Ti	1365.0	.0212	.169
MT6SWDC	1365.8	.0670	.383
MT6SC1, $\frac{1}{4}$ "	1366.3	.799	1.50
MT6SC2, $\frac{1}{4}$ "	1366.3	.799	1.50
MT6SC3, $\frac{1}{8}$ "	1366.6	.400	0.750
Air, 20'	1378.8	.860	.200
Total Up to Wedge Fixture		10.58	22.04

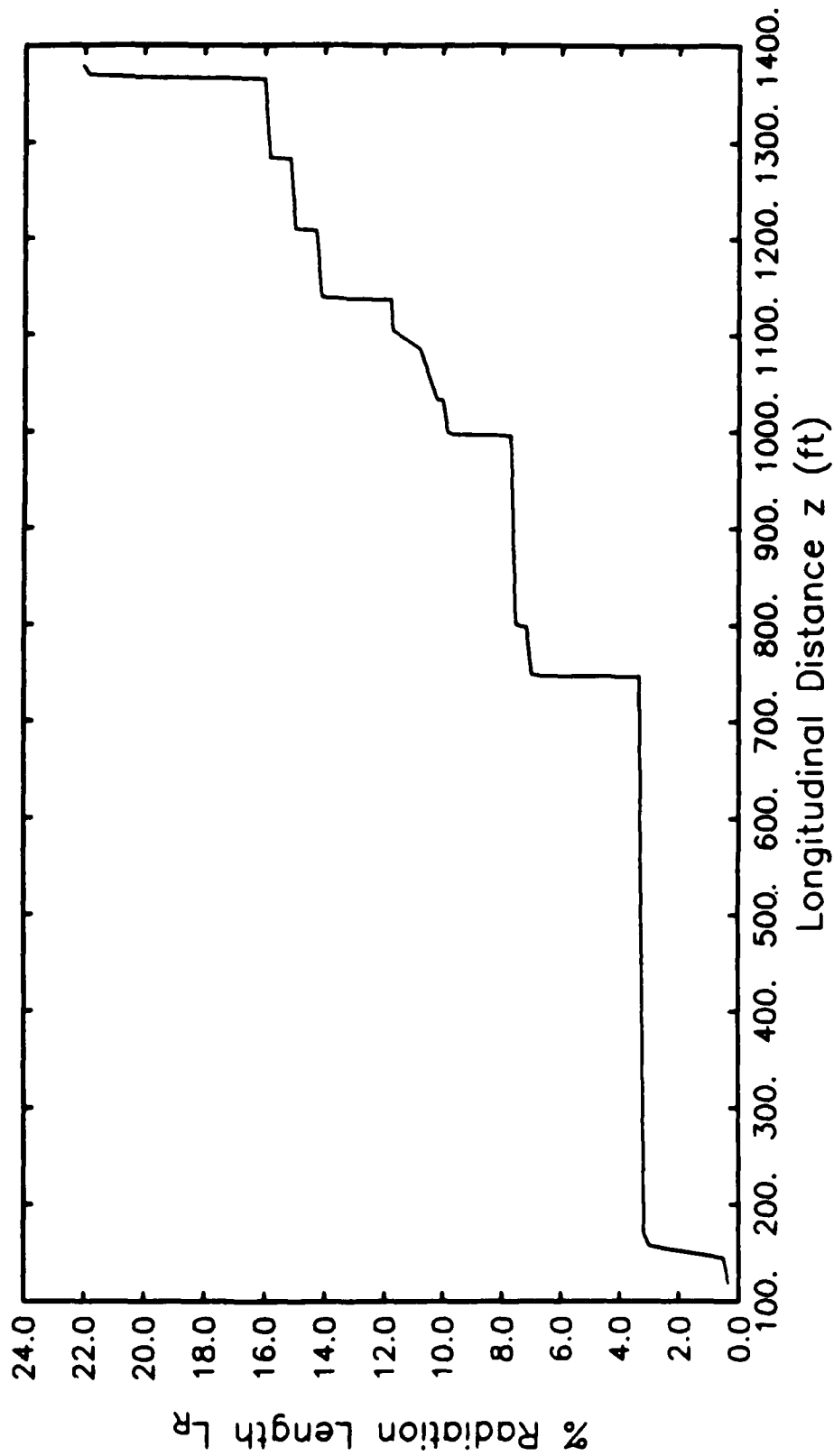


FIG. 37. Radiation lengths L_R accumulated down the MT beamline, excluding moveable targets.

move in the horizontal plane, while the jaws of MT3CV move in the vertical.

The primary use of the collimators in the MT beamline for CDF is to reduce the intensity of the beam at the final target area to the acceptable level of 20,000 particles per spill. The effectiveness of each collimator in reducing yields with the 245 GeV secondary hadron tune is plotted in Figures 38, 39, and 40. Yield is normalized by taking the ratio of the intensity of the beam reaching the final target area as measured by the coincidence of the MT4SC and MT6SC1 scintillation counters (this coincidence is coded MTSC46) to the intensity of the 800 GeV primary proton beam measured by the MW1SEM secondary emission monitor (both measure particles per spill). Effectiveness was determined for each collimator with the other two wide open; each has a full aperture of $4'' \times 4''$.

The other use of collimators is to reduce the angular and momentum acceptance of the beam.

Figure 41 includes schematic diagrams of collimators, and Figure 42 illustrates how collimators may be used to reduce momentum acceptance. Since momentum tagging will be carried out for each particle, this function is not important to CDF. Collimator efficiency in reducing the momentum bite cannot be determined until the momentum tagging system is fully operational.

Note that a collimator is most effective in reducing momentum bite when it is placed at a point in the beamline where the beam has a large profile spread, allowing for more controlled selection than if it were located near a focal point. For the MT beamline, the focal points are at MT3PWC and MT6PWC1. Beam size and momentum spread along the beamline can be estimated using plots of the pertinent transfer matrix elements given by TRANSPORT for a given beam energy.

Except for the collimator effectiveness studies, all other studies were carried

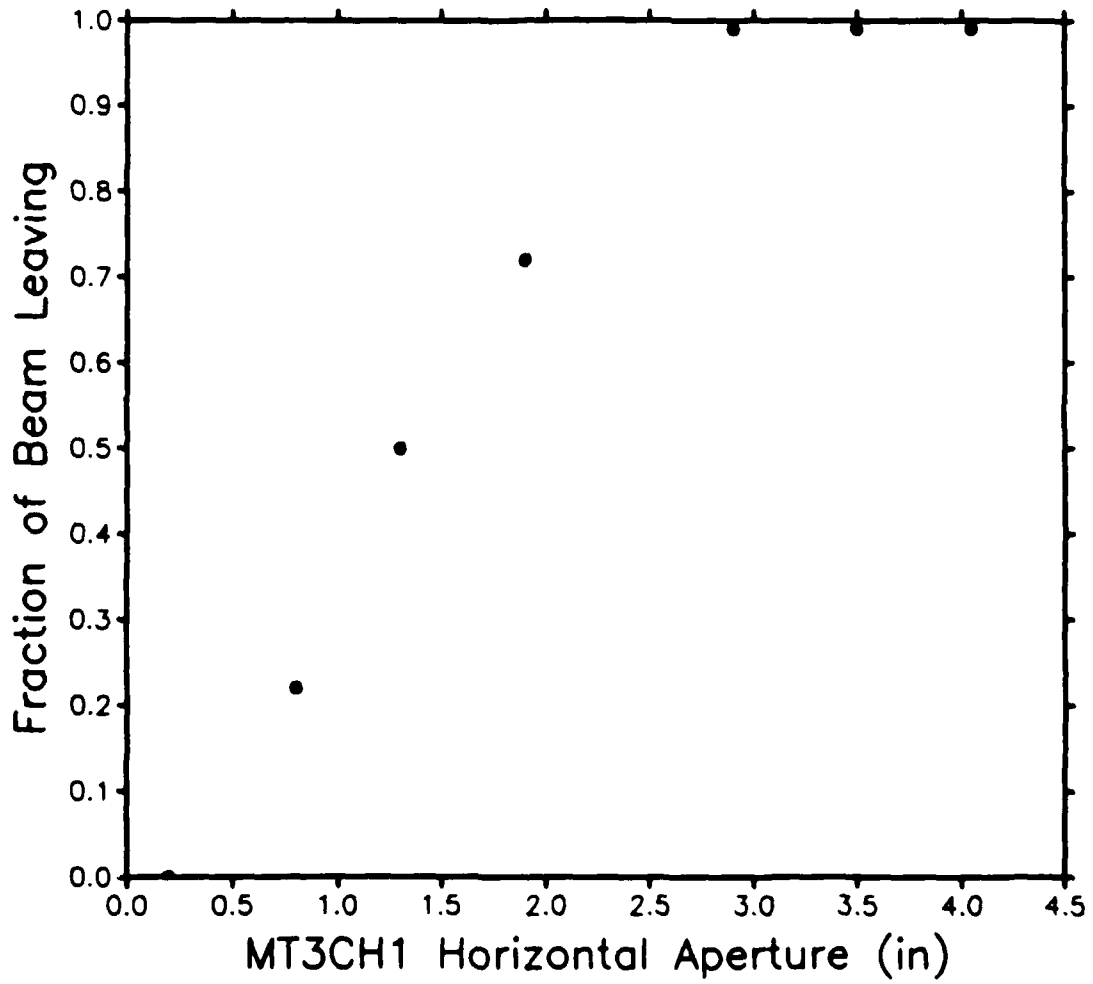


FIG. 38. MT3CH1 collimator effectiveness in reducing the intensity of the 245 GeV secondary hadron beam.

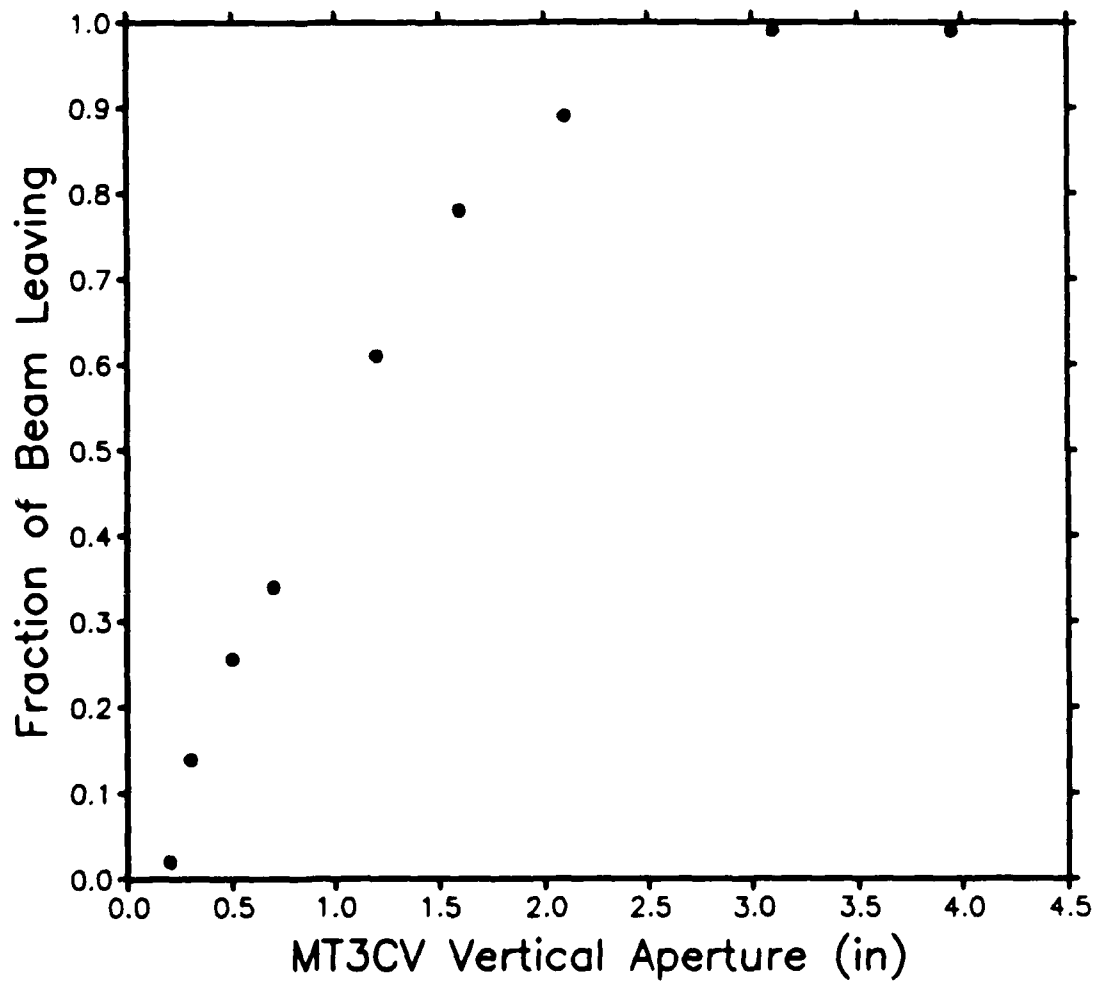


FIG. 39. MT3CV collimator effectiveness in reducing the intensity of the 245 GeV secondary hadron beam.

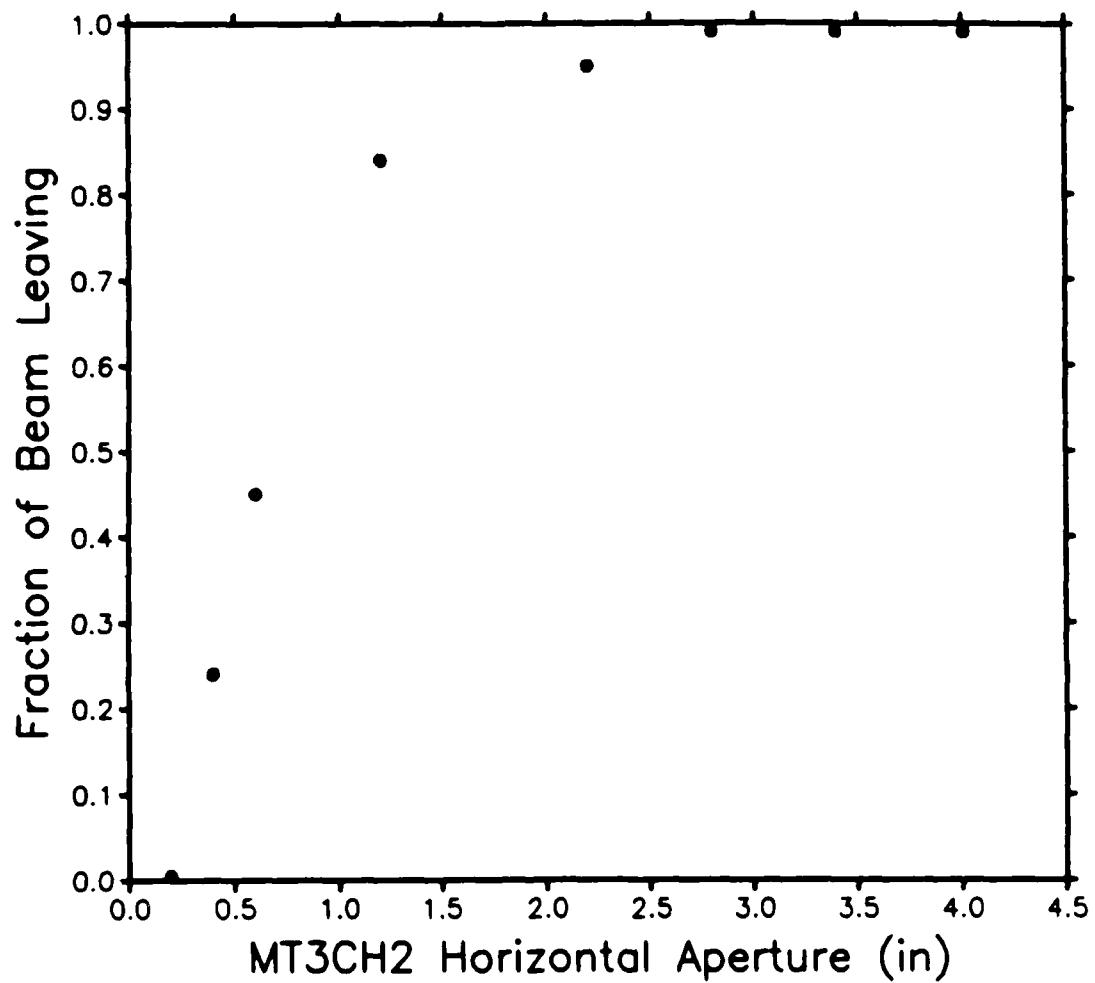


FIG. 40. MT3CH2 collimator effectiveness in reducing the intensity of the 245 GeV secondary hadron beam.

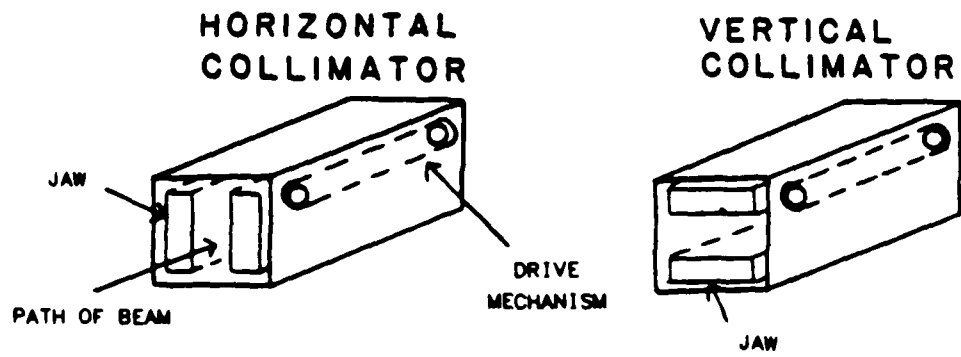


FIG. 41. Schematic diagrams of collimators.

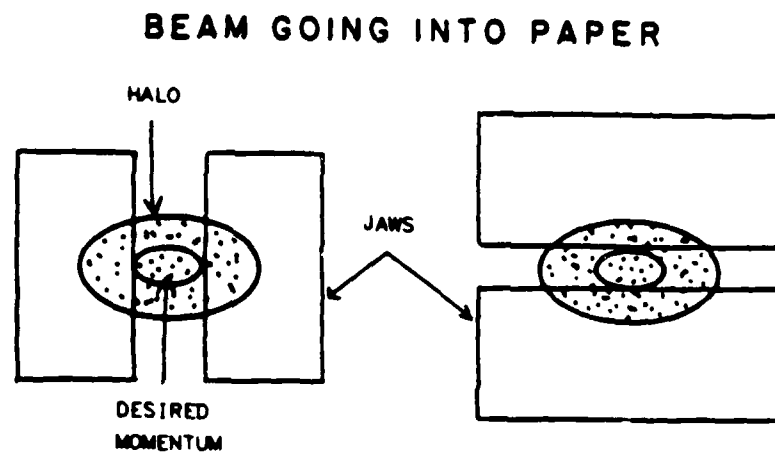


FIG. 42. Reducing momentum acceptance using collimators.

out with all three collimators open at their widest apertures.

D. Magnets

The MT beamline magnets have already received a thorough treatment earlier in Chapter VI. Data sheets and magnetic excitation curves for each type of magnet in the MT beamline will be presented here. Because the MT5E magnet string will be used as part of the momentum tagging system, the magnetic field strengths versus current settings for these five magnets will be determined more precisely after the end of the first run.

The polarity of all magnets in the beamline can be reversed. In the case of the MT beamline, however, only the polarity of MT3V can be changed remotely through the EPICS computer. The polarity of all other magnets can only be reversed at the power supply itself. When this is done, all bending dipoles will bend in the opposite direction in the magnetic midplane to that designed for positively-charged particle transport, effectively sweeping out positively-charged particles and instead transporting negatively-charged ones. While this appears to be a simple way to reverse the charge of particles transported, radiation safety requirements may preclude it. Reversing the polarity of a quadrupole also switches the focusing and defocusing planes of the magnet.

(1) *Dipole magnets.* Dipole magnets are specified according to the gap size and length (in inches), so that the 6-3-120 dipole has a 6" horizontal gap, a 3" vertical gap, and a length of 120". The gap size is determined by the vacuum pipe inserted in the magnet, and not by the walls of the magnet itself. For dipoles, magnetic excitation curves are plotted as magnetic field strength versus current. Data sheets and excitation curves for the 6-3-120 beamline dipole are at Figures 43 and 44.

respectively, and for the 5-1.5-120 EPB dipole at Figures 45 and 46, respectively. Note that all EPB dipoles in the MT beamline are 3.5-1.5-120, except the last magnet in the MT5E string, which is 5-1.5-120. Both have the same excitation curve, because both have their poles separated by the same distance from the magnetic midplane.

While bending dipoles are designed to turn a beam through relatively large angles, vernier or trim dipoles are used strictly to adjust the beam profile at some point in the beamline, often by only a few *mm*. To carry out this function, the trim magnet used in the MT beamline is the only magnet in the beamline whose polarity is regularly changed. The 5-4-30 trim vernier magnet in the MT beamline is not a standard Fermilab magnet. A data sheet and excitation curve, developed from those for the 4-4-30 vernier, are at Figures 47 and 48, respectively. The vernier dipole is the only magnet in the beamline whose excitation curve remains linear, even in the region approaching the maximum operating current.

(2) *Quadrupole magnets.* Quadrupole magnets are specified according to their gap diameter (in inches), their function (by a "Q"), and their length (in inches). The standard focusing quadrupole magnet used in the MT beamline is the 3Q120 EPB quadrupole. Excitation curves for quadrupoles are plotted as magnetic field strength gradient versus current. The data sheet and excitation curve for this magnet are at Figures 49 and 50, respectively.

E. Beam Stops and Beam Dumps

Beam dumps are permanently installed blocks of steel, coated with concrete (to absorb thermal neutrons) which dissipate the beam to acceptable radiation safety levels. The MT beam dump is located immediately behind the T755 experimental

6-3-120 BEAM LINE DIPOLE

Design Field	1.5 T
Power (dc)	47.1 kW
Current	.975 kA
Voltage	48.4 V
Transfer Constant	1.5385 T/kA
Inductance	153 mH
Gross Weight	10,236 kg
Water Flow	3200 liters/hr
Pressure Differential	14.1 kg/cm ²

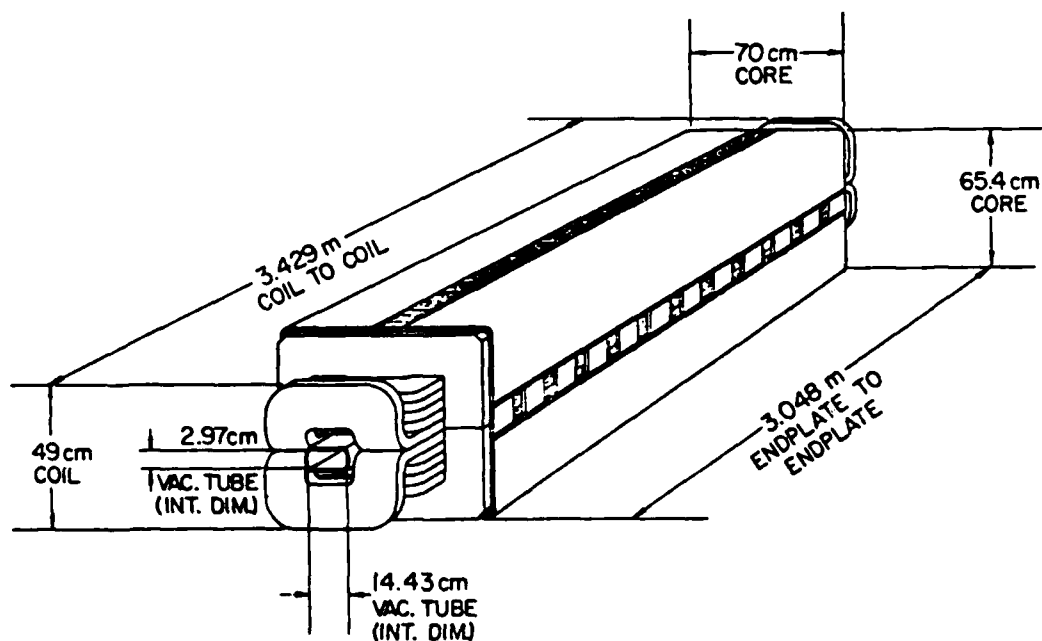


FIG. 43. Data sheet for the 6-3-120 beamline dipole magnet (from Toohig³⁹).

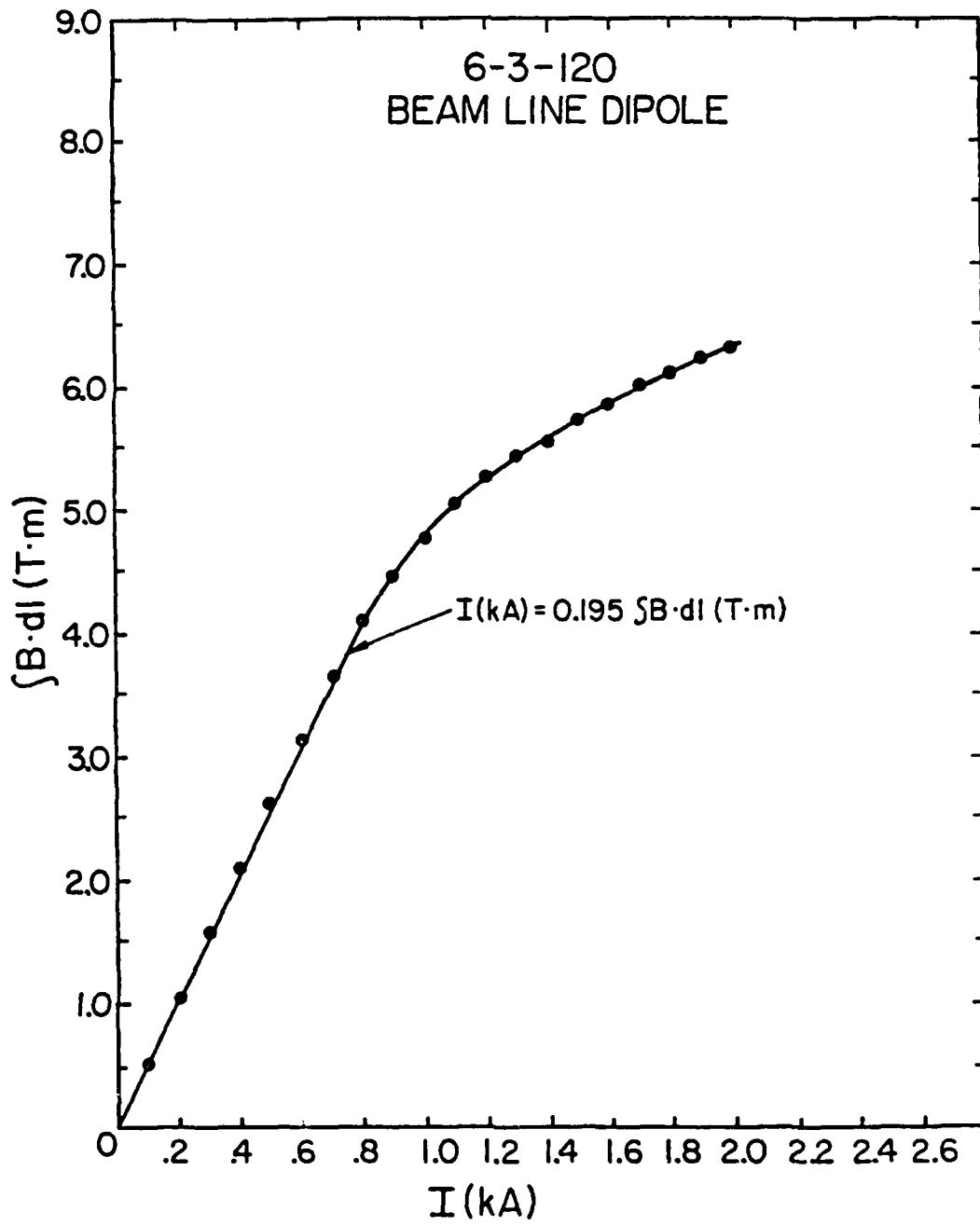


FIG. 44. Magnetic excitation curve for the 6-3-120 beamline dipole magnet (from Toohig³⁹).

5-1.5-120 EPB DIPOLE

Design Field	1.5 T
Power (dc)	50 kW
Current	1.688 kA
Voltage	29.5 V
Transfer Constant	1.0 T/kA
Inductance	30.0 mH
Gross Weight	2558.3 kg
Water Flow	1072 liters/hr
Pressure Differential	7.03 kg/cm ²

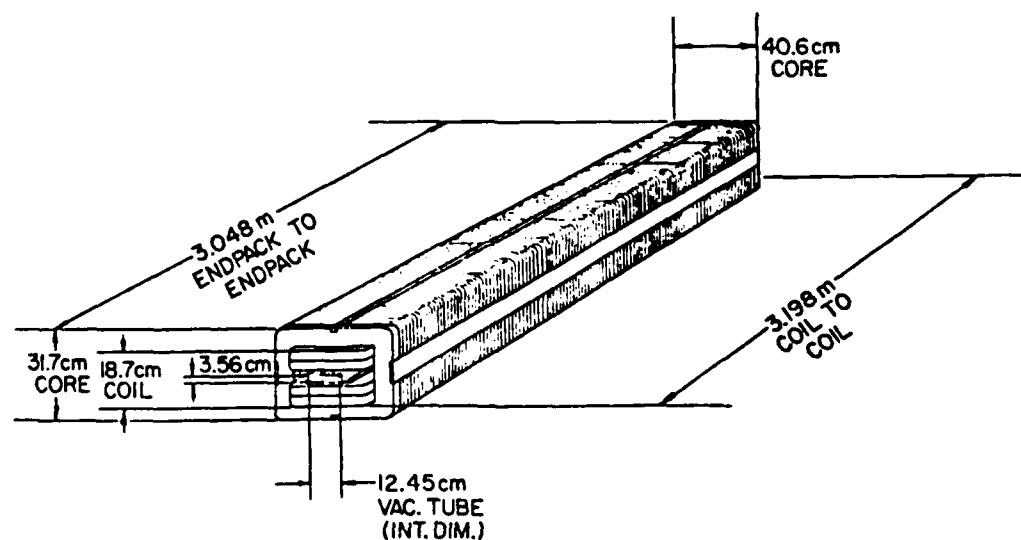


FIG. 45. Data sheet for the 5-1.5-120 EPB dipole magnet (from Toolig³⁹).

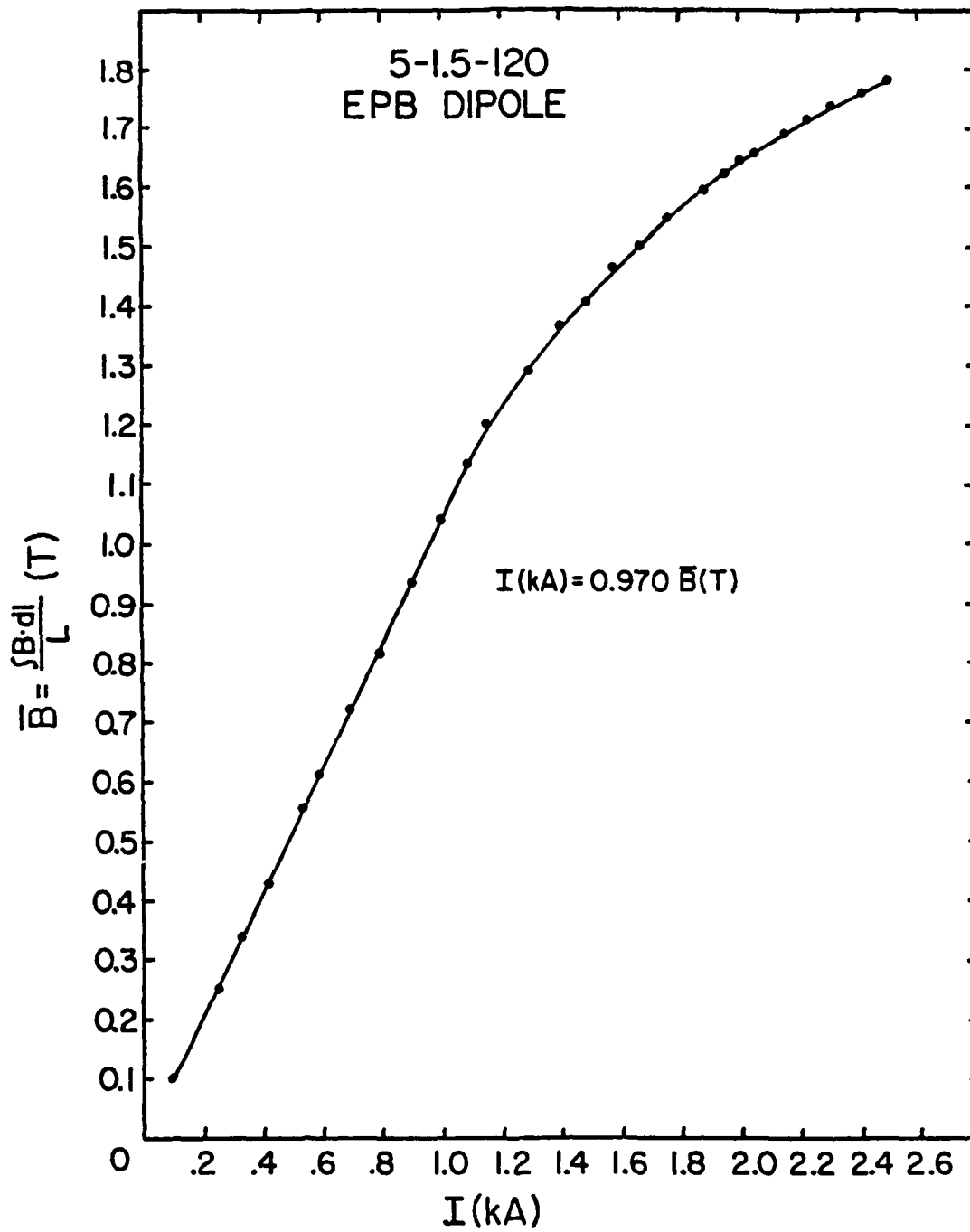


FIG. 46. Magnetic excitation curve for the 5-1.5-120 and 3.5-1.5-120 EPB dipole magnets (from Toolig³⁹).

4-4-30 VERNIER DIPOLE

Design Field	0.4 T
Power (dc)	9 kW
Current	0.18 kA
Voltage	50 V
Transfer Constant	0.4 T/kA
Inductance	mH
Gross Weight	462 kg
Water Flow	1454 liters/hr
Pressure Differential	6.3 kg/cm ²

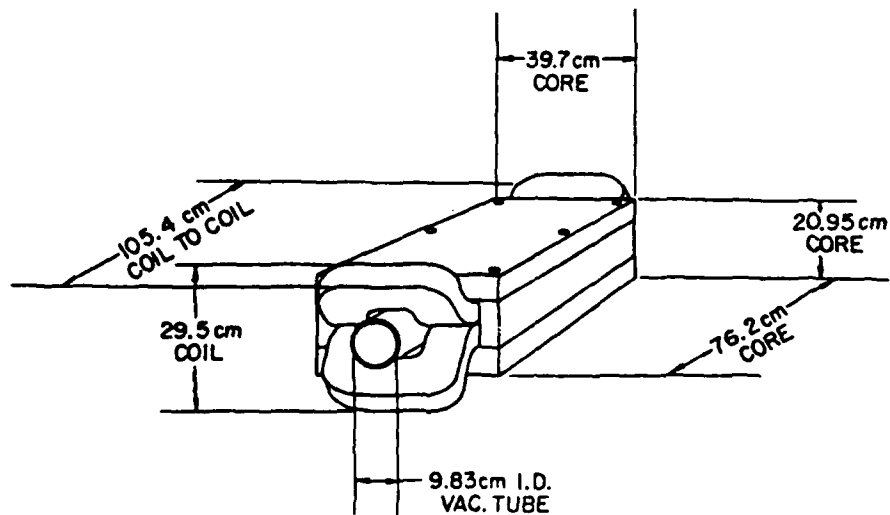


FIG. 47. Data sheet for the 4-4-30 vernier magnet (from Toolig³⁹).

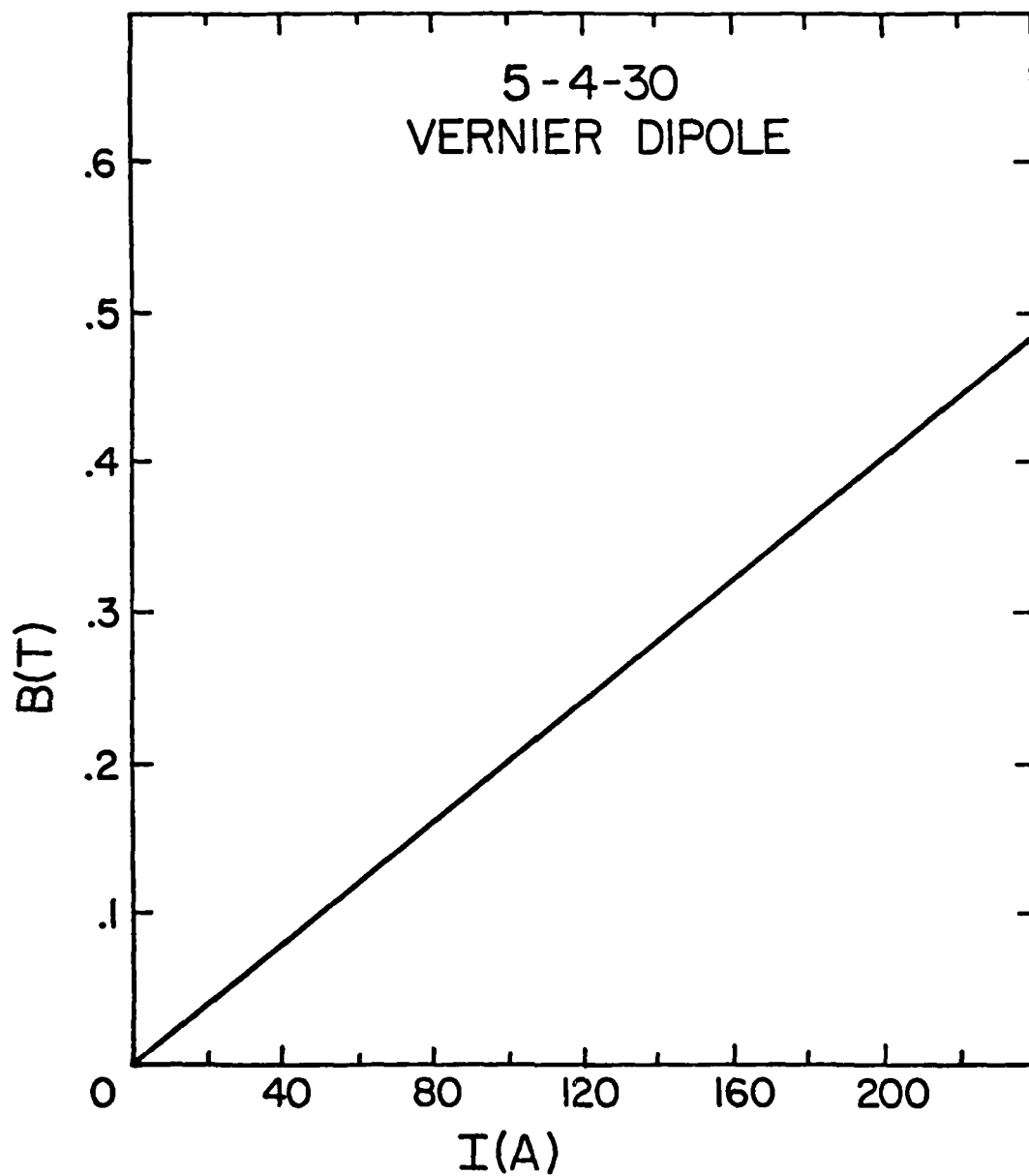


FIG. 48. Magnetic excitation curve for the 5-4-30 trim vernier magnet (from Toohig³⁹).

3Q120 EPB QUADRUPOLE

Design Field Gradient	18.898 T/m
Power (dc)	24.1 kW
Current	0.104 kA
Voltage	234 V
Transfer Constant	5.3848×10^3 T/m/kA
Inductance	1500 mH
Gross Weight	3125.25 kg
Water Flow	681.4 liters/hr
Pressure Differential	5.78 kg/cm ²

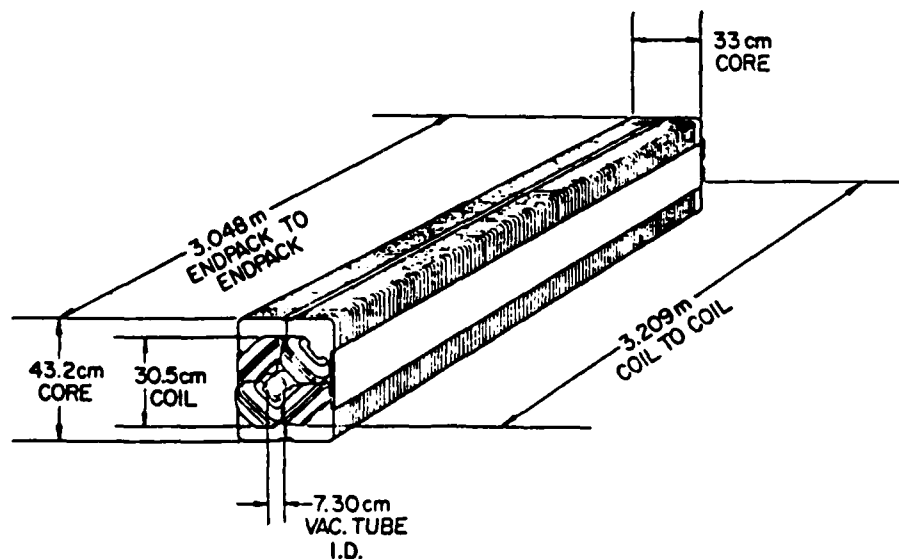


FIG. 49. Data sheet for the 3Q120 EPB quadrupole magnet (from Toolig³⁹).

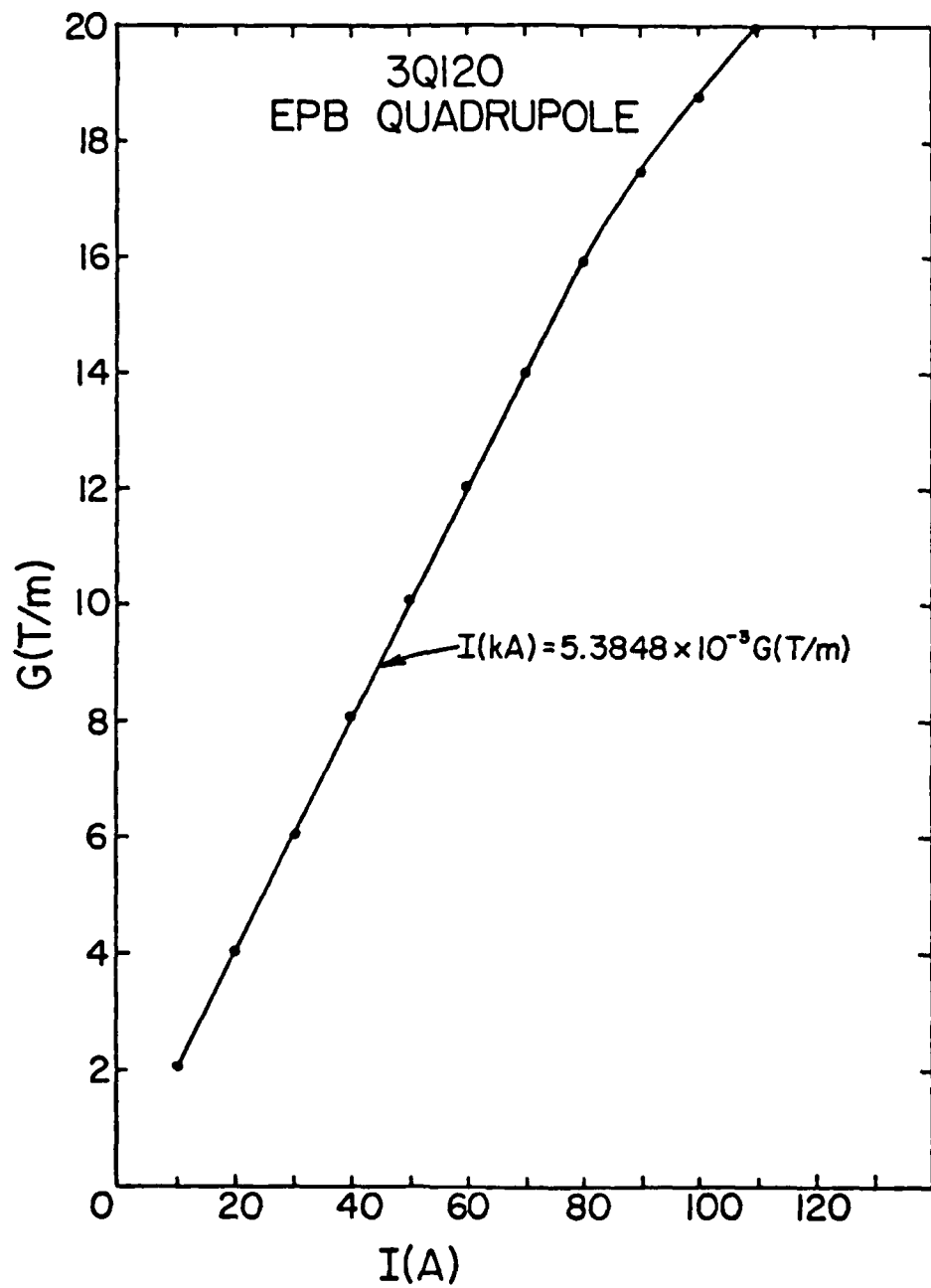


FIG. 50. Magnetic excitation curve for the 3Q120 EPB quadrupole magnet (from Toohig³⁹).

house inside the Meson Lab.

Beam stops are devices which can be opened or closed as desired to control the transport of beam downstream. They serve as critical devices in beamlines since they are designed to automatically close when tripped by safety monitoring equipment. The MT3BS is the one beamstop which stops beam from reaching the CDF target area. A steel jaw is held over the beamline by pneumatic pressure to allow for a 4" x 4" aperture. The MT6BS1 beam stop is a specially designed beam stop controlling beam reaching the T755 experimental area. MT6BS1 is actually two beam stops in series, but their electronics are ganged together so that simultaneous control of both is possible. This beam stop is composed of steel 9' thick and coated with concrete. Two jaws in series, each 4.5' long and made of steel, are held over the beamline pneumatically.

F. Beam Analyzing Devices

The standard beam analyzing devices in a beamline can be divided into two categories: beam counting devices and beam locating devices. Beam counting devices measure beam intensity by providing a count of detectable particles over a particular time interval (normally the duration of a spill). Beam locating devices actually locate the beam and give a beam profile as a distribution of particles in a given plane perpendicular to the beamline, as determined over a given time period. Both give real-time data which can be monitored directly through the EPICS system. These devices will be discussed below.

Specialized nonstandard beam analyzing devices used in the MT beamline include the threshold Čerenkov counter, the synchrotron radiation detector, and the momentum tagging system. Because these devices were not operational during

the preliminary beamline studies, they will not be discussed in detail here.

G. Secondary Emission Monitors²²

The MWISEM secondary emission monitor is immediately upstream of the MT beamline and measures the intensity in particles per spill of the 800 GeV primary proton beam reaching the MT2TGT-series targets. This is a crucial beam counting device for the MT beamline since it provides the incident intensity with which all downstream intensities and yields are normalized.

The MWISEM is one of several standard secondary emission monitors used at Fermilab. As shown in Figure 51, this SEM contains 10 high voltage (or bias) foils and 9 signal (or collector) foils, a configuration which allows for the maximum signal accumulation: each foil is 2 mil thick Al. In addition, titanium (Ti) windows 5 mil thick close off the counter. Negative high voltage is applied to the high voltage foils, so that the signal foils (not wired to a high voltage source) are positively biased.

The SEM is maintained at a vacuum of 10^{-7} to 10^{-9} Torr using an ion pump; even slight gas contamination will severely limit SEM efficiency. For this reason, SEM's are normally baked under vacuum at 300°C for about seven days to minimize degassing by inner components.

A secondary emission monitor receives its name from the process by which the incident beam particles produce ionization. The incident protons' electromagnetic fields interact with the peripheral electrons in the Al atoms on the foil's surface and with the free electrons of the metal, providing the necessary energy (5 to 10 eV), depending on the metal's work function) for an electron to be ejected from the foil. This emission is a surface phenomenon, since the maximum depth for emission to occur is on the order of 10^{-8}m . Due to the foil's thickness, particles rarely interact

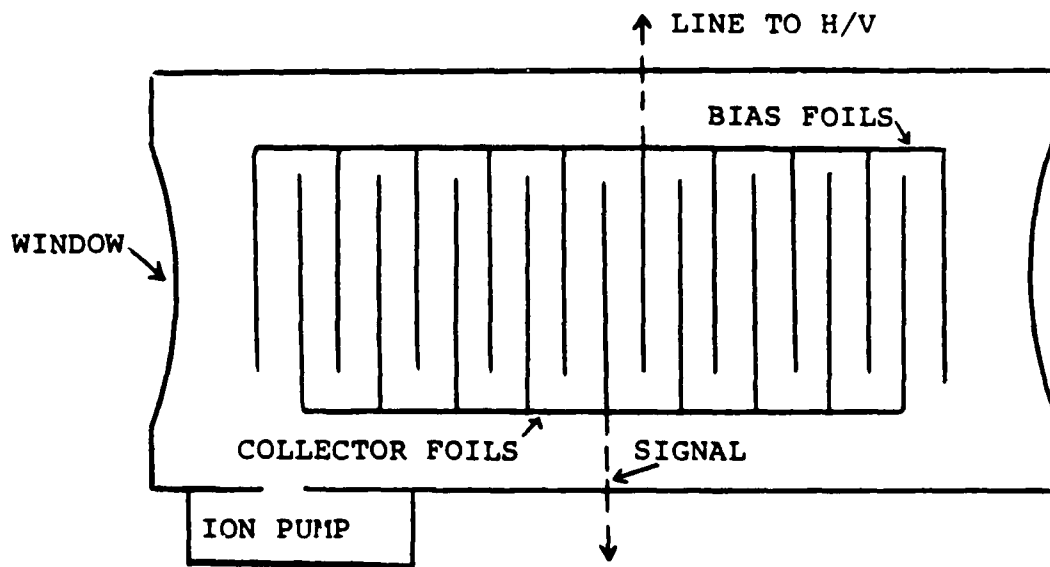


FIG. 51. Cross section of a secondary emission monitor (from Bodnarczuk²²).

directly with the nuclei of the atoms in the foil. Freed electrons are attracted to the positively-biased signal foils, generating a current which is correlated to the intensity of the proton beam.

Proper calibration of the SEM is essential. Calibration is carried out using the foil activation technique, where a 0.0625" thick brass foil is placed directly in front of the SEM for an hour while beam is running. The amount of activity in the brass foil afterwards is measured and compared against the readings given by the SEM during the test period to determine the correlation with beam intensity. This method of calibration is good to $\pm 3\%$. The MW1SEM was last calibrated by this method two years ago. SEM's which have been in a beamline for some time experience fewer fluctuations in readings as activation of the device itself reaches stable levels.

SEM's are normally used to monitor high intensity beams and are capable of counting protons in the range of 10^7 to 10^{14} particles per spill, where they have an efficiency of better than 99%. Signal-to-noise ratios in SEM output become important with beam intensities below 10^7 particles per spill.

H. Proportional Wire Chambers⁴⁰

A small standard proportional wire chamber (PWC) has been developed for use in secondary beamlines at Fermilab. These PWC's may be used purely as beam locating devices, or they may be used as beam counting devices. When employed as beam locating devices, signals from the PWC's sense wires are read out by an electronics module called a scanner, which allows the EPICS system to provide a beam profile on a television screen.^{40,41} When used in this mode, the chamber operates in the limited proportional region; when used as a beam counting device,

it is operated in the plateau region, where efficiency is better than 99%. In either case, the fill gas is 80% argon 20% carbon dioxide.

The PWC's in the MT beamline are MT3PWC, MT4PWC, MT6PWC1, and MT6PWC2. These chambers all provide beam profiles in the horizontal and vertical planes which can be viewed on Fermilab's closed circuit television system.

Because all PWC's are surveyed into position, the beam profile not only displays particle distribution in both the horizontal and vertical planes, but also shows the location of the beam to great accuracy. For the PWC's with 2 mm wire spacing used in the MT beamline, spatial resolution is on the order of 0.2 mm.

PWC's are put together using the modular concept: the experimenter may vary the number of sense wire planes stacked together to make up the PWC to fit his needs. All MT beamline PWC's have two sense planes. Except for MT6PWC2, whose vertical plane has 1 mm wire spacing, all planes have 2 mm wire spacing. These separate wire planes, mounting 64 anode sense wires each (128 for 1 mm wire-spaced planes), are placed perpendicular to each other and used to read out the profile in the horizontal x and vertical y planes. High voltage printed circuit board cathode planes are spaced between sense planes. Exact positioning of these planes is accomplished with connector pins attached to the corners of the PWC frame, so that the location of the center of the PWC, and of each sense wire, is known to great accuracy. A cross sectional view of a PWC is shown in Figure 52.

The chamber has been designed to minimize the amount of matter in the path of the beam. The outside windows are 5 mil thick Al foil. Sense wires are 4 mil diameter gold-plated tungsten. Cathode planes are also 5 mil Al foil. The space filled with gas is 0.75" perpendicular to the beam's path. For PWC's with two sense planes, this adds up to 0.002 interaction lengths or 0.0007 radiation lengths.

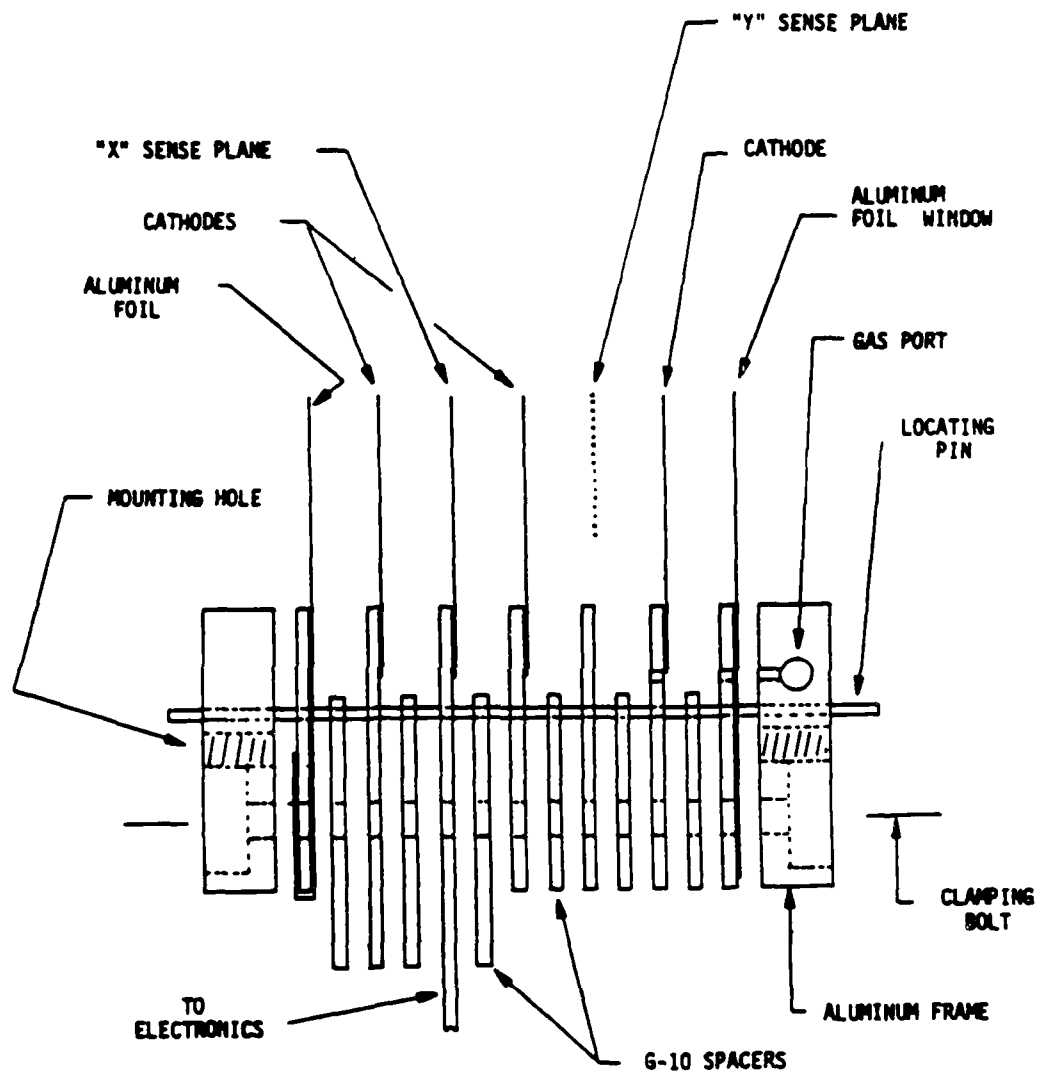


FIG. 52. Cross section of a beam proportional wire chamber (from Fenker⁴⁰).

Currently, all PWC's in the MT beamline also have 0.0625" thick G-10 windows in front and back to provide additional support and protection.

Efficiency plotted against applied voltage for a typical PWC is shown in Figure 53. Chambers used as beam locating devices are normally maintained at an operating voltage of 2700 V, where they are about 98% efficient. Voltages much above this setting degrades the position resolution of the chambers. The chamber output "runs away" at about 2850 V applied voltage.

Chambers are made gas tight with vacuum grease, which allows for a leakage rate of less than $3 \text{ cm}^3/\text{hr}$ at a pressure of 2" of pump oil. The gas flow rate to chambers is normally around 0.03 SCFH.

I. Single Wire Drift Chambers⁴²

John Krider of Fermilab has recently designed and tested a single wire drift chamber (SWDC) to be used in low intensity beamlines (25,000 particles/sec). This SWDC has a spatial resolution in x and y comparable to that of standard Fermilab PWC's with 1 mm wire spacing. The first use of these chambers at Fermilab is in the MT beamline, where their primary use will be in the momentum tagging system. The SWDC is unique in that it serves both as a beam counting device and as a *particle* locating device.

The SWDC functions on the same basis as the drift chambers in CDF. A drift chamber is constructed much like a multi-wire proportional chamber, except that the spacing between wires is increased and the electric field between the wires is shaped so as to be uniform. When a minimum ionizing particle passes through the gas volume of the chamber, ionization of the gas occurs along the track. In the uniform electric field the liberated electrons drift with a constant velocity (determined by

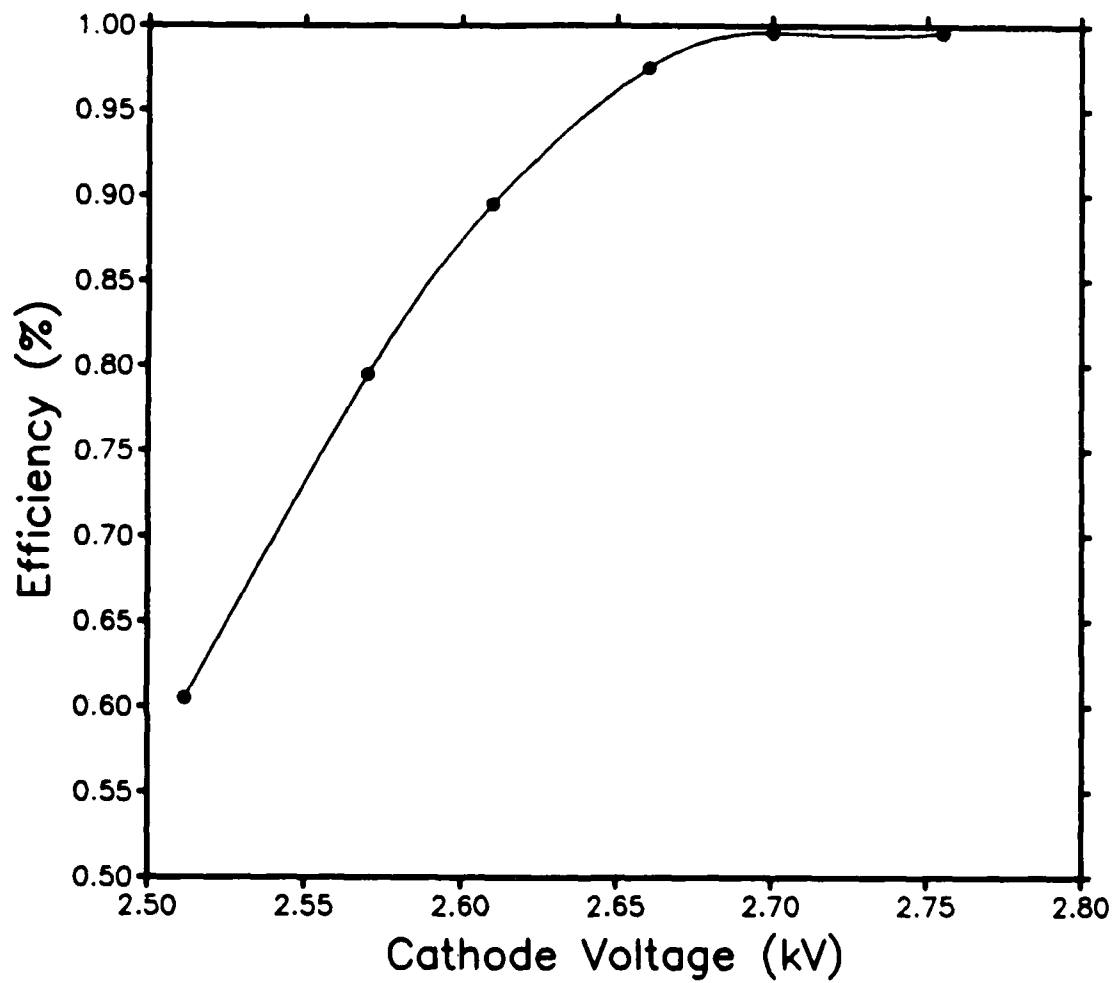


FIG. 53. Efficiency vs. applied high voltage for a typical beam proportional wire chamber.

the gas mixture and the drift field). These electrons eventually reach the high-field amplification region near the anode wire and avalanching occurs. The collection time of the avalanche gives a measure of the original position of the ionization track. Spatial resolution is normally better than with comparable multi-wire proportional chambers (often by a factor of 10). However, it takes a comparatively long time to collect at the anode all the electrons produced along a track, so that multitrack capability for a given wire is excluded. This is why, depending on the spacing between wires (which determines the drift space), reliable detection is only possible with fairly low beam intensities.

The single wire drift chamber is so called because one module consists of four independent single wire drift cells stacked back to back, each with an active area of $4'' \times 4''$. Two cells each have a vertical high voltage anode wire to measure the horizontal coordinate, and the other two cells each have a horizontal high voltage anode wire to measure the vertical coordinate. One cell has its anode offset 20.3 mm to one side of the center, while the other cell measuring the same coordinate has its wire offset 20.3 mm to the other side. This resolves left-right ambiguities and provides a constant monitor of the electron drift velocity.

A cell consists of a single-sided printed circuit anode plane centered between a pair of field-shaping printed circuit cathode planes. A $15 \mu\text{m}$ thick grounded Al foil is located outside of each cathode to electrostatically isolate that cell from the others in the module. A cross section of the edge of a cell is shown in Figure 54. An $85 \mu\text{m}$ diameter Be-Cu field wire is located at either edge of the active area, and each is operated at the same potential as the nearest cathode plane to maintain linearity of the drift field. The cathode plane has 51 field-shaping wires of the same type. The anode wire for a cell is $25 \mu\text{m}$ diameter gold-plated tungsten wire. Each

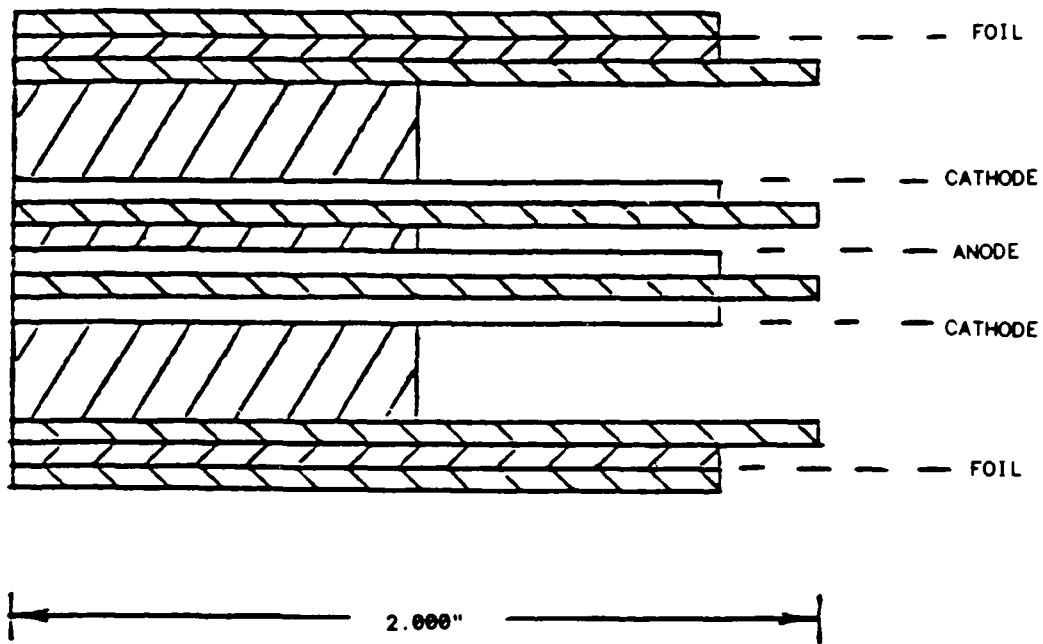


FIG. 54. Cross section of the edge of a cell of a single wire drift chamber.

module is sealed off with 125 μm thick mylar windows.

A 50% argon/50% ethane gas mixture bubbled through isopropyl alcohol at 0° C is used as the fill gas at 1" of water with a flow rate of 0.025 SCFH. Air leakage rates are no more than 5 cm^3/hr .

In general, to "plateau" a counter means to optimize the efficiency of the counter versus such things as acceptable levels of noise, multiple counts, or applied voltage. Most often efficiency is plotted versus applied high voltage and the resulting curve rises rapidly until it flattens out, or plateaus, at some value where such things as noise are acceptable. Counters usually are run well into the plateau region if other considerations permit so that efficiency is less subject to small changes in the applied voltage.

The high voltage efficiency plateau for MT6SWDC is shown in Figure 55, taken for the standard gas mixture; this plot is typical for all SWDC's. The operating applied voltage is 1620 V, about 100 V into the plateau region. Chamber efficiency is normally better than 99%, with the error due mostly to noise in the electronics. Chamber gain is linear with respect to high voltage at least in the range of 1500 to 1700 V.

Figure 56 shows the electron drift velocity for the standard gas mixture as a function of the drift field. Drift velocity saturation occurs at about 450 V/m, although drift velocity continues to increase gradually with increasing field. The normal drift field is 1000 V/m, with an average drift velocity of 5.0 $\text{cm}/\mu\text{sec}$.

When the chamber is operated at a nonsaturating gain the anode pulse rise time is equal to the spread in drift time of the electrons from the initial ionizing track, so that time resolution depends on the distance of the track from the anode wire. Between the effects of this drift path length spread, gas diffusion, and electronics

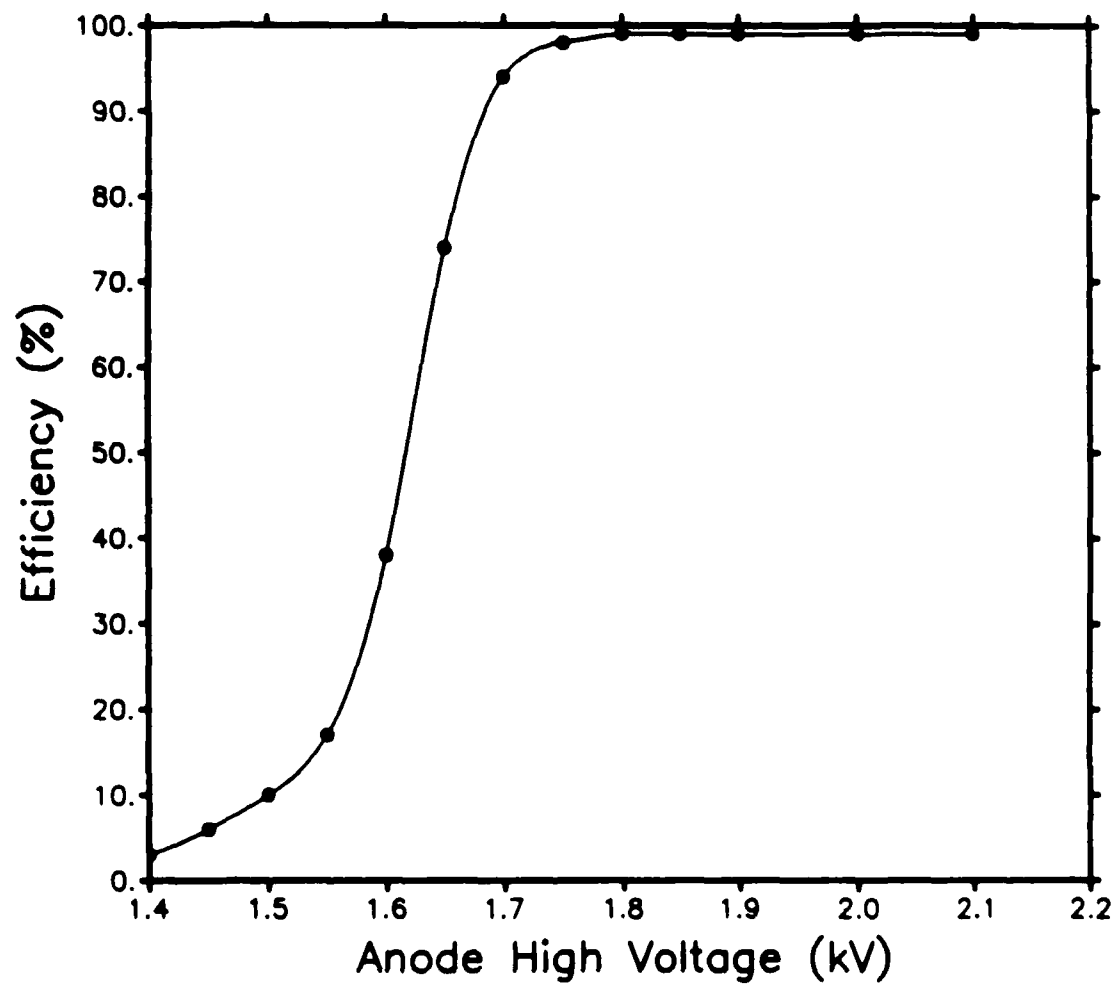


FIG. 55. Efficiency vs. applied high voltage for MT6SWDC.

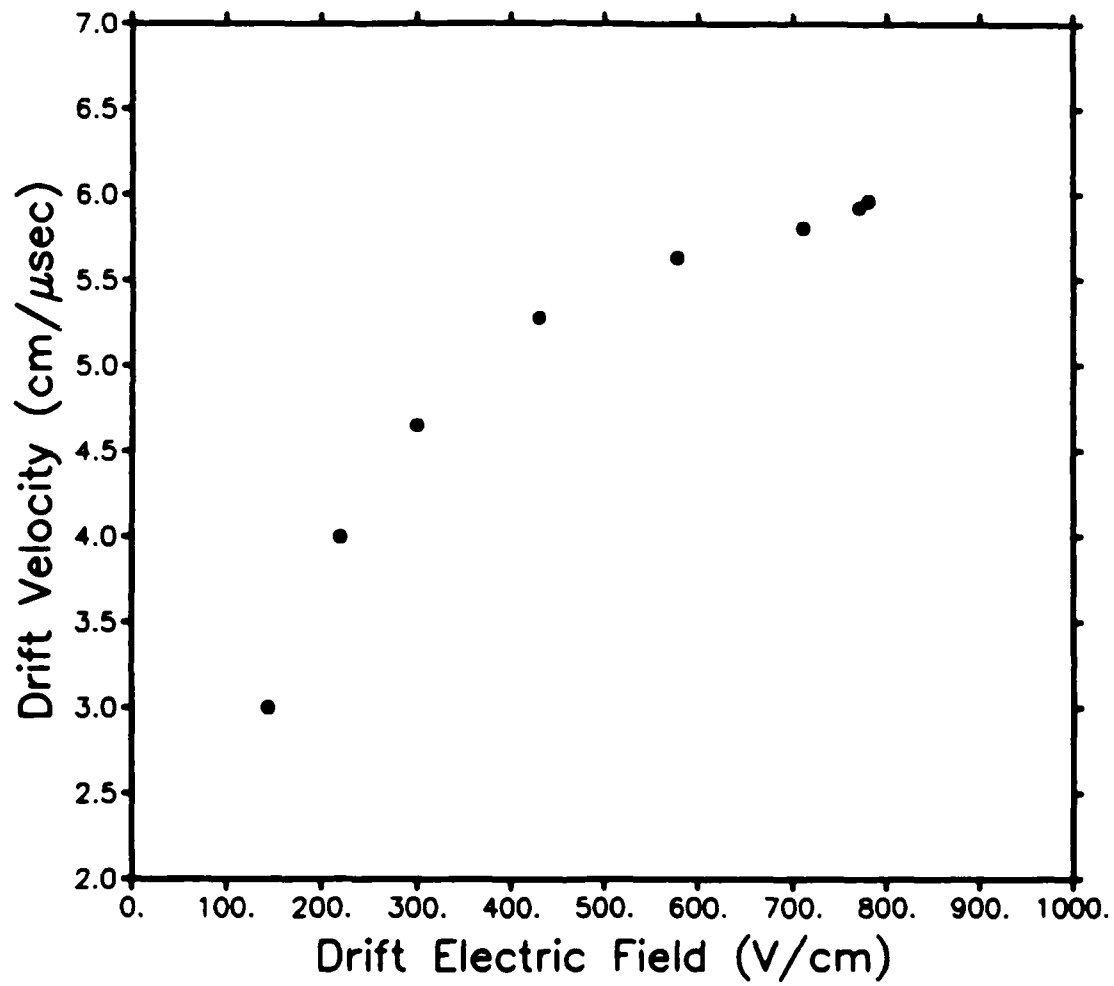


FIG. 56. Electron drift velocity vs. the drift field for a typical single wire drift chamber.

time slewing, the upper limit on spatial resolution is $380 \mu\text{m}$ (at the drift distance of 7 cm). This compares favorably with the $300 \mu\text{m}$ resolution achieved with a 1 mm wire-spaced PWC with two sense planes.

With beam intensity greater than $25,000$ particles/sec, the effect of left-right ambiguities and overlapping particle tracks occurring during an initial particle drift time causes a 1% drop in efficiency.

The SWDC's give an accurate beam count reading during each spill through the EPICS system. Track location for each particle is fed only to the CDF data acquisition system. In the next year, a system will be developed so that beam profiles measured during a spill will be displayed in real time on a television screen, much like those from PWC's. The method used for profile reconstruction, however, will be much different from the standard scanner system used for PWC's. Until then the PWC will remain the only real-time beam locating device in the MT beamline. It is currently possible to use an oscilloscope hooked up directly to an SWDC's electronics to determine beam profile in a given plane.

J. Scintillation Counters

Scintillation counters (SC's) are the most common beam counting device in the MT beamline. Two or more may be placed in coincidence to improve the accuracy of particle counts by eliminating counts due to background noise in separate counters. When coincidences are set, time delay due to length of signal cables and travel time of particles in the beam must be accounted for. Depending on the shape of the scintillators used and the logic tying them together in coincidence, simple triggering or particle tagging systems can be created. SC's are also used to trigger the Time to Digital Converters (TDC's) used to determine electron drift times in the single

wire drift chambers. The phenomenon which is the basis of SC's allows them to only detect charged particles.

The excitation of the atoms in certain media by ionizing particles passing through the medium results in luminescence (scintillation), which is recorded by a photomultiplier. Scintillation occurs in many substances in a variety of phases, but inorganic single crystals and organic liquids and plastics are most common (the fastest scintillator decay times occur in organic scintillators).³⁷

The SC's in the MT beamline all use polystyrene as the scintillation medium, with a decay time of 3 to 5 nsec. In organic materials, the scintillation mechanism is excitation of molecular levels which decay with the emission of light in the UV region. The conversion to light in the visible blue region is achieved by means of the fluorescent excitation of dye molecules (known as wavelength shifters) which are incorporated into the scintillation medium.

The light from the scintillator slab travels by internal reflection down a shaped plastic light guide to the photomultiplier's photocathode, where electrons are liberated by the photoelectric effect. Amplification factors of 10^8 are achieved by means of secondary emission electrodes (called dynodes) at successively higher potentials. A typical scintillation counter is shown in Figure 57.

The individual scintillation counters and the coincidences used in the MT beamline are listed in Table X (note the nomenclature used to designate coincidences between SC's). The original SC's in the beamline are MT3SC, MT4SC, and MT6SC1. CDF added the remainder.

Plateauing of SC's is carried out by putting each in coincidence with an already plateaued counter in the beamline and determining efficiency with respect to the reference counter versus applied voltage. An example of such an efficiency curve is

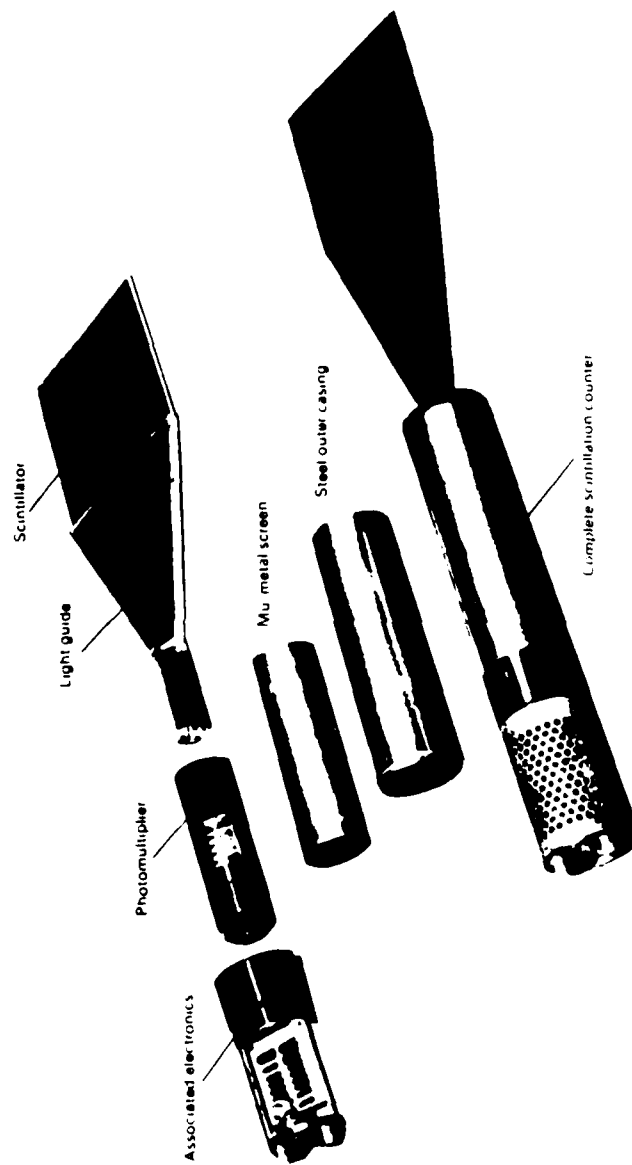


FIG. 57. Typical plastic scintillation counter (from Bodnarczuk^{2,3}).

TABLE X. Scintillation counters in the MT beamline.

Device Name	Function	Thickness <i>m</i>	Width · Height <i>m · m</i>	Voltage <i>V</i>
MT3SC	Counter	$\frac{1}{4}$	4 · 4	2370
MT4SC	Counter	$\frac{1}{4}$	4 · 4	1800
MT6SC1	Counter	$\frac{1}{4}$	4 · 4	1650
MT6SC2	Counter	$\frac{1}{4}$	4 · 4	2050
MT6SC3	Definition	$\frac{1}{8}$	1 · 1	1750
MT6SCV	Veto (Halo)	$\frac{3}{16}$	9 · 6 (1.5 dia hole in center)	1950
MT6SCMU	Muon Det	$\frac{1}{4}$	10 · 10	1800
Coincidences				
MTSC46 ^a	Counter			
MT6SC12	Counter			
MT6SC123V	Trigger			
MT6MUB ^b	Trigger			

- a. Coincidence between MT4SC and MT6SC1.
- b. Coincidence between MT6SC1, MT6SC2, MT6SC3, MT6SCV, and MT6SCMU.

at Figure 58. Most SC's in the MT beamline operate at better than 99% efficiency.

K. Triggers

The additional SC's placed in the MT6 enclosure by CDF (and the coincidences between them) are used to produce triggers for the data acquisition system. The basic trigger logic is illustrated in Figure 59.

The MT6SC3 counter is termed a *beam definition* counter because it is only 1" x 1", defining the maximum size of the beam accepted by the trigger. The MT6SCV counter has a 1.5" diameter hole at its center, so that it only detects particles outside the desired beam profile, thus identifying halo particles. MT6SC1, 2, 3, and "no-V" (i.e., no halo particle detected) are in coincidence (designated as MT6SC123V) and used to determine the passage of particles which are acceptable candidates for recorded events. For data acquisition of an event to be initiated, CDF requires that no other possible event have occurred in the preceding 500 μsec in order to clear out the front-end electronics.

If passage of an acceptable event does not trigger the muon counter, MT6SCMU, the logic sends out a *normal* (i.e., hadron or electron particle) beam trigger to the data acquisition system. Electron and hadron events are further separated by the electron tagging devices in the beamline. If the muon counter is triggered, however, the logic designates an acceptable *muon* trigger. The muon counter can only be used in the logic when the MT6BS1 beam stop is closed, so that particles other than muons can be assumed to be absorbed in the beam stop before reaching the counter.

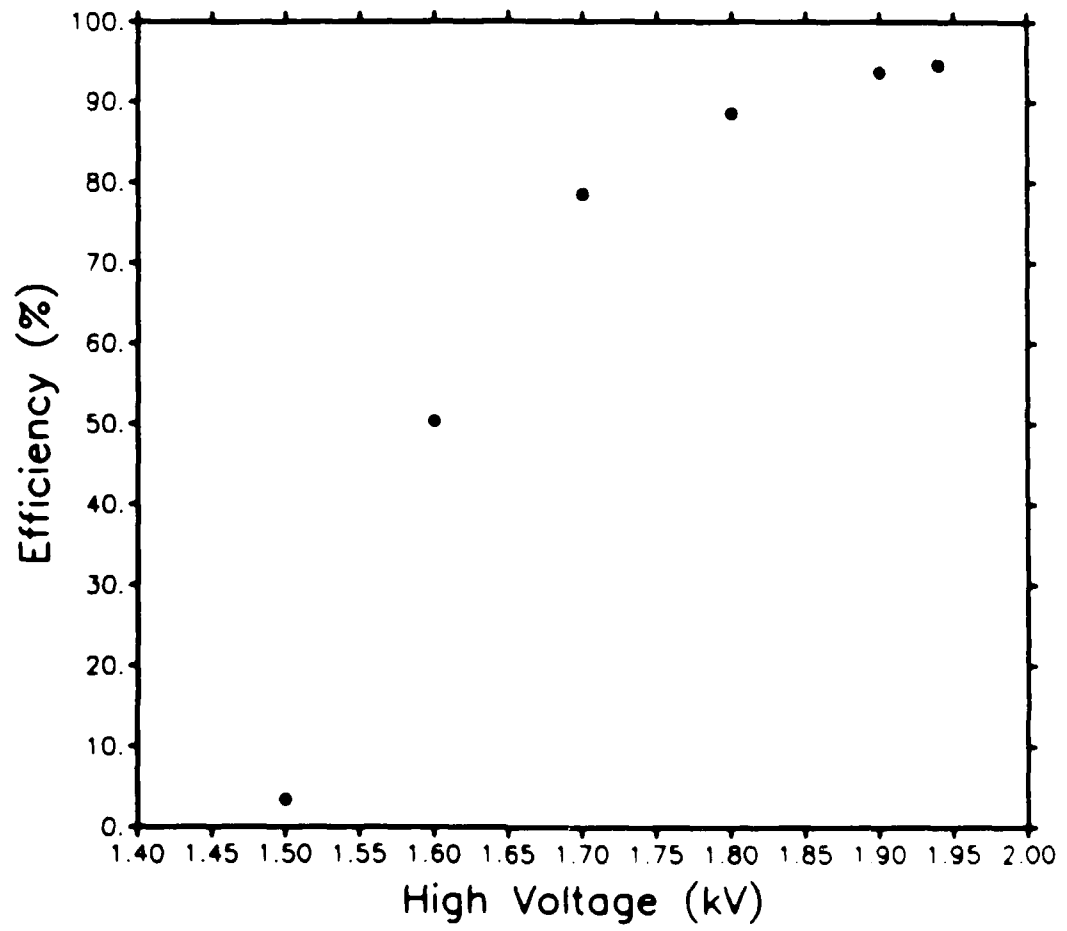


FIG. 58. Efficiency vs. applied high voltage for M16SC1

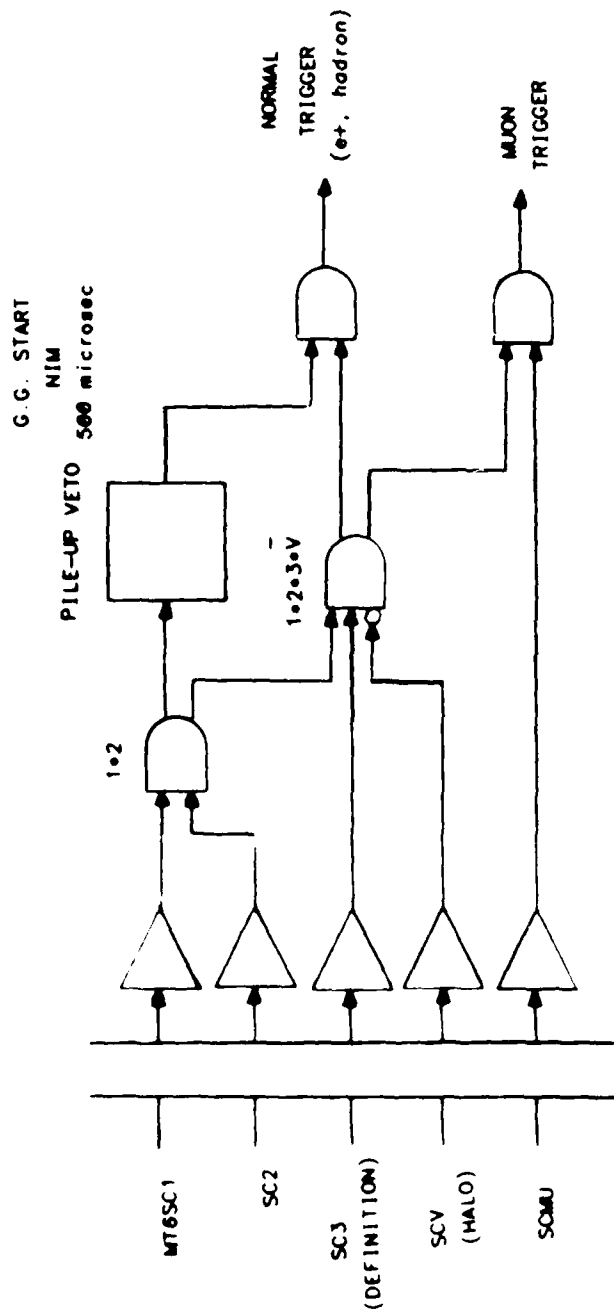


FIG. 59. Beam trigger logic.

L. Tagging Systems

Besides the triggering systems just described, other devices are in the MT beamline to tag particles. The threshold Čerenkov counter and the synchrotron radiation detector can be used independently or in coincidence to identify electrons. The SWDC's, together with the MT5E bending dipole string, and the necessary electronics, will be used to determine the momentum of each particle.

The final pair of SWDC's may also be used for precise measurement of the position for each particle. MT5SWDC2 and MT6SWDC are downstream of all magnets, so that they can be used to project out the x and y coordinates of each particle at the CDF target area.

CHAPTER VIII
BEAM TRANSPORT AND UPDATED COMPUTER ANALYSIS
FOR THE MESON TEST BEAMLINe

A. Beam Tuning

The most significant product of the preliminary beamline studies should be a set of tunes (optimum magnet current settings) necessary to transport particle beams over a range of energies with the maximum possible yields and optimum beam profiles at the final target area.

Tuning the beam is an extremely time consuming process which requires a certain amount of hands-on experience. A beamline's tunes are continually improved upon over the lifetime of the beamline, and may be redone when the beamline configuration is changed or the primary beam itself is altered by the Switchyard.

For the MT beamline, nominal tunes were first determined through computer analysis using TRANSPORT for the three basic energies originally expected to provide the highest yields for secondary hadron transport: 245, 160, and 80 GeV. TURTLE was then used to determine expected beam intensities at the final target area, as well as the spatial extent and momentum spread of the beam.

The 245 GeV tune would be used most often, since it was planned to be used to produce the incident beam on the MT3TGT1 production target to create tertiary beams. It also provided the upper limit energy expected from the beamline because it required the maximum allowable current settings for the MT2WU and MT5E magnet strings. As the baseline tune, it was optimized first and studied in the most detail.

The nominal tune generated by the computer served as the starting point in optimizing magnet current settings experimentally. The experimenter tunes for maximum intensity and proper beam profile, especially at the focal points along the beamline, with the ultimate goal of achieving the best possible beam spot and transported yields at the final target area. Beam intensity is determined by comparing the particle counts from SC's and SWDC's to that from the MW1SEM, which served as the reference counter for testing. This is necessary since the primary proton beam intensity often fluctuates from spill to spill.

PWC's provide the beam profiles used for tuning. These profiles indicate whether beam remains relatively centered in the beampipe after bends, whether quadrupoles are focusing properly, and if beam is lost in the apertures of beamline devices. The two focal points of the MT beamline are at MT3PWC and MT6PWC1. Beam is expected to be unfocused at MT4PWC, which is strictly in the beamline to insure that the beam remains centered and is not lost in apertures between the two focal points. A tight beam spot should not be expected here.

Care must be taken in using MT3PWC and MT6PWC1 because they are at focal points. Tuning of upstream magnets may produce a proper beam spot at the PWC, but the entrance angle at the PWC cannot be determined directly from the readout. An improved beam spot may be attained only at the expense of significant losses downstream since the beam, no longer centered in the beampipe, is obstructed by downstream apertures.

There are as many ways to determine an optimum tune as there are experimenters. Time constraints serve to limit the extent to which they may be carried out. The procedure followed in optimizing the three primary tunes was determined by the beamline physicist and is outlined below.

(1) In all cases the thickest production target was used (0.6" of Pb). First the MT2WU magnet string's current was varied to determine the effect on rates at MT3SC, while maintaining the MT3Q1/Q2 quadrupoles at their nominal values and keeping MT3V turned off. This was basically an exercise in data taking, because for the remainder of the tuning process, the MT2WU magnets were set at the originally calculated nominal current value. This was done since it was believed that the calculated value was correct for selecting the desired central energy. The beam profile at MT3PWC was also checked to insure that no beam was lost in upstream apertures and that the majority of the beam profile actually appeared in the readout, indicating that the beam was relatively centered in the beam pipe.

(2) Rates were maximized at MT4SC by varying the MT3WU string's current in 10 A increments. The MT3Q1/Q2 quadrupoles were set at their nominal current values and MT3V was off. As a check, rates at MT5SWDC1 were also monitored. While no focused profile was expected at MT4PWC, beam profile was checked using the criteria given in (1). The optimum current was determined and set for the remainder of tuning.

(3) Rates were maximized at MT6SC1 by varying the current of the MT5E string in 20 A increments. As a check, rates at MT6SWDC were also monitored. Both pairs of quadrupoles (MT3Q1/Q2 and MT4Q1/Q2) were set at their nominal current values and MT3V was off. The beam profile at MT6PWC1 was checked using the usual criteria. The optimum current value for MT5E was determined and set for the remainder of the tune.

(4) The MT3V current was varied in 10 A increments for each polarity setting, maximizing rates at MT3SC and monitoring rates at MT4SC. The beam profile was checked at MT3PWC, where the beam should be centered vertically as closely

as possible. Optimum current was determined and set.

(5) The MT3Q1/Q2 quadrupoles' current settings were adjusted to maximize rates at MT3SC and MT4SC and to produce the best focus at MT3PWC. Although horizontal spread is expected to be much greater than vertical spread, the goal was to sharpen the profile in both planes and to approximately center the beam on the PWC. The currents of both magnets were adjusted in 2 A increments, with the originally calculated difference in currents between the two magnets maintained. This was done to keep the ratio of currents between the two constant to first order, since this ratio for a doublet was considered crucial in maintaining proper focusing properties. Optimum current settings were determined based on a compromise between maximum rates and optimum beam profile.

(6) The currents of the quadrupoles in the MT4Q1/Q2 doublet were varied to maximize rates at MT6SC1 and MT6SWDC and to produce the best focus at MT6PWC1 using the criteria listed in (5). Magnet currents were altered in 2 or 4 A increments. Again, the ratio between currents was kept relatively constant. For the MT beamline, computer analysis indicated that the MT3Q1/Q2 and MT4Q1/Q2 doublets should have comparable current settings and ratios. However, the MT3Q1/Q2 doublet optimum current settings were found to be 27 A lower than expected for the 245 GeV tune.

(7) Finally, MT5E was tested again, with emphasis on centering the beam profile horizontally. Other dipole strings could have been rechecked as necessary, but only MT3V was quickly retested to maximize rates at MT6SC1 and improve centering of the profile.

(An alternate approach to this tuning method is to leave all quadrupoles off while tuning the dipoles in the sequence given. Then the upstream quadrupole

doublet is tuned, monitoring the rates at MT6SC1 and optimizing beam profile at MT3PWC using the criteria in (5). Finally, the downstream doublet is tuned in a like manner.)

An important point to remember in tuning is that the current setting inputted to the computer is not necessarily the exact current the magnet is set to by the controlling electronics, due to the internal workings of the computer, CAMAC, and the hardware. When differences between the two do occur, they are always the same, so that the recorded input values will reproduce the same tune each time.

A comparison between the original nominal tune and the final experimental tune for 245 GeV secondary hadron transport is made in Table XI. Typical beam profiles at MT3PWC, MT4PWC, and MT6PWC1 are shown in Figure 60. Actual yields at the final target area were found to be within a factor of 2 of those calculated.

Instead of using the nominal tunes determined by TRANSPORT, the beamline physicist decided to simply scale down the optimum experimental 245 GeV tune for 160 and 80 GeV transport using the magnets' excitation curves. These were then taken as the baseline values to be used for experimental optimization of tunes at these energies. Table XI lists these as well.

Because of time constraints, the 160 GeV tune was only optimized with respect to the bending dipoles; all quadrupole currents were left at the calculated nominal values.

The optimum 80 GeV tune, however, was determined following the complete tuning procedure. While testing the MT4Q1/Q2 doublet, it was learned that improved rates and focus were achieved when the current ratio was inverted from the ratio based on nominal values. This was an indication that the polarities of these magnets were actually the reverse of those assumed in all calculations.

TABLE XI. Nominal and experimental current settings for 245, 160, and 80 GeV secondary beam transport.

Magnet	245 GeV		160 GeV		80 GeV	
	Nominal [A]	Exp [A]	Nominal [A]	Exp [A]	Nominal [A]	Exp [A]
MT2WU	1675	1675	959	959	477	465
MT3Q1	87	60	40	40	20	27
MT3Q2	92	65	43	43	22	26.7
MT3V	0	15 (Rev)	10 (Rev)	10 (Rev)	5 (Rev)	5 (Rev)
MT3WU	830	850	567	610	283	290
MT4Q1	96	92	59.5	59.5	29	20
MT4Q2	91	87	57.5	57.5	28.7	22
MT5E	1670	1680	957	1000	478	490

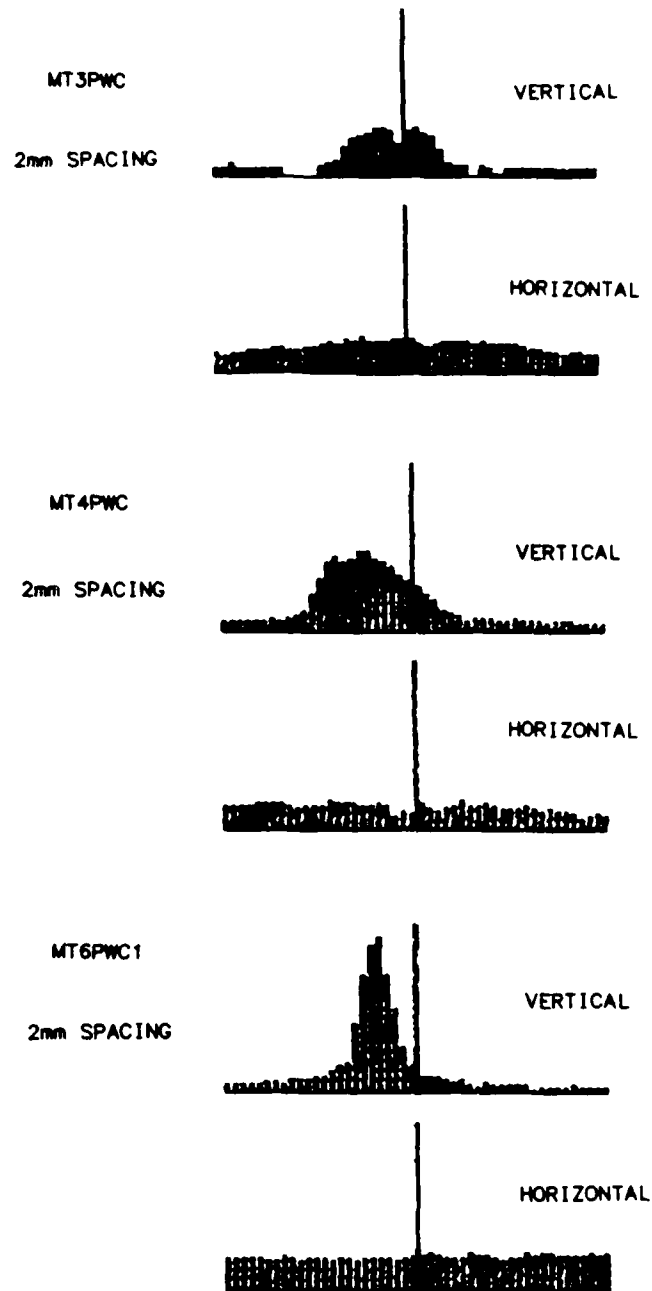


FIG. 60. Beam profiles at MT3PWC, MT4PWC, and MT6PWC1 for the experimental 245 GeV secondary hadron transport tune.

Tunes for intermediate energies were calculated by scaling between experimentally determined optimum tunes at 245, 160, and 80 GeV. There were a number of possible ways to do this, including simply scaling down from the 245 GeV tune and ignoring the other tunes, or by scaling between the 80 and 245 GeV tunes, ignoring the less thoroughly studied 160 GeV tune. The decision was to: (1) scale from the 245 to the 160 GeV tune in 10 GeV increments; in scaling in the nonlinear region of the magnetic excitation curves, these curves were used directly; (2) scale linearly from the 160 to 80 GeV tune in 10 GeV increments; and (3) scale down from the 80 GeV tune linearly in 10 GeV increments to 20 GeV, and then in 5 GeV increments to 5 GeV. Difficulties in this procedure arose from the fact that the MT4Q1, Q2 current ratio went from being greater than 1 to less than 1 at some point and the fact that this procedure created sudden jumps in some magnet values when comparing intermediate tunes just above 160 GeV to those just below. None of these tunes were studied with an eye to experimental optimization.

These intermediate secondary hadron transport tunes were also used as the basis for establishing the tertiary hadron and electron tunes. For the tertiary hadron tunes, current settings from the 245 GeV secondary tune were retained for magnets upstream of MT3TGT1 in order to transport 245 GeV secondary hadron beams to the production target; then current settings for the desired energy to be transported from this target were used for the downstream magnets. For the tertiary electron tunes, tertiary hadron tunes were simply modified by setting the MT3SW magnet, normally off, to its maximum allowed current. (MT3CON1 would be used as a converter just downstream of this sweeper magnet to produce electrons for further transport.)

The exact central energy, as well as the actual energy spread, for all these

tunes has yet to be determined. The momentum tagging system is the only means available to experimentally find these values.

B. Experimental Yields

Besides developing tunes, the most significant goal of the preliminary beamline studies was to determine the yields for these tunes at the final CDF target area over the full range of energies (10 to 245 GeV) for the available modes of operation (secondary hadron, tertiary hadron, and tertiary electron transport).

Yield studies demonstrated that the MT beamline is a very *flexible* beamline, able to transport useful rates to the final target area at least over the energy range 20 to 245 GeV for secondary hadron support, 10 to 140 GeV for tertiary hadron transport (higher energies are possible, but were not studied), and 10 to 220 GeV for tertiary electron transport.

Flexibility is further demonstrated by the fact that significant yields of secondary hadrons are produced over a wide range of energies when using any of the three MT2TGT-series targets in the MW2WD2 string. This string allows a wide range of energies to escape the final aperture, although almost certainly many of the particles making up the emerging beam are created by interactions inside the magnets themselves. Note that the 80 GeV target, MT2TGT3, placed just before the last magnet in the string, allows transport of the full range of energies from 20 to 245 GeV. This is not surprising, since particles must only escape the apertures of the very last magnet.

The significant uncertainty in this yield data is in the actual composition of the transported beams, due to the lack of tagging devices in the beamline during the studies. This is particularly important in the case of the tertiary electron mode,

where yields are already quite low. Even the presence of the MT4CON electron absorber, not available at the time, would have given an indication of the fraction of electrons actually in these beams.

The yield curves (based on counts per spill from the MTSC46 coincidence compared to those from the MW1SEM) for secondary hadron transport are plotted in Figure 61. Curves are shown for production off of each of the three targets, MT2TGT1, 2, and 3. In each case, the thickest (0.6") Pb target was used.

Figure 61 shows that the maximum yield using the so-called 245 GeV target actually occurs at 230 GeV, rather than at 245 GeV. Likewise, the so-called 160 GeV target produces a maximum yield at 150 GeV, instead of at 160 GeV. This is expected, since the requirement to adjust the MW2WD2 current settings to transport an 800 GeV, rather than a 900 GeV, primary proton beam would select correspondingly lower central energies. Figure 61 shows the energies which will be produced at rates of 20,000 particles/spill or more in the case of 5×10^{11} incident primary protons/spill at the production targets.

The yield curve for tertiary hadron production off of the MT3TGT1 target is plotted versus energy in Figure 62. The 245 GeV secondary hadron beam was transported to the thickest (0.3") Pb production target. It is significant that production rates at the lower end of the energy range are no better than the extrapolated values for secondary hadron transport at these energies. Improved production rates at the lower energy end may be possible if lower energy secondary hadron beams, instead of the 245 GeV beam, were delivered to MT3TGT1.

The tertiary electron beam yield curve versus energy is also plotted in Figure 62. Again, the 245 GeV secondary hadron beam was incident on MT3TGT1's thickest (0.3") Pb target. The thickest (0.3") Pb target in the MT3CON1 converter was

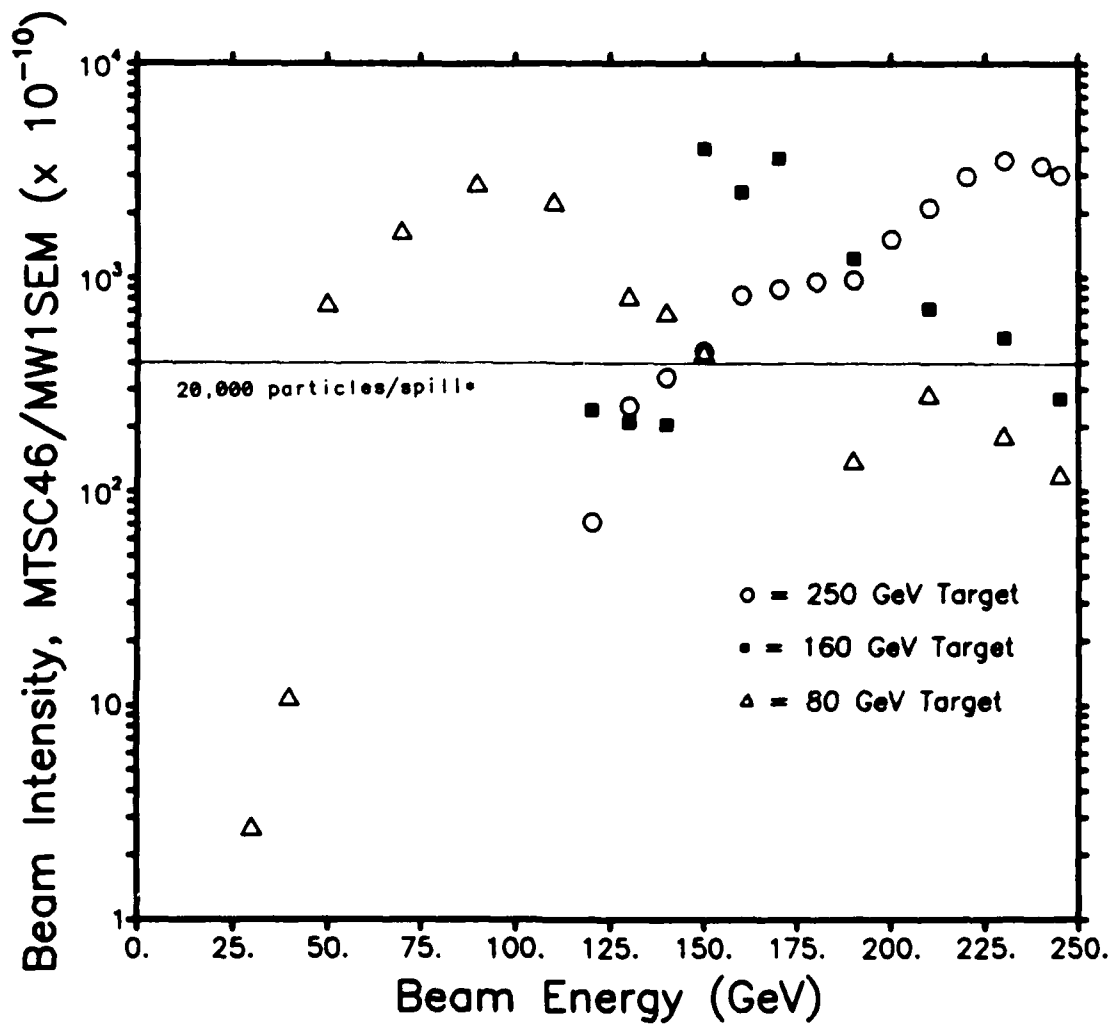


FIG. 61. Normalized experimental yields vs. beam energy for secondary hadron transport. A minimum of 20,000 particles per spill reaching the CDF target area for 5×10^{11} primary protons per spill is marked by a line in the figure.

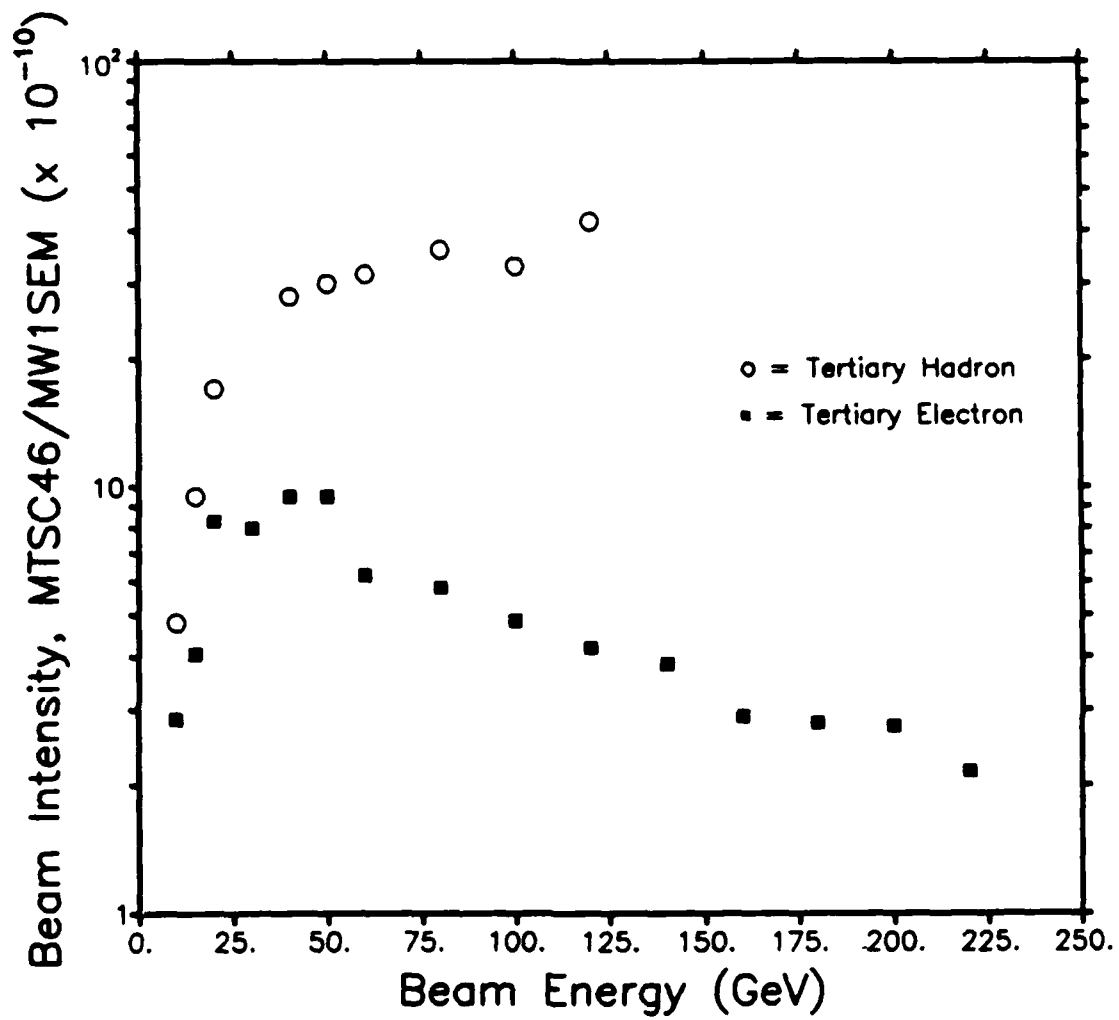


FIG. 62. Normalized experimental yields vs. beam energy for tertiary hadron and electron transport.

used. While the 0.3" Pb target in the converter is nearly the optimum length for Pb when used as a converter, the 0.3" production target in MT3TGT1 may not be of optimum length (due to early conversion of high energy photons in the target). Only further studies with other thicknesses will determine this. Again, contamination studies are crucial because of low production rates.

C. Contamination Studies

Contamination studies would reveal the number of hadrons, electrons, and muons in the beam for various modes of operation at selected energies. This is particularly important in the case of electron transport, where production rates are very low.

Electrons could be detected using one of the beamline electron tagging devices, the *threshold Čerenkov counter* and the synchrotron radiation detector, or by using the Central Electromagnetic Strip chambers mounted on the wedge fixture in the final target area. These CES chambers are well understood detectors with excellent resolution and rejection rates. Unfortunately, none of these devices were operational during the preliminary beamline studies. The electron killer, MT4CON, which would at least have provided an indication of electron beam purity, was installed after these studies were completed.

The muon trigger created with the addition of strategically placed scintillation counters in the CDF target area allowed for determination of muon contamination in the secondary hadron beam for certain energy tunes. Percent muon contamination is plotted in Figure 63.

Fraction of muons in the secondary hadron beams was determined by comparing the rates from the coincidence of MT6SC1, 2, 3, "no-V," and MU compared to

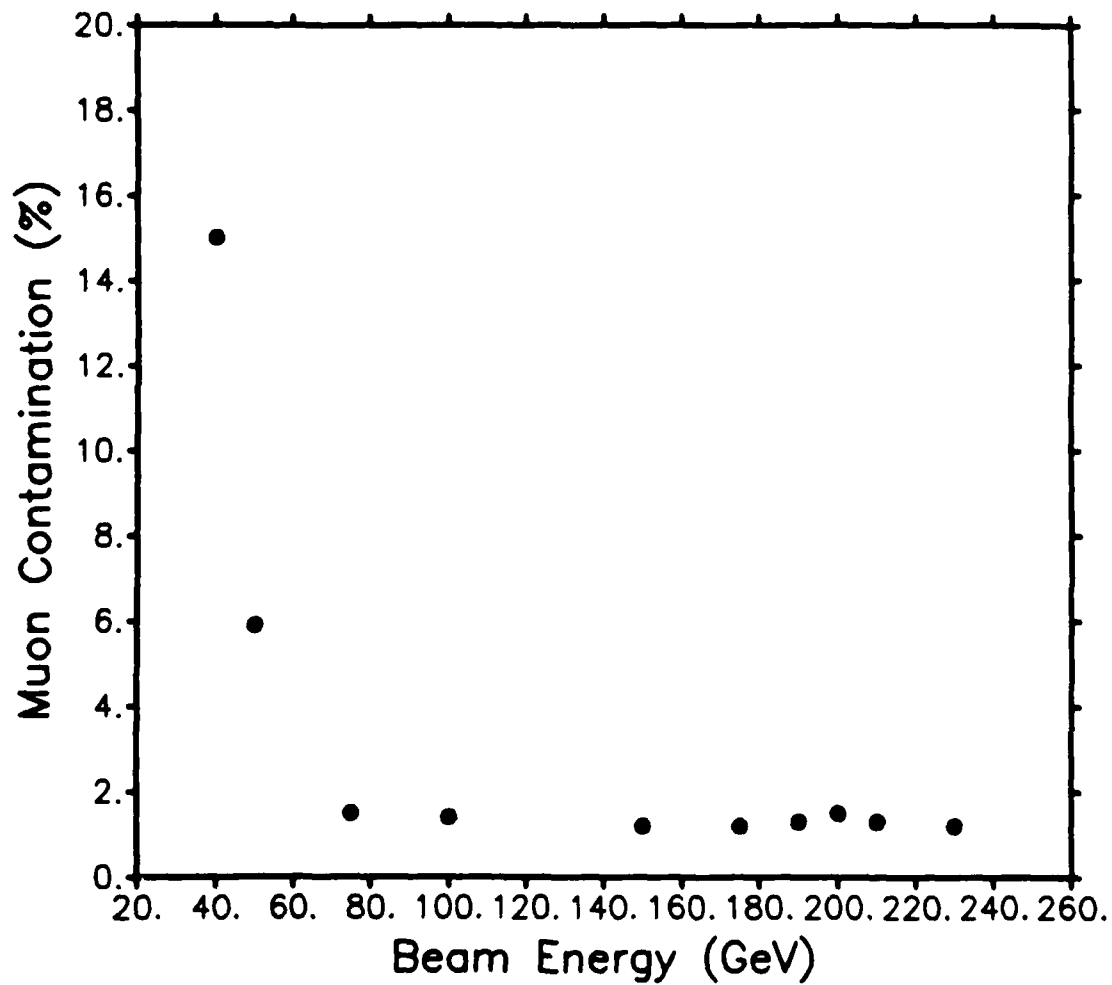


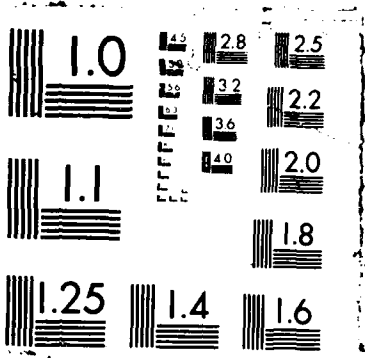
FIG. 63. Percent muon contamination vs. beam energy for secondary hadron transport.

those from the coincidence of MT6SC1, 2, 3, and "no-V;" data was taken when the MT6BS1 beam stop was closed. While most scintillation counters are operating at better than 99% efficiency, MT6SCMU, placed behind the MT6BS1 beam stop, is only operating at 96% efficiency. This produces little error in the results. Because muons lose about 1 GeV in energy while traveling through 1 m of steel, the 9' thick beam stop would absorb muons of 3 GeV energy or lower. The total fraction of muons with these energies reaching the beam stop is undoubtedly small.

D. Updated Computer Analysis

Preliminary beamline studies were conducted based on nominal tunes determined by computer analysis to transport 245, 160, and 80 GeV secondary hadron beams. The original computer analysis found these to be the maximum yield energies for production and transport off of the MT2TGT1, 2, and 3 targets, respectively, and all analysis with TRANSPORT used each of these energies as the central energy of the central trajectory ray. But this analysis assumed that 900 GeV energy primary protons were incident on the MT targets and were also to be transported down the MW beamline.

In reality, 800 GeV energy protons are delivered to the MW2WD1 target; the current settings for these magnets had to be reduced to transport the protons down the MW beamline. These magnets have magnetic field strengths that are lower than those of the MW2WD2 magnets. We cannot adjust MW2WD2 magnets to transport 800 GeV protons as constraints when the MW2WD1 magnets are set to transport 800 GeV protons. The MW2WD2 magnets are set to transport 800 GeV protons and the MW2WD1 magnets are set to transport 800 GeV protons.



TRANSPORT carries out calculations based on the concept of the central trajectory, with a given central energy, so that tunes developed to transport an assumed central energy that is in reality not the central energy leaving the magnet string will not be the optimum tune for the assumed energy. For example, the calculated tune to deliver 245 GeV secondary beams actually would deliver 245 GeV particles (as long as the MW2WD2 string allowed particles of this energy through its apertures), but this tune does not allow for the maximum possible intensity to be transported to the final target area. Since all other tunes were eventually scaled from this one, all tunes, while still able to transport desired energies, are not the best ones possible. (Remember also that the original calculations were made assuming incorrect polarities for the MT4Q1/Q1 quadrupoles.)

For this reason, it was decided to recalculate the three primary tunes at the correct central energies of 227, 151, and 75 GeV. TRANSPORT was applied to determine nominal magnet field strengths and gradients (converted to current settings using excitation curves), and TURTLE was then used to calculate initial phase space acceptance, particle production and transport rates, and expected beam profiles and momentum spreads reaching the final target area.

The nominal tunes for the three correct central energies are listed in Table XII. Ultimately, these values will be used as the baseline to experimentally develop optimum tunes for the three energies. Intermediate tunes will then be found by scaling.

A comparison of the values in Table XII to those listed in Table XI for the three original energies shows that these values are relatively close, as should be expected. The greatest differences are in the current settings for the MT3WU string and for the MT4Q1/Q2 quadrupoles; the differences in quadrupole settings are probably

TABLE XII. Calculated magnetic fields and current settings for 227, 151, and 75 GeV secondary hadron beam transport.

Magnet	227 GeV		151 GeV		75 GeV	
	B ^a	I [A]	B ^a	I [A]	B ^a	I [A]
MT2WU	13.97	1457	9.31	889.2	4.66	444.7
MT3Q1	4.02	78.97	2.68	51.32	1.36	26.04
MT3Q2	-4.32	85.05	-2.88	55.15	-1.45	27.77
MT3WU	8.10	773.0	5.40	515.7	2.70	257.8
MT4Q1	-4.10	80.5	-2.74	52.47	-1.36	26.04
MT4Q2	4.01	79.0	2.69	51.51	1.33	25.47
MT5E	13.90	1445	9.26	884.6	4.63	442.3

- a. For dipole magnets, magnetic field strength is given in units of kG ; for quadrupole magnets, the magnetic field gradient is given in units of kG/in .

due more to the correction in magnet polarities than because of the new central energies. This suggests that the original tunes developed are still quite useful until time is available to find the optimum tunes, and that other results from updated computer analysis, such as production rates, will not be significantly different from earlier results.

Pion, proton, and kaon production rates for the secondary hadron tunes with central energies of 227, 151, and 75 GeV were calculated using TURTLE with the particle production package developed by Malensek. These hadron yields were determined in particles per spill reaching MT3TGT1, the tertiary beam production target, and reaching MT6PWC1, just before the CDF target area. These calculations assumed 5×10^{11} 800 GeV primary protons per spill incident on the thickest (0.6") Pb target at MT2TGT1, 2, and 3, respectively. TURTLE calculates the number of particles by type leaving the production target per interacting proton incident on a Be target of the desired thickness, and also determines the fraction of particles reaching designated points along the beamline. To compute the beam intensity for a given particle reaching one of these points, the following formula is used: (number of primary protons per spill incident on the production target) \times (fraction of produced particles actually transported by the beamline to the point) \times (the efficiency f of the target) \times (Malensek's correction factor for Pb as compared to Be).

Hadron yields at MT3PWC and at the CDF target area for 5×10^{11} incident primary protons per spill for the three primary energies are plotted in Figures 64 and 65, respectively. These curves give a rough indication of the yields to be expected for intermediate energies.

TRANSPORT calculates transfer matrix elements R_{ij} at designated points

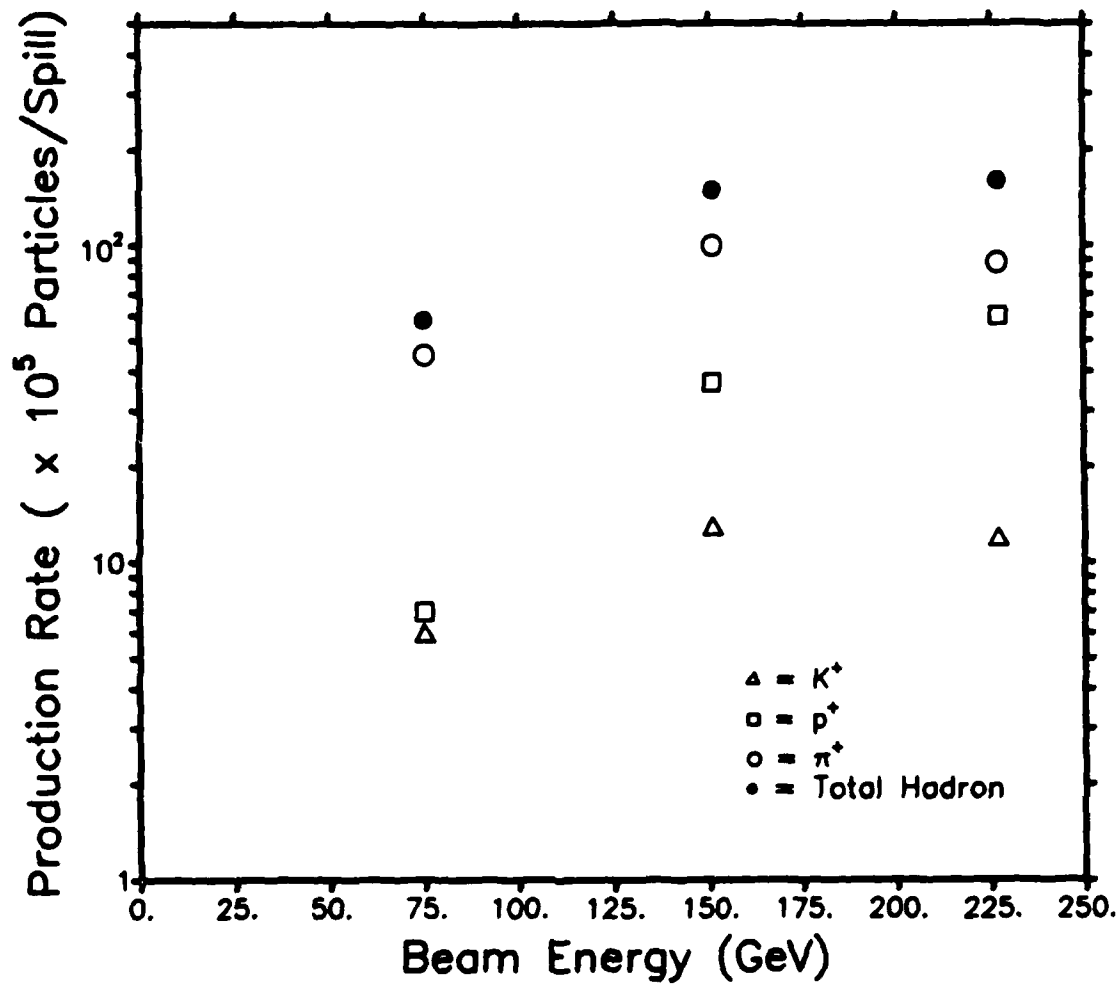


FIG. 64. Computed yields by particle type at MT3PWC for secondary hadron transport at 227, 151, and 75 GeV.

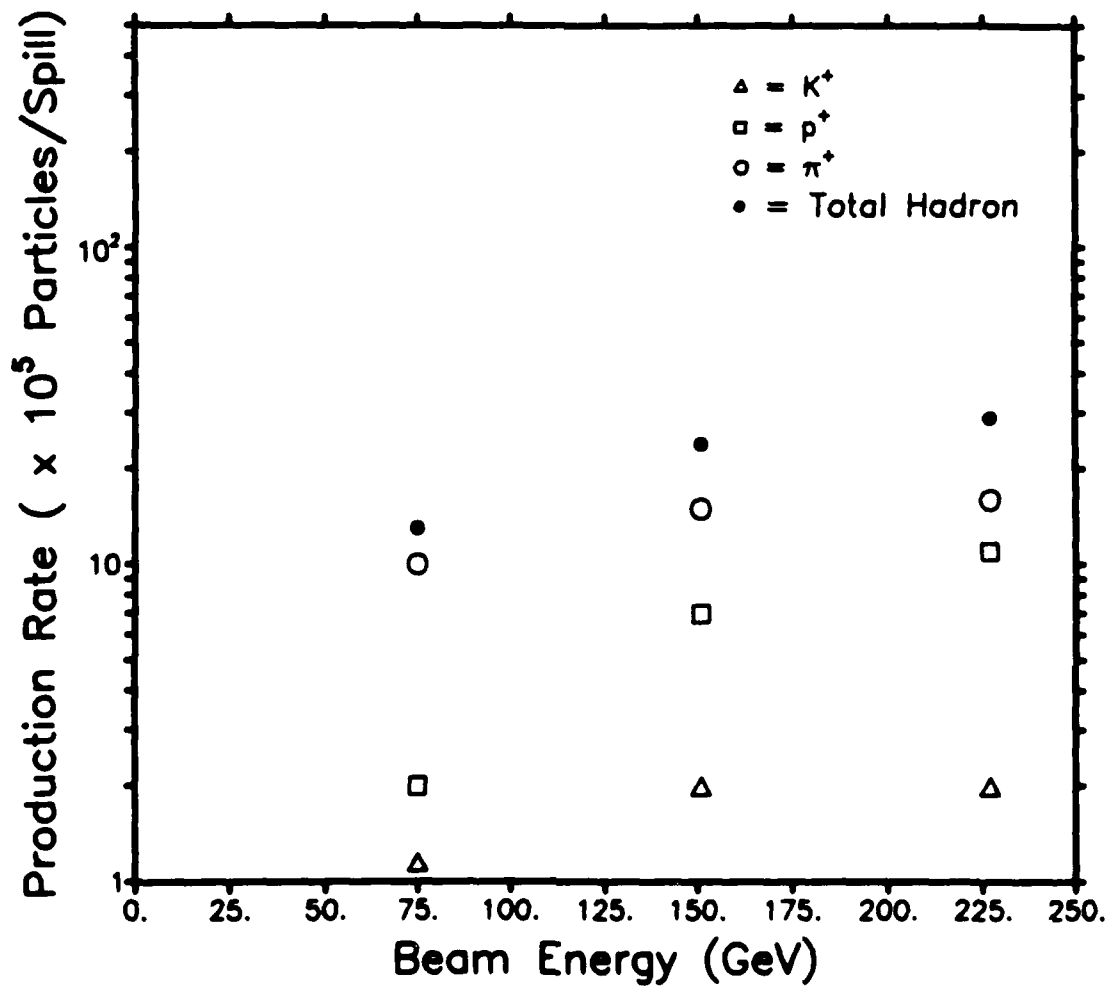


FIG. 65. Computed yields by particle type at MT6PWC1 for secondary hadron transport at 227, 151, and 75 GeV.

along the beamline. As discussed earlier, certain matrix elements have a direct physical meaning in regard to beamline transport characteristics. R_{11} and R_{33} indicate spatial magnification in the horizontal and vertical planes, respectively, and equal the image magnification M_x and M_y , respectively, at focal points. R_{12} and R_{34} indicate the angular magnification, or focusing properties, of the beamline in the horizontal and vertical planes, respectively. R_{16} gives the fractional momentum spread $\delta = \Delta p/p$. Because the magnetic midplanes of the magnets in the MT beamline are not all in the horizontal plane (due to the rolling of some dipoles), calculated matrix elements R_{ij} reflect correlation between the x and y planes. However, Carey has developed a computer package that removes this correlation between the matrix elements, so that values can be determined which directly relate only to the horizontal and vertical planes.

Figures 66, 67, and 68 respectively plot R_{12} , R_{34} , and $|R_{16}| = \Delta p/p$ versus longitudinal distance z along the beamline for 227 secondary beam transport, using uncorrelated matrix element values; for comparison, the location of magnets and collimators is also indicated in the figures. A comparison of these values with those matrix elements found for the 151 and 80 GeV tunes show only minute differences. This is expected, since these two tunes use magnetic field strengths which to first order are scaled down from those in the 227 GeV tune. Only the apertures in the beamline are not scaled down accordingly, but since TRANSPORT ignores apertures in its calculations, this does not matter. Differences mainly are the result of the fact that the lower energy tunes each use a production target which is 12' farther downstream from the next.

The initial phase space acceptance in (x, x', y, y', δ) at the MT2TGT-series targets as calculated by TURTLE for each corresponding primary energy is listed

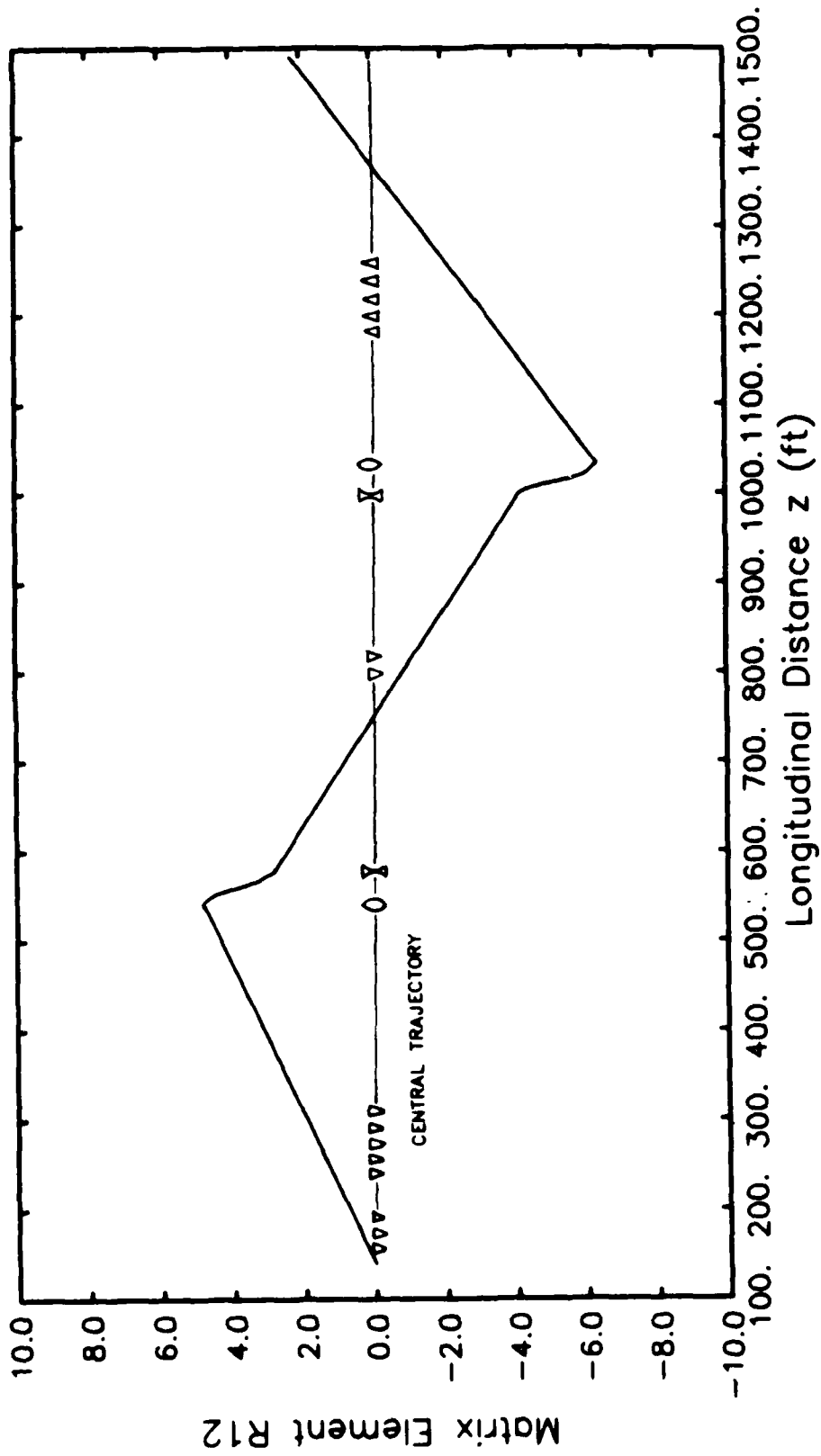


FIG. 66. Computed transfer matrix element R_{12} vs. longitudinal distance z along the MT beamline.

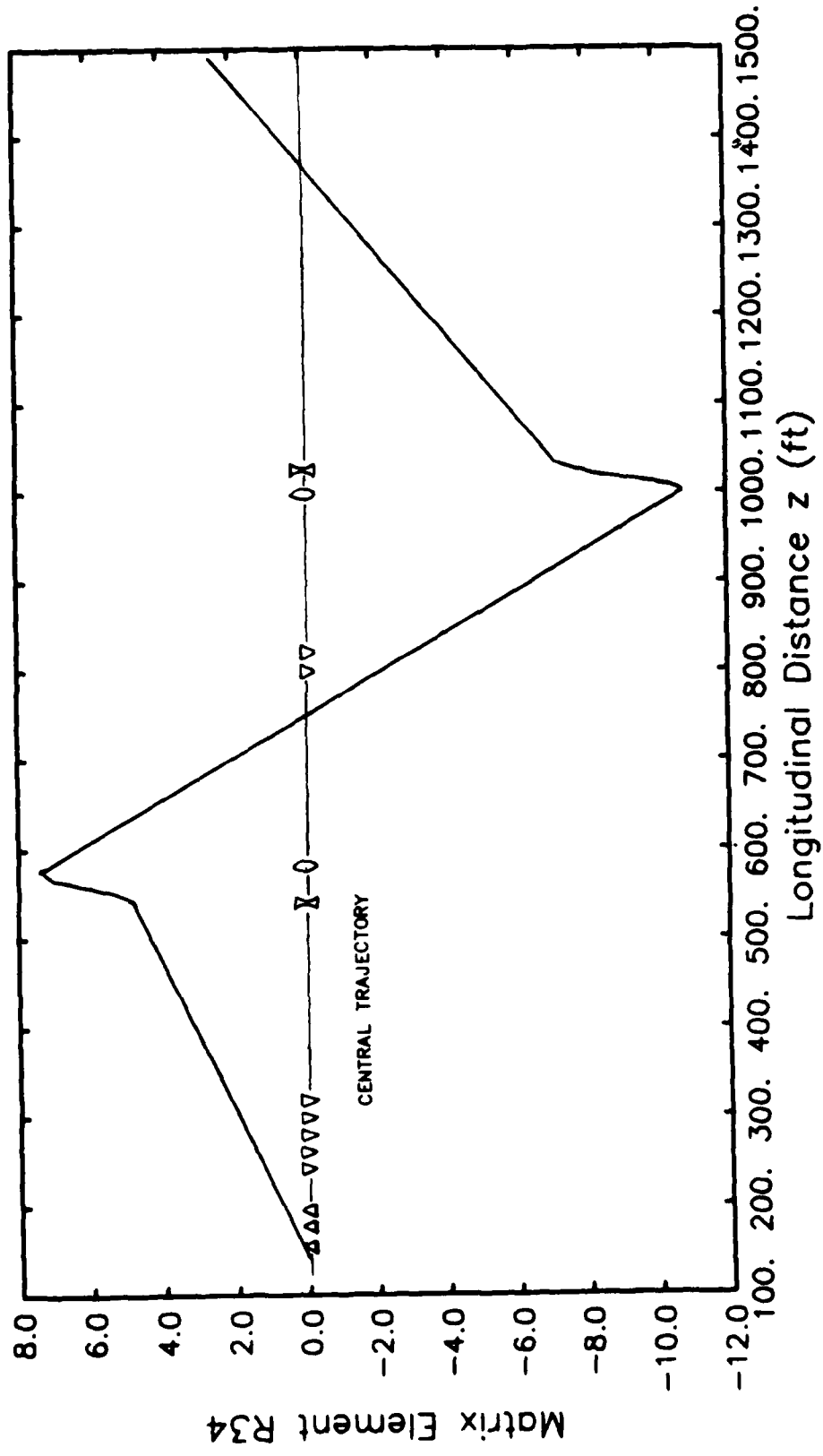


FIG. 67. Computed transfer matrix element R_{34} vs. longitudinal distance z along the MT beamline.

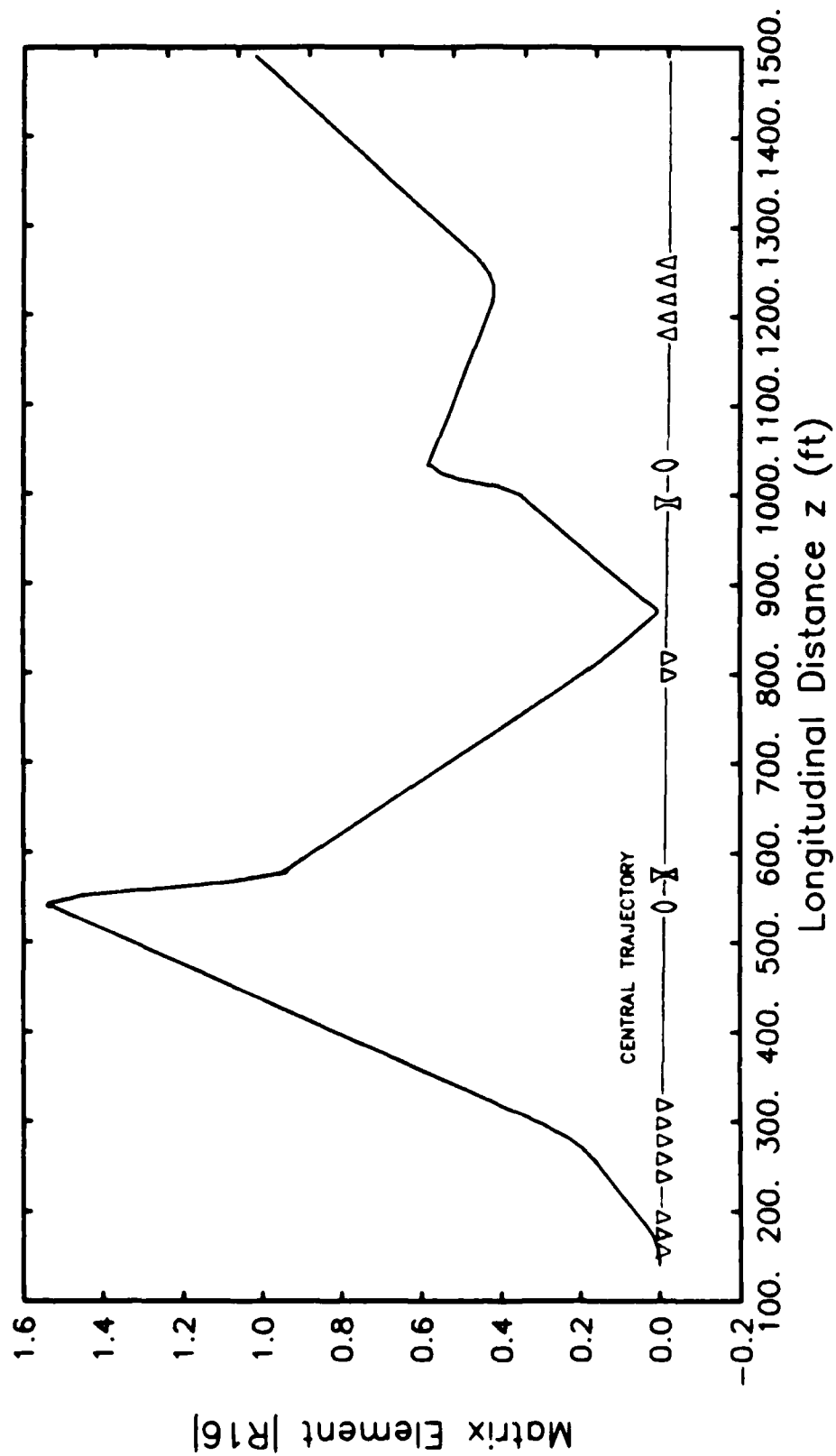


FIG. 68. Computed transfer matrix element $|R_{16}| = |\Delta p/p|$ vs. longitudinal distance z along the MT beamline.

in Table XIII.

TURTLE also determined the beam profile in the horizontal and vertical planes, the momentum distribution in the horizontal plane, and the total momentum spread at the final target area for the three secondary beam tunes. The beam's final spatial extent in x and y and the momentum spread for the three primary energies are listed in Table XIV. The greater spread in the horizontal plane is clearly illustrated. Values for spatial extent can be used as benchmarks during experimental tuning. Until momentum studies are conducted, calculated momentum spreads are relied upon totally.

To better illustrate the beam characteristics at the final target area for the 227 GeV secondary hadron transport tune, Appendix D includes a full set of histograms produced by TURTLE. These histograms include (1) particle distribution versus the horizontal coordinate x , (2) particle distribution versus the vertical coordinate y , (3) particle density in the x - y plane, (4) momentum versus x , and (5) particle distribution over momentum values.

A very preliminary tune optimization for the new 227 GeV secondary hadron transport tune was carried out by adjusting several of the calculated nominal values. A comparison of these current values is made in Table XV, and Figure 69 shows the beam profiles at MT3PWC, MT4PWC, and MT6PWC1. Beam intensity was 40% of the calculated value.

TABLE XIII. Calculated initial phase space acceptance at the MT2TGT-series targets for secondary beam transport.

	MT2TGT1 227 GeV	MT2TGT2 151 GeV	MT2TGT3 75 GeV
Δx [in]	1.1	1.1	1.1
$\Delta x'$ [mrad]	1.8	1.8	1.2
Δy [in]	1.3	1.2	1.2
$\Delta y'$ [mrad]	0.4	0.4	0.4
$\Delta p/p$ [%]	5.0	5.0	5.0

TABLE XIV. Calculated 227, 151, and 75 GeV secondary hadron beam dimensions at the CDF wedge fixture. All values are FWHM.

Energy	Δx [in]	Δy [in]	Δp [GeV/c]	$\Delta p/p$ [%]
227 GeV	2.2	0.8	10	4.4
151 GeV	2.7	0.8	7	4.6
75 GeV	2.9	1.0	4	5.3

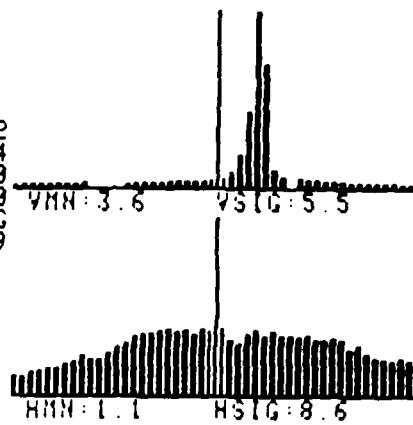
TABLE XV. A preliminary experimental tune for 227 GeV secondary hadron transport.

Magnet	Magnet Currents [A]	
	Nominal	Exp
MW2WD2	735	756
MT2WU	1457	1461.8
MT3Q1	79	78
MT3Q2	85	83
MT3V	-	100 (Rev)
MT3WU	773	760
MT4Q1	80.5	74
MT4Q2	79	76
MT5E	1445	1465

MT3PWC 2 MM

STORE MODE

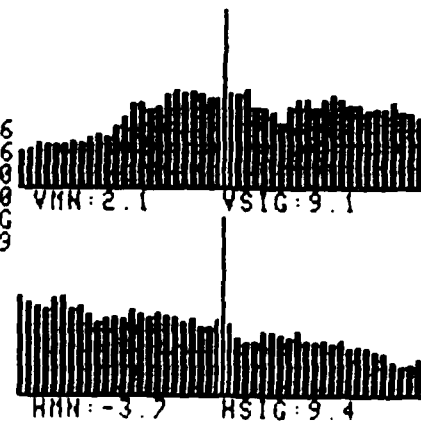
1	VGAIN	32
2	HGAIN	64
3	HOLD	64/60
4	CHARGE	64/60
5	POLARITY	NEG
6	SCANS	9



MT4PWC 2 MM

STORE MODE

1	VGAIN	16
2	HGAIN	16
3	HOLD	64/60
4	CHARGE	64/60
5	POLARITY	NEG
6	SCANS	9



MT6PWC1 2 MM

STORE MODE

1	VGAIN	512
2	HGAIN	1024
3	HOLD	64/60
4	CHARGE	64/60
5	POLARITY	NEG
6	SCANS	10

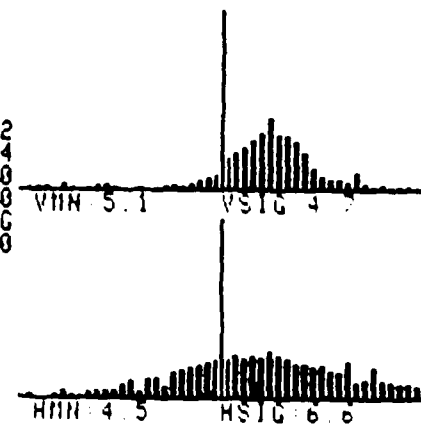


FIG. 69. Beam profiles at MT3PWC, MT4PWC, and MT6PWC1 for the experimental tune for 227 GeV secondary hadron transport.

CHAPTER IX

SUMMARY

The CDF test beam facility at the Meson Test site is operational and tests will be conducted on detector components during the Fall 1987 fixed-target run. This was made possible by the contributions of many individuals in the CDF collaboration. My part in preparing the CDF test beam facility for operation included: (1) assisting in the design and construction of the test beam facility gas delivery system, and (2) conducting preliminary studies of the MT beamline and its components to understand capabilities and limitations in meeting CDF beam requirements.

The test beam gas delivery system is complete and functioning. The final design incorporated all requirements to insure that the delivery system is flexible enough to provide support to all components during the Fall 1987 run and in the future. The gas delivery system actually surpasses the original expectations of CDF test beam facility planners. It can deliver several different gas mixtures simultaneously, with all necessary controls located outside the controlled-access fence. Storage of large amounts of gas mixtures on-site reduces downtime otherwise required by frequent supply changes and assures that the composition of mixtures remains uniform for long periods of time. An exact duplicate of the gas quality monitoring system in the CDF collision hall is operational at the test beam facility. A gas pressure buffer system for both the forward hadron and forward electromagnetic calorimeters is mounted on the forward fixture, reducing the risk of chamber damage and allowing for the testing of improved components to the buffer system because of the ease in access. All safety requirements have been met, including continuous monitoring for

ethane leaks while the gas is in calorimeter chambers.

The preliminary beamline studies have provided a solid understanding of the general operation and capabilities of the MT beamline, despite constraints in equipment availability and operational beam time. A vast amount of detailed information was not expected nor would have been realistic.

The most significant finding was that the MT beamline has a great deal of inherent flexibility. This was not altogether expected by the beamline physicists. The MT beamline will produce and transport required beam intensities to the CDF target area for several modes of operation (secondary hadron, tertiary hadron, and tertiary electron) over a wide range of energies, although exact composition of the beam in these modes is only partly known at this time.

With knowledge of the configuration, capabilities, and limitations of the MT beamline, the originally requested CDF beamline parameters listed in Chapter IV are reviewed to determine the ability of the MT beamline to meet these parameters. Repeating these parameters:

(1) *Supply hadron and electron beams from 1 to 300 GeV energy.* The maximum safe operating currents for the MT2WU and MT5E magnet strings limit the MT tune for secondary beams to about 245 GeV. Computer analysis gives a momentum bite at this energy of $\pm 2.5\%$, so that the maximum expected momentum will not be over 255 GeV, although rates for this momentum will be quite low. If analysis of the secondary electron mode of operation proves this to be an effective method to produce electrons, then electrons with energies up to 245 GeV can also be expected with useful production rates. Tertiary production of hadrons and electrons from an incident 245 GeV secondary hadron beam on MT3TGT1 will produce useful rates from 10 to 245 GeV. Extrapolation of data assuming a primary proton

beam intensity of 5×10^{11} particles per spill suggests that useful rates can be achieved down to energies of 5 GeV. The very low energy end of the requested scale cannot be achieved without the maximum primary proton intensity of 1×10^{12} particles per spill. The possibility of achieving higher tertiary beam yields using lower energy secondary hadron beams incident on MT3TGT1 has not been tested, nor has the effect of tertiary production target and converter thickness been investigated satisfactorily. Finally, the actual composition of hadron and electron beams has not been determined at this time.

Flexibility of the MT beamline to produce a wide range of particle beam energies has been demonstrated.

(2) *Particle identification of hadrons and electrons to an accuracy better than 0.05%.* This accuracy in particle identification is necessary in order to study the rejection rates of the calorimeters, which in some cases are already known to be better than 1×10^{-3} . Since the beam itself cannot be made "pure" in hadron or electron content to the required level of 1/2000 impurities, it is necessary to employ particle-tagging devices in the beamline. To this end the MT beamline includes a threshold Čerenkov counter and a synchrotron radiation detector, both of which will normally be used to identify electrons. They may be put in coincidence for this purpose. Due to delays in installing necessary equipment to make both these devices and the CDF test beam data acquisition system operational, neither device has been studied at all at this time.

(3) *Provide a muon beam.* A muon beam *per se* is not produced by a beamline; muons are a product of the decay of pions and kaons created at production targets and by beam interactions with other matter along the beamline. Muons make up at least 1% of secondary hadron beams, which is satisfactory for CDF requirements.

In the MT beamline, muons are identified using the signals from a coincidence of scintillation counters just upstream of the CDF target area and a counter placed behind the MT6BS1 beam stop just downstream of the target area. With the beam stop closed, it is assumed that only muons of energies of 3 GeV or greater will penetrate the beam stop to reach the downstream counter (MT6SCMU). The CDF data acquisition system trigger logic insures that false muon triggers are rarely initiated. Once electron tagging systems are in place, this same trigger logic will rarely produce false electron triggers. The greatest opportunity for improper identification of particles can be expected for hadrons, which are tagged by a no-electron, no-muon trigger. With the reliance on the MT6SCMU scintillation counter, which currently has a 96% operating efficiency, muons will occasionally be tagged as hadrons.

(4) *A momentum tagging system that can determine the momentum of each particle to an accuracy better than 0.3%. Accurate knowledge of particle momentum is crucial to any response study of the calorimeters. Instead of using an analyzing magnet whose excitation curve (magnetic field strength versus current setting) is already known to great accuracy, the MT beamline momentum tagging system will rely on the MT5E horizontally-bending dipole magnet string. These are the final magnets in the string, so that momentum values determined at their location will reflect those at the target area. Because these magnets only bend horizontally, error in calculations are reduced. Instead of using beam PWC's, for the first time single wire drift chambers of a special design will be used to determine the position of each particle with a high degree of resolution. These chambers will be used in pairs upstream and downstream of MT5E. The distance between chambers in each pair is large enough to reduce the effect of inaccuracies in the longitudinal*

coordinate z . During the first run the current supplied to the MT5E string will be accurately measured by a precision shunt and recorded by the data acquisition system. Following the first run, a detailed study will be conducted to determine the string's excitation curves to the necessary accuracy.

(5) *Less than 20,000 particles but more than 20 particles per spill over the entire energy range.* The maximum allowed beam intensity is determined by the dead time of the front-end data acquisition electronics (about $3.5 \mu\text{sec}$). Intensities above 1000 particles/sec in a 20 sec spill increase the probability of two particles reaching the target area within the dead-time period of the electronics. In the case of secondary hadron beams, collimators must be used to reduce beam intensity reaching the CDF target area over a large part of the energy range from 10 to 245 GeV, depending on the exact intensity of the primary proton beam reaching the production targets. However, rates are so low in the range of 1 to 5 GeV for all modes of operation that optimum tunes must be developed to transport enough particles to the final target area, even with the highest primary proton beam intensities. Exact rates of production are not currently known since the electron-tagging devices are not available. In particular, the electron beam may include a large fraction of other particles, further reducing electron yields per spill reaching the target area. The secondary electron production mode has not been studied at all, so that rates from this mode are unknown.

REFERENCES

1. Y. Asano et al., "Design Report for the Fermilab Collider Detector Facility (CDF)," Fermilab CDF Note 111 (1981).
2. M. Eaton, "Status of CDF," Fermilab CDF Note 487 (1986).
3. R. Schwitters, "A Primer on y - ϕ Space," Fermilab Internal Memo (Apr 1987).
4. F. Abe et al., "CDF Calorimetry," Fermilab CDF Note 515 (1987).
5. F. Abe et al., "The Collider Detector at Fermilab," submitted to Nucl. Instr. and Meth. (1987).
6. D. Theriot, "The Collider Detector at Fermilab - A Progress Report," Fermilab CDF Note 330 (1985).
7. J. Buchholz, S. Cihangir, F. Marchetto, T. Meyer, and R. Webb, "Performance Test of the Forward, Backward Hadron Calorimeter," Fermilab CDF Note 352 (1985).
8. C. Fabjan and T. Ludlam, "Calorimetry in High Energy Physics," CERN-EP/82-37 (1982).
9. F. Sauli, "Principles of Operation of Multi-Wire Proportional Chambers and Drift Chambers," CERN-77-09 (1977).
10. M. Atac, "Wire Chamber Aging and Wire Material," Fermilab CDF Note 467 (1986).
11. M. Atac, "Wire Chamber Aging," Fermilab CDF Note 392 (1986).
12. S. Cihangir et al., "The Forward/Backward Hadron Calorimeter," submitted to Nucl. Instr. and Meth. (1987).
13. S. Cihangir et al., "Energy Corrections and Cluster Separation Capability Studies Applied to the Forward Backward Hadron Calorimeters," Fermilab CDF Note 370 (1985).

14. M. Atac, S. Cihangir, T. Hessing, and R. Webb, "Testing Isopropyl Alcohol for the CDF Gas Calorimetry." Fermilab CDF Note 477 (1986).
15. J.W. Cooper, Internal Fermilab Memo (11 Dec 1985).
16. J.W. Cooper, Internal Fermilab Memo (27 Nov 1985).
17. J. Bensinger et al., "An Electromagnetic Calorimeter for the Small Angle Region of the Collider Detector at Fermilab." Fermilab CDF Note 490 (1985).
18. J. O'Meara, "Argon Ethane Gas Plumes." Fermilab CDF Note 495 (1986).
19. L. Coulson et al., "Storage and Use of Flammable Gases at Physics Experiments." Fermilab SD-45 (1987).
20. J.W. Cooper, "CDF Gas System in the MT Test Beam." Internal Fermilab Memo (13 Jul 1987).
21. D. Johnson, L. Spires, R. Zimmermann, and A. Nallenweg, "Experimental Areas Beamline Control System Operator's Guide" (2d Rev.), Fermilab Publication (unpublished) (1987).
22. M. Bodnarczuk, "Experimental Areas Guide to CAMAC and Beamline Transport Devices" (2d Ed.) Fermilab Publication (unpublished) (1983).
23. M. Bodnarczuk, "Experimental Areas Operations Training Manual for New Employees" (3d Ed.), Fermilab Publication (unpublished) (1985).
24. S. Butala, "Meson Test Run Conditions." Internal Fermilab Memo (3 Sep 1987).
25. H.W. Atherton et al., "Precise Measurements of Particle Production by 400 GeV/c Protons on Beryllium Targets." CERN 80-07 (1980).
26. D.C. Carey, *The Optics of Charged Particle Beams*, Harwood Academic Publishers, New York, 1987, pp. 1-10, 21, 31-32.
27. K.L. Brown, F. Rothacker, D.C. Carey, and C. Iselm, "TRANSPORT Ap

- pendix." Fermilab PM-0008 (1977).
28. E.C. Sedman, "Design of Beam Transport Systems," MPS Internal Report 62-23 (1962).
 29. K.L. Brown, "A First- and Second-Order Matrix Theory for the Design of Beam Transport Systems and Charged Particle Spectrometers," SLAC-75 (1967).
 30. K.L. Brown, F. Rothacker, D.C. Carey, and C. Iselin, "TRANSPORT A Computer Program for Designing Charged Particle Beam Transport System," CERN-80-04 (1980).
 31. D.C. Carey, "New Features in TRANSPORT," Fermilab TM-1064 (1981).
 32. D.C. Carey, K.L. Brown, and C. Iselin, "DECAY TURTLE (Trace Unlimited Rays Through Lumped Elements), a Computer Program for Simulating Charged Particle Beam Transport Systems, including Decay Calculations," SLAC-246 (1982).
 33. A.J. Malensek, "Empirical Formula for Thick Target Particle Production," Fermilab FN-341 (1981).
 34. A.J. Malensek, "Addendum to Empirical Formula for Thick Target Particle Production," Fermilab FN-341A (1982).
 35. A.S. Carroll et al., Phys. Letters **80B**, 319 (1979).
 36. A.E. Brenner et al., Phys. Rev. D **26**, 1497 (1982).
 37. D.H. Perkins, *Introduction to High Energy Physics*, 3d Ed., Addison-Wesley, London, 1987, pp. 16, 48.
 38. D. Luckey, "Tagging Counters for Electrons in the 100 GeV Range," Fermilab TM 49 (1968).
 39. T. Tooling, "Fermilab Magnets, Power Supplies, and Auxiliary Devices: Technical Data," Fermilab TM-632 (1975).

40. H. Fenker, "A Standard Beam PWC for Fermilab," Fermilab TM-1179 (1983).
41. B. Higgins, "User's Manual for Microprocessor-Based SWIC Scanners," Fermilab TM-868 (1979).
42. J. Krider, "Single Wire Drift Chamber Design," Fermilab TM-1455 (1987).

APPENDIX A

THE CDF COLLABORATION

(As of Sep 1987)

F. Abe^o, D. Amidei^o, G. Apollinari^o, G. Ascoli^o, M. Atac^o, P. Auchincloss^o,
 A.R. Baden^o, A. Barbaro-Galtieri^o, V. Barnes^o, E. Barsotti^o, F. Bedeschi^o,
 S. Belforte^o, G. Bellettini^o, J. Bellinger^o, J. Bensinger^o, A. Beretvas^o, P. Berge^o,
 S. Bertolucci^o, S. Bhadra^o, M. Binkley^o, R. Blair^o, C. Blocker^o, J. Boffill^o, A.W. Booth^o,
 G. Brandenburg^o, A. Brenner^o, D. Brown^o, A. Byon^o, K.L. Byrum^o, M. Campbell^o, R. Carey^o,
 W. Carithers^o, D. Carlsmith^o, J.T. Carroll^o, R. Cashmore^o, F. Cervelli^o, K. Chadwick^o, T. Chapin^o,
 G. Chiarelli^o, W. Chinowsky^o, S. Cihangir^o, A.G. Clark^o, D. Cline^o, T. Collins^o, D. Connor^o,
 M. Contreras^o, J. Cooper^o, M. Cordelli^o, M. Curatolo^o, C. Day^o, R. DelFabbro^o, M. Dell'Orso^o,
 L. DeMortier^o, T. Devlin^o, D. DiBitonto^o, R. Diebold^o, F. Dittus^o, A. DiVirgilio^o, R. Downing^o,
 G. Drake^o, T. Droegge^o, M. Eaton^o, J.E. Elias^o, R. Ely^o, S. Errede^o, B. Esposito^o, A. Feldman^o,
 B. Flaughner^o, E. Focardi^o, G.W. Foster^o, M. Franklin^o, J. Freeman^o, H. Frisch^o, Y. Fukui^o, I. Gaines^o,
 A. Garfinkel^o, P. Giannetti^o, N. Giokaris^o, P. Giromini^o, L. Gladney^o, M. Gold^o, K. Goulianos^o,
 J. Grimson^o, C. Grosso-Pilcher^o, C. Haber^o, S.R. Hahn^o, R. Handler^o, R.M. Harris^o, J. Hauser^o,
 Y. Hayashide^o, T. Hessing^o, R. Hollebeck^o, L. Holloway^o, P. Hu^o, B. Hubbard^o, P. Hurst^o, J. Huth^o,
 M. Ito^o, J. Jaekel^o, H. Jensen^o, U. Joshi^o, R.W. Kadel^o, I. Kamon^o, S. Kanda^o, I. Karliner^o,
 H. Kautsky^o, K. Kaslouski^o, E. Kearns^o, R. Kephart^o, P. Kesten^o, H. Keutelian^o, Y. Kikuchi^o,
 S. Kim^o, L. Kirsch^o, S. Kobayashi^o, K. Kondo^o, W. Krshuk^o, U. Kruse^o, S. Kuhlmann^o, A. Laasanen^o,
 W. Li^o, T. Liss^o, N. Lockyer^o, F. Marchetto^o, R. Markeloff^o, L.A. Markosky^o, M. Masuzawa^o,
 P. McIntyre^o, A. Mensione^o, T. Meyer^o, S. Mikamo^o, M. Miller^o, T. Mimaishi^o, S. Miscetti^o,
 M. Mishina^o, S. Miyashita^o, H. Miyata^o, N. Mondal^o, S. Mori^o, Y. Morita^o, A. Mukherjee^o,
 A. Murakami^o, Y. Muraki^o, C. Nelson^o, C. Newman-Holmes^o, J.S.T. Ng^o, L. Nodulman^o,
 J.O'Meara^o, G. Ott^o, T. Ozaki^o, S. Palanque^o, R. Paoletti^o, A. Para^o, J. Patrick^o, R. Perchonok^o,
 T.J. Phillips^o, H. Piskars^o, R. Plunkett^o, L. Pondrom^o, J. Proudfoot^o, G. Punzi^o, D. Quarrie^o,
 K. Ragan^o, G. Redlinger^o, R. Resmer^o, J. Rhoades^o, L. Ristori^o, T. Rohaly^o, A. Roodman^o,
 H. Sanders^o, A. Sansoni^o, R. Sard^o, V. Scarpine^o, P. Schlabach^o, E.E. Schmidt^o, P. Schoessow^o,
 M. Schub^o, R. Schwitters^o, A. Scribano^o, S. Segler^o, M. Sekiguchi^o, P. Sestini^o, M. Shapiro^o,
 M. Sheaff^o, M. Shibata^o, M. Shochet^o, J. Siegrist^o, V. Simaitis^o, J. Simmons^o, P. Sinervo^o,
 M. Siverts^o, J. Skarha^o, D.A. Smith^o, R. Snider^o, L. Spencer^o, R. St. Denis^o, A. Stefanini^o,
 Y. Takaiwa^o, K. Takikawa^o, S. Tarem^o, D. Theriot^o, J. Ting^o, A. Tollestrup^o, G. Tonelli^o,
 W. Trischuk^o, Y. Tsay^o, K. Turner^o, F. Ukegawa^o, D. Underwood^o, C. vanIngen^o, R. VanBerg^o,
 R. Vidal^o, R.G. Wagner^o, R.L. Wagner^o, J. Walsh^o, T. Watts^o, R. Webb^o, T. Westhusing^o,
 S. White^o, V. White^o, A. Wicklund^o, H.H. Williams^o, T. Winch^o, R. Yamada^o,
 T. Yamanouchi^o, A. Yamashita^o, K. Yasuoka^o, G.P. Yeh^o, J. Yoh^o, F. Zetti^o

CDF Member Institutions

- ^o Argonne National Laboratory-^o Brandeis University-^o University of Chicago
- ^o Fermi National Accelerator Laboratory-^o INFN, Frascati, Italy
- ^o Harvard University-^o University of Illinois-^o KEK, Japan
- ^o Lawrence Berkeley Laboratory-^o University of Pennsylvania
- ^o INFN, University of Pisa, Italy-^o Purdue University
- ^o Rockefeller University-^o Rutgers University-^o Texas A&M University
- ^o University of Tsukuba, Japan-^o University of Wisconsin

Visitors

- ^o Oxford University, England-^o INFN Trieste, Italy-^o Saga University, Japan
- ^o ICRR, Tokyo University, Japan-^o Haverford College, Haverford, PA.

APPENDIX B

TEST BEAM GAS SUPPLY SYSTEM

This appendix includes the floor plan for the CDF test beam facility gas supply control area outside the controlled access fence (Figure 70), schematic flow diagrams for the gas supply system up to each of the detector elements (Figures 71 to 76), and schematic flow diagrams for the gas pressure buffer systems located on the forward fixture and supporting the forward EM and hadron calorimeters (Figures 77 to 82). Finally, Table XVI has the current equipment list for the gas supply system. The coded labels for each component matches the label in the schematic flow diagrams.

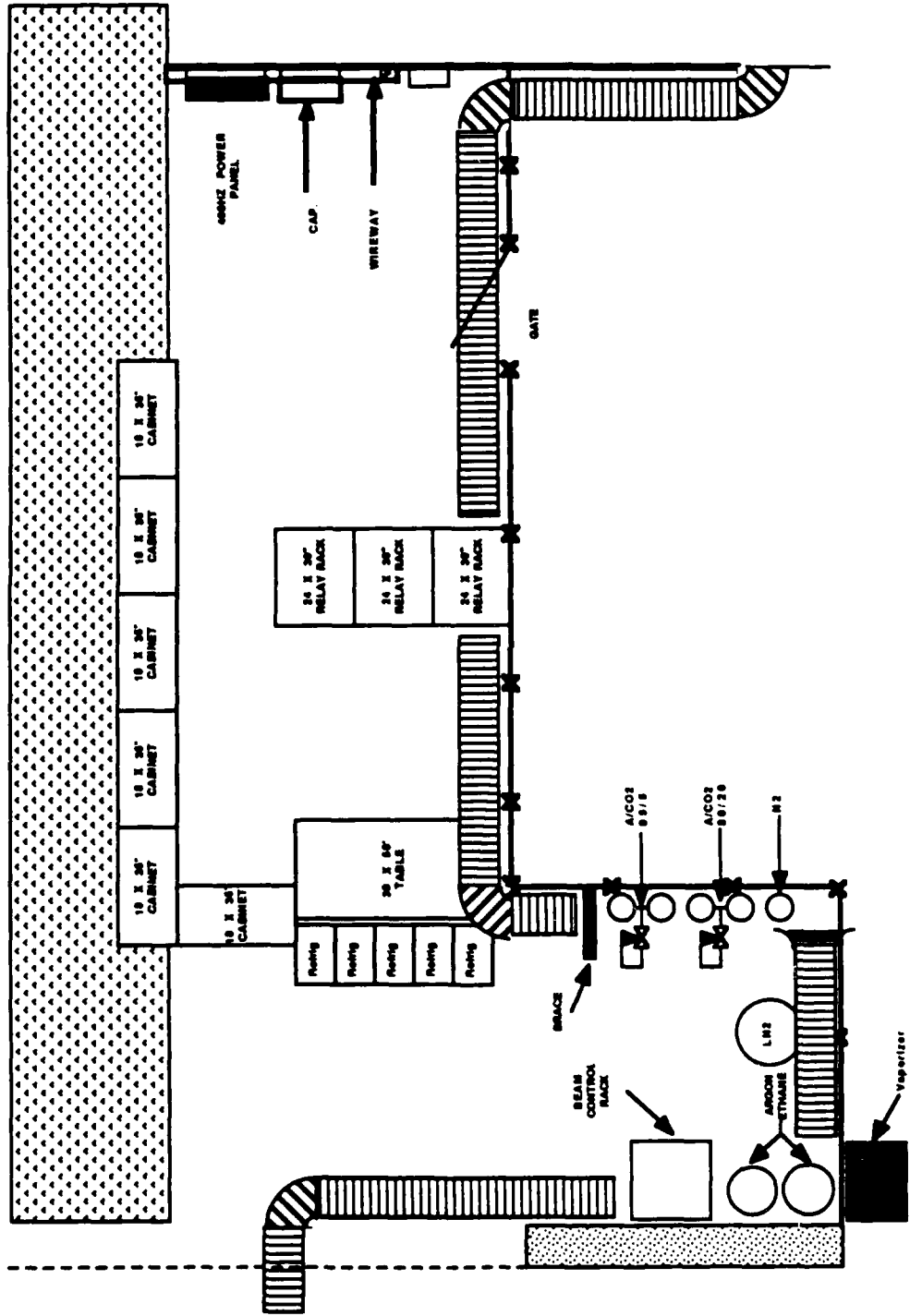


FIG. 70. CDF test beam facility gas supply control area.

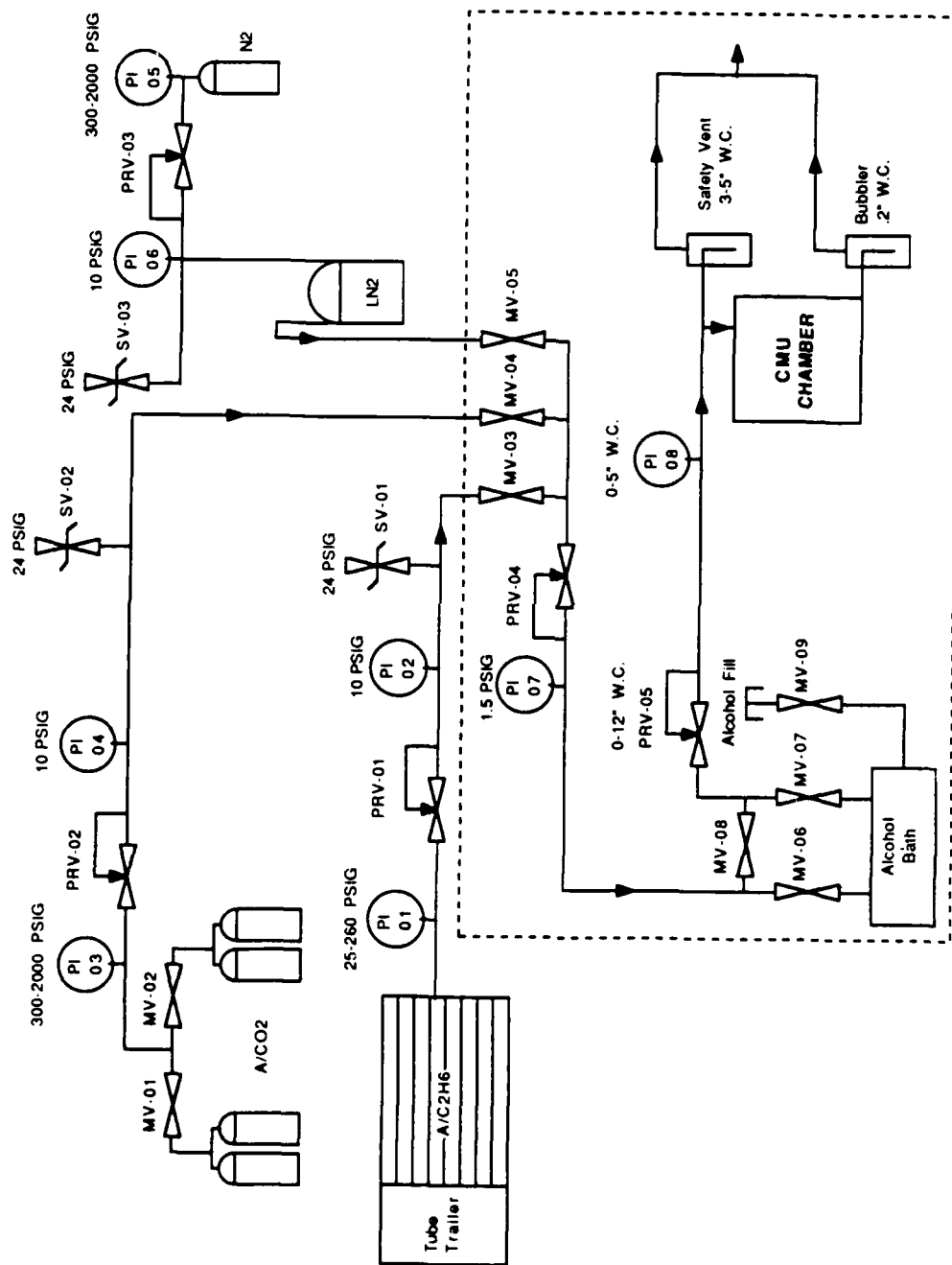


FIG. 71. Schematic flow diagram for the gas supply system to the Central Muon Detector chambers.

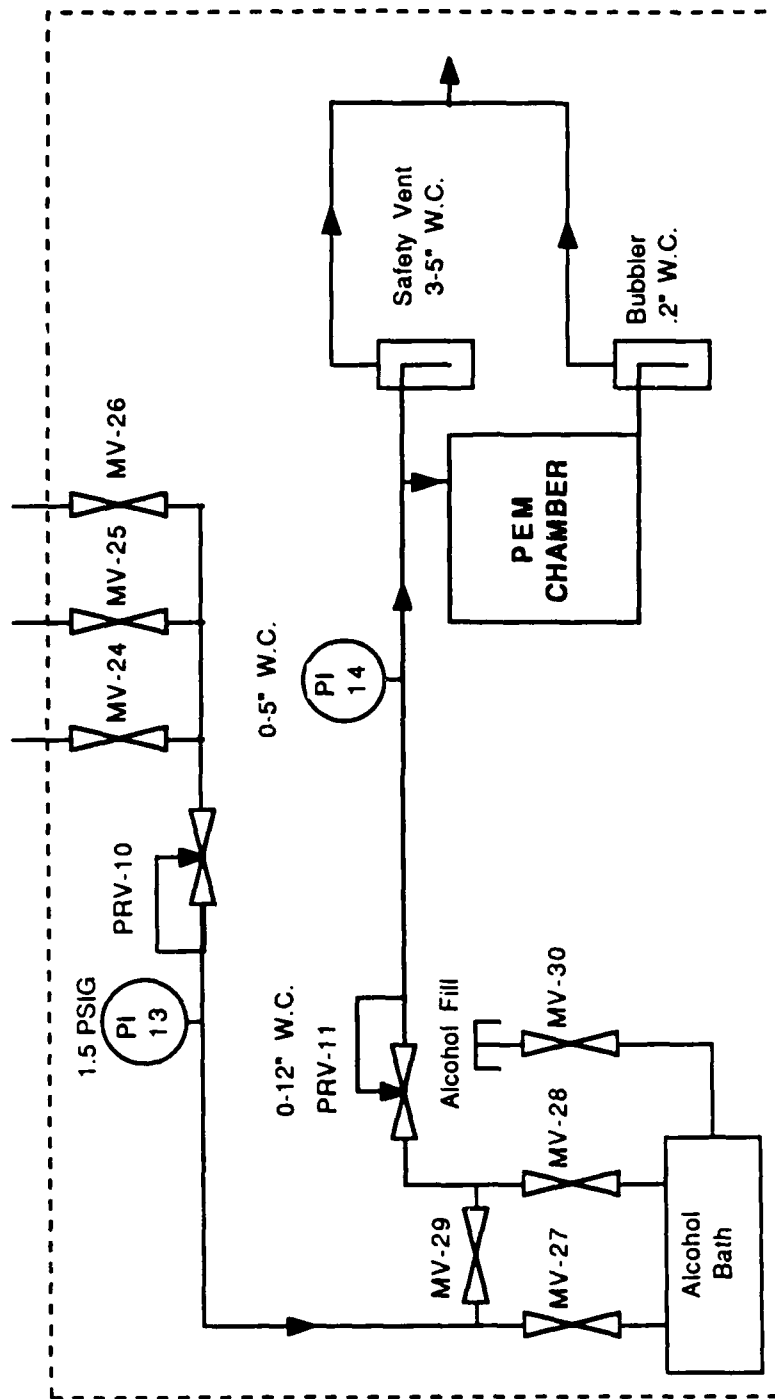


FIG. 72. Schematic flow diagram for the gas supply system to the endplug EM calorimeter chambers.

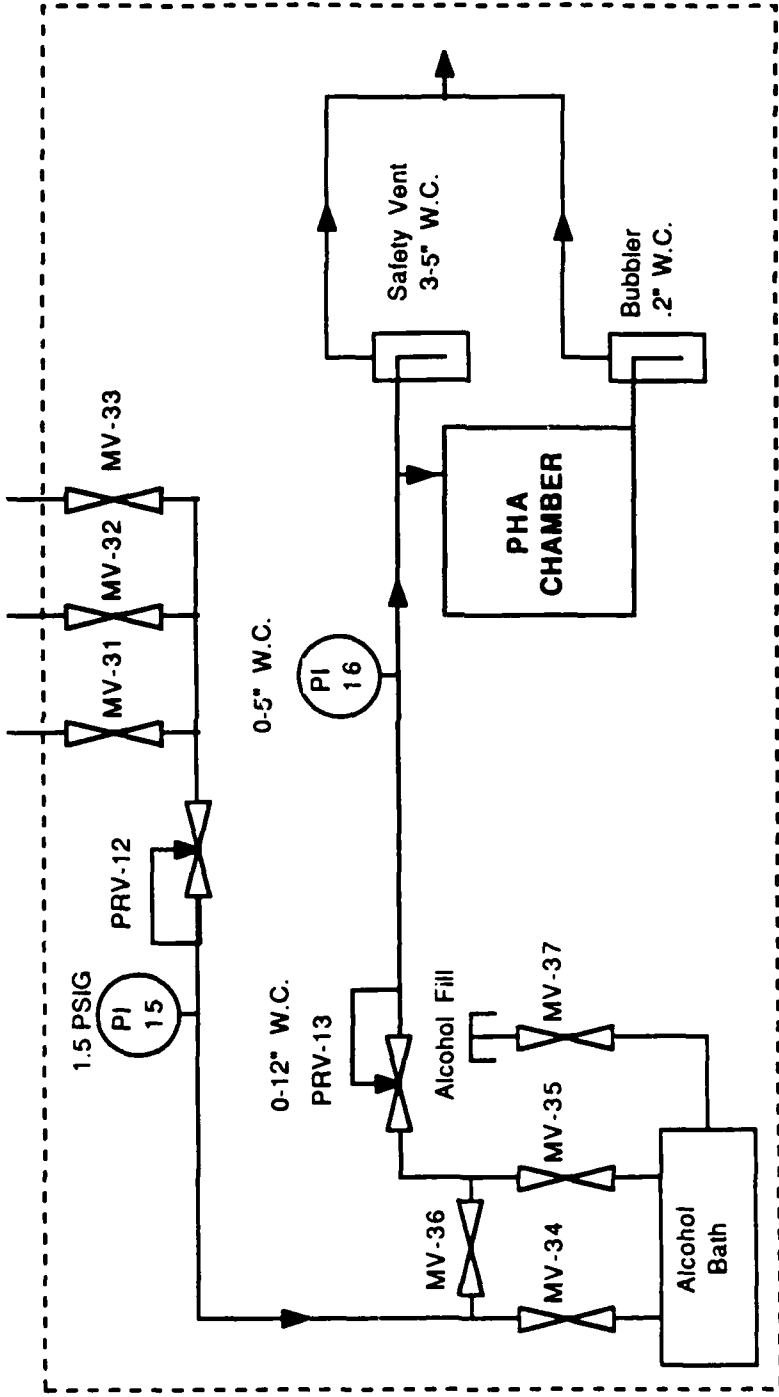


FIG. 73. Schematic flow diagram for the gas supply system to the endplug hadron calorimeter chambers.

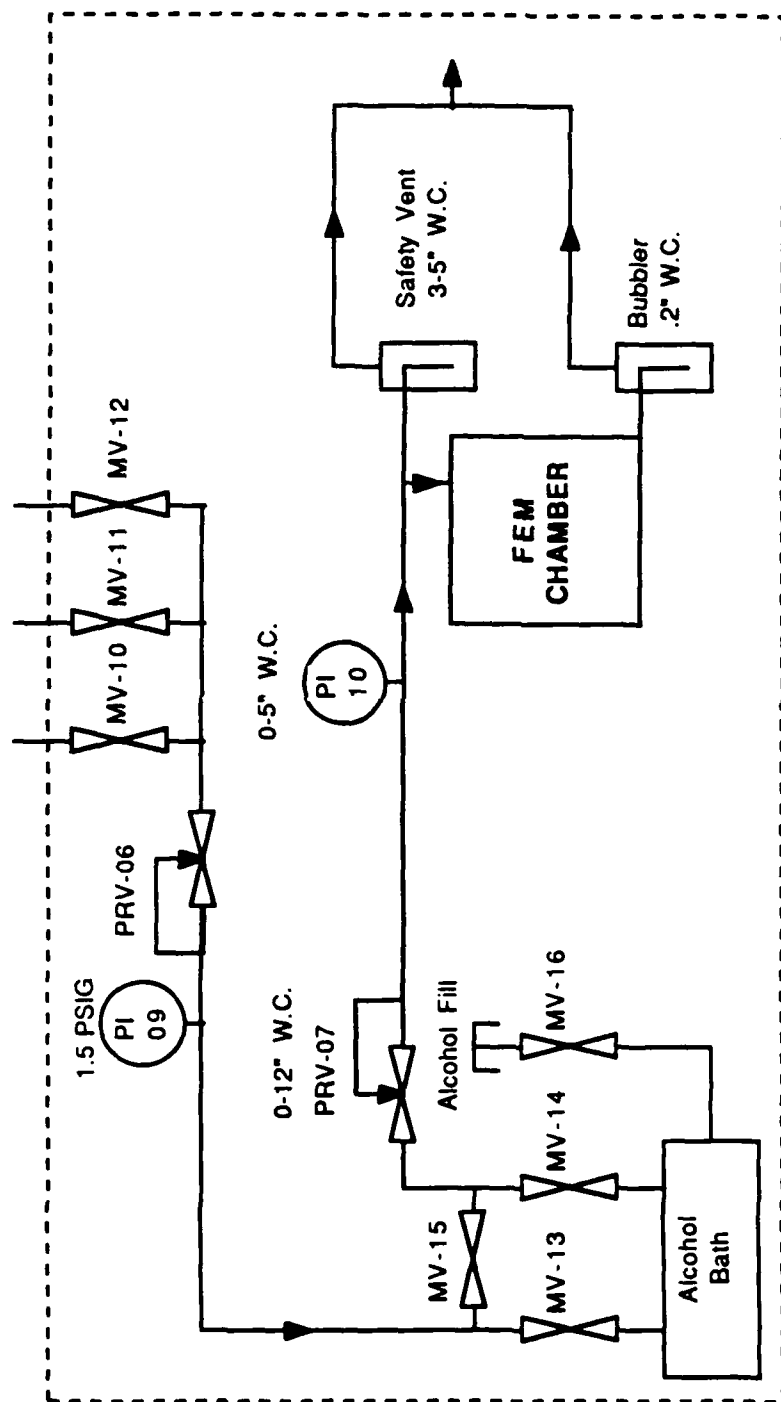


FIG. 74. Schematic flow diagram for the gas supply system to the forward EM calorimeter chambers.

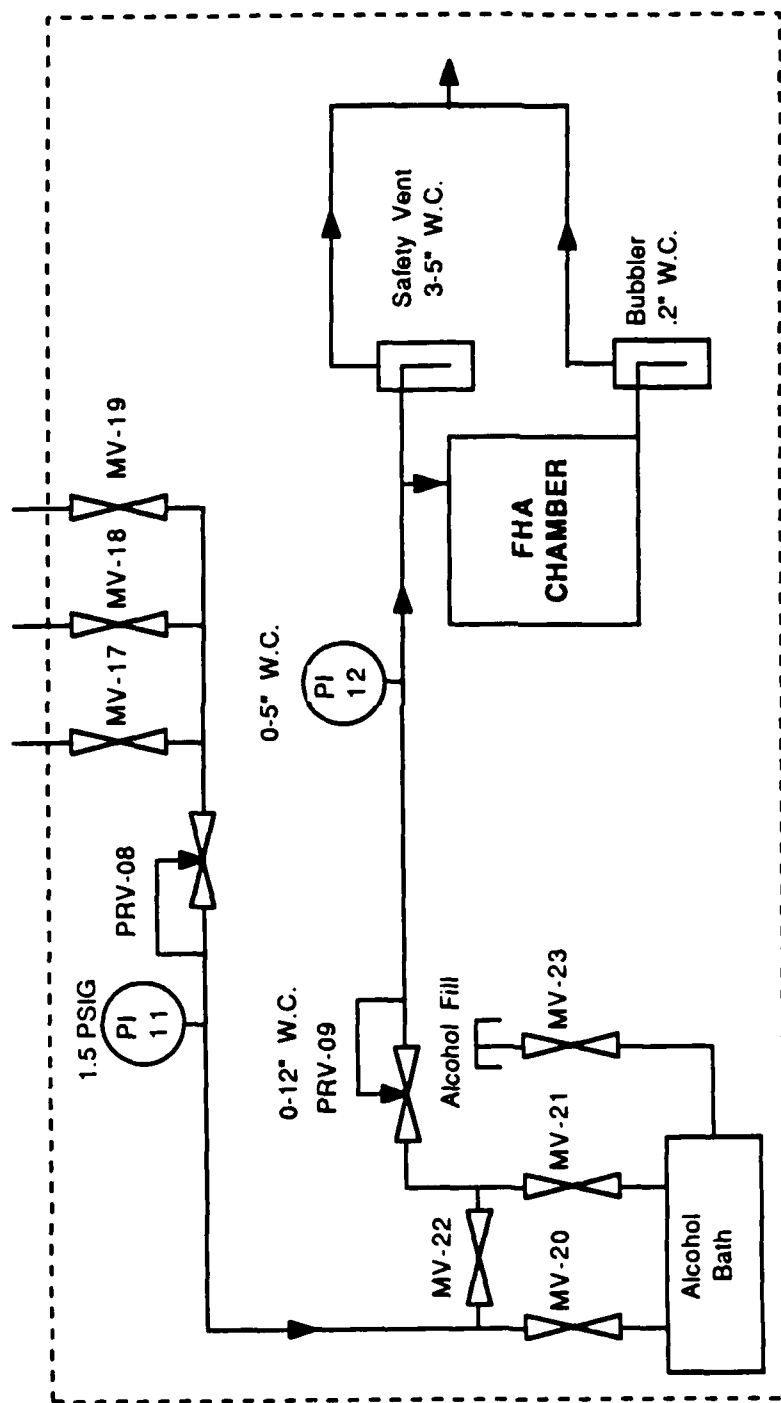


FIG. 75. Schematic flow diagram for the gas supply system to the forward hadron calorimeter chambers.

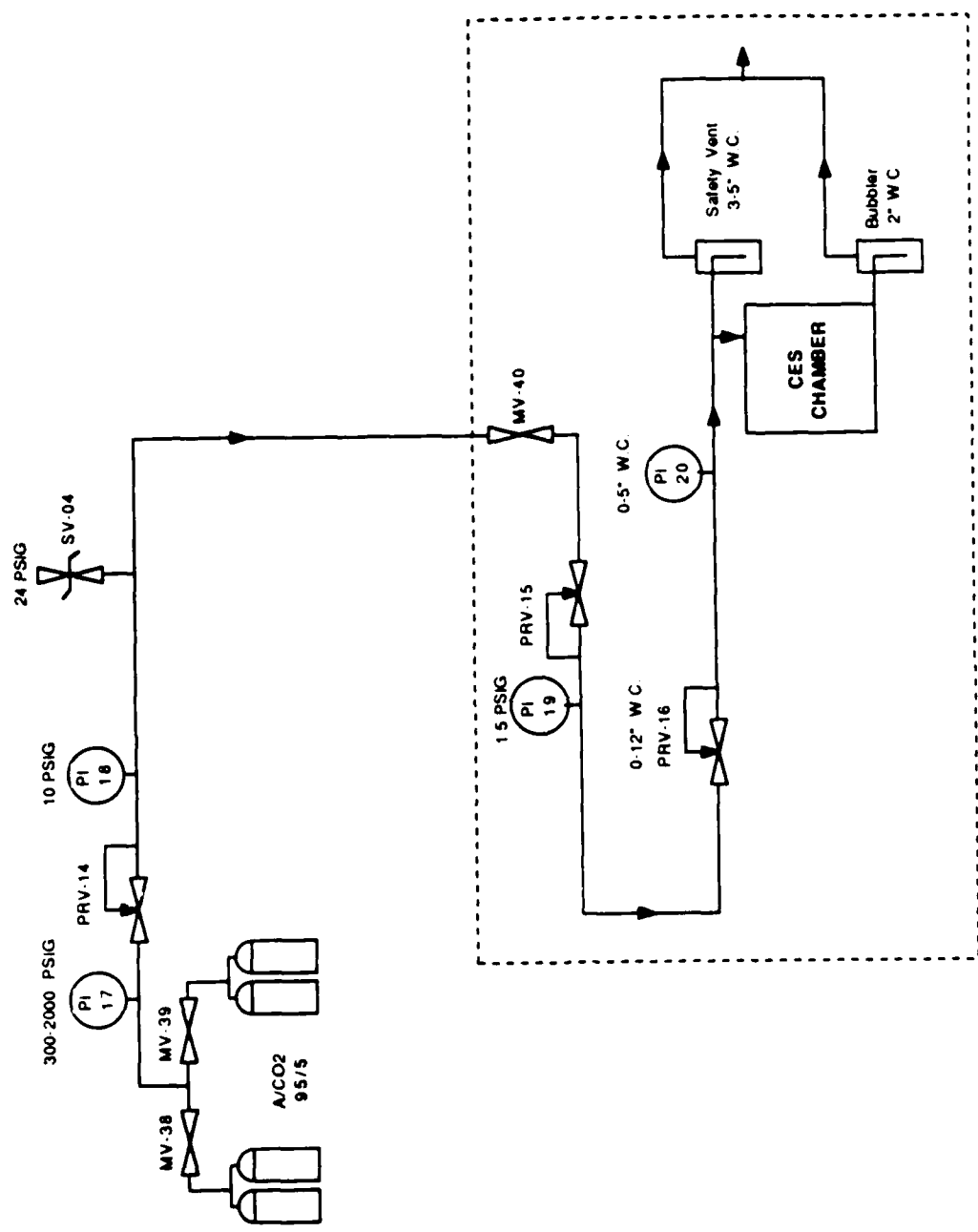


FIG. 76. Schematic flow diagram for the gas supply system to the Central EM Strip chambers.

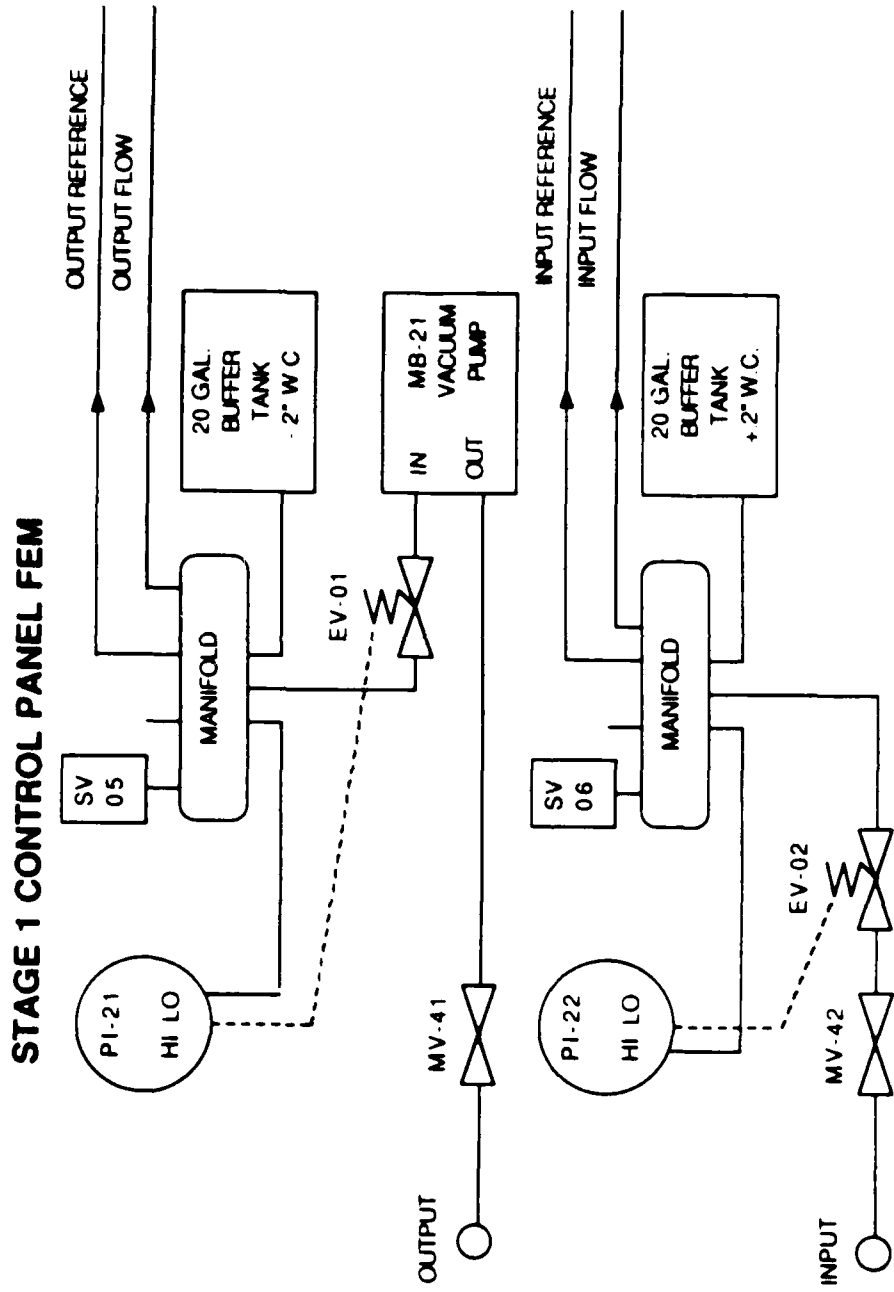


FIG 77. Schematic flow diagram for the stage 1 controls of the gas pressure buffer system for the forward EM calorimeter chambers.

STAGE 2 QUADRANT CONTROL PANEL FEM

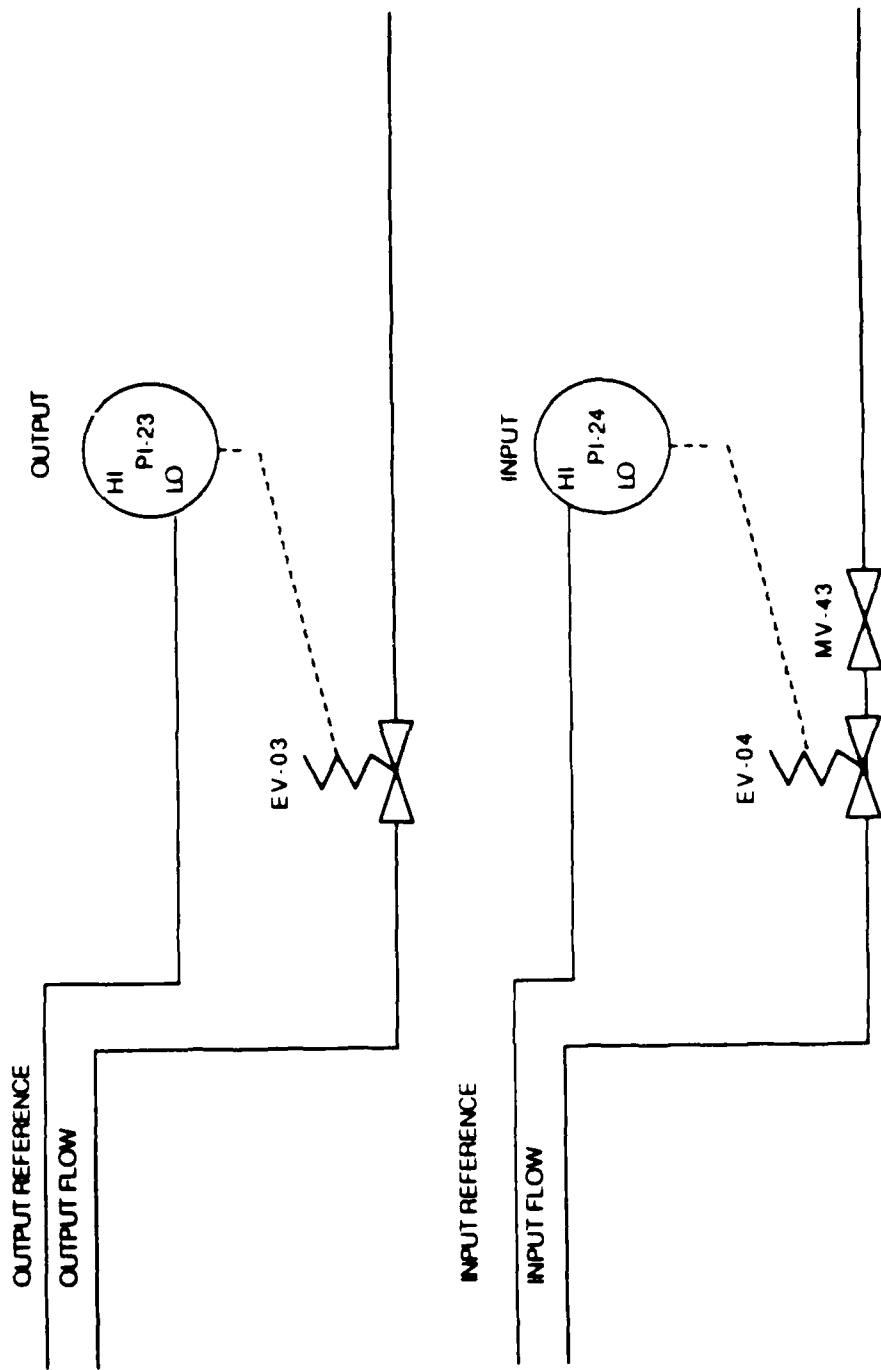


FIG 78. Schematic flow diagram for the stage 2 controls of the gas pressure buffer system for the forward EM calorimeter chambers.

DISTRIBUTION MANIFOLD FEM

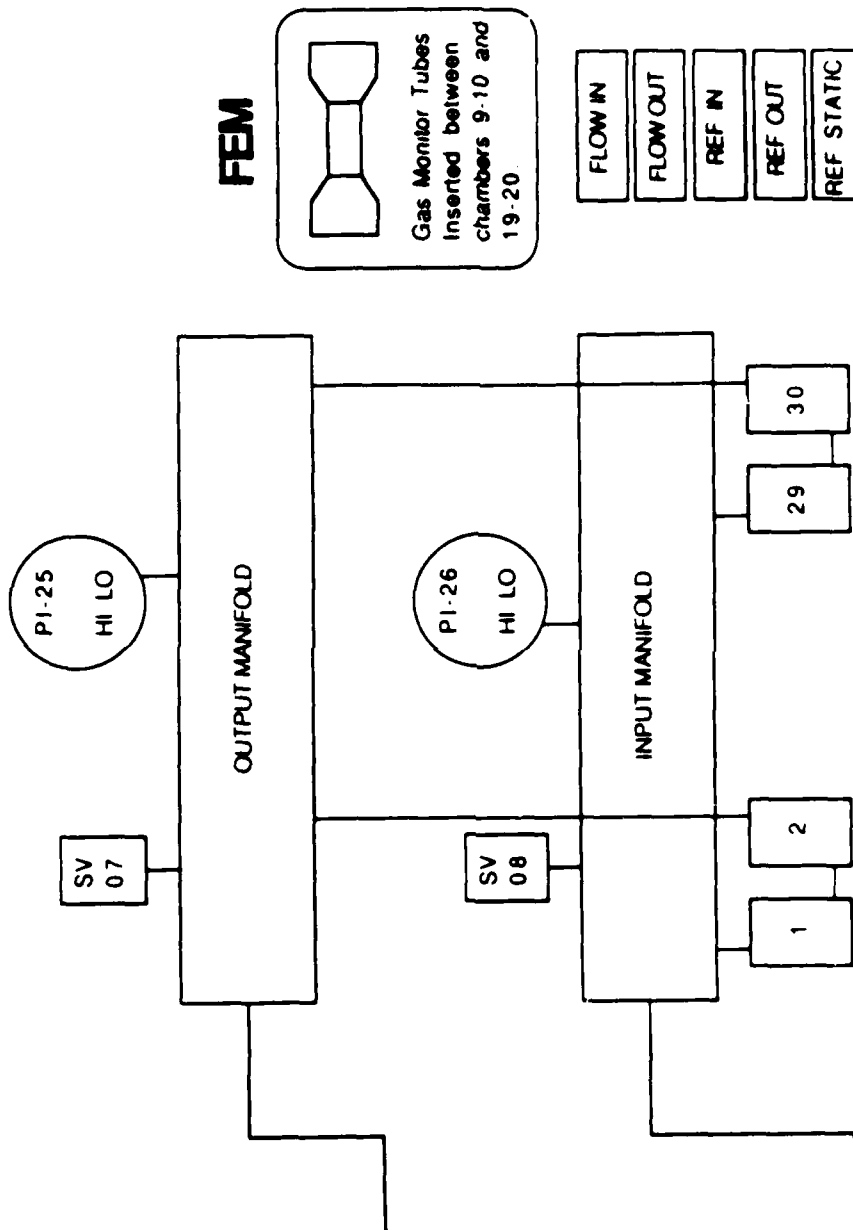


FIG. 79. Schematic flow diagram for the distribution manifold for the forward EM calorimeter chambers.

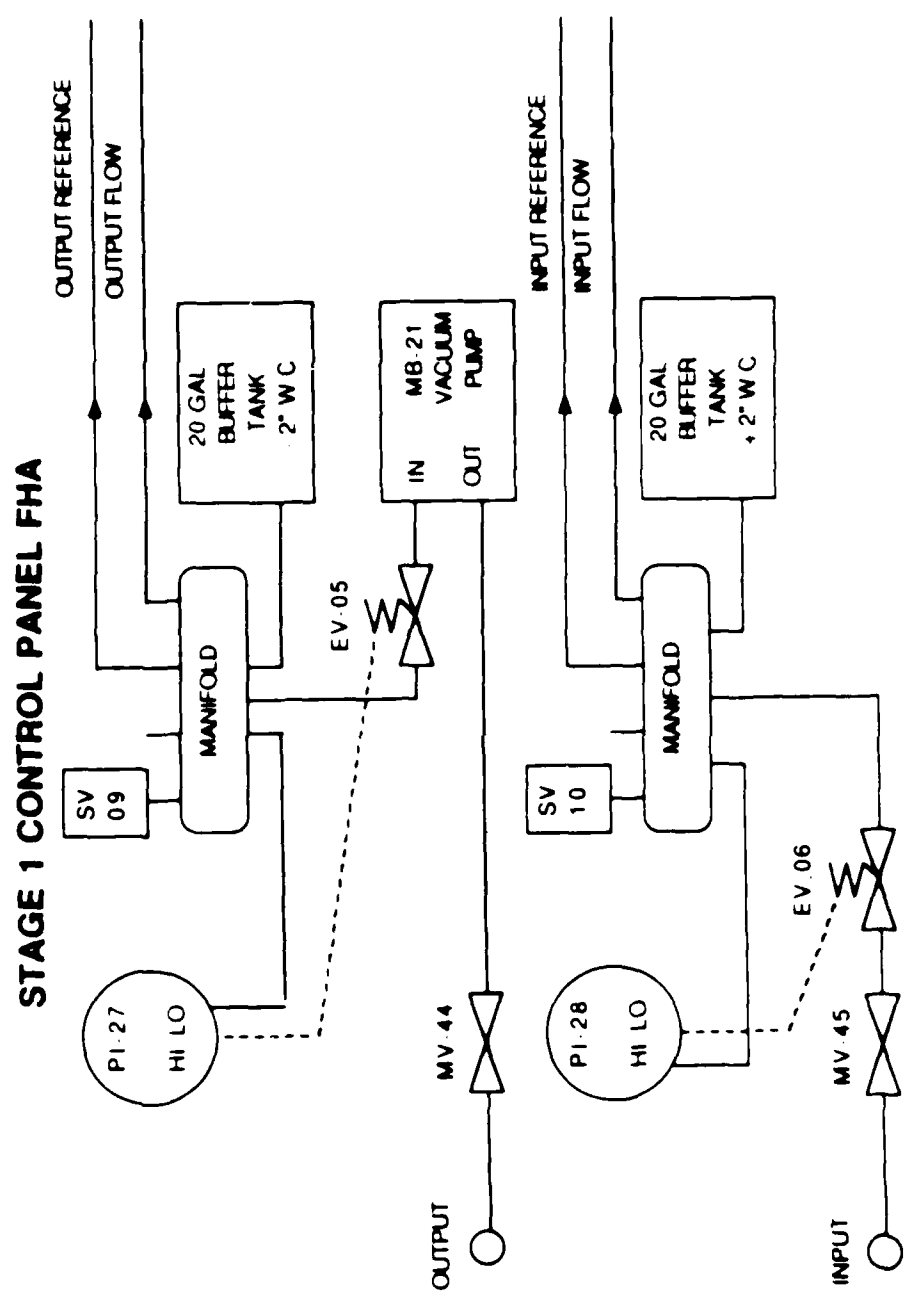


FIG 80. Schematic flow diagram for the stage 1 controls of the gas pressure buffer system for the forward hadron calorimeter chambers.

STAGE 2 QUADRANT CONTROL PANEL FHA

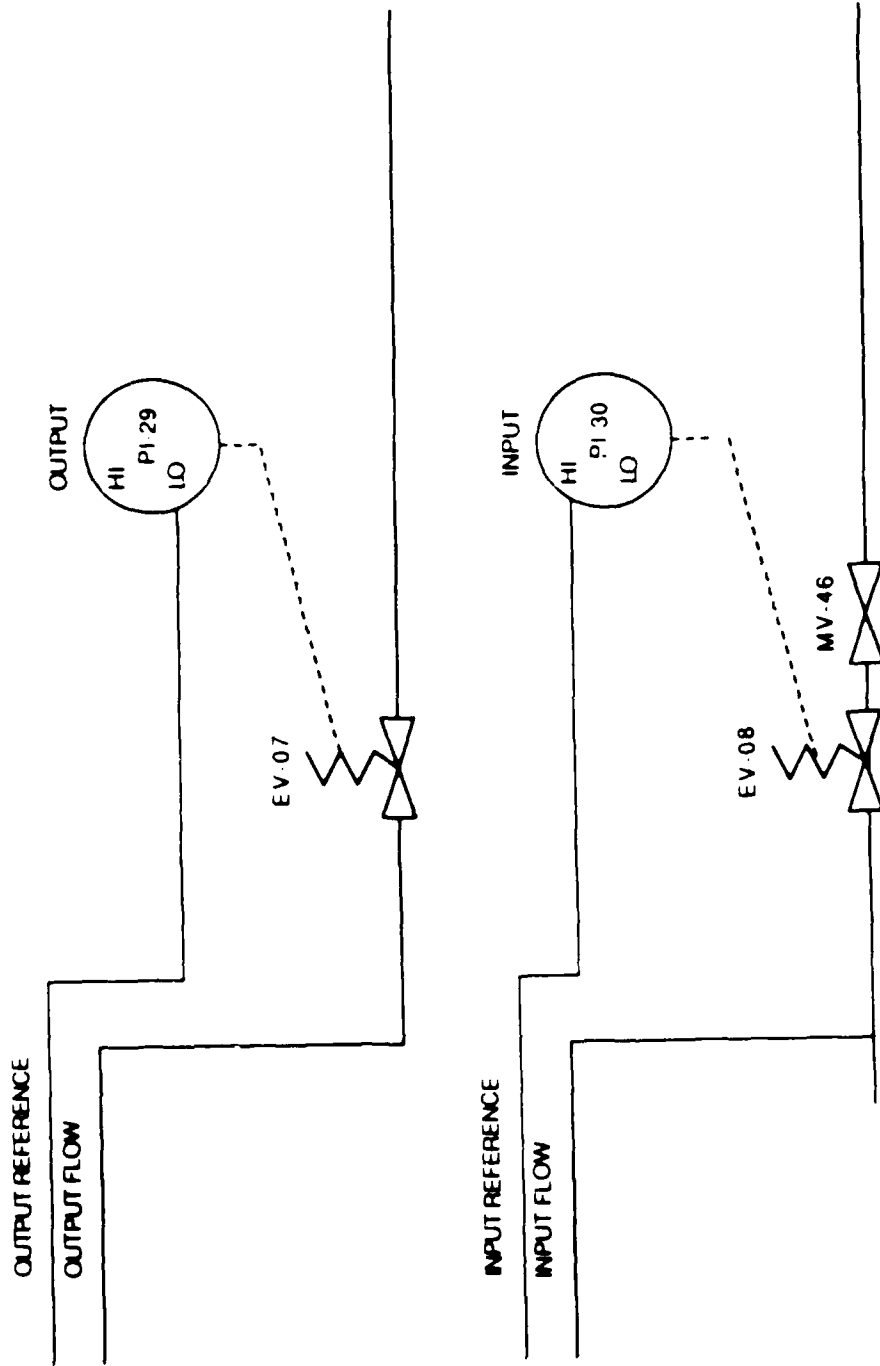


FIG 81. Schematic flow diagram for the stage 2 controls of the gas pressure buffer system for the forward hadron calorimeter chambers.

DISTRIBUTION MANIFOLD FHA

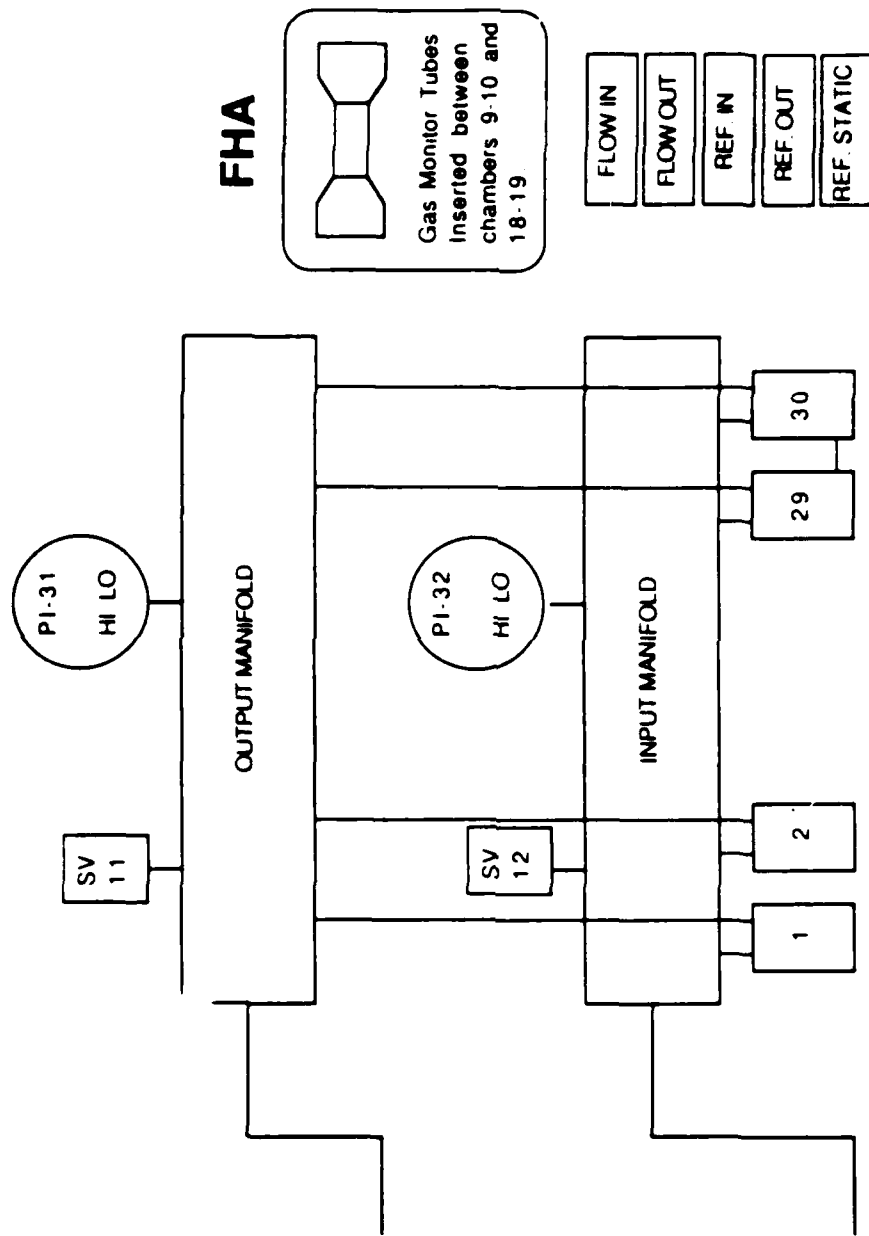


FIG. 82. Schematic flow diagram for the distribution manifold for the forward hadron calorimeter chambers.

TABLE XVI. Equipment list for the CDF test beam facility gas supply system.

10/20/87

CV-01	OIL CHECK VALVE (.2" W.C.)
CV-02	OIL CHECK VALVE (.2" W.C.)
CV-03	OIL CHECK VALVE (.2" W.C.)
CV-04	OIL CHECK VALVE (.2" W.C.)
CV-05	OIL CHECK VALVE (.2" W.C.)
CV-06	OIL CHECK VALVE (.2" W.C.)
EV-01	HUMPHREY V062E1-2-10-21-35 NC
EV-02	HUMPHREY V062E1-2-10-21-35 NC
EV-03	HUMPHREY V062E1-2-11-21-35 NO
EV-04	HUMPHREY V062E1-2-11-21-35 NO
EV-05	HUMPHREY V062E1-2-10-21-35 NC
EV-06	HUMPHREY V062E1-2-10-21-35 NC
EV-07	HUMPHREY V062E1-2-11-21-35 NO
EV-08	HUMPHREY V062E1-2-11-21-35 NO
MV-01	VICTOR #1125-0301
MV-02	VICTOR #1125-0301
MV-03	NUPRO #SS-4P4T4
MV-04	NUPRO #SS-4P4T4
MV-05	NUPRO #SS-4P4T4
MV-06	NUPRO #SS-4H-TW
MV-07	NUPRO #SS-4H-TW
MV-08	NUPRO #SS-4BK-TW
MV-09	NUPRO #SS-4H-TW
MV-10	NUPRO #SS-4P4T4
MV-11	NUPRO #SS-4P4T4
MV-12	NUPRO #SS-4P4T4
MV-13	NUPRO #SS-4H-TW
MV-14	NUPRO #SS-4H-TW
MV-15	NUPRO #SS-4BK-TW
MV-16	NUPRO #SS-4H-TW
MV-17	NUPRO #SS-4P4T4
MV-18	NUPRO #SS-4P4T4
MV-19	NUPRO #SS-4P4T4
MV-20	NUPRO #SS-4H-TW
MV-21	NUPRO #SS-4H-TW
MV-22	NUPRO #SS-4BK-TW
MV-23	NUPRO #SS-4H-TW
MV-24	NUPRO #SS-4P4T4
MV-25	NUPRO #SS-4P4T4
MV-26	NUPRO #SS-4P4T4
MV-27	NUPRO #SS-4H-TW
MV-28	NUPRO #SS-4H-TW
MV-29	NUPRO #SS-4BK-TW

TABLE XVI, Continued

MV-30	NUPRO #SS-4H-TW
MV-31	NUPRO #SS-4P4T4
MV-32	NUPRO #SS-4P4T4
MV-33	NUPRO #SS-4P4T4
MV-34	NUPRO #SS-4H-TW
MV-35	NUPRO #SS-4H-TW
MV-36	NUPRO #SS-4BK-TW
MV-37	NUPRO #SS-4H-TW
MV-38	VICTOR 1125-0301
MV-39	VICTOR 1125-0301
MV-40	NUPRO #B2454
MV-41	NUPRO #B2454
MV-42	NUPRO #B2454
MV-43	NUPRO #B2454
MV-44	NUPRO #B2454
MV-45	NUPRO #B2454
MV-46	NUPRO #B2454
PI-01	VICTOR #SR-450ME
PI-02	VICTOR #SR-450ME
PI-03	HELICOID OR USG
PI-04	HELICOID OR USG
PI-05	HELICOID OR USG
PI-06	HELICOID OR USG
PI-07	HELICOID OR USG
PI-08	MAGNEHELIC #2005
PI-09	HELICOID OR USG
PI-10	MAGNEHELIC #2005
PI-11	HELICOID OR USG
PI-12	MAGNEHELIC #2005
PI-13	HELICOID OR USG
PI-14	MAGNEHELIC #2005
PI-15	HELICOID OR USG
PI-16	MAGNEHELIC #2005
PI-17	HELICOID OR USG
PI-18	HELICOID OR USG
PI-19	HELICOID OR USG
PI-20	MAGNEHELIC #2005
PI-21	PHOTOHELIC 3002
PI-22	PHOTOHELIC 3002
PI-23	PHOTOHELIC 3000-0
PI-24	PHOTOHELIC 3000-0
PI-25	MAGNEHELIC 2002
PI-26	MAGNEHELIC 2002

TABLE XVI, Continued

PI-27	-----	PHOTOHELIC 3002
PI-28	-----	PHOTOHELIC 3002
PI-29	-----	PHOTOHELIC 3000-0
PI-30	-----	PHOTOHELIC 3000-0
PI-31	-----	MAGNEHELIC 2002
PI-32	-----	MAGNEHELIC 2002
PRV-01	-----	VICTOR #VTS-252A
PRV-02	-----	VICTOR #SR-450ME
PRV-03	-----	VICTOR #VTS-450B
PRV-04	-----	REGO #2403-SR9-5
PRV-05	-----	REGO #2403-SR9-5
PRV-06	-----	REGO #2403-SR9-5
PRV-07	-----	REGO #2403-C
PRV-08	-----	REGO #2403-C
PRV-09	-----	REGO #2403-C
PRV-10	-----	REGO #2403-C
PRV-11	-----	REGO #2403-C
PRV-14	-----	VICTOR #SR-450ME
PRV-15	-----	REGO #2403-SR9-5
PRV-16	-----	REGO #2403-C
SV-01	(24 PSIG) -----	ANDERSON GREENWOOD 83MC46-4
SV-02	(24 PSIG) -----	ANDERSON GREENWOOD 83MC46-4
SV-03	(24 PSIG) -----	ANDERSON GREENWOOD 83MC46-4
SV-04	(24 PSIG) -----	ANDERSON GREENWOOD 83MC46-4
SV-05	(1" W.C.) -----	OIL SAFETY VALVE
SV-06	(1" W.C.) -----	OIL SAFETY VALVE
SV-07	(.2" W.C.) -----	OIL SAFETY VALVE
SV-08	(.2" W.C.) -----	OIL SAFETY VALVE
SV-09	(1" W.C.) -----	OIL SAFETY VALVE
SV-10	(1" W.C.) -----	OIL SAFETY VALVE
SV-11	(.2" W.C.) -----	OIL SAFETY VALVE
SV-12	(.2" W.C.) -----	OIL SAFETY VALVE
SV-13	(3" W.C.) -----	OIL SAFETY VALVE
SV-14	(3" W.C.) -----	OIL SAFETY VALVE
SV-15	(3" W.C.) -----	OIL SAFETY VALVE
SV-16	(3" W.C.) -----	OIL SAFETY VALVE
SV-17	(3" W.C.) -----	OIL SAFETY VALVE
SV-18	(3" W.C.) -----	OIL SAFETY VALVE
REFRIGERATORS	-----	NESLAB RTE-210

APPENDIX C

MESON WEST BEAMLINE

The beamsheet for the Meson West (MW) beamline is at Table XVII. A schematic diagram with the MW beamline components plotted (not to scale) in the horizontal coordinate x versus the longitudinal coordinate z up to the MW6 enclosure is in Figure 83.

TABLE XVII. Meson West (MW) beamsheet.

MWEST PRIMARY BEAM			06/01/22		000 GEV	
Z CENT.	X CENT.	Y CENT.	ELEMENT CODE	POWER SUPPLY	B/O(KG) OR (KG/IN)	CURRENT (AMPS)
-1326.0	0.00	-11.07	S.Y. TRIM 2-4-40 ENCL.F2	M00H	0.000	
-1322.1	0.00	-11.02	S.Y. TRIM 2-4-40 ENCL.F2	M00V	0.000	
-702.1	0.00	-5.30	D2-0 VACUUM SWIC, BAYONET TYPE	M00WC		
-346.3	0.00	-0.00	F3-0 VACUUM SWIC, BAYONET TYPE	M01WC1		
-339.3	0.00	-0.01	MW/MC/NE 10FT. MOD. B1	M010-1	-11.312	1072
-320.1	0.00	-0.50	MW/MC/NE 10FT. MOD. B1	M010-2	-11.312	1072
-317.0	0.00	-0.41	MW/MC/NE 10FT. MOD. B1	M010-3	-11.312	1072
-306.0	0.00	-0.34	MW/MC/NE 10FT. MOD. B1	M010-4	-11.312	1072
-295.0	0.00	-0.28	MW/MC/NE 10FT. MOD. B1	M010-5	-11.312	1072
-283.0	0.00	-0.23	MW/MC/NE 10FT. MOD. B1	M010-6	-11.312	1072
-272.0	0.00	-0.20	MW/MC/NE 10FT. MOD. B1	M010-7	-11.312	1072
-200.5	0.00	-0.10	DUMMY 3-WAY LAMBERTSON			
-249.5	0.00	-0.16	MW/MC/NE 3-WAY LAMBERTSON	MW1W-1	-5.724	900
-238.5	0.01	-0.15	MW/MC/NE 3-WAY LAMBERTSON	MW1W-2	-5.724	900
-227.5	0.02	-0.13	MW/MC/NE 3-WAY LAMBERTSON	MW1W-3	-5.724	900
-216.5	0.04	-0.11	MW/MC/NE 3-WAY LAMBERTSON	MW1W-4	-5.724	900
-205.5	0.07	-0.10	MW/MC/NE 3-WAY LAMBERTSON	MW1W-5	-5.724	900
-104.5	0.11	-0.00	MW/MC/NE 3-WAY LAMBERTSON	MW1W-6	-5.724	900
-46.5	0.09	0.15	D1-0 VACUUM SWIC, BAYONET TYPE	MW1WC		
07.3	1.23	0.30	21' ED/S DIPOLE, ROLLED 1.5 DEG.	MW2WD1-1	-23.094	2284
100.3	1.43	0.39	21' ED/S DIPOLE, ROLLED 1.5 DEG.	MW2WD1-2	-23.094	2284
110.0	1.59	0.41	• MT .1% AL TARGET, NOT MOVEABLE	MT2T0T0		
129.3	1.74	0.42	21' ED/S DIPOLE, ROLLED 1.5 DEG.	MW2WD1-3	-23.094	2284
145.2	2.05	0.43	• MT 240 GEV TARGET, MOVEABLE	MT2T0T1		
151.2	2.17	0.44	0-3-120, ROLLED 10.05 DEG.	MW2WD2-1	-12.000	747
167.3	2.31	0.45	• MT 100 GEV TARGET, MOVEABLE	MT2T0T2		
163.5	2.45	0.45	0-3-120, ROLLED 10.05 DEG.	MW2WD2-2	-12.500	747
109.0	2.01	0.45	• MT 80 GEV TARGET, MOVEABLE	MT2T0T3		
175.7	2.77	0.45	0-3-120, ROLLED 10.05 DEG.	MW2WD2-3	-12.500	747
233.5	4.10	0.45	QUAD 3Q120	MW2Q1	2.900	60
202.0	5.27	0.44	QUAD 3Q120	MW2Q2	-4.002	62
200.1	5.40	0.44	5.5-2.07-00	MW2V		
200.0	5.07	0.44	90° VAC. BEAM STOP	MW2B5		

TABLE XVII, Continued

WEST PRIMARY BEAM		Z CENT.	X CENT.	Y CENT.	ELEMENT CODE	POWER SUPPLY	800 GEV B/O(KG) OR (KG/IN)	CURRENT (AMPS)
366.5	5.86	.44	366.5' WALL		MW6WC			
414.0	6.46	.44	414' AREA		MW5Q1-1	3.471	66	
696.3	15.23	.42	700' AREA		MW5Q1-2	3.471	66	
1003.0	22.64	.40	1000' CROSS-OVER		MW5Q2	3.471	66	
1222.0	27.91	.38	1222' AREA		MW5Q3-1	-3.034	72	
1226.3	28.02	.38	D2-G VACUUM SWIC, BAYONET TYPE		MW5Q3-2	-3.034	72	
1232.0	28.15	.38	QUAD 3Q120		MW5Q4-1	-3.034	72	
1243.0	28.42	.38	QUAD 3Q120		MW5Q4-2	-3.034	72	
1254.0	28.60	.38	QUAD 3Q120		MW6H			
1275.0	29.19	.38	QUAD 3Q120		MW6V			
1286.0	29.46	.38	QUAD 3Q120		MW6SEM			
1297.0	29.72	.38	QUAD 3Q120		MW6WC			
1308.0	29.98	.38	QUAD 3Q120		MW6TOT			
1316.5	30.19	.38	5.5-2.87-60 HORIZ. VERNIER					
1322.5	30.33	.38	5-1.6-80 VERT. VERNIER					
1327.0	30.44	.38	SEM					
1421.0	32.71	.87	1 MM AIR SWIC					
1424.0	32.70	.87	PRIMARY TARGET					

TABLE XVII, Continued

MW SECONDARY	Z CENT.	X CENT.	ELEMENT CODE	POSITION	POWER SUPPLY	06/06/12.	
						060 GEV B/Q(KG) OR (KG/IN)	CURRENT (AMPS)
	1424.0	32.70		BEGINNING OF BEAM			
	1430.2	32.93		EARLY BEND MAGNET	MW6W-1	10.500	000
	1444.2	33.30		EARLY BEND MAGNET	MW6W-2	10.500	000
	1450.2	33.69		EARLY BEND MAGNET	MW6W-3	10.500	000
	1477.1	34.25		DUMP COLLIMATOR - 239"			
	1494.0	34.70		S1 SPOILER - 150 X 62 X 80	MW7S-1		
	1506.0	35.09	3Q120		MW7Q1-1	-3.308	07
	1517.0	35.45	3Q120		MW7Q1-2	-3.308	07
	1530.0	35.84		SPOILER - 144 X 98 X 130	MW7S-2		
			WC1 - 2 MM VACUUM SWIC		MW7WC1		
			BEAM STOP		MW7BS		
	1555.3	36.00		VERTICAL COLLIMATOR - 96"	MW7CV1		
	1564.0	36.88		HORIZONTAL COLLIMATOR - 96"	MW7CH1		
	1576.3	37.20	3Q120		MW7Q2-1	2.094	52.3
	1591.0	37.70	82 BEND MAGNET 4 X 2 X 240		MW7W1	9.305	2320
	1600.3	38.24	3Q120		MW7Q2-2	2.094	52.3
	1619.0	38.61	3Q120		MW7Q3-1	2.094	52.3
	1631.3	38.99	3Q120		MW7Q3-2	2.094	52.3
	1670.3	40.47	3Q120		MW7Q4-1	-3.308	07
	1687.0	40.85	3Q120		MW7Q4-2	-3.308	07
	1699.2	41.22	3Q120		MW7Q5	-3.308	07
	1707.2	41.49		VERTICAL VERNIER, X 4 X 30	MW7V-1	0.000	
	1711.2	41.62		VERTICAL VERNIER, X 4 X 30	MW7V-2	0.000	
	1710.2	41.70		HORIZONTAL VERNIER 4 X 4 X 30	MW7H	0.000	
	1770.5	43.03		SWIC - 2MM, VACUUM	MW7WC2		
	1783.7	44.00		VERTICAL COLLIMATOR - 96"	MW7CV2		
	1792.7	44.30		HORIZONTAL COLLIMATOR - 96"	MW7CH2		
	1803.2	44.64	3Q120		MW7Q0-1	3.154	00
	1814.7	45.02	3Q120		MW7Q0-2	3.154	00
	1831.7	45.50	S3 - SPOILER - 30 X 30 X 240		MW7S-3		
	1850.2	46.49	82 BEND MAGNET 4 X 2 X 240		MW7W2-1	7.003	1940
	1860.0	47.25	82 BEND MAGNET 4 X 2 X 240		MW7W2-2	7.003	1940
	1901.7	48.03	S4 - SPOILER - 30 X 30 X 240		MW7S-4		

TABLE XVII, Continued

MW SECONDARY	POSITION			POWER SUPPLY	000 GEV B/G(KG) OR (KG/IN)	00/05/12. CURRENT (AMPS)
	Z CENT.	X CENT.	ELEMENT CODE			
1934.1	49.26		3Q120	MW8Q1-1	-2.075	52
1946.0	49.69		3Q120	MW8Q1-2	-2.075	52
1967.1	50.12		3Q120	MW8Q2	-2.075	52
1975.1	50.00		55 - SPOILER - 36 X 36 X 204	MW7S-5	.020	
1990.1	51.30		3Q120	MW8Q3-1	2.014	40
2001.0	51.79		3Q120	MW8Q3-2	2.014	40
2013.1	52.23		3Q120	MW9Q4	2.014	40
2020.5	52.00		82 BEND MAGNET 4 X 2 X 240	MW7W2-3	7.803	1940
2042.3	53.30		VERTICAL VERNIER, 4 X 4 X 30	MW8V1-1	0.000	
2049.3	53.62		VERTICAL VERNIER, 4 X 4 X 30	MW8V1-2	0.000	
2050.0	53.07		2 MM VACUUM SWIC - AIR	MW8WC1		
2132.4	56.97		DIFF. CERENKOV COUNTER - 150 FT.			
2219.0	00.44		2 MM VACUUM SWIC - AIR	MW8WC2		
2224.0	00.00		VERTICAL COLLIMATOR - 90°	MW8CV		
2234.4	01.00		HORIZONTAL COLLIMATOR - 90°	MW8CH		
2244.2	01.46		3Q120			
2255.7	01.91		3Q120		2.512	50
2272.0	02.69		VERT. CALIB. MAG. - 3 X 6 X 120	MW8Q5-2	2.512	50
2300.0	03.71		3Q120	MW8D	0.000	
2312.1	04.17		3Q120	MW8Q0-1	-3.230	04
2323.0	04.03		3Q120	MW8Q0-2	-3.230	04
2303.0	06.24		3Q120	MW8Q7	-3.230	04
2375.1	06.70		3Q120	MW8Q0-1	2.512	50
2380.0	07.10		3Q120	MW8Q0-2	2.512	50
2394.0	07.48		VERTICAL VERNIER, 4 X 4 X 30	MW8Q9	2.512	50
2398.0	07.04		VERTICAL VERNIER, 4 X 4 X 30	MW8V2-1	0.000	
2403.0	07.04		VERTICAL VERNIER, 4 X 4 X 30	MW8V2-2	0.000	
2450.0	09.70		HORIZONTAL VERNIER, 4 X 4 X 30	MW8H	0.000	
2453.0	09.82		1 MM SWIC	MW9WC		
			END OF BEAM LINE -- EXPERIMENTAL TARGET			

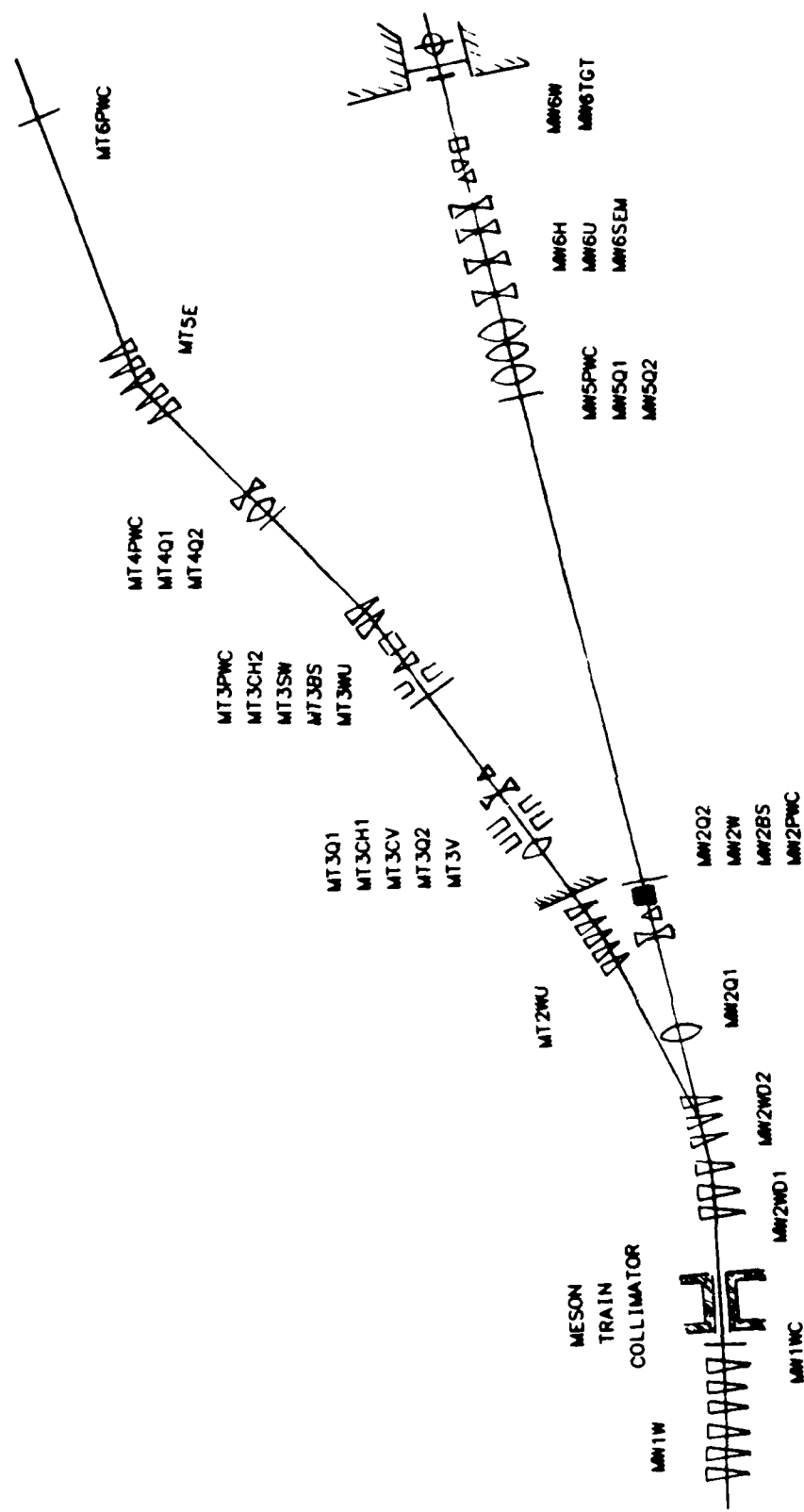


FIG. 83. Meson West (MW) beamline components plotted in x vs. z up to the MW6 enclosure.

APPENDIX D

BEAM TRANSPORT HISTOGRAMS

This appendix includes histograms produced by the TURTLE program package used to analyze beam transport capabilities of the Meson Test (MT) beamline in producing and transporting 227 GeV secondary pions to the CDF target area. The program "threw" 30,000 rays to simulate secondary pions produced at the MT2TGT1 (0.6" Pb) target. All histograms plot the resulting rays reaching the MT6PWC1 proportional wire chamber just upstream of the CDF target area. Information plotted includes: particle distribution versus horizontal coordinate x (Figure 84), particle distribution versus vertical coordinate y (Figure 85), particle density in the x - y plane (Figure 86), particle momentum versus x (Figure 87), and particle distribution versus momentum (Figure 88). These results are quite similar to those for the transport of other 227 GeV secondary hadrons as well those for the transport of 151 and 75 GeV secondary hadron beams.

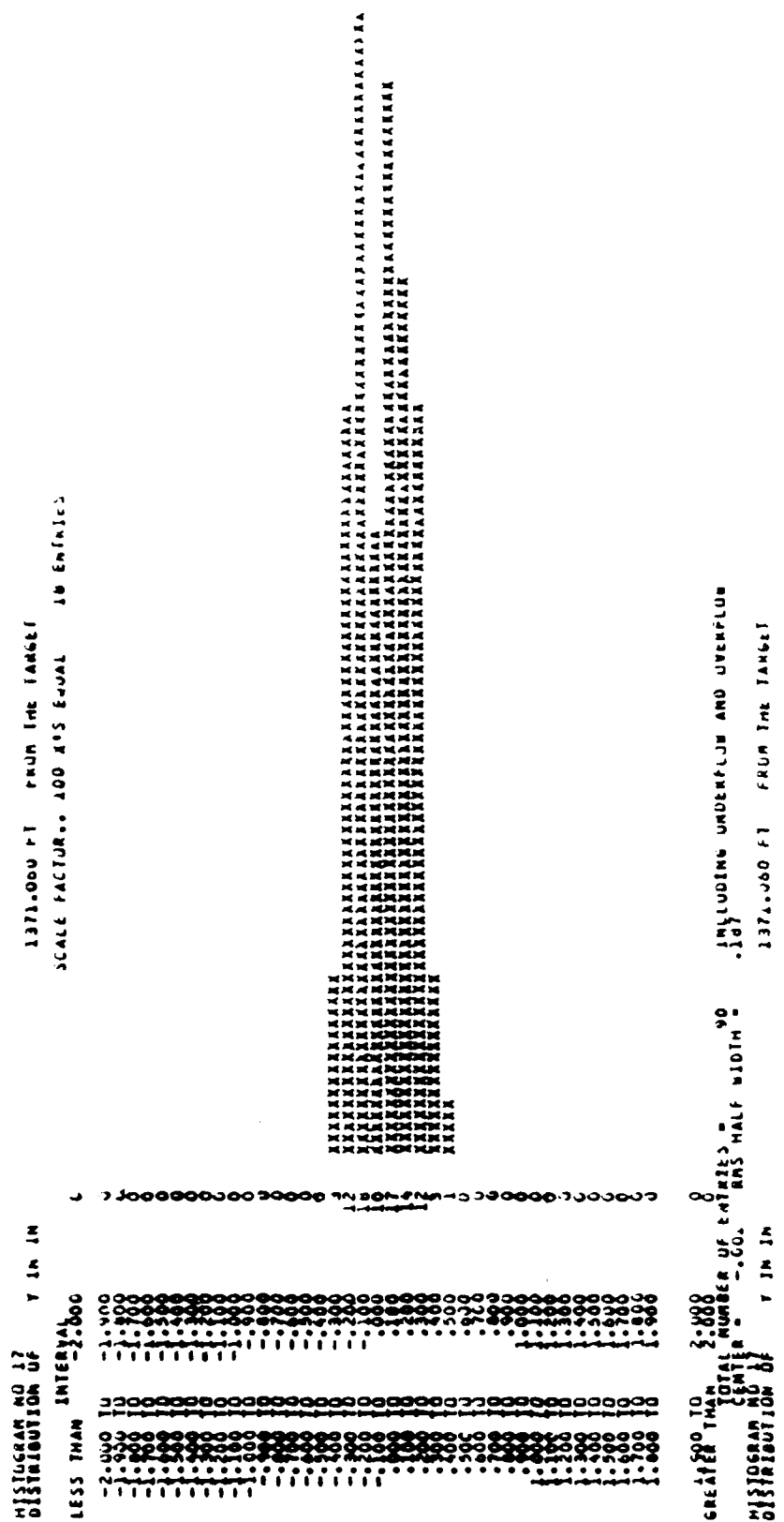


FIG. 85. Particle distribution vs. vertical coordinate y at the CDF target area.

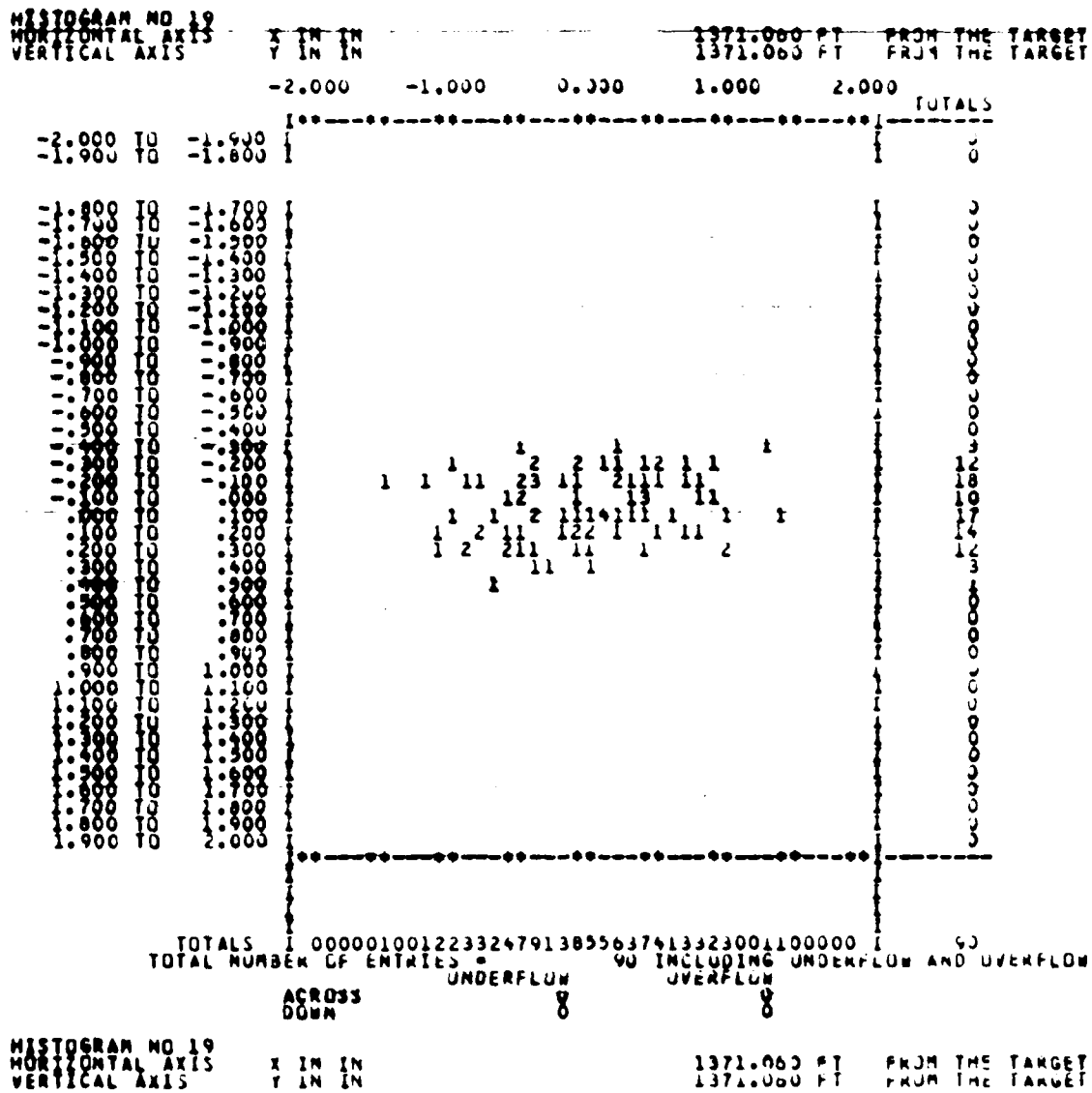


FIG. 86. Particle density in the x y plane at the CDF target area.

VITA

Henry Gerhart Franke III was born in Fort Wayne, Indiana, on 26 September 1955. His parents are Henry G. Franke, Jr. and Gisela Franke. He graduated from Copperas Cove High School in Copperas Cove, Texas, in 1973. He attended Texas A&M University as a member of the Corps of Cadets and graduated with a Bachelor of Science degree in Chemical Engineering in 1977. Upon graduation, he was commissioned a Second Lieutenant in the United States Army Chemical Corps. He has served with the 101st Airborne Division (Air Assault) at Fort Campbell, Kentucky, the 2d Infantry Division in the Republic of Korea, and the 82d Airborne Division at Fort Bragg, North Carolina, where he commanded the 21st Chemical Company (Airborne). His permanent mailing address is: 518 Louise Street, Copperas Cove, Texas 76522.

END

DATE

FILMED

MARCH

1988

DTIC